JSCSEN 80(2)127–277(2015)

ISSN 1820-7421(Online)

Journal of the Serbian Chemical Society

Electronic Version

Volume 80 : : 2015 : : 85 Years of the Journal

1930 Glasnik Hemijskog Društva Kraljevine Jugoslavije
Journal of the Chemical Society of the Kingdom of Yugoslavia

1947 Glasnik hemijskog društva Beograd
Journal of the Chemical Society of Belgrade

1985 Journal of the Serbian Chemical Society

VOLUME 80

No 2

BELGRADE 2015

Available on line at

www.shd.org.rs/JSCS/

The full search of JSCS is available through

DOAJ DIRECTORY OF OPEN ACCESS JOURNALS

www.doaj.org

Journal of the Serbian Chemical Society
JSCS-info@shd.org.rs • www.shd.org.rs/JSCS

J. Serb. Chem. Soc. Vol. 80, No. 2 (2015)

CONTENTS

Published by the Serbian Chemical Society
Karnegijeva 4/III, P.O. Box 36, 11120 Belgrade, Serbia
Printed by the Faculty of Technology and Metallurgy
Karnegijeva 4, P.O. Box 35-03, 11120 Belgrade, Serbia

Journal of the Serbian Chemical Society
JSCS-info@shd.org.rs • www.shd.org.rs/JSCS
J. Serb. Chem. Soc. 80 (2) 127–136 (2015)
JSCS–4703
UDC 547.979.733+547.233+547.962.9+547.21.024+547.497+542.97:615.27
Original scientific paper

Novel hybrids of oxoisoaporphine–tryptamine as inhibitors of acetylcholinesterase-induced *β*-amyloid aggregation with improved antioxidant properties

HAI-TAO ZHAO, SHU-MING ZHONG, JIANG-KE QIN and HUANG TANG*

Key Laboratory for the Chemistry and Molecular Engineering of Medicinal Resources, School of Chemistry and Pharmaceutical Sciences of Guangxi Normal University, Guilin 541004, China

(Received 18 March, revised 3 September, accepted 10 September 2014)

Abstract: A series of dual binding site acetylcholinesterase (AChE) inhibitors was designed, synthesized, and tested for their antioxidant ability and inhibitory potency on AChE and AChE-induced *β*-amyloid (A*β*) aggregation. The new hybrids consisted of a unit of 1-azabenzanthrone and tryptamine or its derivative, connected through an *α*,*ω*-alka(e)nediamide bridge. These hybrids exhibited moderate AChE inhibitory activity with IC_{50} values in the micromolar range and significant *in vitro* inhibitory activity towards AChE-induced A*β* aggregation. Moreover, six of the nine hybrids of this series exhibited a higher oxygen radical absorbance capacity than trolox, which makes them promising anti-Alzheimer drug candidates.

Keywords: Alzheimer's disease; acetylcholinesterase inhibitor; A*β* anti-aggregating activity; oxoisoaporphine–tryptamine.

INTRODUCTION

Alzheimer's disease (AD) is an age-related neurodegenerative disorder characterized by progressive cognitive impairment, a variety of neuropsychiatric and behavioral disturbances, and restrictions in activities of daily life. A century has passed since AD was first described by the German psychiatrist and neuropathologist Alois Alzheimer in 1906. The treatment of Alzheimer's disease remains a challenge for the pharmaceutical community. Although many factors have been implicated in AD, its etiology and pathogenesis remain unclear.

The "cholinergic hypothesis" represents one of the most useful approaches involved in the design of new agents for the treatment of AD.[1] This hypothesis asserts that most of the cognitive impairments suffered by AD patients are the consequence of a deficit in acetylcholine (ACh) and thus in cholinergic neuro-

* Corresponding author. E-mail: hyhth@163.com
doi: 10.2298/JSC140319092Z

transmission. Therefore, inhibition of AChE appears to be a useful therapeutic path to reduce, at least temporarily, the cognitive deficit in AD. To date, most of the drugs available on the market for the treatment of AD are acetylcholinesterase inhibitors (AChEI). However, the practical effectiveness of these drugs remains controversial. Recent AD trials concluded that AChEI therapies were not cost effective and the AD patients treated with cholinesterase inhibitors did not show widespread cortical atrophic changes.

Recently, most approaches to explain the pathogenesis of AD focus on two proteins: the *β*-amyloid peptide (A*β*)[2,3] and the filament protein tau.[4,5]

According to the "amyloid hypothesis", one of the major neuropathological hallmarks of AD is the altered production, aggregation, and deposition of A*β*, which results in amyloid plaque formation. Moreover, oxidative stress and increased intracellular Ca^{2+} generated in response to A*β* were reported to enhance glutamate-mediated neurotoxicity *in vitro*, with additional experiments suggesting that A*β* could increase *N*-methyl-D-aspartic acid (NMDA) responses and therefore excitotoxicity.[6,7] Many *in vivo* and *in vitro* findings showed that amyloidosis could be inhibited by antioxidants and the free radical scavengers, vitamin E and propyl gallate, protected neuronal cells against A*β* toxicity. It is becoming evident that a close relationship may exist between glutamate excitetoxicity, oxidative stress, and A*β* formation. Actually, AChE could also bind to the A*β* non-amyloidogenic form, inducing a conformational transition to the amyloidogenic conformation with subsequent amyloid fibril aggregation.[8] This action involves the peripheral anionic binding site (PAS) of AChE.[8,9] These effects, together with the fact that AD pathogenesis appears to be multifactorial, have led to the current opinion that drugs that interact with the PAS and possess antioxidant activity might exert a multi-pharmacological effect, which combine enhancement of cholinergic neurotransmission, effective antioxidant neuroprotection and the reduction in the pro-aggregating action of AChE, thus opening the way to a new promising therapeutic approach to Alzheimer's disease (AD).[3,10,11]

Recently, it was reported that synthetic derivatives of oxoisoaporphine alkaloids (Fig. 1) exhibited high acetylcholinesterase inhibitory activity and high selectivity for AChE over butyrylcholinesterase (BChE).[12,13] Molecular docking simulations on the oxoisoaporphine derivatives with AChE from *Torpedo californica* demonstrated that the 1-azabenzanthrone moiety of the ligands can interact with the PAS of acetylcholinesterase, especially with Trp 279 of the PAS.[13]

Tryptamine and its derivatives are known as natural antioxidant. Melatonin, one of tryptamine family, was shown to prevent the hyperphosphorylation of the tau protein in rats[14] and to possess neuroprotective properties against A*β* toxicity *in vivo*.[15] Several studies suggested that melatonin might be effective for the treatment of Alzheimer's disease.[15–18]

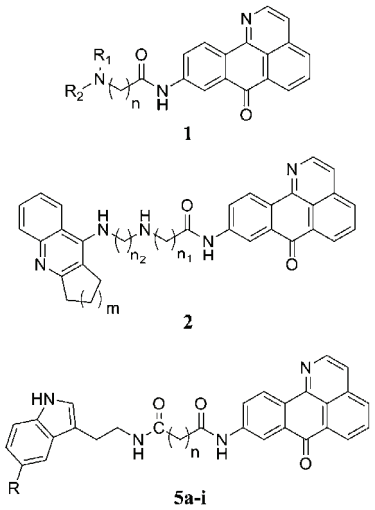

Fig. 1. Chemical structure of synthetic derivatives of oxoisoaporphine alkaloids **1**, hybrids of oxoisoaporphine–tacrine congeners **2** and hybrids of oxoisoaporphine–tryptamine derivatives **5a**–**i**.

It was thus predicted that compounds that combined inhibition of AChE and neuroprotective properties in a single small molecule would exert greater biological activity than tryptamine or oxoisoaporphine themselves and may represent an important pharmacological advance in the management of AD.

Recently, the synthesis of multifunctional compounds that combined 1-azabenzanthrone and tacrine congeners in a single small molecule was reported.[19] These hybrids exhibited high AChE inhibitory activity and significant *in vitro* inhibitory activity towards AChE-induced and self-induced A*β* aggregation. Ongoing research is focused on the design of new multi-activity compounds in which different active units could be anchored to a biocompatible scaffold.

In this paper, a series of hybrids of oxoisoaporphine–tryptamine derivatives were designed and synthesized. Their ability to inhibit AChE, AChE-induced A*β* aggregation and antioxidant activity was tested. These compounds (Fig. 1) consist of a unit of tryptamine, or a derivative that possesses neuroprotective properties, and the 1-azabenzanthrone moiety the position of which along the enzyme gorge and the peripheral site could be modulated by a suitable tether that connects tryptamine and 1-azabenzanthrone.

RESULTS AND DISCUSSION

Chemistry

The synthetic routes to compounds **5a**–**i** are outlined in Scheme 1. Compound **3**[20] was treated with the required anhydride in toluene to afford the corresponding aromatic carboxylic acid **4a**–**c**. Then compounds **4a**–**c** was reacted with the desired tryptamine derivative in dimethylacetamide (DMA) in the presence of BOP reagent, benzotriazol-l-yloxytris(dimethylamino)phosphonium hexafluorophosphate, to afford the target compounds **5a**–**i**.

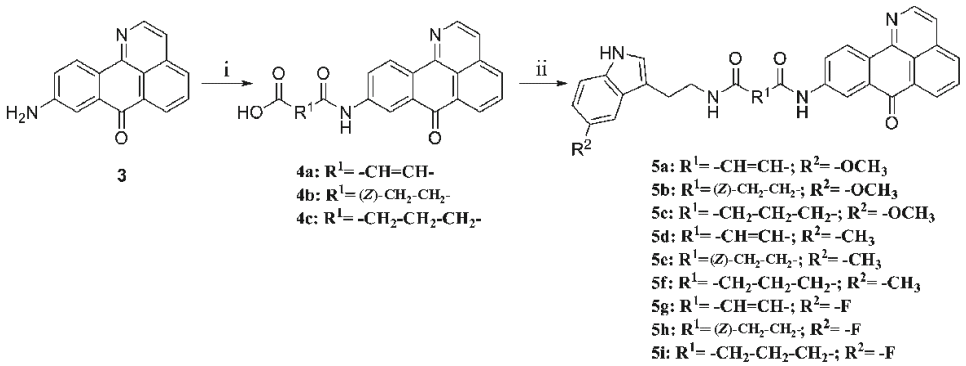

Scheme 1. The synthetic route to the hybrids of oxoisoaporphine–tryptamine. Reagents and conditions: i) the required anhydride, toluene, reflux, 7 h; ii) the corresponding tryptamine derivatives, benzotriazol-1-yloxytris(dimethylamino)phosphonium hexafluorophosphate (BOP), DMA, 65 °C, 6 h.

Pharmacology

The inhibitory activities of the newly synthesized compounds **5a–i** against AChE were investigated by determining the rate of hydrolysis of acetylthiocholine (ATCh) in comparison with reference compound tacrine, using a modified Ellman method.[21] The IC_{50} values of all the investigated compounds are summarized in Table I.

All the synthesized compounds showed moderate inhibitory potency against AChE with inhibitory activity IC_{50} values in the micromolar range. The compounds **5b**, **5e** and **5h**, which had a succinamide linker, showed higher inhibitory effects on AChE compared with the compounds other linkers. This suggested that rigid and long linkers were not favorable for fitting into the enzyme cavity. In the screening results, the structure of the tryptamine derivatives had little effect on the AChE inhibitory potency, showing only a slightly increased effect in the compounds bearing fluorine-substituted tryptamine units (compound **5g–i**).

In fact, AChE directly promotes *in vitro* the assembly of the Aβ peptide into amyloid fibrils, forming stable AChE–Aβ complexes.[8] Structural analysis by X-ray crystallography[22] and competition assays with AChEIs clearly identified the PAS of the enzyme as the locus of protein interaction with Aβ.[23] It was previously demonstrated that 1-azabenzanthrone could interact with the PAS of acetylcholinesterase, especially with Trp 279 of the PAS.[13] To further explore the dual action of these compounds, the AChE-induced Aβ(1–40) aggregation inhibitory activity was examined employing the thioflavin T (ThT)-based fluorometric assay.[24] The Aβ-anti-aggregation activity of the novel hybrids and reference compounds are summarized in Table I. The nine tested oxoisoaporphine–tryptamine derivatives exhibited, at a 100 μM concentration, a significant Aβ--anti-aggregation effect with inhibition ranging from 32.5 to 60.5 %, being 8- to

13-fold more potent than tacrine. There was a clear correlation between the AChE-induced Aβ aggregation inhibitory activity and the AChE inhibitory potency. Compound **5h** bearing fluorine-substituted tryptamine units and a succinamide linker had the highest Aβ-aggregation inhibitory ratio that corresponded to the lowest IC_{50} value for AChE inhibition. Compound **5g** possessing the lowest Aβ-aggregating inhibitory ratio showed the highest IC_{50} for AChE inhibition. A scatter plot of the *in vitro* inhibitory percent of AChE-induced Aβ aggregation *versus* the IC_{50} value for AChE inhibition is shown in Fig. 2. A statistically significant linear fit of the data was obtained, which clearly showed that the inhibitory effects for Aβ aggregation and acetylcholinesterase were positively correlated. These results appear to validate the theory[23] that a compound that binds to the PAS of AChE could strongly inhibit enzyme-mediated Aβ aggregation.

TABLE I. Inhibition of AChE activities, AChE-induced Aβ aggregation and oxygen radical absorbance capacity (*ORAC*) by the synthesized compounds; IC_{50}: 50 % inhibition concentration (means±*SEM* of three experiments) of AChE; inhibition of co-aggregation of Aβ(1–40) and AChE 0.06 U was detected by the ThT assay; the data showed that the test compounds inhibited the co-aggregation at 100 μM. The values are expressed as means±*SEM* of three experiments; the *ORAC* data are expressed as μmol of trolox equivalent per μmol of tested compound and are the mean (n = 3)±*SD*

Compound	IC_{50} / μM, for AChE	Inhibition, %, of Aβ aggregation	*ORAC* trolox-equivalents
5a	14.94±0. 23	35.2±1.2	0.9±0.03
5b	6.10±0.25	50.4±1.5	1.2±0.01
5c	16.77±0.34	41.6±2.3	0.9±0.04
5d	10.85±0.15	38.5±1.7	1.7±0.05
5e	5.10±0.31	57.7±0.9	1.3±0.03
5f	14.0±0.73	49.7±1.9	1.4±0.02
5g	14.95±0.31	32.5±2.1	1.1±0.02
5h	2.37±0.40	60.5±1.5	1.0±0.01
5i	7.12±0.32	59.3±2.2	1.3±0.05
Tacrine	0.13±0.01	4.5±0.7	<0.01
Curcumin	–	32.8±0.5	–
Propidium iodide	–	83.7±1.7	–
Melatonin	–	–	1.9±0.09

The oxygen radical absorbance capacity assay (ORAC) at 37 °C using fluorescein (ORAC–FL) as a fluorescence probe measures the scavenging capacity against peroxyl radicals induced by AAPH. The antioxidant activity of the new oxoisoaporphine–tryptamine hybrids **5a**–**i** was determined by their competition with fluorescein in the radical capture, using a fluorescence microplate reader. The vitamin E analogue trolox was used as a standard, and the results were expressed as trolox equivalents (μmol of trolox equivalents per μmol of tested compound, Table I). Tacrine and melatonin were also checked for comparison.

Tacrine showed rather weak radical capture, whereas melatonin had an ORAC–FL value 1.9-fold higher than that of trolox.

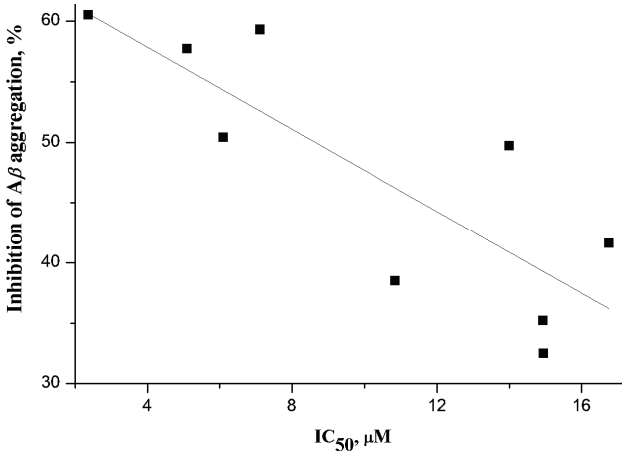

Fig. 2. Scatter plot of the *in vitro* percent inhibition of AChE-induced Aβ aggregation *vs*. the IC_{50} value for AChE inhibition for the series of oxoisoaporphine–tryptamine derivatives **5a**–**i**.

Hybrids **5a**–**i** were tested in 1–10 μM concentrations and they exhibited moderate peroxyl radical absorbance capacities ranging from 0.9- to 1.7-fold the value of trolox. Tryptamine was the main element responsible for increasing the antioxidant activity. Its structure had a direct effect on the antioxidant activity. The derivatives obtained from conjugation with the 5-methyltryptamine (**5d**–**f**) showed the higher radical-scavenger activity with oxygen radical absorbance capacity at 1.7, 1.3 and 1.4 trolox-equivs, respectively. The structure and length of the linker had no effect on their antioxidant capacity.

EXPERIMENTAL

The reactions were monitored by TLC using aluminum plates pre-coated with silica gel containing a fluorescent indicator. Detection was performed with UV (254 nm) irradiation followed by charring with 0.5 % phosphomolybdic acid in 95 % EtOH. Anhydrous $MgSO_4$ was used to dry the organic solutions during work-up and the solvents were removed under vacuum using a rotary evaporator. The ^{1}H-NMR spectra were recorded on a Varian Mercury-Plus 300 and Bruker Avance AV500 NMR Spectrometer with tetramethylsilane (TMS) as an internal standard. Elemental analysis was realized on a PE2400II Elemental Analyzer. Mass spectral analysis was performed on a Bruker HCT mass spectrometer and recorded on an electrospray ionization mass spectrometer as the m/z value.

Characterization data for the synthesized compounds are given in Supplementary material to this paper.

*General procedure for the synthesis of compounds **4a**–**c***

Compound **3**[20] (3.0 mmol) and the required anhydride (30 mmol) were mixed in toluene (40 mL). The mixture was refluxed under stirring for 7 h and then cooled to room tempe-

rature. The resulting precipitate was collected by filtration, washed with toluene, and dried. Recrystallization from toluene afforded the products **4a**–**c** as yellow solids in 43–55 % yields.

*General procedure for the synthesis of compounds **5a**–**i***

BOP (0.9 g, 2 mmol) in DMA (3 mL) was added over 30 min to a solution of compound **4a**–**c** (2 mmol) and the appropriate tryptamine derivatives (20 mmol) in DMA (4 mL) at 65 °C. The mixture was stirred at 65 ° C for 5 h and concentrated under vacuum. The residue was taken up with dichloromethane and the solution washed with a solution of sodium carbonate, dried (Na_2SO_4), and concentrated under vacuum. Column chromatography of the residue, eluting with 5% methanol in dichloromethane, afforded compounds **5a**–**i** in 43–55 % yields.

In vitro *inhibition studies on AChE*

All the assays[21] were performed in 0.1 M KH_2PO_4/K_2HPO_4 buffer, pH 8.0, using a PerkinElmer LAMBDA 45 Spectrophotometer. AChE from *Electrophorus electricus* (Sigma) were prepared to give 2.0 units mL^{-1} in 2 mL aliquots. The assay medium contained phosphate buffer, pH 8.0 (1 mL), 50 μL of 0.01 M 5,5'-dithiobis(2-nitrobenzoic acid) (DTNB), 10 μL of enzyme, and 50 μL of 0.01 M substrate (acetylthiocholine chloride). The substrate was added to the assay medium containing enzyme, buffer, and DTNB with inhibitor after 15 min of incubation time. The activity was determined by measuring the increase in absorbance at 412 nm in 1 min intervals at 37 °C. The calculations were performed using the Ellman equation.[21]

Inhibition of AChE-induced Aβ(1–40) peptide aggregation assay

To analyze the inhibition of co-aggregation, the ThT fluorescence method was employed. The fluorescence emission was measured at 490 nm for excitation at 446 nm. For the co-incubation experiments,[24,25] mixtures of A*β*(1–40) peptide (GL Biochem) and AChE from *E. electricus*, were incubated for 8 h at 37 °C in the presence or absence of the test inhibitors. The final concentrations of A*β* (2.3 mM A*β* DMSO solution added to 0.215 M sodium phosphate buffer, pH 8.0) and AChE (dissolved in 0.1 M sodium phosphate buffer, pH 8.0) were 23 μM and 0.06 U, respectively. After co-incubation, 180 μL of 1.5 μM ThT was added to 20 μL of the solution mixtures. The percent inhibition (*I*) of AChE-induced aggregation due to the presence of the tested compound was calculated by the following expression:

$$I\ /\ \% = 100 - \left(\frac{IF_\mathrm{i}}{IF_0} \times 100 \right)$$

where IF_i and IF_0 are the fluorescence intensities obtained for A*β* plus AChE in the presence and in the absence of inhibitor, respectively, minus the fluorescence intensities due to the respective blanks.

Determination of antioxidant activity

The antioxidant activity was determined by the oxygen radical absorbance capacity––fluorescein (ORAC–FL) assay of Ou *et al*.[26] and modified by Rodriguez-Franco *et al*.[27] 2,2′--Azobis(2-amidinopropane) dihydrochloride (AAPH) and (±)-6-hydroxy-2,5,7,8-tetramethylchromane-2-carboxylic acid (trolox) solutions were prepared daily and fluorescein (FL) was diluted from a stock solution (1.17 mM) in 75 mM phosphate buffer (pH 7.4). The reaction was performed in 75 mM phosphate buffer (pH 7.4) and the final reaction mixture was 200 μL. Antioxidant (20 μL) and FL (120 μL; 70 nM, final concentration) solutions were preincubated for 10 min at 37 °C. AAPH solution (60 μL; 12 mM, final concentration) was added and after shaking before the first reading, the fluorescence was recorded every 56 s for 96

min. Trolox was used as standard (1–10 μM, final concentration) and the sample was measured at different concentrations (1–10 μM). An Infinite® M1000 PRO plate reader (Tecan Trading AG, Switzerland) with λ_{ex} = 485 nm and λ_{em} = 520 nm was used. The equipment was controlled by Magellan™ software for fluorescence measurements. Black 96-well microplates were used. All reaction mixtures were prepared in duplicate and at least three independent runs were performed for each sample. Fluorescence measurements were normalized to the curve of the blank (no antioxidant). From the normalized curves, the area under the fluorescence decay curve (*AUC*) was calculated as:

$$AUC = 1 + \sum_{i=1}^{i=80} \frac{f_i}{f_0}$$

where f_0 is the initial fluorescence reading at 0 min and f_i is the fluorescence reading at time *i*. The net *AUC* for a sample was calculated as follows:

$$\text{net } AUC = AUC_{\text{antioxidant}} - AUC_{\text{blank}}$$

The regression equation between net *AUC* and antioxidant concentration was calculated. The slope of the equation was used to calculate the ORAC–FL value by using the trolox curve obtained for each assay. Final ORAC–FL values were expressed as μmol of trolox equivalent per μmol of pure compound.

CONCLUSIONS

The present study reports the synthesis and biological evaluation of a series of new hybrids of oxoisoaporphine–tryptamine derivatives. Regarding AChE inhibition, synthesized compounds show less inhibitory potency than that of 9-substituted 1-azabenzanthrone derivatives which were previously reported.[12,19] However, these new synthetic derivatives showed strong AChE-induced Aβ anti-aggregation activity, being more potent than tacrine and curcumin. In addition, these derivatives showed moderate antioxidant activity, though their activities were less than that of melatonin. This could be related to the poor solubility of the hybrids. Overall, these results were encouraging for the further development of Aβ aggregation inhibitors with higher antioxidant activity and AChE inhibitory activity based on oxoisoaporphine in the future.

SUPPLEMENTARY MATERIAL

Characterization data of the prepared compounds and their IR spectra are available electronically from http://www.shd.org.rs/JSCS/, or from the corresponding author on request.

Acknowledgments. This work was financially supported by grants from the National Natural Science Foundation of PRC (81260471), Natural Science Foundation of Guangxi (2013GXNSFAA019038) and Key Laboratory for the Chemistry and Molecular Engineering of Medicinal Resources (Guangxi Normal University), Ministry of Education of China (CMEMR2012-A05).

ИЗВОД

НОВИ ДЕРИВАТИ ОКСОИЗОАПОРФИН–ТРИПТАМИНА КАО ИНХИБИТОРИ АГРЕГАЦИЈЕ β-АМИЛОИДА ИНДУКОВАНЕ АЦЕТИЛХОЛИНЕСТЕРАЗОМ, КОЈИ ПОСЕДУЈУ УНАПРЕЂЕНЕ АНТИОКСИДАТИВНЕ ОСОБИНЕ

HAI-TAO ZHAO, SHU-MING ZHONG, JIANG-KE QIN и HUANG TANG

Key Laboratory for the Chemistry and Molecular Engineering of Medicinal Resources, School of Chemistry and Pharmaceutical Sciences of Guangxi Normal University, Guilin 541004, China

Серија инхибитора ацетилхолинестеразе (AChE) са двоструким везивањем у активном месту је дизајнирана и синтетисана, а тестирана су њихова антиоксидативна својства и инхибиторни потенцијал према AChE и AChE-индукованој (Aβ) агрегацији β-амилоида. Нови деривати садрже 1-азабензантрон и триптамин или његове деривате, повезане α,ω-алка(е)ндиамидним мостом. Ови деривати показују умерену инхибиторну активност према AChE са IC_{50} вредностима у микромоларном опсегу, и значајну *in vitro* AChE-индуковану Aβ агрегацију. Осим тога, шест од девет деривата показује већи капацитет апсорпције кисеоничних радикала у поређењу са тролоксом, што их чини перспективним кандидатима за лечење Алцхајмерове болести.

(Примљено 18. марта, ревидирано 3. септембра, прихваћено 10. септембра 2014)

REFERENCES

1. R. T. Bartus, R. L. Dean 3rd, B. Beer, A. S. Lippa, *Science* **217** (1982) 408
2. P. Cras, M. Kawai, D. Lowery, P. Gonzalez-DeWhitt, B. Greenberg, G. Perry, *Proc. Natl. Acad. Sci. USA* **88** (1991) 7552
3. A. Castro, A. Martinez, *Curr. Pharm. Des.* **12** (2006) 4377
4. C. X. Gong, K. Iqbal, *Curr. Med. Chem.* **15** (2008) 2321
5. I. Khlistunova, J. Biernat, Y. Wang, M. Pickhardt, M. von Bergen, Z. Gazova, E. Mandelkow, E.-M. Mandelkow, *J. Biol. Chem.* **281** (2006) 1205
6. A. Lipton Stuart, *Nat. Rev. Drug. Discov.* **5** (2006) 160
7. M. Rosini, E. Simoni, M. Bartolini, A. Cavalli, L. Ceccarini, N. Pascu, D. W. McClymont, A. Tarozzi, M. L. Bolognesi, A. Minarini, V. Tumiatti, V. Andrisano, I. R. Mellor, C. Melchiorre, *J. Med. Chem.* **51** (2008) 4381
8. N. C. Inestrosa, A. Alvarez, C. A. Perez, R. D. Moreno, M. Vicente, C. Linker, O. I. Casanueva, C. Soto, J. Garrido, *Neuron* **16** (1996) 881
9. Y. Bourne, P. Taylor, P. E. Bougis, P. Marchot, *J. Biol. Chem.* **274** (1999) 2963
10. L. M. Espinoza-Fonseca, *Bioorg. Med. Chem.* **14** (2006) 896
11. D. Alonso, I. Dorronsoro, L. Rubio, P. Munoz, E. Garcia-Palomero, M. Del Monte, A. Bidon-Chanal, M. Orozco, F. J. Luque, A. Castro, M. Medina, A. Martinez, *Bioorg. Med. Chem.* **13** (2005) 6588
12. H. Tang, F.-X. Ning, Y.-B. Wei, S.-L. Huang, Z.-S. Huang, A. S.-C. Chan, L.-Q. Gu, *Bioorg. Med. Chem. Lett.* **17** (2007) 3765
13. H. Tang, Y.-B. Wei, C. Zhang, F.-X. Ning, W. Qiao, S.-L. Huang, L. Ma, Z.-S. Huang, L.-Q. Gu, *Eur. J. Med. Chem.* **44** (2009) 2523
14. X.-C. Li, Z.-F. Wang, J.-X. Zhang, Q. Wang, J.-Z. Wang, *Eur. J. Pharmacol.* **510** (2005) 25
15. M. Ionov, V. Burchell, B. Klajnert, M. Bryszewska, A. Y. Abramov, *Neuroscience* **180** (2011) 229
16. D. P. Cardinali, A. M. Furio, L. I. Brusco, *Curr. Neuropharmacol.* **8** (2010) 218
17. E. Esposito, S. Cuzzocrea, *Curr. Neuropharmacol.* **8** (2010) 228

18. H. He, W. Dong, F. Huang, *Curr. Neuropharmacol.* **8** (2010) 211
19. H. Tang, L.-Z. Zhao, H.-T. Zhao, S.-L. Huang, S.-M. Zhong, J.-K. Qin, Z.-F. Chen, Z.-S. Huang, H. Liang, *Eur. J. Med. Chem.* **46** (2011) 4970
20. H. Tang, X.-D. Wang, Y.-B. Wei, S.-L. Huang, Z.-S. Huang, J.-H. Tan, L.-K. An, J.-Y. Wu, A. Sun-Chi Chan, L.-Q. Gu, *Eur. J. Med. Chem.* **43** (2008), 973
21. G. L. Ellman, K. D. Courtney, V. Andres Jr., R. M. Featherstone, *Biochem. Pharmacol.* **7** (1961) 88
22. Y. Bourne, P. Taylor, Z. Radic, P. Marchot, *EMBO J.* **22** (2003) 1
23. M. L. Bolognesi, A. Cavalli, C. Melchiorre, *Neurotherapeutics* **6** (2009) 152
24. M. Bartolini, C. Bertucci, V. Cavrini, V. Andrisano, *Biochem. Pharmacol.* **65** (2003) 407
25. Y. E. Kwon, J. Y. Park, K. T. No, J. H. Shin, S. K. Lee, J. S. Eun, J. H. Yang, T. Y. Shin, D. K. Kim, B. S. Chae, J.-Y. Leem, K. H. Kim, *Bioorg. Med. Chem.* **15** (2007) 6596
26. B. Ou, M. Hampsch-Woodill, R. L. Prior, *J. Agric. Food. Chem.* **49** (2001) 4619
27. M. I. Rodriguez-Franco, M. I. Fernandez-Bachiller, C. Perez, B. Hernandez-Ledesma, B. Bartolome, *J. Med. Chem.* **49** (2006) 459.

Journal of the Serbian Chemical Society
JSCS@tmf.bg.ac.rs • www.shd.org.rs/JSCS
J. Serb. Chem. Soc. 80 (2) S24–S27 (2015) *Supplementary material*

SUPPLEMENTARY MATERIAL TO

Novel hybrids of oxoisoaporphine–tryptamine as inhibitors of acetylcholinesterase-induced *β*-amyloid aggregation with improved antioxidant properties

HAI-TAO ZHAO, SHU-MING ZHONG, JIANG-KE QIN and HUANG TANG*

Key Laboratory for the Chemistry and Molecular Engineering of Medicinal Resources, School of Chemistry and Pharmaceutical Sciences of Guangxi Normal University, Guilin 541004, China

J. Serb. Chem. Soc. 80 (2) (2015) 127–136

CHARACTERIZATION DATA FOR THE SYNTHESIZED COMPOUNDS

*4-Oxo-4-[(7-oxo-7*H*-dibenzo[*de,h*]quinolin-9-yl)amino](2Z)-but-2-enoic acid (**4a**)*. From compound **3** (0.74 g, 3 mmol) and maleic anhydride (2.9 g, 30 mmol), a yellow powder maleic acid derivative **4a** (0.57 g, 55 % yield) was obtained from toluene; ^{1}H-NMR (500 MHz, DMSO-d_6, δ / ppm): 6.38 (1H, *d*, *J* = 12.2 Hz), 6.54 (1H, *d*, *J* = 12.2 Hz), 7.98 (1H, *d*, *J* = 5.5 Hz), 8.03 (1H, *t*, *J* = 7.9 Hz), 8.11 (1H, *d*, *J* = 7.3 Hz), 8.41 (1H, *d*, *J* = 8.5 Hz), 8.53–8.56 (2H, *m*), 8.75 (1H, d, *J* = 9.2 Hz), 8.77 (1H, *d*, *J* = 5.5 Hz), 10.83 (1H, *s*); ESI-MS (*m*/*z*): 343 $[M–H]^-$.

*4-Oxo-4-[(7-oxo-7*H*-dibenzo[*de,h*]quinolin-9-yl)amino]butanoic acid (**4b**)*. From compound **3** (0.74 g, 3 mmol) and succinic anhydride (2.9 g, 30 mmol), a yellow powder succinic acid derivative **4b** (0.76 g, 73 % yield) was obtained from toluene; ^{1}H-NMR (500 MHz, DMSO-d_6, δ / ppm): 2.58 (2H, *t*, *J* = 6.7 Hz), 2.66 (2H, *t*, *J* = 6.7 Hz), 8.00 (1H, *d*, *J* = 5.5 Hz), 8.05 (1H, *dd*, J_1 = 7.3 Hz, J_2 = = 7.9 Hz), 8.09 (1H, *d*, *J* = 8.5 Hz), 8.43 (1H, *d*, *J* = 8.5 Hz,), 8.55–8.57 (2H, *m*), 8.76 (1H, *d*, *J* = 8.5 Hz,), 8.79 (1H, *d*, *J* = 5.5 Hz), 10.46 (1H, *s*), 12.17 (1H, *brs*); ESI-MS (*m*/*z*): 345 $[M–H]^-$.

*5-Oxo-5-[(7-oxo-7*H*-dibenzo[*de,h*]quinolin-9-yl)amino]pentanoic acid (**4c**)*. From compound **3** (0.74 g, 3 mmol) and glutaric anhydride (3.4 g, 30 mmol), a yellow powder glutaric acid derivative **4c** (0.73 g, 68 % yield) was obtained from toluene; ^{1}H-NMR (500 MHz, DMSO-d_6, δ / ppm): 1.83–1.89 (2H, *m*), 2.33 (2H, *t*, *J* = 7.3 Hz), 2.44 (2H, *t*, *J* = 7.3 Hz), 7.97 (1H, *d*, *J* = 5.5 Hz), 8.0.3 (1H, *dd*, J_1 = 7.9 Hz, J_2 = 7.3 Hz,), 8.09 (1H, *d*, *J* = 8.5 Hz), 8.40 (1H, *d*, *J* = 8.5 Hz),

* Corresponding author. E-mail: hyhth@163.com

8.52–8.55 (2H, *m*), 8.72 (1H, *d*, *J* = 9.2 Hz), 8.76 (1H, *d*, *J* = 5.5 Hz), 10.38 (1H, *s*); ESI-MS (*m*/*z*): 359 $[M–H]^-$.

N^1-*(2-(5-Methoxy-1*H*-indol-3-yl)ethyl)*-N^4-*(7-oxo-7*H*-dibenzo[*de,h*]quinolin--9-yl)-(2*Z*)-2-butenediamide (**5a**)*. Yield: 0.62 g, 60 %; orange solid; Anal. Calcd. for $C_{31}H_{24}N_4O_4 \cdot 2H_2O$: C, 67.38; H, 5.11; N, 10.14 %. Found: C, 67.19; H, 5.37; N, 10.41 %; ^{1}H-NMR (500 MHz, DMSO-d_6, δ / ppm): 2.87 (2H, *t*, *J* = 7.1 Hz), 3.46–3.49 (2H, *m*), 3.76 (3H, *s*), 6.72 (1H, *d*, *J* = 8.5 Hz), 7.04–7.14 (4H, *m*), 7.23 (1H, *d*, *J* = 8.6 Hz), 8.02 (1H, *d*, *J* = 5.5 Hz), 8.06 (1H, *dd*, J_1 = 7.6 Hz, J_2 = 7.7 Hz), 8.16 (1H, *d*, *J* = 7.3 Hz), 8.44 (1H, *d*, *J* = 8.6 Hz), 8.58 (1H, *d*, *J* = 7.0 Hz), 8.65 (1H, *s*), 8.70 (1H, *t*, *J* = 5.2 Hz), 8.78–8.80 (2H, *m*), 10.68 (1H, *s*), 10.93 (1H, *s*); ^{13}C-NMR (125 MHz, DMSO-d_6, δ / ppm): 24.9, 45.3, 55.2, 100.0, 111.4, 111.9, 116.5, 120.6, 121.4, 123.3, 124.5, 125.9, 127.4, 128.0, 129.6, 130.7, 131.3, 131.4, 132.2, 132.3, 134.0, 134.6, 134.7, 140.8, 143.8, 147.2, 152.9, 162.7, 163.2, 169.4, 181.9; ESI-MS (*m*/*z*): 517 $[M+H]^+$.

N^1-*(2-(5-Methoxy-1*H*-indol-3-yl)ethyl)*-N^4-*(7-oxo-7*H*-dibenzo[*de,h*]quinolin--9-yl)butanediamide (**5b**)*. Yield: 0.67 g, 65 %; orange solid; Anal. Calcd. for $C_{31}H_{26}N_4O_4 \cdot H_2O$: C, 69.39; H, 5.26; N, 10.44 %. Found: C, 69.12; H, 5.21; N, 10.07 %; ^{1}H-NMR (500 MHz, DMSO-d_6, δ / ppm): 2.47–2.50 (2H, *m*), 2.66 (2H, *t*, *J* = 7.1 Hz), 2.79 (2H, *t*, *J* = 7.7 Hz), 3.32–3.36 (2H, *m*), 3.75 (3H, *s*), 6.7 (1H, *dd*, J_1 = 2.3 Hz, J_2 = 8.3 Hz), 7.02 (1H, *d*, *J* = 2.1 Hz), 7.12 (1H, *s*), 7.22 (1H, *d*, *J* = 8.7 Hz), 7.97 (1H, *d*, *J* = 5.6 Hz), 8.01–8.08 (3H, *m*), 8.40 (1H, *d*, *J* = 8.1 Hz), 8.54 (2H, *d*, *J* = 7.9 Hz), 8.72 (1H, *d*, *J* = 8.6 Hz), 8.76 (2H, *d*, *J* = 5.6 Hz), 10.46 (1H, *s*), 10.64 (1H, *s*); ^{13}C-NMR (125 MHz, DMSO-d_6, δ / ppm): 25.2, 30.2, 31.7, 45.3, 55.2, 100.1, 110.9, 111.6, 111.9, 116.0, 120.4, 121.2, 123.2, 124.1, 125.7, 127.4, 128.0, 129.4, 130.6, 130.7, 131.3, 132.3, 134.0, 134.5, 141.4, 143.9, 147.5, 152.9, 170.9, 171.0, 182.0; ESI-MS (*m*/*z*): 519 $[M+H]^+$.

N^1-*(2-(5-Methoxy-1*H*-indol-3-yl)ethyl)*-N^5-*(7-oxo-7*H*-dibenzo[*de,h*]quinolin--9-yl)pentanediamide (**5c**)*. Yield: 0.65 g, 61 %; orange solid; Anal. Calcd. for $C_{32}H_{28}N_4O_4 \cdot 2H_2O$: C, 67.59; H, 5.67; N, 9.85 %. Found: C, 67.65; H, 5.91; N, 9.62 %; ^{1}H-NMR (500 MHz, DMSO-d_6, δ / ppm): 1.83–1.89 (2H, *m*), 2.17 (2H, *t*, *J* = 7.2 Hz), 2.39 (2H, *t*, J_1 =7.1 Hz, J_2 = 7.2 Hz), 2.78 (2H, *t*, *J* = 7.0 Hz), 3.30–3.34 (2H, *m*), 3.73 (3H, *s*), 6.69 (1H, *d*, *J* = 8.9 Hz), 7.03 (1H, *s*), 7.12 (1H, *s*), 7.21 (1H, *d*, *J* = 8.7 Hz), 7.94 (1H, *d*, *J* = 5.5 Hz), 7.99–8.04 (3H, *m*), 8.37 (1H, *d*, *J* = 8.1 Hz), 8.51 (2H, *d*, *J* = 7.3 Hz), 8.57 (1H, *d*, *J* = 8.7 Hz), 8.73 (1H, *d*, *J* = 5.5 Hz), 10.42 (1H, *s*), 10.61 (1H, *s*); ^{13}C-NMR (125 MHz, DMSO-d_6, δ / / ppm): 22.9, 25.2, 34.6, 35.8, 45.4, 55.3, 100.1, 110.9, 111.6, 111.9, 116.2, 120.7, 121.4, 123.1, 124.4, 126.0, 127.5, 128.2, 129.7, 130.9, 131.0, 131.3, 132.4, 134.1, 134.7, 141.4, 144.0, 147.5, 152.9, 171.4, 171.5, 182.2; ESI-MS (*m*/*z*): 533 $[M+H]^+$.

N^1-*(2-(5-Methyl-1*H*-indol-3-yl)ethyl)*-N^4-*(7-oxo-7*H*-dibenzo[*de,h*]quinolin-9--yl)-(2*Z*)-2-butenediamide (**5d**)*. Yield: 0.52 g, 52 %; orange solid; Anal. Calcd.

for $C_{31}H_{24}N_4O_3 \cdot H_2O$: C, 71.80; H, 5.05; N, 10.80 %. Found: C, 71.42; H, 5.22; N, 10.71 %; ^{1}H-NMR (500 MHz, DMSO-d_6, δ/ ppm): 2.63 (3H, *s*), 3.01 (2H, *t*, *J* = 6.9 Hz), 3.58–3.61 (2H, *m*), 7.02 (1H, *d*, *J* = 8.4 Hz), 7.20 (1H, *s*), 7.25 (1H, *d*, *J* = 8.2 Hz), 7.36 (1H, *d*, *J* = 8.5 Hz), 7.45 (1H, *s*), 8.13 (1H, *d*, *J* = 5.5Hz), 8.19 (1H, *dd*, J_1 = 7.5 Hz, J_2 = 8.0 Hz), 8.29 (1H, *d*, *J* = 8.6 Hz), 8.56 (1H, *d*, *J* = = 8.2 Hz), 8.70 (1H, *d*, *J* = 7.2 Hz), 8.77 (1H, *s*), 8.82 (1H, *dd*, J_1 = 4.4 Hz, J_2 = = 4.9 Hz), 8.89–8.93 (2H, *m*), 10.84 (1H, *s*), 11.08 (1H, *s*); ^{13}C-NMR (125 MHz, DMSO-d_6, δ / ppm): 21.2, 24.9, 45.3, 110.9, 111.1, 116.5, 117.7, 120.6, 121.4, 123.2, 124.6, 125.9, 126.9, 127.3, 128.1, 129.6, 130.8, 131.5, 132.2, 132.3, 134.0, 134.5, 134.6, 134.7, 140.9, 143.9, 147.3, 162.7, 163.3, 169.5, 182.0; ESI--MS (*m*/*z*): 501 $[M+H]^+$.

N^1-*(2-(5-Methyl-1*H*-indol-3-yl)ethyl)*-N^4-*(7-oxo-7*H*-dibenzo[*de,h*]quinolin-9--yl)butanediamide (**5e**)*. Yield: 0.55 g, 55 %; orange solid; Anal. Calcd. for $C_{31}H_{26}N_4O_3$: C, 74.09; H, 5.21; N, 11.15 %. Found: C, 74.45; H, 5.47; N, 10.86 %; ^{1}H-NMR (500 MHz, DMSO-d_6, δ / ppm): 2.35 (3H, *s*), 2.49 (2H, *t*, *J* = 7.0 Hz), 2.66 (2H, *t*, *J* = 6.9 Hz), 2.79 (2H, *t*, *J* = 7.5 Hz), 3.32–3.38 (2H, *m*), 6.88 (1H, *d*, *J* = 8.2 Hz), 7.10 (1H, *s*), 7.22 (1H, *d*, *J* = 8.2 Hz), 7.29 (1H, *s*), 7.97 (1H, *d*, *J* = 5.4 Hz), 8.01–8.08 (2H, *m*), 8.41 (1H, *d*, *J* = 8.1 Hz), 8.53–8.54 (2H, *m*), 8.72 (1H, *d*, *J* = 8.5 Hz), 8.76 (1H, *d*, *J* = 5.4 Hz), 10.46 (1H, *s*), 10.67 (1H, *s*); ^{13}C-NMR (125 MHz, DMSO-d_6, δ / ppm): 21.2, 25.2, 30.1, 31.7, 45.4, 110.9, 111.2, 116.0, 117.7, 120.5, 121.3, 122.4, 122.6, 124.2, 125.8, 126.4, 127.4, 128.1, 129.5, 130.6, 130.7, 132.2, 134.0, 134.5, 134.6, 141.4, 143.8, 147.4, 170.9, 171.1, 182.0. ESI-MS (*m*/*z*): 503 $[M+H]^+$.

N^1-*(2-(5-Methyl-1*H*-indol-3-yl)ethyl)*-N^5-*(7-oxo-7*H*-dibenzo[*de,h*]quinolin-9--yl)pentanediamide (**5f**)*. Yield: 0.44 g, 43 %; orange solid; Anal. Calcd. for $C_{32}H_{28}N_4O_3 \cdot H_2O$: C, 71.89; H, 5.66; N, 10.48 %. Found: C, 71.77; H, 5.92; N, 10.26 %; ^{1}H-NMR (500 MHz, DMSO-d_6, δ /ppm): 1.86–1.91 (2H, *m*), 2.18 (2H, *t*, *J* = 7.3 Hz), 2.36 (3H, *s*), 2.43 (2H, *t*, *J* = 7.2 Hz), 2.78 (2H, *t*, J_1 = 7.7 Hz), 3.30–3.34 (2H, *m*), 6.86 (1H, *d*, *J* = 8.2 Hz), 7.09 (1H, *s*), 7.20 (1H, *d*, *J* = 8.2 Hz), 7.29 (1H, *s*), 7.98–8.01 (2H, *m*), 8.05 (1H, *dd*, J_1 = 8.0 Hz, J_2 = 7.4 Hz), 8.11 (1H, *d*, *J* = 8.7 Hz), 8.43 (1H, *d*, *J* = 8.2 Hz), 8.55–8.58 (2H, *m*), 8.74 (1H, *d*, *J* = 8.6 Hz), 8.77 (1H, *d*, *J* = 5.5 Hz), 10.50 (1H, *s*), 10.69 (1H, *s*); ^{13}C-NMR (125 MHz, DMSO-d_6, δ / ppm): 21.1, 21.2, 25.2, 34.6, 35.8, 45.5, 110.9, 111.3, 116.1, 117.7, 120.5, 121.3, 122.3, 122.5, 124.3, 125.8, 126.4, 127.4, 128.1, 129.5, 130.7, 130.8, 132.2, 134.0, 134.5, 134.6, 141.4, 143.8, 147.4, 171.4, 171.5, 182.1; ESI-MS (*m*/*z*): 517 $[M+H]^+$.

N^1-*(2-(5-Fluoro-1*H*-indol-3-yl)ethyl)*-N^4-*(7-oxo-7*H*-dibenzo[*de,h*]quinolin-9--yl)-(2*Z*)-2-butanediamide (**5g**)*. Yield: 0.57 g, 57 %; orange solid; Anal. Calcd. for $C_{30}H_{21}FN_4O_3 \cdot H_2O$: C, 68.96; H, 4.44; N, 10.72 %. Found: C, 69.23; H, 4.72; N, 10.51 %; ^{1}H-NMR (500 MHz, DMSO-d_6, δ / ppm): 2.88 (2H, *t*, J_1 = 7.0 Hz), 3.45–3.49 (2H, *m*), 6.91 (1H, *t*, J_1 = 9.2 Hz, J_2 = 9.0 Hz), 7.04–7.14 (2H,

m), 7.27–7.35 (2H, *m*), 7.99 (1H, *d*, *J* = 5.5 Hz), 8.03 (1H, *dd*, J_1 = 7.6 Hz, J_2 = = 8.2 Hz), 8.14 (1H, *d*, *J* = 8.0 Hz), 8.42 (1H, *d*, *J* = 8.1 Hz), 8.55 (1H, *d*, *J* = 7.1 Hz), 8.62 (1H, *s*), 8.69 (1H, *d*, *J* = 5.3 Hz), 8.74–8.78 (2H, *m*), 10.94 (1H, *s*), 10.97 (1H, *s*); ^{13}C-NMR (125 MHz, DMSO-d_6, δ / ppm): 24.7, 45.3, 102.9, 111.9, 112.2, 116.5, 120.7, 121.4, 123.3, 124.6, 125.9, 127.4, 128.1, 129.6, 130.8, 131.5, 132.3, 132.4, 132.8, 134.0, 134.6, 134.7, 140.8, 143.9, 147.3, 157.5, 162.7, 163.3, 169.3, 181.9. ESI-MS (*m*/*z*): 505 $[M+H]^+$.

N^1-*(2-(5-Fluoro-1*H*-indol-3-yl)ethyl)*-N^4-*(7-oxo-7*H*-dibenzo[*de,h*]quinolin-9--yl)butanediamide (**5h**)*. Yield: 0.49 g, 48 %; orange solid; Anal. Calcd. for $C_{30}H_{23}FN_4O_3$: C, 71.14; H, 4.58; N, 11.06 %. Found: C, 70.86; H, 4.84; N, 10.74 %; ^{1}H-NMR (500 MHz, DMSO-d_6, δ / ppm): 2.47 (2H, *t*, *J* = 7.2 Hz), 2.66 (2H, *t*, *J* = 7.1 Hz), 2.79 (2H, *t*, *J* = 7.4 Hz), 3.32 (2H, *t*, *J* = 7.2 Hz), 6.87 (1H, *t*, *J* = 9.2 Hz), 7.24 (1H, *s*), 7.26–7.33 (2H, *m*), 7.98 (1H, *d*, *J* = 5.6 Hz), 8.03 (1H, *t*, *J* = 7.7 Hz), 8.07 (1H, *d*, *J* = 8.5 Hz), 8.41 (1H, *d*, *J* = 8.1 Hz,), 8.53–8.55 (2H, *m*), 8.72 (1H, *d*, *J* = 8.6 Hz), 8.77 (1H, *d*, *J* = 5.6 Hz), 10.48 (1H, *s*), 10.93 (1H, *s*); ^{13}C-NMR (125 MHz, DMSO-d_6, δ / ppm): 25.0, 30.1, 31.7, 45.4, 102.9, 111.9, 112.2, 116.3, 120.5, 121.4, 124.2, 124.7, 125.9, 127.3, 127.4, 128.1, 129.6, 130.8, 132.2, 132.7, 134.0, 134.6, 141.4, 143.9, 147.3, 155.6, 157.5, 170.9, 171.0, 182.1; ESI-MS (*m*/*z*): 507 $[M+H]^+$.

N^1-*(2-(5-Fluoro-1*H*-indol-3-yl)ethyl)*-N^5-*(7-oxo-7*H*-dibenzo[*de,h*]quinolin-9--yl)pentanediamide (**5i**)*. Yield: 0.42 g, 40 %; orange solid; Anal. Calcd. for $C_{31}H_{25}FN_4O_3$: C, 71.53; H, 4.84; N, 10.76 %. Found: C, 71.77; H, 5.15; N, 10.57 %; ^{1}H-NMR (500 MHz, DMSO-d_6, δ / ppm): 1.85–1.91 (2H, *m*), 2.18 (2H, *t*, *J* = 7.3 Hz), 2.42 (2H, *t*, *J* = 7.3 Hz), 2.79 (2H, *t*, *J* = 7.5 Hz), 3.30–3.33 (2H, *m*), 6.89 (1H, *t*, *J* = 9.1 Hz), 7.23 (1H, *s*), 7.27–7.33(2H, *m*), 7.97 (1H, *d*, *J* = 5.6 Hz), 8.03 (1H, *t*, *J* = 7.9 Hz), 8.09 (1H, *d*, *J* = 8.6 Hz), 8.40 (1H, *d*, *J* = 8.2 Hz), 8.53–8.56 (2H, *m*), 8.71 (1H, *d*, *J* = 8.6 Hz), 8.76 (1H, *d*, *J* = 5.6 Hz), 10.43 (1H, s), 10.93 (1H, *s*); ^{13}C-NMR (125 MHz, DMSO-d_6, δ / ppm): 21.3, 25.0, 34.5, 35.7, 45.4, 102.9, 112.1, 116.1, 120.5, 121.3, 124.3, 124.6, 125.8, 127.3, 127.4, 128.1, 129.6, 130.8, 130.9, 132.2, 132.7, 134.0, 134.6, 141.4, 143.8, 147.4, 155.6, 157.4, 171.4, 171.5, 182.1. ESI-MS (*m*/*z*): 521 $[M+H]^+$.

Journal of the Serbian Chemical Society
JSCS-info@shd.org.rs • www.shd.org.rs/JSCS
J. Serb. Chem. Soc. 80 (2) 137–142 (2015)
JSCS–4704
UDC **Astragalus depressus*:577.121:547.918:543.422.25:543.51
Short communication

SHORT COMMUNICATION

An isoflavane and saponins from *Astragalus depressus* L.

LEYLA MAAMRIA[1], HAMADA HABA[1], CATHERINE LAVAUD[2], DOMINIQUE HARAKAT[2] and MOHAMMED BENKHALED[1]*

[1]*Laboratoire de Chimie et Chimie de l'Environnement (L.C.C.E), Département de Chimie, Faculté des Sciences, Université de Batna, Batna 05000, Algeria and* [2]*Laboratoire de pharmacognosie, Institut de Chimie Moléculaire de Reims, CNRS UMR 6229, BP 1039, 51097 Reims Cedex 2, France*

(Received 26 May, revised 14 September, accepted 16 September 2014)

Abstract: In this study, nine known secondary metabolites were isolated from ethyl acetate and *n*-butanol extracts of *Astragalus depressus* L. (Fabaceae family), including one isoflavane, namely pendulone (**1**) and eight saponins, namely cyclogaleginoside A (**2**), astrasieversianin II (**3**), astrasieversianin IV (**4**), astrasieversianin VIII (**5**), astrasieversianin VI (**6**), astrasieversianin XIV (**7**), dehydrosoyasaponin I (**8**) and soyasaponin I (**9**). The structures of compounds **1**–**9** were elucidated by spectroscopic methods, including 1D and 2D NMR, ESI mass spectrometry and comparison with literature data.

Keywords: Fabaceae; *Astragalus depressus*; saponins; pendulone; NMR; ESI.

INTRODUCTION

Astragalus depressus L. belongs to the genus *Astragalus* L.,[1] which is the largest genus in the Leguminosae (Fabaceae) family.[2] This Mediterranean species that is grazed by livestock is a perennial herb that grows in the rocks of the high mountains of Algeria.[1]

Astragalus, a member of the tribe Galegeae under the subfamily Papilionoideae (or Faboideae),[3] is found mainly in the temperate and arid regions of the world. Several *Astragalus* species are used worldwide in traditional medicine as antiperspirants, diuretics, tonics, in the treatment of nephritis, diabetes, leukemia and uterine cancer.[4,5]

In the course of previous investigations on Algerian Fabaceae plants, oleanane-type triterpene glycosides and flavonoids were isolated from *Astragalus cruciatus* Link[3] and *Lotus pusillus* Medik.[6] Saponins, cycloartane-type glycosides particularly, are the major class of chemical compounds that were isolated

* Corresponding author. E-mail: mbenkhaled@yahoo.fr
doi: 10.2298/JSC140526094M

previously from *Astragalus* species. Saponin compounds are known to possess immunostimulating,[7] cytotoxic[8] and antiviral activities.[9]

Hitherto, there have been no literature reports on the chemical constituents of *A. depressus*. A phytochemical investigation of the ethyl acetate and *n*-butanol extracts of this species was undertaken in order to determine its major components, such as saponins, which could be helpful for the chemotaxonomic profile of this species and *Astragalus* genus for further investigations.

EXPERIMENTAL

General

UV spectra were recorded on a Beckman DU-600 spectrometer. Positive and negative ion mode mass spectra were obtained on a Bruker Esquire Ion trap spectrometer. 1D and 2D NMR spectra (COSY, HSQC, HMBC, TOCSY, NOESY and ROESY) were obtained on a Bruker Avance spectrometer (^{1}H, 600 MHz, ^{13}C, 150 MHz). Optical rotations were measured on a Perkin-Elmer 241 polarimeter. CC was performed on silica gel 60 (320–400 mesh) and Sephadex LH-20. Analytical and preparative (1 mm thickness) TLCs were run on silica gel (Kieselgel 60 F254, Merck).

Plant material

The plant material (aerial parts and roots) was collected in May 2011 nearby Khenchela (Algeria) and was identified by Prof. Bachir Oudjehih, Agronomic Institute of the University of Batna, where a voucher specimen was deposited, with the identification number 659/LCCE.

Extraction and isolation

The air-dried and powdered whole plant of *Astragalus depressus* (800 g) was macerated with EtOH–H_2O (70:30 *V*/*V*, 8 L×2) for 3 days at room temperature. After filtration and evaporation of the aqueous alcoholic solution, the aqueous residue (0.5 L) was extracted successively with petroleum ether, EtOAc and *n*-butanol (each solvent, 0.5 L×3). The solvents were removed under vacuum to yield the following extracts: petroleum ether (3 g), ethyl acetate (8 g) and *n*-butanol (40 g). The details related to isolation are given in the Supplementary material to this paper.

RESULTS AND DISCUSSION

Nine known compounds were isolated from the ethyl acetate and *n*-butanol extracts of *A. depressus*, including eight saponins and one isoflavan. The structures of the compounds (Fig. 1) were identified clearly by comparison of ^{1}H- and ^{13}C-NMR data, ESI mass spectra and values of optical rotation with published data. The isolated compounds were identified as pendulone (**1**),[10,11] cycloglaeginoside A (**2**),[12] astrasieversianin II (**3**),[13] astrasieversianin IV (**4**),[13] astrasieversianin VIII (**5**),[13] astrasieversianin VI (**6**),[13] astrasieversianin XIV (**7**),[13] dehydrosoyasaponin I (**8**)[14] and soyasaponin I (**9**).[15]

Pendulone (**1**) was previously found in *Millettia pendula*,[16] *Oxytropis falcata*[17] and *Astragalus membranaceus*[18] that belong to the Fabaceae family. This is the second report of the occurrence of pendulone in the *Astragalus* genus. This

isoflavan has potent leishmanicidal activity[10] and showed potent anti-tumor-promoting activity.[19]

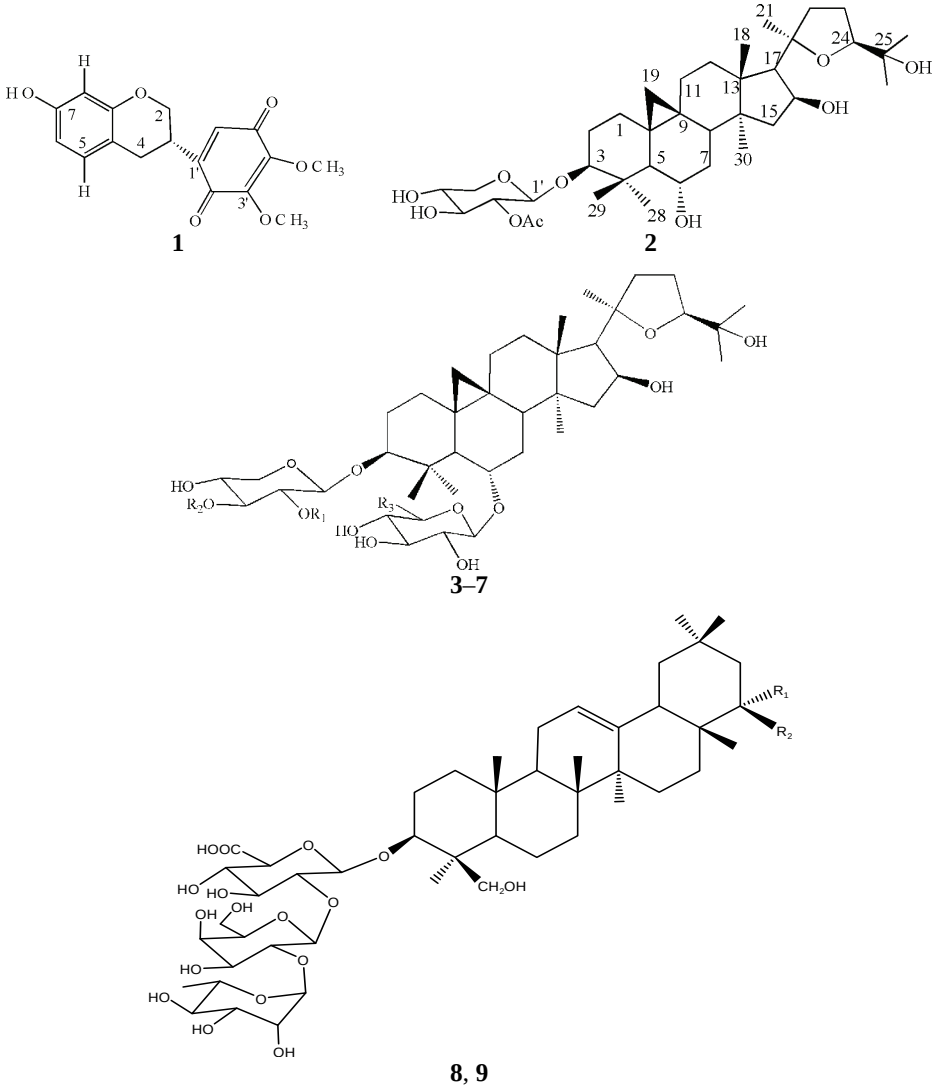

Fig. 1. Structures of compounds **1**–**9**; **3** – $R_1 = R_2 = Ac$, $R_3 = H$; **4** – $R_1 = R_2 = Ac$, $R_3 = CH_2OH$; **5** – $R_1 = Ac$, $R_2 = H$, $R_3 = CH_2OH$; **6** – $R_1 = Ac$, $R_2 = R_3 = H$; **7** – $R_1 = R_2 = H$, $R_3 = CH_2OH$; **8** – R_1, $R_2 = O$; **9** – $R_1 = \alpha H$, $R_2 = \beta OH$.

The cycloartane-type triterpene glycosides **2**–**7** isolated previously from several *Astragalus* species are considered as common saponins for the genus *Astragalus*.[12,13,20–26]

Dehydrosoyasaponin I (**8**) was found in many genera of the Fabaceae family, such as *Medicago sativa*[27] and *Pisum sativum* L.[28] This study reports its first identification in the *Astragalus* genus. Soyasaponin I (**9**) was identified previously from several *Astragalus* species, such as *A. crysopterus*,[29] *A. shikokianus*[30] and *A. trimestris*[31] besides some other Fabaceae genus, such as *Pisum*,[28] *Hedysarum*[32] and *Melilotus*.[33]

CONCLUSIONS

This is the first report on the chemical composition of *Astragalus depressus*. This work, which is in full agreement with the previous studies performed on the *Astragalus* genus, confirmed the importance of saponins as major compounds of this genus. Soyasaponin I (**9**), largely distributed in Fabaceae plants, is used as a chemotaxonomic marker for the family Fabaceae and *Astragalus* genus.[34]

To the best of our knowledge, the full ^{1}H- and ^{13}C-NMR data of pendulone (**1**) and cyclogaleginoside A (**2**) are given here for the first time.

SUPPLEMENTARY MATERIAL

The experimental details about isolation of the fractions, as well as the characterization data for pendulone (**1**) and cyclogaleginoside A (**2**) are available electronically from http://www.shd.org.rs/JSCS/, or from the corresponding author on request.

Acknowledgement. The authors wish to express thanks to the Algerian Minister of Higher Education and Scientific Research for providing a research grant and the University of Reims Champagne-Ardenne (France) for providing research facilities and technical support.

ИЗВОД

ИЗОФЛАВОНИ И САПОНИНИ ИЗОЛОВАНИ ИЗ *Astragalus depressus* L.

LEYLA MAAMRIA[1], HAMADA HABA[1], CATHERINE LAVAUD[2], DOMINIQUE HARAKAT[2] и MOHAMMED BENKHALED[1]

[1]*Laboratoire de Chimie et Chimie de l'Environnement (L.C.C.E), Département de Chimie, Faculté des Sciences, Université de Batna, Batna 05000, Algeria и* [2]*Laboratoire de pharmacognosie, Institut de Chimie Moléculaire de Reims, CNRS UMR 6229, BP 1039, 51097 Reims Cedex 2, France*

Током овог истраживања изоловано је девет познатих секундарних метаболита из етил-ацетатног екстракта и *n*-бутанолног екстракта *Astragalus depressus* L. (Fabaceae фамилија), и то пендулон (**1**) и осам сапонина, циклогалегинозид A (**2**), астрасиверсијанин II (**3**), астрасиверсијанин IV (**4**), астрасиверсијанин VIII (**5**), астрасиверсијанин VI (**6**), астрасиверсијанин XIV (**7**), дехидросојасапонин I (**8**) и сојасапонин I (**9**). Структуре једињења **1**–**9** утврђене су спектроскопским методама које подразумевају 1D и 2D NMR спектроскопију и ESI масену спектрометрију и поређене са подацима из литературе.

(Примљено 26. маја, ревидирано 14. септембра, прихваћено 16. септембра 2014)

REFERENCES

1. P. Quezel, S. Santa, *Nouvelle flore de l'Algérie et des régions désertiques méridionales*, Vol. 1, CNRS, Paris, 1963, p. 552

2. D. Podlech, *Proc. Roy. Soc. Edinburgh* **89** (1986) 37
3. W. Benchadi, H. Haba, C. Lavaud, D. Harakat, M. Benkhaled, *Rec. Nat. Prod*. **7** (2013) 105
4. S. Avunduk, A. C. Mitaine-Offer, Ö. Alankus-Caliskan, T. Miyamoto, S. G. Senol, M. A. Lacaille-Dubois, *J. Nat. Prod.* **71** (2008) 141
5. M. I. Choudhary, S. Jan, A. Abbaskhan, S. G. Musharraf, Samreen, S. A. Sattar, Atta-ur-Rahman, *J. Nat. Prod*. **71** (2008) 1557
6. L. Golea, H. Haba, C. Lavaud, L. Christophe, M. Benkhaled, *Biochem. Syst. Ecol*. **45** (2012) 12
7. E. Bedir, N. Pugh, I. Calis, D. S. Pasco, I. A. Khan, *Biol. Pharm. Bull*. **23** (2000) 834
8. M. M. Radwan, N. A. El-Sebakhy, A. M. Asaad, S. M. Toaima, D. G. I. Kingston, *Phytochemistry* **65** (2004) 2909
9. P. Gariboldi, F. Pelizzoni, M. Tatò, L. Verotta, N. A. El-Sebakhy, A. M. Asaad, R. M. Abdallah, S. M. Toaima, D. G. I. Kingston, *Phytochemistry* **40** (1995) 1755
10. M. Takahashi, H. Fuchino, S. Sekita, M. Satake, F. Kiuchi, *Chem. Pharm. Bull*. **54** (2006) 915
11. W. H. Chen, Z. Y. Ren, R. Wang, Y. P. Shi, *Anal. Sci*. **24** (2008) 209
12. M. D. Alaniya, M. I. Isaev, M. B. Gorovits, N. D. Abdullaev, E. P. Kemertelidze, N. K. Abubakirov, *Khim. Prir. Soedin*. **20** (1984) 451
13. G. Li-Xiang, H. Xiao-Bing, C. Yu-Qun, *Phytochemistry* **25** (1986) 2389
14. H. Miyao, Y. Sakai, T. Takeshita, J. Kinjo, T. Nohara, *Chem. Pharm. Bull*. **44** (1996) 1222
15. I. Kitagawa, M. Yosikawa, I. Yosioka, *Chem. Pharm. Bull*. **24** (1976) 121
16. Y. Hayashi, T. Shirato, K. Sakurai, T. Takahashi, *Mokuzai Gakkaishi* **24** (1978) 898 (in Japanese)
17. W. H. Chen, R. Wang, Y. P. Shi, *J. Nat. Prod.* **73** (2010) 1398
18. L. J. Zhang, H. K. Liu, P. C. Hsiao, L. M. Y. Kuo, I. J. Lee, T. S. Wu, W. F. Chiou, Y. H. Kuo, *J. Agric. Food Chem*. **59** (2011) 1131
19. T .Konoshima, M. Takasaki, M. Kozuka, H. Tokuda, H. Nishino, E. Matsuda, M. Nagai, *Biol. Pharm. Bull*. **20** (1997) 865
20. M. D. Alaniya, *Izv. Akad Nauk Gruz. SSR, Ser. Khim*. **14** (1988) 73
21. I. Calis, A. Yuruker, D. Tasdemir, A. D. Wright, O. Sticher, Y. D. Luo, J. M. Pezzuto, *Planta Med.* **63** (1997) 183
22. M. T. Baratta, G. Ruberto, *Planta Med.* **63** (1997) 280
23. S. Nikolov, N. Benbassat, *Farmatsiya (Sofia)* **44** (1997) 34 (in Bularian)
24. F. Pan, J. Yan, Y. Feng, *Zhiwu Xuebao* **38** (1996) 836 (in Chinese)
25. L. Verotta, N. A. El-Sebakhy, *Studies in natural products chemistry: Bioactive natural products*, Elsevier, Amsterdam, 2001
26. F. N. Yalcin, S. Piacente, A. Perrone, A. Capasso, H. Duman, I. Calis, *Phytochemistry* **73** (2012) 119 (in Japanese)
27. I. Kitagawa, T. Taniyama, T. Murakami, M. Yoshihara, M. Yoshikawa, *Yakugaku Zasshi* **108** (1988) 547 (in Japanese)
28. W. G. Taylor, P. G. Fields, D. H. Sutherland, *J. Agric. Food Chem*. **52** (2004) 7484
29. H. K. Wang, K. He, H. X. Xu, Z, L. Zhang, Y. F. Wang, T. Kikuchi, Y. Tezuka, *Yaoxue Xuebao* **25** (1990) 445 (in Japanese)
30. S. Yahara, M. Kihjyouma, H. Kohoda, *Phytochemistry* **53** (1990) 469
31. A. M. El-Hawiet, S. M. Toaima, A. M. Asaad, M. M. Radwan, N. A. El-Sebakhy, *Rev. Bras. Pharmacogn.* **20** (2010) 860

32. Y. Liu, Q. Y. Zhang, Y. Y. Zhao, B. Wang, L. Q. Hai, Y. P. Ying, H. B. Chen, *Biochem. Syst. Ecol*. **35** (2007) 389
33. T. Hirakawa, M. Okawa, J. Kinjo, T. Nohara, *Chem. Pharm. Bull*. **48** (2000) 286
34. W. Oleszek, A. Stochmal, *Phytochemistry* **61** (2002) 165.

Journal of the Serbian Chemical Society
JSCS@tmf.bg.ac.rs • www.shd.org.rs/JSCS
J. Serb. Chem. Soc. 80 (2) S28–S30 (2015) *Supplementary material*

SUPPLEMENTARY MATERIAL TO

An isoflavane and saponins from *Astragalus depressus* L.

LEYLA MAAMRIA[1], HAMADA HABA[1], CATHERINE LAVAUD[2], DOMINIQUE HARAKAT[2] and MOHAMMED BENKHALED[1]*

[1]*Laboratoire de Chimie et Chimie de l'Environnement (L.C.C.E), Département de Chimie, Faculté des Sciences, Université de Batna, Batna 05000, Algeria and* [2]*Laboratoire de pharmacognosie, Institut de Chimie Moléculaire de Reims, CNRS UMR 6229, BP 1039, 51097 Reims Cedex 2, France*

J. Serb. Chem. Soc. 80 (2) (2015) 137–142

ISOLATION OF THE FRACTIONS

7 g of ethyl acetate extract were subjected to vacuum liquid chromatography (VLC) using silica gel as the stationary phase (5 cm×5 cm; fractions of 100 mL). The elution was performed with a gradient of solvents $CHCl_3$–MeOH (100:0, 99:1, 95:5, 90:10, 80:20 and 70:30 *V*/*V*) and then $CHCl_3$–MeOH–H_2O (70:30:1, 70:30:3, 70:30:5, 70:30:7, 60:40:7 and 50:50:1 *V*/*V*/*V*). Fractions having similar TLC profiles were pooled to give 10 fractions (F1––F10). Fraction F4 (1.3 g) was applied to silica gel CC (70 cm×5 cm, fractions of 50 mL) and eluted with $CHCl_3$–MeOH (100:0, 99.5:0.5, 99:1, 95:5, 93:7, 90:10 and 80:20 *V*/*V*) to obtain 8 fractions. The fractions (175 mg) eluted with $CHCl_3$–MeOH (99:1 and 95:5 *V*/*V*) were purified on Sephadex LH-20 CC (40 cm×2.5 cm, fractions of 30 mL), eluted with $CHCl_3$ to provide two compounds **1** (15 mg) and **4** (5 mg). Fraction F5 (1.34 g) was chromatographed over silica gel column (70 cm×5 cm, fractions of 50 mL) using a $CHCl_3$–MeOH gradient system as for F4 providing 15 fractions. Fractions (130 mg) eluted with $CHCl_3$–MeOH (95:5 *V*/*V*) were purified on Sephadex LH-20 CC (40 cm×2.5 cm, fractions of 30 mL) using $CHCl_3$ as eluent to give 7 mg of **3**. The fraction (34 mg) eluted with $CHCl_3$–MeOH (95:5 *V*/*V*) was purified by silica gel column chromatography (30 cm×2.5 cm, fractions of 20 mL) eluted with $CHCl_3$–MeOH (100:0, 99:1, 95:5 and 93:7 *V*/*V*) to yield pure compound **6** (4 mg). Fraction (38 mg) eluted with $CHCl_3$–MeOH (95:5 *V*/*V*) was chromatographed through a silica gel SiO_2 column (30 cm×2.5 cm, fractions of 20 mL) using a gradient of $CHCl_3$–MeOH (97:3, 96:4, 95:5, 94:6 and 93:7 *V*/*V*) to give **2** (5.8 mg). Fraction F7 (614 mg) was subjected to silica gel CC (50 cm×3 cm, fractions of 30 mL) eluting with $CHCl_3$–MeOH (100:0, 99.5:0.5, 99:1, 95:5 and 90:10 *V*/*V*) to give 5 fractions. Fractions (25 mg) eluted with $CHCl_3$–MeOH (90:10 *V*/*V*) were purified by preparative TLC using CH_2Cl_2–MeOH (75:25) yielding 2 mg of **5**.

The *n*-butanol extract (8 g) was subjected to reversed phase RP-18 vacuum liquid chromatography (VLC) using a gradient of solvents water–methanol (80:20, 60:40, 20:80 and 0:100 *V*/*V*). Fractions having similar TLC profiles were pooled to afford 10 fractions (F1 to F10). Fraction F4 (545 mg) was subjected to silica gel CC (50 cm×3 cm, fractions of 30 mL)

* Corresponding author. E-mail: mbenkhaled@yahoo.fr

and eluted with $CHCl_3$–MeOH (100:0, 99:1, 98:2, 97:3, 95:5, 90:10, 80:20, 70:30 and 60:40 *V*/*V*) to provide 20 fractions. Fractions (50 mg) eluted with $CHCl_3$–MeOH (95:5 and 90:10 *V*/*V*) were precipitated in acetone to obtain 10 mg of **7**. The fraction (26.6 mg) eluted with $CHCl_3$–MeOH (60:40 *V*/*V*) was purified on TLC RP-18 using MeOH–H_2O (80:20 *V*/*V*) as eluent, which enabled the isolation of **9** (5 mg). Fraction F5 (330 mg) was applied to silica gel CC (50 cm×3 cm, fractions of 30 mL) eluting with $CHCl_3$–MeOH–H_2O (90:10:0.5, 90:10:1, 80:20:1, 80:20:2, 70:30:2 and 70:30:3 *V*/*V*/*V*) to give 3 mg of **8**.

CHARACTERIZATION DATA FOR COMPOUNDS **1** AND **2**

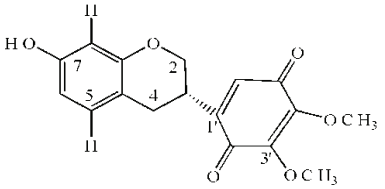

Structure of pendulone (**1**)

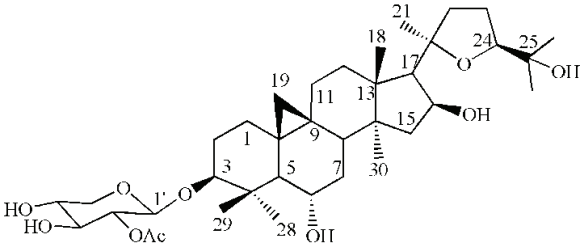

Structure of cyclogaleginoside A (**2**)

*Pendulone (**1**)*. Red powder; ^{1}H-NMR (600 MHz, $CDCl_3$, δ / ppm): 2.72 (1H, *dd*, *J* = 16.0, 6.2 Hz, H-4b), 3.05 (1H, *dd*, *J* = 16.0, 6.2 Hz, H-4a), 3.45 (1H, *qd*, *J* = 6.2, 2.5 Hz, H-3), 4.04 (6H, *s*, OCH_3), 4.07 (1H, *dd*, *J* = 10.6; 6.2 Hz, H-2b), 4.27 (1H, *dd*, *J* = 10.6, 2.5 Hz, H-2a), 4.97 (1H, *br s*, 7-OH), 6.34 (1H, *d*, *J* = 2.5 Hz, H-8), 6.39 (1H, *s*, H-6′), 6.43 (1H, *dd*, *J* = 8.3, 2.5 Hz, H-6), 6.93 (1H, *d*, *J* = 8.3 Hz, H-5); ^{13}C-NMR (150 MHz, $CDCl_3$, δ / ppm): 28.9 (CH_2, C-4), 30.8 (CH, C-3), 61.2 (CH_3, 4′-OMe), 61.4 (CH_3, 3′-OMe), 68.1 (CH_2, C-2), 103.4 (CH, C-8), 108.8 (CH, C-6), 112.3 (C, C-4a), 130.4 (CH, C-5), 131.0 (CH, C-6′), 144.6 (C, C-4′), 145.1 (C, C-3′), 146.6 (C, C-1′), 154.7 (C, C-8a), 155.2 (C, C-7), 183.5 (C, C-2′), 184.1 (C, C-5′); ESI-MS (*m/z* (relative abundance, %)): 339 ($(M+Na)^+$, 100); optical rotation, α (589 nm, 20 °C, 10 g dm^{-3} in MeOH, 10 cm): –70.3°.

*Cyclogaleginoside A (**2**)*. Amorphous powder; ^{1}H-NMR (600 MHz, CD_3OD, δ / ppm): 0.28 (1H, *d*, *J* = 4.3 Hz, H-19exo), 0.60 (1H, *d*, *J* = 4.3 Hz, H-19endo), 0.93 (3H, *s*, H-29), 1.02 (3H, *s*, H-30), 1.14 (3H, *s*, H-26), 1.22 (2H, *m*, H-1b, H-11b), 1.22 (3H, *s*, H-28), 1.23 (3H, *s*, H-21), 1.28 (3H, *s*, H-27), 1.29 (3H, *s*, H-18), 1.37 (2H, *m*, H-5, H-15b), 1.38 (1H, *m*, H-7b), 1.48 (1H, *dt*, *J* = 12.1, 4.1 Hz, H-7a), 1.56 (1H, *td*, *J* = 13.2, 2.4 Hz, H-1a), 1.65 (2H, *m*, H-2b, H-22b), 1.68 (2H, *m*, H-12a, H-12b), 1.82 (1H, *dd*, *J* = 12.1, 4.1 Hz, H-8), 1.96 (1H, *m*, H-2a), 1.97 (1H, *dd*, *J* = 12.9, 7.8 Hz, H-15a), 2.04 (1H, *m*, H-11a), 2.05 (2H, *m*, H-23a, H-23b), 2.38 (1H,*d*, *J* = 7.8 Hz, H-17), 2.63 (1H, *q*, *J* = 10.7 Hz, H-22a), 3.17 (1H, *dd*, *J* = 11.6, 4.5 Hz, H-3), 3.22 (1H, *t*, *J* = 10.7 Hz, H-5′b), 3.45 (1H, *td*, *J* = 9.6, 4.1 Hz, H-6), 3.46 (1H, *t*, *J* = 9.3 Hz, H-3′), 3.56 (1H, *ddd*, *J* = 10.7, 9.3, 5.4 Hz, H-4′), 3.78 (1H, *dd*, *J* = 8.3; 6.0 Hz, H-24), 3.86 (1H, *dd*, *J* = 10.7, 5.4

Hz, H-5′a), 4.42 (1H, *d*, *J* = 7.9 Hz, H-1′), 4.68 (1H, *q*, *J* = 7.8 Hz, H-16), 4.73 (1H, *dd*, *J* = 9.3, 7.9 Hz, H-2′), additional signal: 2.10 (3H, *s*, OAc); ^{13}C-NMR (150 MHz, CD_3OD, δ / ppm): 15.0 (CH_3, C-29), 19.1 (CH_3, C-30), 20.4 (C, C-9), 20.6 (CH_3, C-18), 25.2 (CH_3, C-26), 25.4 (CH_2, C-11), 25.5 (CH_2, C-23), 26.2 (CH_3, C-27), 27.1 (CH_3, C-21), 27.2 (CH_3, C-28), 29.0 (CH_2, C-2), 29.2 (C, C-10), 30.8 (CH_2, C-19), 31.7 (CH_2, C-1), 32.5 (CH_2, C-12), 34.1 (CH_2, C-22), 37.6 (CH_2, C-7), 41.4 (C, C-4), 44.5 (C, C-13), 45.4 (CH_2, C-15), 45.6 (C, C-14), 47.3 (CH, C-8), 53.0 (CH, C-5), 57.7 (CH, C-17), 65.5 (CH_2, C-5′), 68.1 (CH, C-6), 69.9 (CH, C-4′), 71.0 (C, C-25), 73.2 (CH, C-16), 74.3 (CH, C-2′), 74.8 (CH, C-3′), 81.2 (CH, C-24), 86.9 (CH, C-20), 88.6 (CH, C-3), 103.8 (CH, C-1′), additional signals: 19.8 (CH_3, OAc), 170.4 (C, OAc); ESI-MS (*m/z* (relative abundance, %)): 687 ($(M+Na)^+$, 100); Optical rotation, α (589 nm, 20 °C, 10 g dm^{-3} in MeOH, 10 cm): +36.1°.

Journal of the Serbian Chemical Society
JSCS-info@shd.org.rs • www.shd.org.rs/JSCS
J. Serb. Chem. Soc. 80 (2) 143–157 (2015)
JSCS–4705
UDC 615.27+615.35:616.12–089
Original scientific paper

Markers of inflammation and antioxidant enzyme activities in restenosis following percutaneous coronary intervention

SNEŽANA PANTOVIĆ[1], DRAGICA BOŽOVIĆ[2], GORAN NIKOLIĆ[1,3], MILICA MARTINOVIĆ[1], PREDRAG MITROVIĆ[4,5], LENKA RADULOVIĆ[1], ALEKSANDRA ISAKOVIĆ[6] and IVANKA MARKOVIĆ[6]*

[1]*Faculty of Medicine, University of Montenegro, Kruševac bb, Podgorica, Montenegro,* [2]*Center for Clinical Laboratory Diagnostic, Clinical Centar of Montenegro, Podgorica, Montenegro,* [3]*Center for Radiology Diagnostics, Clinical Center of Montenegro, Ljubljanska bb, Podgorica, Montenegro,* [4]*Cardiology Clinic, Clinical Center of Serbia, Belgrade, Serbia,* [5]*Faculty of Medicine, University of Belgrade, Belgrade, Serbia and* [6]*Institute of Medical and Clinical Biochemistry, Faculty of Medicine, University of Belgrade, Pasterova 2, 11000 Belgrade, Serbia*

(Received 17 June, revised 30 August, accepted 2 September 2014)

Abstract: The efficacy of percutaneous coronary intervention (PCI) is often compromised by the need for repeat revascularization because of restenosis development. Numerous studies have tried to establish the predictive value of different biochemical markers of restenosis, with conflicting results. The aim of this study was to assess the prognostic significance of inflammatory and lipid markers, and major antioxidant enzyme activity for the development of in-stent restenosis (ISR) following PCI. Serum high sensitive C-reactive protein (hs-CRP), soluble intercellular cell adhesion molecule-1 (sICAM-1), transforming growth factor-beta (TGF-β), lipoprotein(a) (LP(a)) and oxidized low-density lipoprotein (oxLDL) levels, as well as serum extracellular superoxide dismutase (EC-SOD) and catalase (CAT) activities were determined in 44 patients before the stent implantation procedure, and after 6-month follow-up. The results after follow-up revealed that in patients that developed angiographically confirmed ISR, the increase in serum hs-CRP levels was significantly higher compared to those without stenosis. Stent implantation induced compensatory increases in the activities of serum antioxidant enzymes at follow-up, with significantly lower CAT activity in patients with ISR, possibly contributing to stenosis development. No significant changes in the circulating levels of ICAM-1, TGF-β, oxLDL and Lp(a) were observed between the groups. In conclusion, serum hs-CRP level and CAT activity may be considered as useful biochemical markers for monitoring patients during follow-up after stent implantation.

Keywords: coronary restenosis; hs-CRP; EC-SOD; catalase; oxLDL; Lp(a).

* Corresponding author. E-mail: ivanka@med.bg.ac.rs
doi: 10.2298/JSC140617088P

INTRODUCTION

Percutaneous coronary intervention (PCI) with stent implantation has revolutionized the management of coronary artery disease (CAD), enabling greater efficacy in the prevention of acute occlusions. The efficacy of PCI is limited because of the development of in-stent restenosis (ISR), a long-term complication that occurs in 20–30 % of patients 6 months after the procedure.[1] Great efforts have been made in attempts to elucidate the molecular mechanism(s) leading to ISR, and to search for potential markers that would help identify patients at higher risk for ISR.

Experimental studies showed that ISR is a complex and multifactorial process strongly influenced by the inflammatory response of the arterial wall to stent deployment. Previous studies also reported that percutaneous coronary interventions induce the production of vascular reactive oxygen species (ROS). The increase in ROS after stent implantation was shown to induce a chain reaction resulting in oxidative stress, which could lead to endothelial dysfunction, neointimal formation, stent thrombosis and eventual restenosis.[2] Stent implantation, in particular, can precipitate arterial intimal cellular proliferation and extracellular matrix synthesis, which is mediated largely by inflammatory processes.[3] There is evidence that inflammatory response further enhances oxidative stress in the growing lesions, while, on the other hand, oxidative stress, which has pro-inflammatory properties, could cause inflammation.[4] Several studies suggested that restenosis after PCI is associated with increased circulating levels of inflammatory markers, such as pro-inflammatory cytokines and C-reactive protein (CRP) before or after the procedure.[5] Several studies demonstrated that CRP could induce oxidative stress *in vitro*. It was also published that cardiomyocytes from patients with CAD produce CRP locally and that human recombinant CRP induces significant increase in the production of reactive species in endothelial cells, leading to a concentration-dependent induction of apoptotic cell death, which can be attenuated in the presence of antioxidants.[6]

Similar relations were shown with serum levels of other inflammatory markers, such as adhesion molecules (ICAM-1 or VCAM-1). It was noted that arterial endothelial expression and raised serum concentrations of the soluble form of intercellular adhesion molecule-1 (sICAM) are implicated in the development of CAD after coronary artery bypass surgery.[7] A significant correlation between raised concentrations of CRP and soluble ICAM1 concentrations after transplantation was also reported.[7] In addition, immunohistochemical analyses of human and animal samples showed that TGF-beta expression is upregulated following balloon- or stent-induced vascular injury.[8] Furthermore, upregulation of TGF-beta was shown to increase intimal thickening, whereas blockade of TGF-β attenuated this process.[9]

The characteristic histological finding of restenotic tissue is intimal hyperplasia, with a variable lipid component. This histological appearance suggests that similar cellular processes may play important roles in both atherogenesis and restenosis. Many previous studies revealed that serum levels of low- and high-density lipoprotein cholesterol (LDL-C and HDL-C, respectively) are the major predictors of atherosclerotic coronary artery disease, and an inverse relation between HDL levels and the restenosis rate in patients following PCI was demonstrated,[10] possibly attributed to the scavenger function of HDL cholesterol. In addition, it was shown that hypercholesterolemia is associated with increased level of oxidative stress, contributing to an increased oxidation of LDL.[11] The accumulation of oxidized low-density lipoproteins (oxLDLs) in atherosclerotic lesions from coronary and carotid arteries was demonstrated,[12] as well as an elevation of circulating levels of oxLDLs in patients with unstable angina or acute myocardial infarction.[13] Lipoprotein(a) [Lp(a)] is a low-density lipoprotein (LDL)-like particle in which apolipoprotein (apo)B-100 is bound by a disulfide bridge to apo(a).[14] Lp(a) was identified in the atherosclerotic plaque and it was shown that Lp(a) plaque levels correlate with its concentration in plasma.[15] In numerous reports, associations between elevated serum concentrations of Lp(a) and CAD, myocardial infarction, cerebrovascular disease and stenosis of coronary artery bypass vein grafts were established.[13,15] However, to the best of our knowledge, data on the association between the level of circulating oxLDL and Lp(a) with clinical outcome after coronary stenting are limited, even though some studies suggested that elevated plasma concentration of lipoprotein(a) could be a risk factor for restenosis after PCI.[15]

Bearing in mind the role of inflammatory and lipid markers, as well as the serum antioxidative status, it was hypothesized that several inflammation (hs--CRP, sICAM-1, TGF-β) and lipid markers (Lp(a), oxLDL), as well as the activity of major plasma antioxidant enzymes (EC-SOD and catalase) could be regarded as prognostic markers for the development of in-stent restenosis following PCI.

EXPERIMENTAL

Study group

The study group consisted of 81 consecutive patients with CAD who were successfully treated with either balloon coronary angioplasty or stent implantation in the Clinical Center of Montenegro during 2010 and 2011. Out of this cohort, 44 patients who had successful coronary stent implantation underwent follow-up angiography and a series of biochemical analyses were performed prior to PCI (percutaneous coronary intervention) (baseline) and at follow-up, 6 months after the procedure. All patients fulfilled the following criteria: confirmed myocardial ischemia, coronary vessel constriction (defined reduction > 50 % vessel lumen diameter), no contraindications to the administration of antiplatelet agents, and written agreement to undergo follow-up angiography. Conventional clinical risk factors for CAD were recorded such as age, gender, current smoking habit (>5 cigarettes/day), hypertension (systolic

blood pressure >140 mm Hg, diastolic blood pressure >90 mm Hg or antihypertensive medication), and hyperlipidemia (total cholesterol > 5.17 mmol L^{-1}, LDL-cholesterol > 2 mmol L^{-1} or cholesterol-lowering medications). The patients received a single heparin injection (5000 I.U.) after obtaining blood sample and prior to PCI, followed by post-operative administration of treatment oral antiplatelet agents (aspirin, 100 mg and clopidogrel, 75 mg) that was continued throughout follow-up period.

The clinical and angiographic exclusion criteria were fasting glucose levels > 6.5 mmol L^{-1}, obesity (*BMI* > 25 kg m^{-2}), acute or chronic inflammatory conditions, liver or kidney dysfunction, treatment with steroids, pregnancy and presence of mental disorders. The study was conducted in accordance with the principles of the Declaration of Helsinki. The study protocol was approved by the Ethical Committee of the Clinical Center of Montenegro and written informed consent was obtained from all patients for routine control angiographic examination after 6 months.

Angiographic assessment

Coronary intervention and angiographic assessment were performed with a digital angiographic system (Siemens Axiom interventional cardiology systems), and quantitative coronary analysis (QCA) was performed on a digital angiographic workstation (Axiom Syngo artis zee family of C-arm system). Restenosis was defined as a percent diameter stenosis *DS* > 50 % at the site of the treated lesion in at least 2 orthogonal views.

Laboratory tests

Blood samples were obtained two hours before PCI (baseline), and at follow-up, 6 months after the procedure, after fasting for at least 10 h. All the analyses were performed at the Center for Clinical Laboratory Diagnostics of the Clinical Center of Montenegro, unless stated otherwise. Peripheral venous blood (10 mL) was collected in the morning, after fasting for a minimum of 10 h. Serum was separated at 3000 rpm at 4 °C for 15 min. The supernatant was collected, and aliquots were stored at –80 °C until analysis. The presence of hemolysis was followed by measurement of plasma hemoglobin and all patients with hemoglobin concentration > 50 mg L^{-1} were excluded from the study. Serum levels of glucose, triacylglycerol, cholesterol, VLDL and LDL were determined using standard commercial kits (Abbott Laboratories), whereas the concentration of hs-CRP was determined using laser nephelometry (BNII Siemens). The concentrations of ICAM-1, TGF-β, Lp(a) and oxLDL were determined employing a ChroMate 4300 microplate reader (Awareness Technology Inc., Palm City, FL, USA) using enzyme-linked immunosorbent assays (DRG International, Springfield, NJ, USA) at the Laboratory for Research at the Faculty of Medicine, University of Montenegro. Measurement of the serum activity of antioxidative enzymes was performed at the Institute of Medical and Clinical Biochemistry, Faculty of Medicine, Belgrade, Serbia. The superoxide dismutase (SOD) activity in serum was measured spectrophotometrically, using the method of Misra and Fridovich, based on the ability of SOD to inhibit auto-oxidation of epinephrine at alkaline pH (pH 10.2).[16] Catalase activity was determined spectrophotometrically by measureing the degradation of H_2O_2 using ammonium molybdate.[17]

Statistical analysis

Data are expressed as mean ± *SD* or median, as indicated in the text or Figure legends. The student's *t*-test was used to compare differences between continuous variables. The significance of differences between the frequencies of incidence of risk factors was tested using the χ^2-test. *P* values < 0.05 were considered significant. All statistical calculations were realized using a trial version of IBM 17 SPSS for Windows.

RESULTS AND DISCUSSION

The results of role of the investigated inflammatory (hs-CRP, sICAM-1 and TGF-β) and lipid (Lp(a) and oxLDL) markers, as well as the serum antioxidative status and their prognostic significance for the development of ISR following PCI are as follows.

Baseline characteristics

Of the 44 patients who underwent stent implantation, 31 (70.5 %) were male and 13 (29.5 %) were female and all were between the ages of 38 and 75 (56.0±5.5 years). In-stent restenosis (ISR) occurred within 6 months of stent implantation in 8 patients (18.2 %). In univariate analysis, age and gender did not differ between the groups with and without restenosis ($p > 0.05$). No significant association between restenosis and hypercholesterolemia, hypertension or smoking was observed (Table I). However, there were significant differences in positive family history for CAD and previous angina.

TABLE I. Baseline characteristics of the patients stratified by stent implantation with restenosis or without restenosis. CAD - coronary artery disease; Values are mean ± *SD*, *$p < 0.05$

Risk factor	No restenosis ($n = 36$)	Restenosis ($n = 8$)
Age, years	60.2±8.1	61.2±7.3
Male, %	69.4	75.0
Smoking, %	44.4	33.3
Hypercholesterolemia, %	55.6	33.3
Hypertension, %	75.0	66.7
Family history for CAD, %	33.3	55.6 *
Previous angina, %	36.1	50.0 *

This study focused on the association between the biochemical risk factors (inflammatory biomarkers, level of anti-oxidant protection and lipid markers) and ISR as an adverse event following coronary angioplasty and stent implantation. Moreover, the standard panel of biochemical analyses (serum concentration of glucose, triacylglycerol, cholesterol, VLDL, LDL, HDL, troponin I, AST, CK-MB and cystatin C) was also performed at the same time points, in order to assess the patients glycemic and lipid profile (Table II). No significant difference was observed in the biochemical profile neither at the pre-procedural time point nor after 6-month follow-up between the patients without restenosis and those developing ISR.

Inflammatory biomarkers in restenosis

Even though it is well established that multiple factors can contribute to ISR, the underlying mechanisms remain elusive. Numerous studies in animal models and on human arterial segments *in vitro* have reported the critical role of inflammation in the restenotic process, either because of pre-existing inflammatory lesion,

TABLE II. Biochemical parameters determined in serum of those that underwent stent implantation prior to PCI (baseline) and after 6-month follow-up; values are mean ± *SD*; $p > 0.05$

Parameter	No stenosis		In-stent restenosis	
	Baseline	Follow-up	Baseline	Follow-up
Glucose, mmol L^{-1}	5.05±0.75	4.85±0.69	5.17±0.64	4.92±0.45
Triacylglycerol, mmol L^{-1}	2.08±0.85	2.07±0.78	1.79±1.07	1.63±0.87
Cholesterol, mmol L^{-1}	5.63±1.03	5.44±0.99	4.60±0.9	5.43±1.83
VLDL / mmol L^{-1}	1.47±1.08	1.54±1.18	2.28±2.04	2.04±1.73
LDL / mmol L^{-1}	3.83±0.74	3.70±0.54	3.81±1.32	3.69±1.08
HDL / mmol L^{-1}	1.06±0.26	1.05±0.25	1.14±0.16	1.13±0.16
AST / U L^{-1}	21.25±7.18	24.74±14.25	18.75±5.52	21.68±10.21
CK-MB / U L^{-1}	16.0±0.32	16.97±6.64	15.6±3.73	19.48±5.06
Troponin I, ng L^{-1}	0.05±0.04	0.17±0.44	0.02±0.01	0.08±0.16
Cystatin C, ng L^{-1}	0.88±0.22	0.90±0.20	0.8±0.17	0.79±0.17

or an inflammatory response developing after the procedure. However, the data regarding the relationship between inflammatory marker levels prior to PCI and after the follow-up period in human subjects have been somewhat controversial. Some reports revealed association between the hs-CRP concentration before the intervention and restenosis during the following 6–12 months,[5] whereas other studies failed to establish a relationship between ISR and preprocedural hs-CRP levels.[18] Hence, the aim of the present study was to investigate the serum hs-CRP level both before and 6 months after PCI, and to assess if an increase in the hs-CRP level during the follow-up period was be more pronounced in patients with angiographically confirmed restenosis. The obtained results showed that the preprocedural hs-CRP level was not significantly different between patients with no stenosis and those developing ISR ($p = 0.8117$, Fig. 1). However, the increase in serum hs-CRP concentrations after 6-month follow-up was more pronounced ($p = 0.029$) in patients who developed restenosis (from 9.08±6.53 to 13.91±5.53 mg L^{-1}), compared to those without ISR (10.29±0.29 to 12.27±6.48 mg L^{-1}, Fig. 1). It was previously demonstrated that stent deployment itself is associated with an increase in the hs-CRP level up to 48 h after the procedure, resulting in an increased ISR rate.[19] Elevated hs-CRP levels were also associated with increased rate of death or myocardial infarction 30 days after stenting, most likely due to the pro-thrombotic action of CRP.[19] The present results confirmed the previously published data that the post-intervention rise in inflammatory markers reflected the inflammatory response,[18] and indicated towards a link between raised post-intervention CRP levels and development of ISR. This rise in the hs-CRP level may be an indicator of the extent of inflammation in atheromatous lesions, and such plaques could be prone to the development of ISR. Moreover, CRP appeared to be involved in foam cell formation, promotion of monocyte chemotaxis and facilitation of LDL (low-density lipoprotein) uptake by macrophages *in*

vitro.[20] These findings suggest that CRP may play a causal role in vascular disease and therefore could be considered as a possible target of therapy.

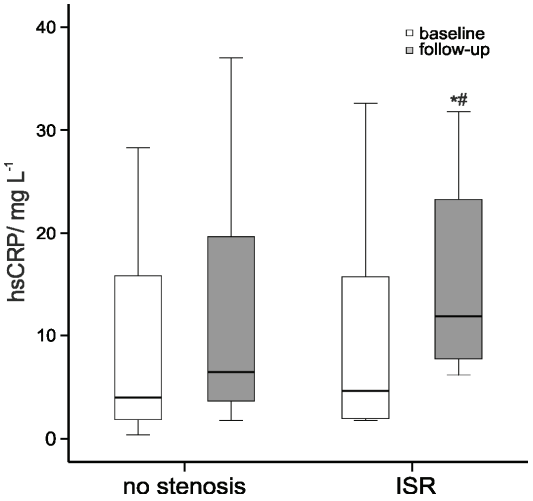

Fig. 1. The concentration of high-sensitivity CRP (hs-CRP) in the serum of patients that underwent stent implantation prior to PCI (baseline) and after 6-month follow-up. * – $p < 0.05$ compared to baseline enzyme activity, # – $p < 0.05$, compared to patients without stenosis at the same time point.

One of the events contributing the inflammatory response following PCI is leukocyte activation and infiltration (*e.g.*, monocyte, T-lymphocyte and granulocyte). Vascular injury induced by PCI may upregulate local cytokine expression leading to the release of pro-inflammatory factors. The cytokines released from activated macrophages, smooth muscle cells, lymphocytes and cells forming the vascular wall may stimulate neointimal formation.[15] Animal models showed that various cell components of the vascular wall express adhesion molecules, such as ICAM-1 or VCAM-1, for up to 30 days after balloon injury, which facilitates leukocyte interaction with the arterial wall.[21] Furthermore, inflammatory cytokines, such as tumor necrosis factor-α or interleukin-1, stimulate adhesion molecule expression, and these cytokines were shown to be upregulated at the arterial site after angioplasty.[22] However, results of studies that investigated the use of sICAM-1 as a biomarker of prognosis for cardiovascular disease are contradictory.[23] In this study, it was evaluated whether the levels of circulating adhesion molecule ICAM increased following the development of ISR. The results failed to confirm changes in sICAM-1 in the group of patients with ISR, compared to patients without stenosis (Table II). These results are in accordance with a previously published study that suggested a more dominant role for sVCAM-1, but not sICAM-1, in development of restenosis following PCI.[24]

The role of the transforming growth factor-beta (TGF-β) in restenosis has been studied for over two decades. TGF-β is a family of cytokines with a variety of functions, including fibrosis, growth, differentiation and apoptosis. Both human and animal studies demonstrated that TGF-β is upregulated at sites of vas-

cular injury. However, emerging data indicated that the role of TGF-β in restenosis is complex, and could be attributed not only to TGF-β-mediated vascular fibrosis, but to intimal thickening and arterial remodeling as important events in restenosis development.[9] In animal studies, systemic suppression of TGF-β activity accelerated the development of atherosclerosis, but in humans, the plasma TGF-β concentration was found to be negatively correlated with atherosclerosis.[25] In the present study, the plasma TGF-β concentration did not differ in patients with ISR, in comparison with patients without stenosis, neither before the procedure nor after 6-month follow-up (Table II). Even though most studies are based on the rationale that TGF-β promotes intimal hyperplasia, it appears that some components of the TGF-β signaling cascade may favor outward or adaptive remodeling.[9] Therefore further studies are required to help delineate the multifunctional role and mechanisms of TGF-β signaling in different restenotic lesions.

Antioxidative enzyme activity in restenosis

Previous studies on the mechanisms of restenosis post-balloon angioplasty showed increased oxidative stress and impaired redox processes as possible factors contributing to restenosis development.[26] Although the mechanisms participating in redox imbalance are not fully elucidated, it is certain that the increased oxidative stress is in close association with the inflammatory response that is observed following stent implantation. It was shown that the oxidative stress in the vascular wall developed immediately after the procedure, and persisted during all stages of ISR, including the stage of neointimal hyperplasia (proliferation and migration of smooth muscle cells and synthesis of an extracellular matrix), which is the leading mechanism of ISR development.[26] In addition, active forms of oxygen are known to modify the aggregation functions of platelets, thus also contributing to restenosis development.[27]

In contrast to the role of ROS in immune defense against microbial agents, ROS in vascular cells could be regarded as signaling molecules,[4] playing a role in activation and expression of pro-atherogenic genes.[28] Signal transmission *via* ROS occurs at free sulfhydryl groups of cysteine residues, which are present in many enzymes, including kinases, phosphatases, phospholipases, *etc*., as well as transcriptional factors (*e.g*., NF-κB). For instance, reactive oxygen species (ROS) are known to stimulate TGF-β-induced gene expression *via* Smad-dependent and Smad-independent pathways.[9]

Bearing in mind the important role of oxidative stress in ISR development, the protective scavenging function of plasma enzymes seems crucial to prevent the deleterious action of ROS. The most important plasma enzymes participating in scavenging activity are extracellular superoxide dismutase (EC-SOD), a major component of antioxidative defense in blood vessels, and catalase.[29] EC-SOD

represents a major defense system against superoxide, being a target for oxidative damage as well. It also inhibits the reaction between superoxide and NO, maintaining endothelium-dependent vasodilatation.[30] Numerous studies provided evidence that decreased activity of antioxidant enzymes contributed to development of atherosclerosic lesions, but the data on EC-SOD activity in heart diseases were not consistent. It was shown that the levels of EC-SOD protein appearing in the plasma was reduced in subjects with coronary artery disease,[31] or history of miocardial infarction.[32] In addition, the activities of EC-SOD and catalase in blood of patients with myocardial infarction after reperfusion were shown to be significantly decreased compared to the controls.[33] It was also reported that local gene therapy with EC-SOD in atherosclerotic hyperlipidemic rabbits could inhibit ISR.[29] However, other studies failed to establish a difference in activities of EC-SOD and catalase between patients that developed in-stent restenosis, compared to those with CAD, but no stenotic lesions.[33]

In the present study, the serum EC-SOD activity was increased after 6-month follow up in patients without stenosis (from 67.3±9.49 to 108.92±12.87 U mL^{-1}, $p < 0.01$), as well as in patients with ISR (73.4±11.98 to 117.28±11.96 U mL^{-1}, $p < 0.05$). However, no significant change in the rate of increase in EC-SOD activity was observed after 6-month follow-up between the two groups, as shown in Fig. 2 ($p > 0.05$). Given the role of SOD in dismutation of superoxide anions, it is possible that the observed increase in its activity after follow-up was an adaptive phenomenon in response to increased $O_2^{\bullet-}$ concentration that inevitably follows stent implantation. It is important to note that, in this study, only EC-SOD released into the plasma was determined, whereas the majority of enzyme remained attached to endothelial cell membrane glycoproteins. It is possible that, although there was increased EC-SOD release into plasma after follow-up in both

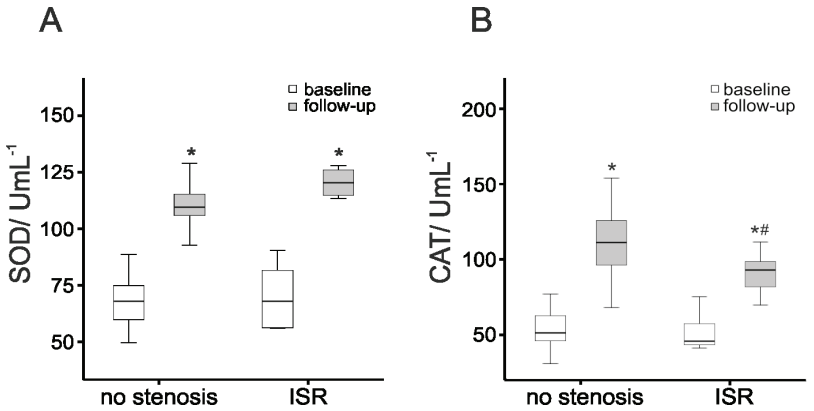

Fig. 2. SOD (A) and catalase (B) activities in the serum of patients that underwent stent implantation prior to PCI (baseline) and after 6-month follow-up. * – $p < 0.05$ compared to baseline enzyme activity, # – compared to patients without stenosis at the same time point.

groups, there will be a difference in overall amount of available enzyme between patients with ISR and patients without stenosis, as suggested previously.[29]

SOD dismutates $O_2^{\bullet -}$ into H_2O_2, which, in turn, is scavenged by catalase. It was shown that CRP can directly induce ROS formation in endothelial progenitor cells (EPC) by inducing expression of MnSOD and down regulating glutathione peroxidase expression, leading to excessive production of H_2O_2, resulting in H_2O_2-induced EPC death.[31] In addition, increased H_2O_2 production in patients with restenosis was reported.[34] The protective role of catalase against hydrogen peroxide-induced endothelial cell injury was documented *in vitro* and in animal models. Catalase overexpression protected the endothelium of human aorta against apoptosis caused by the oxidized forms of low-density lipoproteins (oxLDL),[35] whereas a 3-day catalase treatment *in vivo* decreased the blood pressure of spontaneously hypertensive wild-type mice and ameliorated the *ex vivo* function of the aorta endothelium.[36] In the present study, the increased EC-SOD activity during follow-up resulted in increased availability of the catalase substrate (H_2O_2). The present results showed that the increase in catalase activity ($X \pm SD$) was significantly lower in patients with ISR after 6-month follow-up – from 51.61±12.84 U L^{-1} at the baseline to 87.06±12.90 U L^{-1} after follow-up ($p = 0.0036$), In patients without stenosis the changes were from 54.07±12.66 to 119.25±29.86 U L^{-1} ($p = 0.0001$) compared to subjects without stenosis, as shown in Fig. 2. The difference between the groups at follow-up was statistically significant ($p = 0.0142$), despite the difference in the sample size. The data showed, for the first time, that a decrease in catalase protective activity might be one of the factors contributing to the development of ISR.

Lp(a) and oxLDL in restenosis

The role of lipoproteins as risk factors for the development of coronary restenosis after PCI was investigated in several studies. Lp(a) was independently associated with the presence of coronary atherosclerosis on angiography in the general population.[13] However, there are fewer data on the role of Lp(a) in patients with established CAD, implicating that Lp(a) might be less predictive of vascular risk in patients with established vascular disease.[37] Since it was shown that Lp(a) has a high degree of homology to plasminogen, thus inhibiting plasminogen activation,[14] the hypothesis was that patients with elevated Lp(a) concentrations in blood may have a greater tendency to thrombosis, after platelet activation initiated by arterial injury during stent implantation, leading to increased growth factor release and a propensity to coronary restenosis.

In the present study, the preprocedural level of Lp(a) was higher in patients that had developed ISR, but due to small sample number of patients included in the study, it did not reach the level of significance (Table III). Further studies are

needed to help clarify how relevant the Lp(a) concentration might be as a predictive factor for ISR.

TABLE III. Concentration of soluble intercellular cell adhesion molecule-1 (sICAM-1), and transforming growth factor-beta (TGF-β) in serum of patients that underwent stent implantation prior to PCI (baseline) and after 6-month follow-up; values are mean ± *SD*

Species	No stenosis		In-stent restenosis	
	Baseline	Follow-up	Baseline	Follow-up
sICAM-1 / ng mL^{-1}	62.68 ± 12.49	62.02 ± 17.84	60.55 ± 18.54	59.91 ± 17.25
TGF-β / pg mL^{-1}	248.61 ± 24.39	244.47 ± 26.32	228.38 ± 52.26	246.13 ± 48.78

It was shown that oxLDL impairs endothelium relaxation by inhibition of the expression of eNOS,[37] reduces the responsiveness of smooth muscle cell to NO,[71] induces the expression of adhesion and inflammatory molecules.[38] All of the above contribute directly to dysfunction of the endothelium. OxLDL levels, auto-antibodies against epitopes of oxLDL and oxLDL:LDL ratio[39] were independently associated with increased risk for coronary atheromatosis and ischemic heart disease, with increased levels of oxLDL and MDA-LDL being related to plaque instability. However, other studies failed to find a significant association between oxLDL and clinical presentation of coronary artery disease or rate of complications in the first year after coronary stenting.[40] In the present study, the plasma concentration of oxLDL was increased after 6-month follow-up, with a trend of more pronounced increase in the group with ISR, but further study including larger number of patients with restenosis is required to assess whether this finding is relevant (Table IV).

TABLE IV. Concentration of oxLDL and Lp(a) in serum of patients that underwent stent implantation prior to PCI (baseline) and after 6-month follow-up; values are mean ± *SD*

Species	No stenosis		In-stent restenosis	
	Baseline	Follow-up	Baseline	Follow-up
oxLDL / U L^{-1}	169.10±20.23	182.47±17.02	166.19±15.36	188.02±14.22
Lp(a) / U L^{-1}	194.28±68.71	195.11±52.64	209.55±480.90	191.35±33.13

Further investigation is required to determine the appropriate biochemical markers and the algorithm of their changes during follow-up will ameliorate diagnostic and prognostic assessment of patients undergoing PCI. Taking into account the fact that PCI has replaced more invasive surgical procedures for dealing with coronary stenosis, and that it has become the golden standard for treatment of acute myocardial infarction, follow-up of these patients and early detection of complications of myocardial ischemia using serum/plasma markers could contribute to better selection of patients for which the invasive procedure of follow-up angiography is indicated.

CONCLUSIONS

Based on the results of this and other studies, it may be concluded that inflammatory processes and oxidative stress play important roles in the formation of in-stent restenosis after coronary stent implantation. It is proposed that the serum hs-CRP level and catalase activity may be useful for monitoring and planning management of patients during follow-up after stent implantation, but warrants confirmation by larger, well-designed prospective and randomized studies.

STUDY LIMITATIONS

The main limitation of this study is the relatively small number of patients, as only patients that fulfilled the inclusion criteria and who were subjected to follow-up angiography were included in the study.

LIST OF ABBREVIATIONS

PCI – percutaneous coronary intervention
ISR – in-stent restenosis
CAD – coronary artery disease
hs-CRP – high sensitive C-reactive protein
sICAM-1 – soluble intercellular cell adhesion molecule-1
sVCAM-1 – soluble vascular cell adhesion molecule-1
TGF-β – transforming growth factor-beta
Lp(a) – lipoprotein(a)
oxLDL – oxidized low-density lipoprotein
SOD – superoxide dismutase
CAT – catalase
ROS – reactive oxygen species
EPC – endothelial progenitor cells
LDL-C – low-density lipoprotein cholesterol
HDL-C – high-density lipoprotein cholesterol
VLDL – very low-density lipoprotein
LDL – low- density lipoprotein
HDL – high-density lipoprotein
AST – aspartate transaminase
NF-κB – nuclear factor kappa
CK-MB – creatine kinase-MB
eNOS – endothelial NO synthase
MDA – malondialdehyde

Acknowledgement. This work was supported by the Ministry of Science of the Republic of Montenegro (Grant Nos. 05-1/3-3377 and 01-1366).

ИЗВОД

ПОКАЗАТЕЉИ ЗАПАЉЕЊА И АКТИВНОСТ ЕНЗИМА АНТИОКСИДАТИВНЕ ЗАШТИТЕ КОД РЕСТЕНОЗЕ НАКОН ПЕРКУТАНЕ КОРОНАРНЕ ИНТЕРВЕНЦИЈЕ

СНЕЖАНА ПАНТОВИЋ[1], ДРАГИЦА БОЖОВИЋ[2], ГОРАН НИКОЛИЋ[1,3], МИЛИЦА МАРТИНОВИЋ[1], ПРЕДРАГ МИТРОВИЋ[4,5], ЛЕНКА РАДУЛОВИЋ[1], АЛЕКСАНДРА ИСАКОВИЋ[6] и ИВАНКА МАРКОВИЋ[6]

[1]Медицински факултет, Универзитет Црне Горе, Крушевац бб, 81000 Подгорица, Црна Гора, [2]Центар за клиничко-лабораторијску дијагностику, Клинички центар Црне Форе, Подгорица

, [3]Центар за радиолошку дијагностику, Клинички центар Црне Горе, Љубљанска бб, Подгорица, Црна гора, [4]Клиника за кардиологију, Клинички центар Србије, Београд, [5]Медицински факултет, Универзитет у Београду, Београд, [6]Институт за медицинску и клиничку биохемију, Медицински факултет, Универзитет у Београду, Пастерова 2, 11000 Београд

Успешност перкутане коронарне интервенције је често угрожена потребом да се понови реваскуларизација услед појаве стенозе. Иако је, с тим у вези, у бројним истраживањима процењиван предиктивни значај различитих биохемијских показатеља, нису добијени конзистентни резултати. Циљ овог истраживања је био да се процени прогностички значај појединих маркера запаљења, као и активност ензима антиоксидативне заштите, у развоју рестенозе након уградње стента. Концентрације С-реактивног протеина (hs-CRP), солубилног међућелијског адхезивног молекула-1 (sICAM-1), фактора трансформације раста бета (TGF-β), липопротеина(a) (Lp(a)) и оксидованог липопротеина мале густине (oxLDL), као и активност супероксид-дисмутазе (SOD) и каталазе (CAT) у серуму одређиване су код 44 пацијента пре уградње стента, као и након шестомесечног периода праћења. Резултати након периода праћења указали су на значајан пораст концентрације hs-CRP-а у серуму код пацијената са ангиографски потврђеном поновном стенозом, у односу на пацијенте без стенозе. Уградња стента је довела до пораста активности SOD и CAT у серуму, али је након шестомесечног праћења активност CAT била значајно нижа код пацијената са стенозом, што би могао бити један од чинилаца који доприноси њеном развоју. Није уочена разлика у концентрацији sICAM-1, TGF-*β*, oxLDL и Lp(a) између испитиваних група. У закључку, концентрација hs-CRP и активност CAT у серуму би се могли у будућности размотрати као корисни показатељи праћења пацијената након уградње стента у циљу благовременог уочавања претеће стенозе.

(Примљено 17. јуна, ревидирано 30. августа, прихваћено 2. септембра 2014)

REFERENCES

1. B. Bhargava, G. Karthikeyan, A. S. Abizaid, R. Mehran, *BMJ [Br. Med. J.]* **327** (2003) 274
2. T. Inoue, T. Kato, Y. Hikichi, S. Hashimoto, T. Hirase, T. Morooka, Y. Imoto, Y. Takeda, F. Sendo, K. Node, *Thromb. Haemost*. **95** (2006) 43
3. A. Gaspardone, F. Versaci, *Am. J. Cardiol*. **96** (Suppl.) (2005) 65L
4. A. M. Shah, K. M. Channon, *Heart* **90** (2004) 486
5. M. Angioi, I. Abdelmouttaleb, R. M. Rodriguez, I. Aimone-Gastin, C. Adjalla, J. L. Guéant, N. Danchin, *Am. J. Cardiol*. **87** (2001) 1189
6. M. S. Joshi, L. Tong, A. C. Cook, B. L. Schanbacher, H. Huang, B. Han, L. W. Ayers, J. A. Bauer, *Cardiovasc. Pathol*. **21** (2012) 428
7. C. A. Labarrere, J. B. Lee, D. R. Nelson, M. Al-Hassani, S. J. Miller, D. E. Pitts, *Lancet* **360** (2002) 1462
8. C. Yutani, H. Ishibashi-Ueda, T. Suzuki, A. Kojima, *Cardiology* **92** (1999) 171

9. P. A. Suwanabol, K. C. Kent, B. Liu, *J. Surg. Res.* **167** (2011) 287
10. G. P. K. Shah, J. Amin, *Circulation* **85** (1992) 1279
11. M. A. Nasar, A. Jarrari, M. A. Naseer, T. F. Subhani, B. V. Shetty, F. Shakeel, *J. Serb. Chem. Soc*. **74** (2009) 1063
12. K. Nishi, H. Itabe, M. Uno, K. T. Kitazato, H. Horiguchi, K. Shinno, S. Nagahiro, *Arterioscler., Thromb., Vasc. Biol.* **22** (2002) 1649
13. S. Tsimikas, C. Bergmark, R. W. Beyer, R. Patel, J. Pattison, E. Miller, J. Juliano, J. L. Witztum, *J. Am. Coll. Cardiol*. **41** (2003) 360
14. L. Berglund, R. Ramakrishnan, *Arterioscler. Thromb. Vasc. Biol.* **24** (2004) 2219
15. K. Tziomalos, V. G. Athyros, A. S. Wierzbicki, D. P. Mikhailidis, *Curr. Opin. Cardiol*. **24 (**2009) 351
16. H. P. Misra, I. Fridovich, *J. Biol. Chem.* **247** (1972) 3170
17. L. Góth, *Clin. Chim. Acta* **196** (1991) 143
18. A. Dibra, J. Mehilli, S. Braun, M. Hadamitzky, H. Baum, J. Dirschinger, H. Schühlen, A. Schömig, A. Kastrati, *Am. J. Med.* **114** (2003) 715
19. M. Gottsauner-Wolf, G. Zasmeta, S. Hornykewycz, M. Nikfardjam, E. Stepan, P. Wexberg, G. Zorn, D. Glogar, P. Probst, G. Maurer, K. Huber, *Eur. Heart J.* **21** (2000) 1152
20. T. P. Zwaka, V. Hombach, J. Torzewski, *Circulation* **103** (2001) 1194
21. H. Tanaka, G. K. Sukhova, S. J. Swanson, S. K. Clinton, P. Ganz, M. I. Cybulsky, P. Libby, *Circulation* **88** (1993) 1788
22. M. Hashimoto, M. Shingu, I. Ezaki, M. Nobunaga, M. Minamihara, K. Kato, H. Sumioki, *Inflammation* **18** (1994) 163
23. A. D. Pradhan, N. Rifai, P. M. Ridker, *Circulation* **106** (2002) 820
24. S. Bayata, E. Arıkan, M. Yeşil, N. Postacı, A. Taş, M. Köseoğlu, *Anat. J. Cardiol.* **10** (2010) 405
25. E. Lutgens, M. Gijbels, M. Smook, P. Heeringa, P. Gotwals, V. E. Koteliansky, M. J. Daemen, *Arterioscler., Thromb., Vasc. Biol.* **22** (2002) 975
26. L. C. Azevedo, M. A. Pedro, L. C. Souza, H. P. de Souza, M. Janiszewski, P. L. da Luz, F. R. M. Laurindo, *Cardiovasc. Res*. **47** (2000) 436
27. A. Fortuno, G. San Jose, M. U. Moreno, J. Díez, G. Zalba, *Exp. Physiol.* **90** (2005) 457
28. C. Kunsch, R. M. Medford, *Circ. Res*. **85** (1999) 753
29. J. H. Bräsen, O. Leppänen, M. Inkala, T. Heikura, M. Levin, F. Ahrens, J. Rutanen, H. Pietsch, D. Bergqvist, A. L. Levonen, S. Basu, T. Zeller, G. Klöppel, M. O. Laukkanen, S. Ylä-Herttuala, *J. Am. Coll. Cardiol.* **50** (2007) 2249
30. U. Landmesser, R. Merten, S. Spiekermann, K. Buttner, H. Drexler, B. Hornig, *Circulation* **101** (2000) 2264
31. H. Fujii, S.-H. Li, P. E. Szmitko, P. W. M. Fedak, S. Verma, *Arterioscler., Thromb., Vasc. Biol*. **26** (2006) 2476
32. X. L. Wang, T. Adachi, A. S. Sim, D. E. Wilcken, *Arterioscler., Thromb., Vasc. Biol*. **18** (1998) 1915
33. V. K. Dwivedi, M. Chandra, P. C. Misra, A. Misra, M. K. Misra, *J. Enzym. Inhib. Med. Chem.* **21** (2006) 43
34. A. Wykretowicz, M. Dziarmaga, A. Szczpanik, P. Guzik, H. Wysocki, *Int. J. Cardiol.* **89** (2003) 173
35. S. J. Lin, S. K. Shyue, P. L. Liu, Y. H. Chen, H. H. Ku, J. W. Chen, K. B. Tam, Y. L. Chen, *J. Mol. Cell Cardiol.* **36** (2004) 129

36. T. Fukai, M. R. Siegfried, M. Ushio-Fukai, Y. Cheng, G. Kojda, D. G. Harrison, *J. Clin. Invest.* **105** (2000) 1631
37. S. Braun, G. Ndrepepa, N. von Beckerath, J. Mehilli, O. Gorchakova, W. Vogt, A. Schömig, A. Kastrati, *Am. Heart J.* **150** (2005) 550
38. J. D. Steinberg, *J. Biol. Chem.* ***272*** (1997) 20963
39. A. I. Papathanasiou, E. S. Lourida, L. D. Tsironis, J. A. Goudevenos, A. D. Tselepis. *Atherosclerosis* **196** (2008) 289
40. T. Vasankari, M. Ahotupa, J. Toikka, J. Mikkola, K. Irjala, P. Pasanen, K. Neuvonen, O. Raitakari, J. Viikari, *Atherosclerosis* **155** (2001) 403.

Journal of the Serbian Chemical Society
JSCS-info@shd.org.rs • www.shd.org.rs/JSCS
J. Serb. Chem. Soc. 80 (2) 159–169 (2015)
JSCS–4706
UDC 547.474.6+618.36:532.74:576
Original scientific paper

Molecular forms of galectin-1 from human placenta and trophoblast cells

DANICA ĆUJIĆ[1], ŽANKA BOJIĆ-TRBOJEVIĆ[1*#], NIKOLA KOLUNDŽIĆ[1], TOSHIHIKO KADOYA[2] and LJILJANA VIĆOVAC[1]

[1]*Institute for the Application of Nuclear Energy – INEP, University of Belgrade, Banatska 31b, 11080 Belgrade, Serbia and* [2]*Department of Biotechnology, Maebashi Institute of Technology, Maebashi, Gunma, Japan*

(Received 28 April, revised 3 September 2014, accepted 9 September 2014)

Abstract: Galectin-1 (gal-1) is the best-studied member of the galectin family of the human placenta, which is assumed to play important roles in pregnancy. Standard isolation of gal-1 from human placenta using lactose extraction and affinity chromatography in the presence of a reducing agent produced several known forms of gal-1, which were compared to the recombinant human gal-1 (rhgal-1) and oxidized recombinant human gal-1 (Ox-gal-1). The isolated placental gal-1 retained lectin-binding activity, evidenced by hemagglutination and dot blot lectin assays. Characterization of the forms present by surface-enhanced laser desorption/ionization time-of-flight mass spectrometry (SELDI–TOF MS), based on hydrophilic interactions or immunorecognition, provided a sensitive tool for the detection of the fine differences among the diverse molecular forms. The forms detected included previously established biologically active oxidized gal-1 and reduced gal-1, as well as some other currently uncharacterized (less investigated forms).

Keywords: galectin-1; placenta; molecular form; SELDI-TOF MS.

INTRODUCTION

Galectin-1 (gal-1) is a member of the animal lectin family with binding capacity for *β*-galactoside residues of glycoconjugates. It exists as a non-covalent dimer composed of identical ≈14.6 kDa subunits, with evident carbohydrate-binding activity in the reduced state only.[1,2] Although gal-1 shows characteristics of typical cytoplasmic proteins, it can be found on the extracellular side of cell membranes and in the extracellular matrices of various normal and pathological tissues.[3] Its localization indicates that gal-1 could act intracellularly through protein–protein interactions and extracellularly via sugar-dependent interactions.[4,5]

* Corresponding author. E-mail: zana@inep.co.rs
# Serbian Chemical Society member.
doi: 10.2298/JSC140428091C

Most of the gal-1 isolation protocols are performed in the presence of a reducing agent in order to prevent oxidation and maintain carbohydrate-binding activity.[6–8] The relatively high content of cysteine residues in the gal-1 molecule, *i.e.*, six cysteine residues per monomer, implicates gal-1 sensitivity to oxidative inactivation and loss of lectin activity.[9,10] For example, during purification of gal-1 from bovine heart, the lectin activity was lost upon oxidation, suggesting that this isolation protocol results in the presence of both reduced and oxidized lectin.[9] In addition, gal-1 from a transfected cell line COS1, was isolated and the relevance of oxidation for functional characteristics shown.[11] In nerve regeneration models *in vivo* and *in vitro* oxidized recombinant human gal-1 (Ox-rhgal-1) was recognized as a factor that promotes Schwann cell migration followed by axonal growth.[11,12] This form of human gal-1 obtained from bacterially expressed recombinant gal-1 by the air oxidation with $CuSO_4$ as a catalyst is a protein with a molecular mass of 14.579 kDa and is characterized by reduced or no lectin activity.[12,13] Experimental strategies involving construction of diverse gal-1 mutants have been devised in order to elucidate relevance/contribution of specific domains to gal-1 interaction with potential ligands and function.[10,14] In this context, a stabilized gal-1 form (CS-gal-1) in which six cysteine residues were replaced with serine, expressed in and purified from *E. coli*, functions like a lectin with molecular mass of 14.886 kDa.[12]

It is well known that gal-1 is abundantly expressed in human placenta and in trophoblast derived cell lines.[15–17] Gal-1 was the first isolated and purified galectin from the human placenta.[6,18] More recently, other members of the galectin family were localized in human and non-human placenta.[19,20] Functionally, gal-1 acts as an important stimulator of the trophoblast invasion *in vitro*.[13] Furthermore, it was shown that CS–gal-1 was more potent than Ox-rhgal-1 in inducing trophoblast invasion,[13] confirming a previous finding of a molecular form dependent effect in an axonal regeneration model.[12] No direct data are yet, however, available regarding the presence of different gal-1 forms in trophoblast. Therefore, the present study was aimed at investigating whether gal-1 isolated from the human placenta or present in extravillous trophoblast cell line HTR-8/SVneo is homogenous or comprised of different molecular forms.

EXPERIMENTAL

Reagents

RPMI 1640, antibiotic/antimycotic solution and fetal calf serum (FCS) were obtained from PAA Laboratories (Linz, Austria). Matrigel, Collagen Type I (Col I) and serum fibronectin (sFN) were purchased from BD Biosciences (Bedford, MA, USA). Acrylamide, *N*,*N*′-methylenebisacrylamide, *N*,*N*,*N*′,*N*′-tetramethylethylenediamine, Ponceau S, glycine, lactose and asialofetuin (ASF) were obtained from Sigma-Aldrich (St. Louis, MO, USA). Sodium dodecyl sulfate-polyacrylamide gel electrophoresis (SDS-PAGE) protein standards and silver stain kit were from Bio-Rad, Inc. (Hercules, CA, USA). The oxidized form of recombinant

human gal-1 and rabbit anti-rhgal-1 with gal-1 neutralizing activity were obtained from Kirin Brewery (Tokyo, Japan). Recombinant human gal-1 was from Acris Antibodies GmbH (Hiddehausen, Germany). Biotinylated goat anti-rabbit, avidin-biotinylated peroxidase complex (ABC) and diaminobenzidine (DAB) substrate kit for peroxidase were obtained from Vector Laboratories (Burlingame, CA, USA). Anti-rabbit IgG HRP-linked antibody was from Cell Signaling Technology, Inc. (Danvers, MA, USA).

All other chemicals were of *p.a*. grade.

Isolation of gal-1 from human placenta

Galectin-1 was isolated from three fresh term human placentas by lactose extraction with phosphate buffered saline (PBS), 0.05 mol L^{-1}, pH 7.2 containing 0.01 mol L^{-1} 2-mercapto-ethanol (ME) and 0.002 mol L^{-1} ethylenediaminetetraacetic acid (EDTA) (EDTA–MEPBS) and purified by affinity chromatography on a lactosyl-Sepharose 4B column.[6] The obtained preparations were not pooled and produced identical results. Bound protein was then eluted with 0.1 mol L^{-1} Gly–HCl, pH 2.5 and concentrated.[21] The purity and homogeneity of the isolated protein was tested by silver staining and Western blot analysis after SDS–PAGE under reducing conditions. After isolation, gal-1 was extensively dialyzed against PBS in order to remove ME and stored in PBS at –20 °C.

Assays for lectin activity

The lectin activity of the isolated placental gal-1 was determined by hemagglutination and dot blot analysis. Agglutination assays were performed using trypsinized rabbit erythrocytes and purified placental gal-1. Lectin solutions prepared in PBS containing 0.005 mol L^{-1} dithiothreitol (DTT) as a reducing agent were gently mixed with a 2 % suspension of erythrocytes without or with 0.1 mol L^{-1} lactose. Results were read after 1 h incubation at room temperature (RT).

To assay the binding of placental gal-1 to different glycoproteins, dot blot analysis was performed. Asialofetuin, sFN, Col I and matrigel (containing 3 μg protein each) were spotted on a nitrocellulose membrane and dried at RT. Unspecific binding sites were blocked with 3 % bovine serum albumin (BSA) for 2 h at RT. Solutions of isolated gal-1 (6 μg mL^{-1}) were pre-incubated without or with different lactose concentrations (0.025, 0.05, 0.1 or 0.2 mol L^{-1}) in EDTA–MEPBS for 1 h at RT, and then used for incubation with individual strips overnight at 4 °C. Strips were further incubated with anti-gal-1 antibodies (1 μg mL^{-1}) for 2 h at RT, followed by incubation with biotinylated anti-rabbit IgG for 30 min and with ABC for another 30 min. The reaction was visualized using DAB as the chromogen.

SDS-PAGE, silver stain and Western blot

Isolated placental gal-1 was subjected to SDS-PAGE on 5–20 % gradient polyacrylamide gel under reducing conditions, and analyzed using a Bio-Rad Silver Stain Kit, according to manufacturer's instructions. Recombinant human gal-1, ox-rhgal-1, placental gal-1, HTR-8/SVneo cell lysate and culture media were resolved by SDS–PAGE under reducing conditions on 12.5 % polyacrylamide gel and 4 % stacking gel and subsequently transferred to nitrocellulose membranes. The membranes were incubated with rabbit anti-gal-1 antibody (1μg mL^{-1}) overnight at 4 °C, with constant shaking. After incubation with anti-rabbit IgG HRP-linked antibody, a gal-1 band was detected using Pierce ECL Western blotting substrate. The membranes were scanned with an ImageScanner from Amersham Biosciences, Inc. (Piscataway, NJ, USA) and densitometric analysis was performed using the ImageMaster Total-Lab v2.01 program (Amersham Bioscience).

Cell culture

Human extravillous trophoblast cell line HTR-8/SVneo was cultured and propagated as previously described.[13,22] For lectin affinity chromatography and surface-enhanced laser desorption/ionization time-of-flight mass spectrometry (SELDI–TOF MS), the HTR-8/SVneo cells were grown in complete media for 48 h, lysed in 0.02 mol L^{-1} 2-[4-(2-hydroxyethyl)piperazin-1-yl]ethanesulfonic acid (HEPES) with 1 % Triton X-100, pH 8. The cell culture media were collected, centrifuged at 700 g for 5 min, and then analyzed using SDS-PAGE and SELDI–TOF MS. For SDS-PAGE, trypsinized HTR-8/SVneo cells were washed with PBS pH 7.2, lysed in a sample buffer containing a protease inhibitor cocktail (6×10^6 cells mL^{-1}), centrifuged (1600 g for 5 min at 4 °C) and the supernatant reserved. Cell lysates were heated for 5 min in boiling water and subjected to SDS-PAGE.

Lectin affinity chromatography

Asialofetuin was covalently linked to CNBr-activated Sepharose (Pharmacia, Sweden) at 1 mg mL^{-1} of gel according to the manufacturer's instructions. HTR-8/SVneo cell lysate (6×10^6 cells mL^{-1}) prepared in 0.02 mol L^{-1} HEPES with 1 % Triton X-100, pH 8, was applied to ASF column under reducing or non-reducing conditions. Non-bound material was eluted with PBS or EDTA–PBSME. Under non-reducing conditions, the elution was performed with 0.1 mol L^{-1} Gly–HCl, pH 2.5, while under reducing conditions PBS containing 0.1 mol L^{-1} lactose was used for elution. The collected fractions were pooled and concentrated prior to SDS–PAGE analysis.

Surface-enhanced laser desorption/ionization time-of-flight mass spectrometry

In this study, gal-1 was analyzed by SELDI–TOF MS. Protein chip arrays were processed according to manufacturer's instructions. Briefly, 5 μL of sample (placental gal-1, rhgal-1 or ox-rhgal-1) per spot was applied to normal phase NP20 chip array, left to air-dry at RT and rinsed three times with PBS. The pre-activated-surface protein chip array PS20 was coated with anti-gal-1 antibody (5 μL per spot) in a humid chamber overnight at 4 °C. After rinsing with PBS, the spots were blocked with 0.5 mol L^{-1} Tris–HCl, pH 8 for 1 h in the humid chamber at RT. After another washing step with PBS, 5 μL of sample (HTR-8/SVneo whole cell lysate, conditioned medium or placental gal-1) was loaded on each spot and incubated for 2 h in a humid atmosphere at RT. Unbound material was removed from the spot by intensive rinsing with PBS, followed by deionized water. Both NP20 and PS20 protein chip arrays were left to completely air-dry, before the energy-absorbing matrix (EAM) was added. Sinapinic acid (SPA) dissolved in 50 % acetonitrile/0.5 % trifluoroacetic acid was used as the EAM. To each spot, 1 μL of 50 % SPA solution was applied twice, and after drying, the protein arrays were ready for processing. The protein chips were read in ProteinChip Reader, Series 4000, Personal edition (Bio-Rad Laboratories, Inc., Hercules, CA, USA). External calibration was realized using ProteinChip all-in-one protein standards II. Mass analysis was performed at a laser energy of 6000 nJ, with 8815 laser shots per spot. The spectra were acquired in 25 kV positive ion acquisition, in the mass range between 2.5 and 200 kDa, with the focus mass at 15 kDa. The spectra were analyzed using Ciphergen Express Software 3.0 (Bio-Rad Laboratories, Inc., Hercules, CA, USA). The peaks were normalized according to the total ion current between 2500 and 70000 *m*/*z* and detected automatically for signal to noise ratio >3.

RESULTS AND DISCUSSION

In the present study, gal-1 isolated from human term placenta was characterized and compared to two different forms of recombinant gal-1, as well as the gal-1 from the trophoblast cell line HTR-8/SVneo. Most of the commonly used procedures for gal-1 isolation and purification are based on lactose extraction from tissue and lactose affinity column, in the presence of a reducing agent, which is critical for the assessment of lectin activity of gal-1.[2,23] In the absence of a reducing agent, gal-1 from placental tissue extract lost lectin activity and was unable to bind to a lactose affinity column (Fig. 1A). Therefore, a procedure with 2-mercaptoethanol was used for the isolation of placental gal-1 (Fig. 1A). The presence of gal-1 was confirmed by dot blot in fractions eluted with 0.1 mol L^{-1} Gly–HCl, pH 2.5, and gal-1 was further analyzed by SDS-PAGE and immunoblot using polyclonal rabbit antibody raised against human gal-1 (Fig. 1B). The production, characterization and specificity of the polyclonal anti-gal-1 was previously described.[11] Both analyses showed the presence of a single prominent band

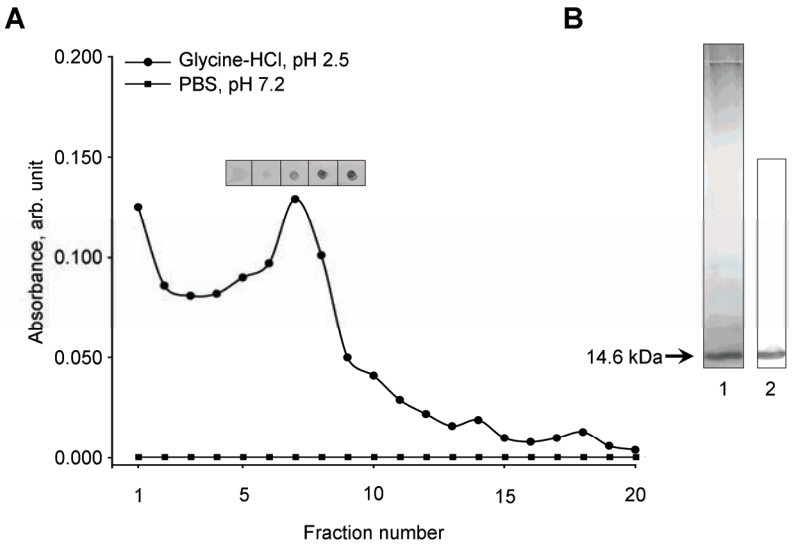

Fig. 1. Isolation and identification of gal-1 from human term placenta. A) Preparative affinity chromatography was performed under reducing conditions. Unbound material was washed with EDTA–MEPBS buffer pH 7.2. Gal-1 was eluted from lactosyl-Sepharose 4B column with Gly–HCl pH 2.5 (circles) under 3 mL min^{-1} flow rate. The absorbance was measured at 280 nm and additionally, the presence of gal-1 in fractions 5–9 was confirmed by dot blot using anti-gal-1 antibodies. In the absence of reducing agent, gal-1 was not detected in the eluted fractions (squares). B) SDS-PAGE and Western blot of isolated gal-1. 1) Purity of isolated gal-1 was confirmed using silver staining after SDS-PAGE electrophoresis under reducing conditions. A band of ≈14.6 kDa was observed by silver staining. 2) Western blot analysis using anti-gal-1 antibodies confirmed that the ≈14.6 kDa band was gal-1.

of ≈14.6 kDa, which was consistent with the molecular mass of gal-1. Although other galectin family members are known to be present in human placenta and to share binding characteristics with gal-1,[13,24] only gal-1 is isolated from term placenta using lactose extraction and affinity purification, most likely, due to the specific cell type composition of the starting material (containing low amounts of cytotrophoblast expressing gal-3 and gal-8). One of the most characteristic features of gal-1 is high affinity binding of *β*-galactoside containing glycoconjugates, which is commonly inhibited by lactose for experimental purposes.[25,26] The lectin activity of gal-1 was determined by hemagglutination and binding to several glycoproteins or their mixture Matrigel (Fig. 2A and B). Placental gal-1 induced agglutination in the presence of DTT as a reducing agent. As expected, lectin-mediated agglutination was inhibited in the presence of lactose (Fig. 2A). Binding of the placental gal-1 to different glycoproteins was tested by the dot blot assay in the absence or presence of lactose. Some of the *β*-galacto-

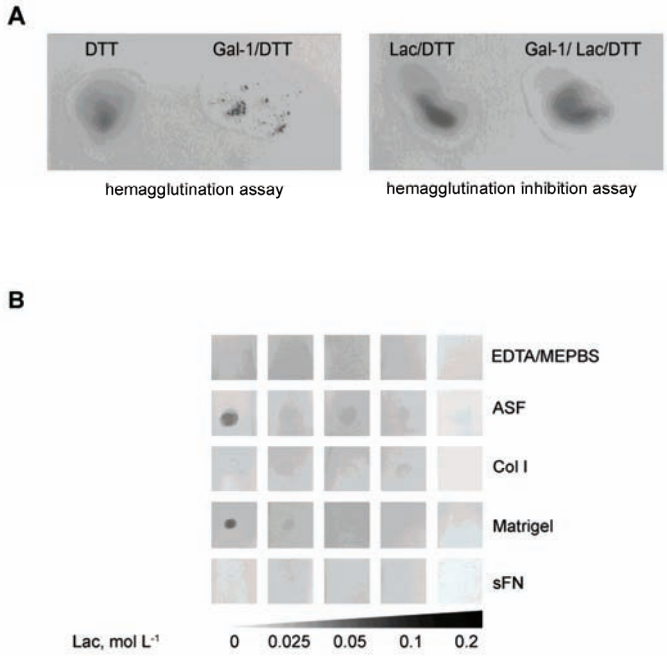

Fig. 2. Lectin properties of gal-1 from the human placenta. A) Hemagglutination activity of placental gal-1 under reducing conditions (in the presence of DTT). Addition of lactose inhibited hemagglutination, confirming that the isolated placental gal-1 had lectin activity. DTT or DTT/lactose served as the negative controls. B) Binding of placental gal-1. Gal-1 ligands (ASF and Matrigel), negative control (sFN, Col I) and blank probe (EDTA–MEPBS) were spotted onto nitrocellulose membranes. The membranes were incubated with gal-1 pre-incubated without or with different concentrations of lactose (0.025–0.2 mol L^{-1}) in EDTA–MEPBS. Bound gal-1 was detected using anti-gal-1 antibodies.

side-containing ligands that are bound by gal-1 are found in trophoblast, including heavily glycosylated proteins of the extracellular matrix (laminin and cell fibronectin),[27] as well as the cell membrane glycoproteins, integrins[28] and mucins.[29] In this study placental gal-1 was shown to bind ASF, the commercial basement membrane protein preparation Matrigel that contains laminin, collagen type IV and heparan sulfate proteoglycan, but not sFN or Col I (Fig. 2B). The binding of gal-1 to ASF or Matrigel was reduced by lactose (0.025–0.2 mol L^{-1}), which confirms that gal-1 binds *via* carbohydrate recognition. In different tissues and cell types, gal-1 is implicated in many biological processes, such as cell adhesion, invasion, differentiation, and most of these effects are supposed to be mediated through binding to *β*-galactoside cell membrane glycoconjugates participating in signal transduction.[30,31] In this study, HTR-8/SVneo derived gal-1 monomer was shown to differently bind ASF in the presence or absence of a reducing agent (Fig. 3A), resulting in a different proportion of bound/unbound gal-1 (Fig. 3B). A similar finding was reported for the recombinant and mutant forms

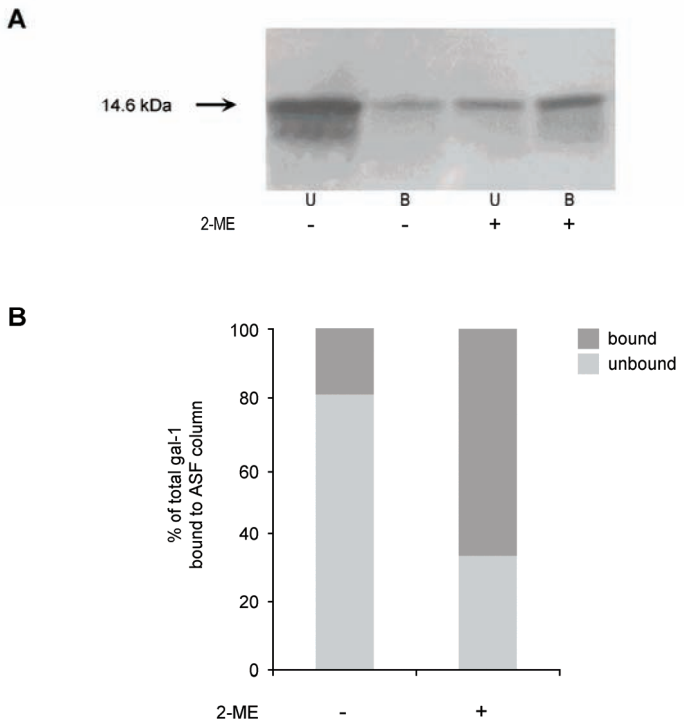

Fig. 3. Binding of gal-1 from HTR-8/SVneo cell lysates to ASF in the absence or presence of 2-mercaptoethanol (ME). A) Western blot analysis of unbound (U) or bound (B) gal-1 containing fractions eluted in the absence (–) or presence (+) of the reducing agent. B) Relative proportion of unbound/bound gal-1 as detected by Western blot and densitometric analysis.

of gal-1 binding to lactose,[12,14] showing that redox status influences the structure and binding properties of gal-1.

Placental gal-1 was compared to rhgal-1 and ox-rhgal-1. All gal-1 samples were trapped on NP20 arrays due to hydrophilic interactions, and the resulting proteomic spectra were analyzed by SELDI–TOF MS (Fig. 4A). Although the

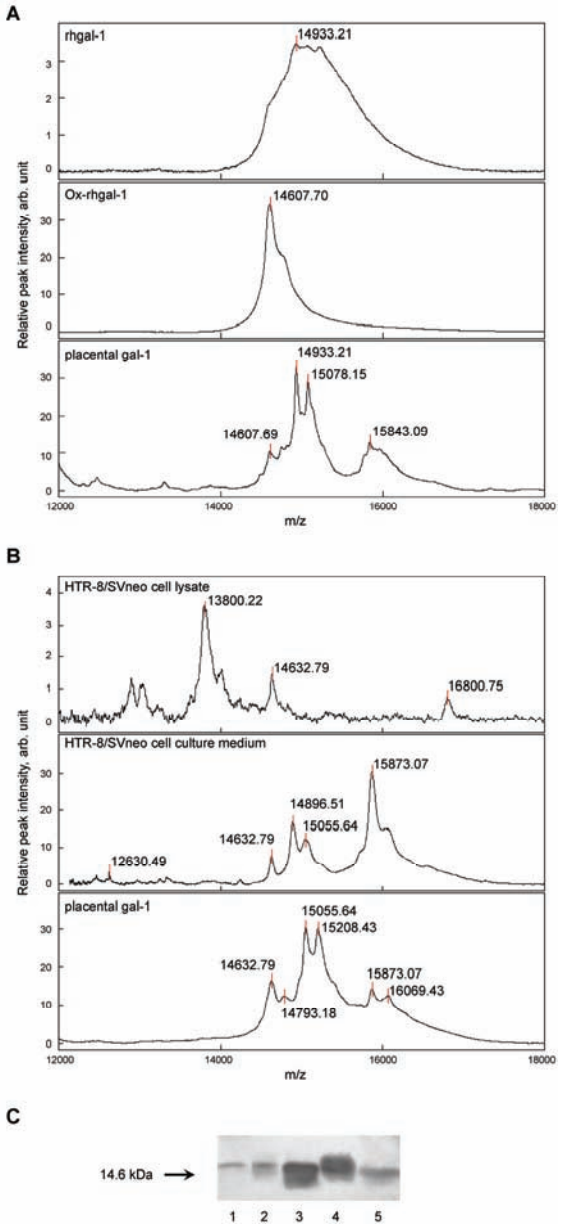

Fig. 4. SELDI–TOF and Western blot analysis of gal-1 in different samples. A) Mass spectra on NP20 protein chip array of isolated placental gal-1 compared to rhgal-1 and ox-rhgal-1. B) Mass spectra of isolated placental gal-1 and gal-1 from HTR-8/SVneo cell line (whole cell lysate and secreted) identified on a PS20 protein chip array, using anti-gal-1 antibodies as bait. Spectra (A and B) are represented as relative peak intensity *vs.* mass to charge ratio. Protein peaks are identified automatically, for signal to noise ration (S/N) > 3. C) Western blot analysis of gal-1 from different sources: HTR-8/SVneo cell lysate (1) and the corresponding medium (2), ox-rhgal-1 (3), rhgal-1 (4), gal-1 from human term placenta (5).

obtained protein profiles of gal-1 were similar, some subtle differences were noted. The dominant gal-1 forms in trophoblast were of 14.6, 14.933, 15.078 and 15.843 kDa. In the sample of ox-rhgal-1, a 14.6 kDa protein was detected, in keeping with the molecular mass of 14.579 kDa previously determined by MALDI–TOF MS.[12] A prominent peak at 14.9 kDa was detected in the sample of rhgal-1 used in the present study, the molecular mass of which is slightly higher, compared to the size of the mutant CS-gal-1 and reduced form of rhgal-1 measured by MALDI–TOF MS.[12] Four relatively high intensities peaks at 14.6 kDa, 14.933, 15.078 and 15.843 kDa were observed in the preparation of placental gal-1, two of which, at 14.6 and 14.933 kDa, coincided with the ox-rhgal-1 and rhgal-1 peaks (Fig. 4A).

The analysis based on the antibody binding (immobilized to a PS20 array) of gal-1 from different biological sources also revealed multiple forms of gal-1 (Fig. 4B). All the preparations, including cell lysate, and secreted gal-1, as well as the gal-1 isolated from placenta, contained a form of 14.6 kDa consistent with the oxidized gal-1. There was considerable overlap in the presence of other forms, while the 13.8 kDa form was specific to HTR-8/SVneo cell lysate. In addition, differences in the mobility between the same gal-1 containing preparations were detected by Western blot (Fig. 4C). A similar molecular form (of 14.2 kDa) was previously identified by MALDI-TOF[32] in a gal-1 form lacking the first six amino acids, but also in other human cell lines (of 13.5 kDa, by Western blot).[33] The molecular nature and biological function of this form is not clear at present. On the other hand, higher molecular forms were detected in other cell models and might be related to the unconventional secretion and membrane targeting of gal-1.[26] The obtained data showed that the placental tissue at term contains multiple molecular forms of gal-1, and among them all of the known biologically active ones.

CONCLUSION

Isolation of gal-1 from the human placenta using lactose and affinity column produced several known forms of gal-1. The system devised for the characterization of the forms present, based on either hydrophilic interactions or immunorecognition on chips followed by SELDI–TOF MS, provided a sensitive tool for the detection of fine differences among the diverse molecular forms. The forms detected contained previously established biologically active entities, but also some the potential significance of which remains to be investigated in the future.

Acknowledgement. This work was supported by the Ministry of Education, Science and Technological Development of the Republic of Serbia, Grant No. 173004. The authors are thankful to Dr. Marijana Petković, Iva Popović and Marija Nišavić from the Laboratory for Physical Chemistry, Vinča Institute of Nuclear Sciences, University of Belgrade, for the assistance in performing the SALDI–TOF MS analysis.

ИЗВОД

МОЛЕКУЛСКЕ ФОРМЕ ГАЛЕКТИНА-1 ИЗ ПЛАЦЕНТЕ ЧОВЕКА И ЋЕЛИЈА ТРОФОБЛАСТА

ДАНИЦА ЋУЈИЋ[1], ЖАНКА БОЈИЋ-ТРБОЈЕВИЋ[1], НИКОЛА КОЛУНЦИЋ[1], TOSHINIKO KADOYA[2] и ЉИЉАНА ВИЋОВАЦ[1]

[1]Институт за примену нуклеарне енергије – ИНЕП, Универзитет у Београду, Банатска 31б, 11080 Београд и [2]Department of Biotechnology, Maebashi Institute of Technology, Maebashi, Gunma, Japan

Галектин-1 (gal-1) је највише изучаван члан фамилије галектина у ћелијама трофобласта хумане плаценте. Применом стандардне процедуре изоловања gal-1 лактозном екстракцијом и афинитетном хроматографијом у присуству редукујућег средства, добијено је неколико познатих форми gal-1 које су упоређене са рекомбинантним хуманим gal-1 (rhgal-1) и оксидованим рекомбинантним хуманим gal-1 (ox-rhgal-1). Изоловани плацентни gal-1 је био лектински активан, што је показано хемаглутинацијом и лектинским тестом на чврстој фази. Карактеризација форми применом SELDI–TOF масене спектрометрије, засноване на хемијском или имунолошком препознавању, омогућила је детекцију дискретних разлика између молекулских форми плацентног gal-1. У изолованом gal-1 биле су присутне форме оксидованог и редукованог gal-1, чија је биолошка активност претходно показана. Поред ових, уочене су и мање испитиване форме gal-1.

(Примљено 28. априла, ревидирано 3. септембра, прихваћено 9. септембра 2014)

REFERENCES

1. L. B. Clerch, P. Whitney, M. Hass, K. Brew, T. Miller, R. Werner, D. Massaro, *Biochemistry* **27** (1988) 692
2. W. M. Abbott, T. Feizi, *J. Biol. Chem.* **266** (1991) 5552
3. I. Camby, M. Le Mercier, F. Lefranc, R. Kiss, *Glycobiology* **16** (2006) 137R
4. R. C. Hughes, *Biochim. Biophys. Acta* **1473** (1999) 172
5. D. N. Cooper, S. H. Barondes, *J. Cell Biol.* **110** (1990) 1681
6. J. Hirabayashi, K. Kasai, *Biochem. Biophys. Res. Commun.* **122** (1984) 938
7. C. P. Sparrow, H. Leffler, S. H. Barondes, *J. Biol. Chem.* **262 (**1987) 7383
8. V. I. Teichberg, I. Silman, D. D. Beitsch, G. Resheff, *Proc. Natl. Acad. Sci. USA* **72** (1975) 1383
9. B. M. Tracey, T. Feizi, W. M. Abbott, R. Carruthere, B. N. Green, A. M. Lawson, *J. Biol. Chem.* **267** (1992) 10342
10. M. F. López-Lucendo, D. Solís, S. André, J. Hirabayashi, K. Kasai, H. Kaltner, H. J. Gabius, A. Romero, *J. Mol. Biol.* **343** (2004) 957
11. H. Horie, Y. Inagaki, Y. Sohma, R. Nozawa, K. Okawa, M. Hasegawa, N. Muramatsu, H. Kawano, M. Horie, H. Koyama, I. Sakai, K. Takeshita. Y. Kowada, M. Takano, T. Kadoya, *J. Neurosci.* **19** (1999) 9964
12. Y. Inagaki, Y. Sohma, H. Horie, R. Nozawa, T. Kadoya, *Eur. J. Biochem.* **267** (2000) 2955
13. N. Kolundžić, Ž. Bojić-Trbojević, T. Kovačević, I. Stefanoska, T. Kadoya, Lj. Vićovac, *PLoS ONE* **6** (2011) e28514
14. C. M. Guardia, J. J. Caramelo, M. Trujillo, S. P. Méndez-Huergo, R. Radi, D. A. Estrin, G. A. Rabinovich. *Glycobiology* **24** 428
15. E. Maqui, F. A. van den Brule, V. Castronovo, J. M. Foidart, *Placenta* **18** (1997) 433
16. Lj. Vićovac, M. Janković, M. Čuperlović, *Hum. Reprod.* **13** (1998) 730
17. Ž. Bojić-Trbojević. M. Božić, Lj. Vićovac, *Arch. Biol. Sci.* **60** (2008) 11

18. J. Hirabayashi, H. Kawasaki, K. Suzuki, K. Kasai, *J. Biochem.* **101** (1987) 987
19. N. G. Than, R. Romero, C. J. Kim, M. R. McGowen, Z. Papp, D. E. Wildman, *Trends Endocrinol. Metab.* **23** (2012) 23
20. R. Froehlich, N. Hambruch, J. D. Haeger, M. Dilly, H. Kaltner, H. J. Gabius, C. Pfarrer, *Placenta* **33** (2012) 195
21. T. Lekishvili, S. Hesketh, M. W. Brazier, D. R. Brown, *Eur. J. Neurosci.* **24** (2006) 3017
22. D. Ćujić, Ž. Bojić-Trbojević, N. Tošić, S. Pavlović, Lj. Vićovac, *Arch. Biol. Sci.* **65** (2013) 1331
23. P. L. Whitney, J. T. Powell, G. L. Sandford, *Biochem. J.* **238** (1986) 683
24. H. Leffler, S. Carlsson, M. Hedlund, Y. Quian, F. Poirier, *Glycoconjugate J.* **19** (2004) 433
25. Q. Zhou, R. D. Cummings, *Arch. Biochem. Biophys.* **300** (1993) 6
26. E. P. Moiseeva, Q. Javed, E. L. Spring, D. P. de Bono, *Cardiovasc. Res.* **45** (2000) 493
27. Y. Ozeki, T. Matsui, Y. Yamamoto, M. Funahashi, J. Hamako, K. Titani, *Glycobiology* **5** (1995) 255
28. E. P. Moiseeva, B. Williams, A. H. Goodall, N. J. Samani, *Biochem. Biophys. Res. Commun.* **310** (2003) 1010
29. Ž. Bojić-Trbojević, M. Jovanović Krivokuća, N. Kolundžić, M. Petronijević, S. Vrzić-Petronijević, S. Golubović, Lj. Vićovac, *Histochem. Cell Biol.* **142** (2014) 541
30. Y.-L. Hsu, C.-Y. Wu, J.-Y. Hung, Y.-S. Lin, M.-S. Huang, P.-L. Kuo, *Carcinogenesis* **34** (2013) 1370
31. I. Fischer, S. Shulze, C. Kuhn, K. Friese, H. Walzel, U. R. Markert, U. Jeschke, *Placenta* **30** (2009) 1078
32. T. Miura, M. Takahashi, H. Horie, H. Kurushima, D. Tsuchimoto. K. Sakumi, Y. Nakabeppu, *Cell Death Differ*. **11** (2004) 1076
33. A. Satelli, P. S. Pao, P. K. Gupta, P. R. Lockman, K. S. Srivenugopal, U. Subrahmanyeswara Rao, *Oncol. Rep.* **19** (2008) 587.

Journal of the Serbian Chemical Society
JSCS-info@shd.org.rs • www.shd.org.rs/JSCS
J. Serb. Chem. Soc. 80 (2) 171–178 (2015)
JSCS–4707
UDC **Alpinia blepharocalyx*:665.52/.54+54547.599.6:632.951:615.9
Original scientific paper

Chemical constituents and insecticidal activities of the essential oil from *Alpinia blepharocalyx* rhizomes against *Lasioderma sericorne*

YING WANG[1,2], CHUN XUE YOU[1,2], KAI YANG[1,2], RAN CHEN[1,2], WEN JUAN ZHANG[1,2], YAN WU[3], ZHI LONG LIU[4], SHU SHAN DU[1,2]* and ZHI WEI DENG[5]

[1]*Beijing Key Laboratory of Traditional Chinese Medicine Protection and Utilization, Beijing Normal University, Beijing 100875, China,* [2]*State Key Laboratory Breeding Base of Dao-di Herbs, China Academy of Chinese Medical Sciences, Beijng 100700, China,* [3]*Technical Center of China Tobacco Guangxi Industrial Co., Ltd., Nanning 530001, China,* [4]*Department of Entomology, China Agricultural University, Beijing 100193, China and* [5]*Analytical and Testing Center, Beijing Normal University, Beijing 100875, China*

(Received 22 April, revised 24 June, accepted 3 July 2014)

Abstract: The aim of this research was to determine the chemical constituents and toxicities of the essential oil derived from *Alpinia blepharocalyx* rhizomes against the cigarette beetle, *Lasioderma sericorne* (Fabricius). The essential oil of *A. blepharocalyx* rhizomes was obtained by hydrodistillation and was investigated by gas chromatography–mass spectrometry (GC–MS). A total of 46 components of the essential oil of *A. blepharocalyx* rhizomes were identified. The principal compounds in *A. blepharocalyx* essential oil were camphor (23.13 %), sabinene (11.27 %), *α*-pinene (9.81 %) and eucalyptol (8.86 %) followed by camphene (8.05 %), sylvestrene (5.61 %) and *α*-phellandrene (5.00 %). Among them, the four active constituents, predicted with a bioactivity-test, were isolated and identified as camphor, sabinene, *α*-pinene and eucalyptol. The essential oil of *A. blepharocalyx* possessed strong contact toxicity against the cigarette beetle with ad LD_{50} value of 15.02 μg adult^{-1}, and exhibited strong fumigant toxicity against *L. sericorne* adults with an LC_{50} value of 3.83 mg L^{-1} air. The results indicate that the essential oil of *A. blepharocalyx* shows potential in terms of contact and fumigant toxicities against stored product insects.

Keywords: cigarette beetle; camphor; eucalyptol; contact toxicity; fumigant toxicity.

INTRODUCTION

The cigarette beetle, *Lasioderma sericorne* (Fabricius) (Coleoptera: Anobiidae), is one of the most serious pests of stored tobacco, tobacco

* Corresponding author. E-mail: dushushan@bnu.edu.cn
doi: 10.2298/JSC140422068W

products, cereal grains and processed foods throughout the world.[1] Control of *L. serricorne* populations around the world is primarily dependent upon continued applications of phosphine.[2] Although effective, its repeated use for decades has led to serious problems, including insecticide resistance, disruption of biological control by natural enemies, environmental and human health concerns, the rising cost of production and lethal effects on non-target organisms.[3,4] There is, therefore, an urgent need to find an alternative strategy for the control of these pests. Among integrated pest management tactics, plants have played a significant role because they constitute an important source of insecticides.[5] In recent years, essential oils have received much attention as pest control agents. They are characterized by low toxicity to human and animals, high volatility, and toxicity to insect pests of stored grain.[6] In a previous report,[7] it was suggested that essential oils might be applicable to the protection of stored products.

Antagonistic storage has been used as one of traditional Chinese medicinal materials conservation methods. It mainly utilizes some traditional Chinese medicinal materials having special volatile odor to store with medicinal materials vulnerable to insects, to prevent the insects. In order to inherit and develop the traditional method of prevention and control of stored grain insects, *Alpinia blepharocalyx* K. Schum, used as flavor and fragrance, a new plant resource was taken as the study sample. *A. blepharocalyx* belongs to the Zingiberaceae family and is widely distributed in the south–west of China (*e.g.*, in the Yunnan Province).[8] The rhizomes of *A. blepharocalyx* are used in Chinese traditional medicine for the treatment of abdominal distension and abdominal pain.[9] The chemical constituents of rhizomes of this medicinal herb were studied.[10] During the mass screening program for new agrochemicals from wild plants, the essential oil of *A. blepharocalyx* rhizomes was found to possess strong insecticidal activity against the cigarette beetle. A literature survey showed that there are no reports on the insecticidal activity of the essential oil of *A. blepharocalyx* rhizomes. Thus, it was decided to investigate insecticidal activities of the essential oil from *A. blepharocalyx* rhizome parts and its chemical constituents against *L. serricorne*. It was expected that this research work would provide some theoretical basis for the conception of antagonistic storage.

EXPERIMENTAL

Plant material and essential oil extraction

The fresh rhizomes (2.0 kg) of *Alpinia blepharocalyx* were harvested from Xishuangbanna (21°08'–22°36' N and 99°56'–101°50' E), Yunnan Province, China, in August 2013. The plant was identified, and a voucher specimen (BNU-dushushan-2013-08-12-24) was deposited at the Herbarium (BNU) of the College of Resources Science and Technology, Beijing Normal University, China. The sample was air-dried and ground to powders using a grinding mill. The powders were subjected to hydrodistillation using a modified clevenger-

type apparatus for 6 h and extracted with *n*-hexane. Anhydrous sodium sulfate was used to remove water after the extraction. The essential oil was stored in airtight containers at 4 °C for subsequent experiments.

Insects

Cultures of the cigarette beetle, *L. serricorne*, were maintained in the laboratory without exposure to any insecticide. They were reared on sterilized diet (wheat flour/yeast mass ratio of 10:1) at 29–30 °C, 70–80 % r.h. in the dark. The unsexed adult beetles used in all the experiments were about 1–2 weeks old. All containers housing insects used in experiments were made escape proof with a coating of polytetrafluoroethylene (Fluon).

GC–MS analysis

The essential oil was subjected to GC–MS analysis on a Thermo Finnigan Trace DSQ instrument equipped with a flame ionization detector and an HP-5MS (30 m×0.25 mm×0.25 μm) capillary column. The column temperature was programmed at 50 °C for 2 min, then increased at 2 °C min^{-1} to a temperature of 150 °C and held for 2 min, and then increased at 10 °C min^{-1} until the final temperature of 250 °C was reached, which was held for 5 min. The injector temperature was maintained at 250 °C. The samples (1 μL) were diluted to 1 % with *n*-hexane. The carrier gas was helium at a flow rate of 1.0 mL min^{-1}. The spectra were scanned from *m*/*z* 50 to 550. Most constituents were identified by gas chromatography by comparison of their retention indices with those in the literature or with those of available authentic compounds. The retention indices were determined in relation to a homologous series of *n*-alkanes (C_8–C_{24}) obtained under the same operating conditions. Further identification was made by comparison of their mass spectra with those stored in the NIST 05 and Wiley 275 libraries or with mass spectra from the literature.[11] The relative percentages of the component were calculated based on the normalization method without the use of correction factors.

Isolation and characterization of the four main constituent compounds

The crude essential oil (9 mL) was chromatographed on a silica gel (Qingdao Marine Chemical Plant, Shandong province, China) column (30 mm i.d., 500 mm length) by gradient elution with *n*-hexane first, then with *n*-hexane–ethyl acetate (in volume ratios of 100:1, 50:1, 20:1 and 5:1, with gradient elution), and finally with ethyl acetate to obtain 25 fractions, with flow rate of 0.50 cm^3/s; the size of each fraction was 80 g and then the solvent was changed. Based on contact toxicity, fractions 3, 9 and 15 were chosen for further fractionation. With PTLC, four purified compounds were obtained. The isolated compounds were elucidated from their NMR spectra. The NMR experiments were performed on a Bruker Avance DRX 500 instrument using $CDCl_3$ as solvent with TMS as internal standard.

Contact toxicity bioassay

The insecticidal activities of *A. blepharocalyx* essential oil and the four main compositions were determined by direct contact application. Range-finding studies were run to determine the appropriate testing concentrations. A serial dilutions (five concentrations: 2.20–10.00 % for the oil, 1.97–10.00 % for camphor, eucalyptol and sabinene and 5.93–30.00 % for *α*-pinene) were prepared in *n*-hexane. Aliquots of 0.5 μL of the dilutions were applied topically to the dorsal thorax of the insects. Controls were determined using *n*-hexane. Five replicates were performed for all treatments and controls, and the experiment was replicated three times. Both treated and control insects were then transferred to glass vials (10 insects per vial)

with culture media and kept in incubators. Mortality was observed after 24 h. The LD_{50} values were calculated using Probit analysis.[12]

Fumigant toxicity bioassay

Serial dilutions of the essential oil and the four main compositions (five concentrations: 0.44–2.00 % for oil, 0.59–3.00 % for camphor, 0.99–5.00 % for eucalyptol, 5.21–20.00 % for sabinene and 3.95–20.00 % for α-pinene) were prepared in *n*-hexane. A Whatman filter paper (diameter 2.0 cm) was placed on the underside of the screw cap of a glass vial (diameter 2.5 cm, height 5.5 cm, volume 25 mL). Ten microliters of an appropriate concentration was added to the filter paper. The solvent was allowed to evaporate for 20 s before the caps were placed tightly on the glass vials, each of which contained 10 insects, to form a sealed chamber. Preliminary experiments demonstrated that 20 s was sufficient for the evaporation of solvents. Fluon was used inside each glass vial to prevent insects reaching the treated filter paper. *n*-Hexane was used as a control. Five replicates were performed for all treatments and controls, and they were incubated for 24 h. The experiments were repeated three times. The mortality was recorded. The LC_{50} values were calculated by using Probit analysis.[12]

RESULTS AND DISCUSSION

Chemical constituents of essential oil

The brownish red essential oil yield of *Alpinia blepharocalyx* rhizome parts was 0.45 % (*V*/*w*) and the density of the concentrated essential oil was determined to be 0.82 g mL^{-1}. GC–MS analysis of the essential oil of *A. blepharocalyx* rhizome parts led to the identification and quantification of a total of 46 major components, accounting for 96.38 % of the total components present (Table S-I of the Supplementary material to this paper). The main constituents of *A. blepharocalyx* rhizomes essential oil were camphor (23.13 %), sabinene (11.27 %), α-pinene (9.81 %) and eucalyptol (8.86 %).

However, the principal components of the essential oil from *A. blepharocalyx* rhizomes analyzed in this work differed from those in previous reports. For example, in several previous studies, cinnamic acid methyl ester was isolated and identified as the main component; it made up 90.88 % of the essential oil from *A. blepharocalyx*.[10–13] However, in another study, γ-cadinene (18.70 %), linalool (5.45 %), geranyl acetate (3.86 %) and δ-cadinene (3.08 %) were the dominant components in the essential oil of *A. blepharocalyx*.[14] These differences were possibly due to the differences in the place of origin and plant parts used.

Structure confirmation of isolated compounds

With further isolation, four purified compounds were obtained and they were analyzed by several of NMR techniques including ^{1}H-NMR and ^{13}C-NMR. Combining all the NMR spectra data, the four isolated compounds were finally recognized as camphor (0.46 g),[15] sabinene (0.22 g),[16–18] α-pinene (0.20 g)[19] and eucalyptol (0.15 g).[20]

Insecticidal activities of the essential oil

The essential oil of *A. blepharocalyx* rhizome parts showed contact toxicity against *L. serricorne* adults with an LD_{50} value of 15.02 μg adult^{-1}. Among the four main compounds, only camphor possessed stronger contact toxicity against *L. serricorne* (LD_{50} = 13.44 μg adult^{-1}), eucalyptol and sabinene exhibited the same level contact toxicity against *L. serricorne* (LD_{50} = 15.58 and 15.74 μg adult^{-1}) as the essential oil, while *α*-pinene showed weaker contact toxicity than the essential oil of *A. blepharocalyx* rhizomes (Table I). Compared with the famous botanical insecticide, pyrethrins, the essential oil was 63 times less active against *L. serricorne* adults because pyrethrins displayed LD_{50} value of 0.24 μg adult^{-1} (Table I). However, the essential oil of *A. blepharocalyx* rhizome parts showed stronger contact toxicity against *L. serricorne* than the essential oil of *Zanthoxylum schinifolium* seeds (LD_{50} = 18.71 μg adult^{-1}).[21]

TABLE I. Toxicities of the essential oil of *Alpinia blepharocalyx* rhizome parts against *Lasioderma serricorne* adults; contact toxicity: LD_{50} / μg adult^{-1}; fumigant: LC_{50} / mg L^{-1} air

Toxicity	Treatment	Concentrations	LD_{50}/LC_{50}	95 % Fiducial interval	χ^2
Contact	*A. blepharocalyx*	2.20–10.00	15.02	12.88–17.21	9.660
	Camphor	1.97–10.00	13.44	10.39–16.07	15.38
	Eucalyptol	1.97–10.00	15.58	12.88–18.02	15.18
	Sabinene	1.97–10.00	15.74	10.33–20.70	7.31
	α-Pinene	5.93–30.00	77.28	69.02–87.30	14.71
	Pyrethrum	0.010–0.40	0.24	0.16–0.35	17.36
Fumi-gant	*A. blepharocalyx*	0.44–2.00	3.83	3.55–4.25	18.52
	Camphor	0.59–3.00	2.36	1.91–2.71	14.29
	Eucalyptol	0.99–5.00	5.18	4.63–5.70	16.79
	Sabinene	5.21–20.00	44.17	39.28–50.66	25.07
	α-Pinene	3.95–20.00	37.57	34.31–41.19	14.90
	Phosphine	7.20×10^{-3}–11.12×10^{-3}	9.23×10^{-3}	7.13×10^{-3}–11.37×10^{-3}	11.96

The essential oil of *A. blepharocalyx* rhizomes also possessed fumigant activity against *L. serricorne* with an LC_{50} value of 3.83 mg L^{-1} air (Table I). In comparison, only camphor possessed stronger fumigant toxicity against *L. serricorne* (LC_{50} = 2.36 mg L^{-1} air), eucalyptol exhibited the same level fumigant toxicity against *L. serricorne* (LC_{50} = 5.18 mg L^{-1} air) as the essential oil, while sabinene and *α*-pinene showed weaker fumigant toxicity than the essential oil of *A. blepharocalyx* rhizomes (Table I). However, the currently used grain fumigant, phosphine has a fumigant activity against *L. serricorne* adults with an LC_{50} value of 9.23×10^{-3} mg L^{-1} air. The fumigant activity of the essential oil against the *L. serricorne* was thus many magnitudes lower than that of the commercial fumigants phosphine. Compared with the other essential oils investigated in previous studies, the essential oil of *A. blepharocalyx* rhizomes exhibited stronger fumigant toxicity against *L. serricorne*, than, *e.g.*, the essential oils of

Pistacia lentiscus (LC_{50} = 8.44 mg L^{-1} air), *Elsholtzia stauntonii* (LC_{50} = 10.99 mg L^{-1} air) and *Agastache foeniculum* (Lamiaceae) (LC_{50} = 21.57 mg L^{-1} air).[5,22,23]

In this work, the results suggested that among the four main components, camphor showed the strongest contact and fumigant toxicity against *L. serricorne*. In previous reports, the four components were demonstrated to possess insecticidal activities against several stored product insects, such as *Sitophilus zeamais*, *Tribolium castaneum*, *Leptinotarsa decemlineata*, and broadbean weevil.[24–28] The high volatility of these toxic compounds likely delivered fumigant toxicity by vapor action *via* the respiratory system, but further work is needed to confirm their exact mode of action.

A. blepharocalyx is one of the Dai drug types, the rhizome of which is used in the treatment of abdominal bloating and pain. Essential oil, which is a mixture of plant secondary metabolites, plays an important role in plant–insect interaction, and is commonly responsible for plant resistance to insects. The components of essential oil often biodegrade to non-toxic products and hence, they could be much safer insect control agents and more suitable for use in integrated pest management (IPM). As far as our literature survey could ascertain, no information concerning the insecticidal activity of the essential oil of *A. blepharocalyx* has been openly published. For this reason, in the present paper, the identification of the chemical components of *A. blepharocalyx* by a gas chromatography–mass spectroscopy (GC–MS) method was described, and the insecticidal property of the essential oil were evaluated against *L. serricorne*.

CONCLUSIONS

This study revealed that the essential oil of *A. blepharocalyx* rhizomes and its main compound camphor demonstrated significant insecticidal activity on *L. serricorne*. These findings also suggest that the bioactivities of the essential oil may be due to the bioactive compounds. Considering the currently used fumigants are synthetic insecticides, the essential oil of *A. blepharocalyx* rhizomes and camphor are quite promising, and they show potential for development as possible natural fumigants for the control of stored product insects. However, for the practical application of the essential oil and compounds as novel fumigants, further studies on the safety of the essential oil and compounds to humans and on development of formulation are necessary to improve the efficacy and stability, and to reduce cost.

SUPPLEMENTARY MATERIAL

Compounds identified in the essential oil of *Alpinia blepharocalyx* rhizome parts are available electronically from http://www.shd.org.rs/JSCS/, or from the corresponding author on request.

Acknowledgments. This project was supported by the National Natural Science Foundation of China (No. 81374069). The authors thank Dr. Q. R. Liu from College of Life Sciences, Beijing Normal University, Beijing 100875, China, for the identification of the investigated medicinal herb.

ИЗВОД

ХЕМИЈСКИ САСТАВ И ИНСЕКТИЦИДНА АКТИВНОСТ ЕТАРСКОГ УЉА РИЗОМА *Alpinia blepharocalyx* СПРАМ ДУВАНОВЕ БУБЕ *Lasioderma serricorne*

YING WANG[1,2], CHUN XUE YOU[1,2], KAI YANG[1,2], RAN CHEN[1,2], WEN JUAN ZHANG[1,2], YAN WU[3], ZHI LONG LIU[4], SHU SHAN DU[1,2] и ZHI WEI DENG[5]

[1]Beijing Key Laboratory of Traditional Chinese Medicine Protection and Utilization, Beijing Normal University, China, [2]State Key Laboratory Breeding Base of Dao-di Herbs, China Academy of Chinese Medical Sciences, Beijng, China, [3]Technical Center of China Tobacco Guangxi Industrial Co., Ltd., Nanning, China, [4]Department of Entomology, China Agricultural University, Beijing, China и [5]Analytical and Testing Center, Beijing Normal University, Beijing, China

Циљ рада је био одређивање хемијског састава и токсичности етарског уља ризома *Alpinia blepharocalyx* спрам дуванове бубе *Lasioderma serricorne* (Fabricius). Етарско уље из ризома *A. blepharocalyx* је добијено дестилацијом воденом паром и испитивано је методом GC–MS. Идентификовано је укупно 46 састојака. Главна једињења у етарском уљу *A. blepharocalyx* су била камфор (23,13 %), сабинен (11,27 %), α-пинен (9,81 %) и еукалиптол (8,86 %), а нађени су и камфен (8,05 %), силвестрен (5,61 %) и α-феландрен (5,00 %). Применом теста биоактивности идентификована су 4 активна састојка: камфор, сабинен, α-пинен и еукалиптол. Етарско уље *A. blepharocalyx* је испољило јаку контактну токсичност спрам дуванове бубе, уз LD_{50} вредност од 15,02 μg по одраслој јединки, као и јаку фумигантну токсичност, уз LC_{50} вредност од 3,83 mg L^{-1} ваздуха. Резултати су показали да етарско уље *A. blepharocalyx* може имати потенцијалну примену у заштити од инсеката током чувања дувана.

(Примљено 22. априла, ревидирано 24. јуна, прихваћено 3. јула 2014)

REFERENCES

1. S. Kim, C. Park, M. H. Ohh, H. C. Cho, Y. J. Ahn, *J. Stored Prod. Res.* **39** (2003) 11
2. N. D. G. White, J. G. Leesch, *Integrated Management of Insects in Stored Products*, Marcel Dekker Inc, New York, 1995
3. S. Rajendran, K. S. Narasimhan, *Int. J. Pest. Manage.* **40** (1994) 207
4. Z. Jovanovic, M. Kostic, Z. Popovic, *Ind. Crops Prod.* **26** (2007) 100
5. O. Bachrouch, J. M. B. Jemaa, T. Talou, B. Marzouk, M. Abderraba, *Bull. Insectol.* **63** (2010) 129
6. D. R. Batish, P. H. Sing, K. R. Kohli, S. Kaur, *Forest Ecol. Manage.* **256** (2008) 2166
7. B. Z. Sahaf, S. Moharramipour, M. H. Meshkatalsadat, *J. Asia-Pac. Entomol.* **11** (2008) 175
8. C. X. Wang, C. H. Xu, A. L. Tian, S. H. Fu, C. X. Wang, *Color. Technol.* **129** (2013) 32
9. Chinese Academy of Medical Sciences, *Chinese medicinal herbal*, People's Medical Publishing House, Beijing, 1993
10. Z. Na, *J. Plant Resour. Environ.* **15** (2006) 73
11. R. P. Adams, *J. Am. Soc. Mass Spectrom.* **16** (2001) 1902
12. M. Sakuma, *Appl. Entomol. Zool.* **33** (1998) 339
13. H. Z. Qin, L. Liu, X. Q. Wang, *Nat. Prod. Res. Develop.* **24** (2012) 190
14. R. Y. He, Q. Meng, Y. G. Fan, X. J. Yu, J. K. Ding, *Acta Bot. Yunnanica* **17** (1995) 226

15. H. Tanaka, J. Y. Chou, M. Mine, M. Kuroboshi, *Bull. Chem. Soc. Jpn.* **77** (2004) 1745
16. F. Bohlmann, R. Zeisberg, E. Klein, *Org. Magn. Reson.* **7** (1975) 426
17. R. P. Adams, P. Weyerstahl, *J. Essent. Oil Res.* **4** (1991) 197
18. A. Guerrini, G. Sacchetti, M. Muzzoli, G. Moreno Rueda, A. Medici, E. Besco, R. Bruni, *J. Agric. Food Chem.* **54** (2006) 7778
19. A. Y. Badiah-Hadj-Ahmed, B. Y. Meklati, H. Waton, Q. T. Pham, *Magn. Reson. Chem.* **30** (1992) 807
20. A. Ashnagar, N. G. Naseri, A. Bayemani, *Asian J. Chem.* **21** (2009) 4969
21. C. F. Wang, K. Yang, Z. F. Geng, J. Xu, S. S. Guo, H. P. Chen, S. S. Du, Z. L. Liu, Z. W. Deng, Y. Y. Wang, *Molecules* **18** (2013) 1
22. J. H. Lv, X. H. Su, J. J. Zhong, *S. Afr. J. Sci.* **108** (2012) 7
23. A. Ebadollahi, M. Safaralizadeh, A. Pourmirza, S. Gheibi, *J. Plant Prot. Res.* **50** (2010) 215
24. S. S. Chu, S. S. Du, Z. L. Liu, *J. Chem.* **2013** (2013) 1
25. C. F. Wang, K. Yang, H. M. Zhang, J. Cao, R. Fang, Z. L. Liu, S. S. Du, Y. Y. Wang, Z. W. Deng, L. Zhou, *Molecules* **16** (2011) 3077
26. Z. L. Liu, G. H. Jiang, L. Zhou, Q. Z. Liu, *J. Biosci.* **68** (2013) 13
27. S. Kordali, I. Aslan, O. A. Calmasur, A. Cakir, *Ind. Crops Prod.* **23** (2006) 162
28. S. Kordali, M. Kesdek, A. Cakir, *Ind. Crops Prod.* **26** (2007) 278.

Journal of the Serbian Chemical Society
JSCS@tmf.bg.ac.rs • www.shd.org.rs/JSCS
J. Serb. Chem. Soc. 80 (2) S31–S32 (2015) *Supplementary material*

SUPPLEMENTARY MATERIAL TO

Chemical constituents and insecticidal activities of the essential oil from *Alpinia blepharocalyx* rhizomes against *Lasioderma serricorne*

YING WANG[1,2], CHUN XUE YOU[1,2], KAI YANG[1,2], RAN CHEN[1,2], WEN JUAN ZHANG[1,2], YAN WU[3], ZHI LONG LIU[4], SHU SHAN DU[1,2]* and ZHI WEI DENG[5]

[1]Beijing Key Laboratory of Traditional Chinese Medicine Protection and Utilization, Beijing Normal University, Beijing 100875, China, [2]State Key Laboratory Breeding Base of Dao-di Herbs, China Academy of Chinese Medical Sciences, Beijing 100700, China, [3]Technical Center of China Tobacco Guangxi Industrial Co., Ltd., Nanning 530001, China, [4]Department of Entomology, China Agricultural University, Beijing 100193, China and [5]Analytical and Testing Center, Beijing Normal University, Beijing 100875, China

J. Serb. Chem. Soc. 80 (2) (2015) 171–178

TABLE S-I. Constituents identified from the essential oil of *Alpinia blepharocalyx* rhizome parts; *RI* – retention index as determined on a HP–5MS column using the homologous series of *n*-hydrocarbons

Compound	*RI*	Content, %
β-Terpinene	1069	0.53
1R-*α*-Pinene	1087	9.81
Camphene	1205	8.05
Sabinene	1228	11.27
Unknown compound	1245	1.00
2-Methylheptenone	1248	0.07
α-Phellandrene	1255	5.00
2,4(8)-*p*-Menthadiene	1267	0.52
2-Isopropyltoluene	1275	4.50
Sylvestrene	1278	5.61
Eucalyptol	1283	8.86
2,2-Dimethylheptane	1403	0.13
2,5,9-Trimethyldecane	1415	0.09
DL-Malic acid	1426	0.06
8,8-Dimethyl-4-methylene-1-oxaspiro[2.5]oct-5-ene	1455	0.07
Linalool propionate	1460	0.64
n-Butylbenzene	1498	0.48
Camphor	1604	23.13

* Corresponding author. E-mail: dushushan@bnu.edu.cn

TABLE S-I. Continued

Compound	*RI*	Content, %
Camphene hydrate	1609	0.30
Borneol	1634	1.88
α-Phellandren-8-ol	1641	0.11
(–)-4-Terpineol	1651	2.54
Xylitol	1667	0.08
Cryptone	1669	0.08
α-Terpineol	1671	2.63
Myrtenal	1677	0.27
(–)-Myrtenol	1680	0.43
Bicyclo[3.2.2]nona-6,8-dien-3-one	1687	0.19
Fenchyl acetate	1912	1.02
(+)-Citronellol	1934	0.74
Citral	1951	1.96
Benzylacetone	1953	0.76
3,5-Dimethoxytoluene	1989	0.08
Methyl atropate	2106	0.24
Decyl methyl ketone	2111	0.17
Carvacrylacetate	2115	0.36
α-Cedrene	2146	0.37
Methyl eugenol	2165	0.64
1,2-Vinylidenecyclohexane	2166	0.49
(1*S*,8*aβ*)-Decahydro-4*aβ*-methyl-8-methylene-2*α*-(1-methyl-ethyl)naphthalen-1*β*-ol acetate	2185	0.06
5,7-Diethyl-5,6-decadien-3-yne	2195	0.12
(*S*,1*Z*,5*E*)-1,5-Dimethyl-8-isopropenyl-1,5-cyclodecadiene	2197	0.30
δ-Cadinene	2723	0.47
3,7-Dimethylnonane	2773	0.10
4,4-Dimethylundecane	2860	0.06
Tetrapropylmethane	2900	0.11
Total		96.38

Journal of the Serbian Chemical Society
JSCS-info@shd.org.rs • www.shd.org.rs/JSCS
J. Serb. Chem. Soc. *80* (2) 179–186 (2015)
JSCS–4708
UDC 546.732:66.061+547.565.2:543.4/.5
Original scientific paper

Liquid–liquid extraction of ion-association complexes of cobalt(II)–4-(2-pyridylazo)resorcinol with ditetrazolium salts

VIDKA V. DIVAROVA[1], KIRILA T. STOJNOVA[1], PETYA V. RACHEVA[2], VANYA D. LEKOVA[1]* and ATANAS N. DIMITROV[1]

[1]*Department of General and Inorganic Chemistry, Faculty of Chemistry, University of Plovdiv "Paisii Hilendarski", 24 Tsar Assen Street, 4000 Plovdiv, Bulgaria and* [2]*Department of Chemistry and Biochemistry, Faculty of Pharmacology, Medical University Plovdiv, 15A Vasil Aprilov Boulevard, 4002 Plovdiv, Bulgaria*

(Received 14 May, revised 8 October, accepted 20 October 2014)

Abstract: The formation and liquid–liquid extraction of ion-association complexes between Co(II)–4-(2-pyridylazo)resorcinol (Co(II)–PAR) anionic chelates and cations of three ditetrazolium chlorides (DTC), *i.e.*, blue tetrazolium chloride (BTC), neotetrazolium chloride (NTC) and nitro blue tetrazolium chloride (NBTC), were studied. The optimum conditions for the formation and solvent extraction of the ion-association complex chelates were determined. It has been found that in the Co(II)–PAR–DTC systems, the reactants are present in the mole ratio 1:2:1 and the general formula of complexes was suggested. The extraction equilibria were investigated and quantitatively characterized by the equilibrium constants and the recovery factors. The analytical characteristics of the complexes were calculated.

Keywords: spectrophotometry; solvent extraction; chelates; extraction equilibria.

INTRODUCTION

Azo compounds are widely used as chromogenic reagents and metallochromic indicators for many metals. 4-(2-Pyridylazo)resorcinol (PAR) was one of the first azo reagents used for the spectrophotometric determination of cobalt due to its high sensitivity as a chromogenic reagent.[1–28] PAR forms intensively colored anionic chelates with cobalt, which can readily react with bulky organic compounds to give ternary complexes with good extraction behavior and analytical potential.[21–32]

Tetrazolium cations (TZ^{n+}) form analytically important ion-association complexes with $Co(SCN)_4^{2-}$,[33,34] and M–PAR anionic chelates, where M is V(V), V(IV), In(III) and Ga(III).[35–39]

* Corresponding author. E-mail: vanlek@uni-plovdiv.bg
doi: 10.2298/JSC140514102V

Of particular interest are the negatively charged complex ions of cobalt(II) with PAR, which interact with the monotetrazolium moiety to form ion-association complexes.[40]

This investigation was aimed at studying the formation of ternary ion-associates complexes between the anionic chelates Co(II)–4-(2-pyridylazo)resorcinol (Co(II)–PAR) with ditetrazolium cations in the liquid–liquid extraction system Co(II)–PAR–DTC–H_2O–$CHCl_3$. The purpose is future application of the extraction system for the determination of cobalt(II) in alloys, as well as biological and pharmaceutical samples.

EXPERIMENTAL

Reagents and apparatus

$CoSO_4 \cdot 7H_2O$ (Sigma–Aldrich, *p.a.*). A 1.7×10^{-2} mol dm^{-3} aqueous stock solution was prepared, from which a working solution ($c_{Co} = 1.7\times10^{-4}$ mol dm^{-3}) was obtained by dilution.

4-(2-Pyridyazo)-resorcinol (PAR) (Sigma–Aldrich, 96 %). PAR was dissolved in slightly alkaline distilled water to give a 2.0×10^{-3} mol dm^{-3} solution.

Neotetrazolium Chloride (NTC) (Sigma–Aldrich, p.a.). 3,3′-(4,4′-Biphenylene)bis(2,5--diphenyl-2*H*-tetrazolium chloride). An aqueous 2.0×10^{-3} mol dm^{-3} solution was prepared.

Blue tetrazolium chloride (BTC) (Sigma–Aldrich, *p.a*). 3,3′-(3,3′-Dimethoxy-4,4′-biphenylene)bis(2,5-diphenyl-2*H*-tetrazolium chloride). An aqueous 2.0×10^{-3} mol dm^{-3} solution was prepared.

Nitro blue tetrazolium chloride (NBTC) (Merck, p.a.). 3,3′-(3,3′-Dimethoxy-4,4′-biphenylene)bis[2-(4-nitrophenyl)-5-phenyl-2*H*-tetrazolium chloride). An aqueous 2.0×10^{-3} mol dm^{-3} solution was prepared.

The acidity of the aqueous medium was set using a buffer solution prepared by mixing 2.0 mol dm^{-3} aqueous solutions of CH_3COOH and NH_3.

The organic solvent, $CHCl_3$, was additionally distilled.

The pH was checked using an HI 83140 pH meter (Hanna Instruments, Romania).

A Camspes M 508 spectrophotometer (UK), equipped with 10 mm path length cells, was employed for reading the absorbance values.

Procedure for establishing the optimum operating conditions

The required volumes of the solutions of Co(II), PAR, DTC (NBTC, NTC or BTC) and buffer solution to adjust the pH of the aqueous phase were introduced into a 100 cm^3 separatory funnel. The volume was then brought up to 10 cm^3, 10 cm^3 of chloroform were added and the sample extracted. The phases were left to separate, the organic phase was transferred through a filter paper into a 1 cm cell and its absorbance measured against a blank run in parallel.

RESULTS AND DISCUSSION

Absorption spectra

The absorption spectra of the extracts of the ternary ion-association complexes (TIAC) Co(II)–PAR–DTC in chloroform were characterized by absorption maxima in the visible range (λ_{max}, 515–520 nm), Fig. 1. They are shifted by 5–10 nm as compared to the maximum of the binary Co(II)–PAR complex in

aqueous medium (510 nm; pH 3.5–10,[12,30,41]). As the optimum wavelength, λ_{max} = 520 nm was used in all three cases.

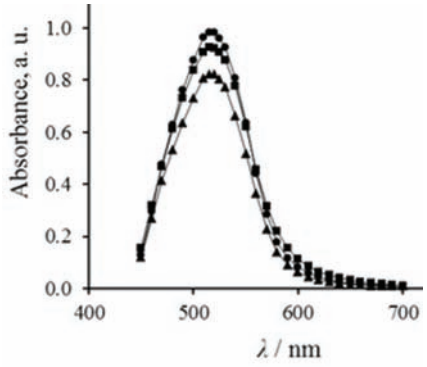

Fig. 1. Absorption spectra of the ternary complexes of Co–PAR–DTC in $CHCl_3$ against blanks: $c_{Co(II)}$ = 1.7×10^{-5} mol dm^{-3} = const; ●: c_{PAR} = 1.4×10^{-4} mol dm^{-3}, c_{BTC} = 2.0×10^{-4} mol dm^{-3}; ■: c_{PAR} = 1.4×10^{-4} mol dm^{-3}, c_{NBTC} = = 2.6×10^{-4} mol dm^{-3} and ▲: c_{PAR} = 0.8×10^{-4} mol dm^{-3}, c_{NTC} = 3.0×10^{-4} mol dm^{-3}.

Effect of pH

The acidity of the aqueous phase has a substantial effect on the extraction of TIAC into the organic phase. The results of pH change on the absorption spectra of the complexes are represented in Fig. 2. The maximum extraction of the TIAC Co(II)–PAR–BTC could be achieved at a pH in the range of 5.0–6.0, the maximum extraction the Co(II)–PAR–NTC at a pH in the range 4.8–7.0, while the maximum extraction of the third complex Co(II)–PAR–NBTC was achieved at a pH in the range 4.2–5.2.

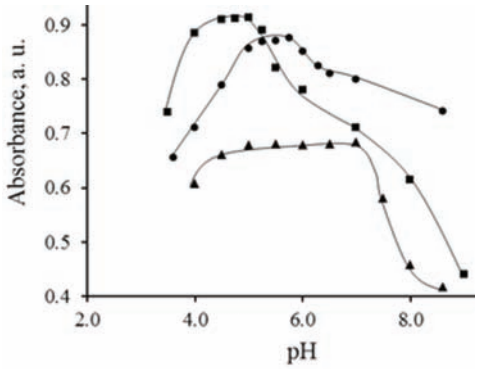

Fig. 2. Absorbance of Co–PAR–DTC extracts against PAR–DTC extracts *vs.* pH of the aqueous phase plots: $c_{Co(II)}$ = 1.7×10^{-5} mol dm^{-3} = const; c_{PAR} = 2.0×10^{-4} mol dm^{-3} = const; c_{DTC} = 2.0×10^{-4} mol dm^{-3} (DTC: ●, BTC; ■, NBTC; ▲, NTC).

Effect of shaking time

The performed experiments showed that maximum extraction of the ion--association complexes in chloroform is achieved at shaking time of not less than 30 s. In all three cases, a longer shaking time did not affect the absorbance. A shaking time of 2 min was used in the further experiments.

Effect of the concentration of the reagents

The complete bonding of Co(II) into a chelate complex requires a 4.2-fold excess of PAR for the TIAC with NTC, a 6.0–fold excess for the TIAC with BTC, and a 9.4–fold excess for the TIAC with NBTC. For maximum association and extraction, the amount of DTC should not be lower than an 8.2-fold excess for NTC, a 9.4-fold excess for BTC, and a 15.5–fold excess for NBTC.

The Beer law and analytical characteristics

To find the region of linear relationship between the cobalt concentration in aqueous phase and the absorbance in the organic phase after extraction, further studies were performed using regression analysis. The analytical characteristics are presented in Table I.

Table I. Characteristics concerning the application of TIAC for extractive–spectrophotometric determination of cobalt in the extraction systems Co(II)–PAR–DTC–H_2O–$CHCl_3$

Analytical characteristic	Ditetrazolium salt (DTC)		
	NTC	BTC	NBTC
[a]$\varepsilon' / 10^4$ dm^3 mol^{-1}cm^{-1}	4.81±0.26	5.75±0.20	5.65±0.22
[b]Beer Law, μg cm^{-3}	up to 1.6	up to 2.2	up to 2.2
[c]*SS* / 10^{-3} μg cm^{-2}	1.22	1.02	1.04
[d]*LOD* / μg cm^{-3}	0.05	0.32	0.19
[e]*LOQ* / μg cm^{-3}	0.16	1.07	0.65

[a]Apparent molar absorptivity; [b]adherence to Beer's Law; [c]Sandell's sensitivity; [d]limit of detection; [e]limit of quantification

Mole ratios of the complexes and suggested general formula

Using known methods, the mobile equilibrium method[42] and the straight--line method of Asmus,[42,43] it was confirmed the mole ratio of reaction between Co(II):PAR was1:2.[35,37,40,41] The main studies were aimed at establishing the mole ratios of interaction between Co(II) and DTC. In this direction, the mobile equilibrium method (Fig. 3) and the straight-line method of Asmus (Fig. 4) were

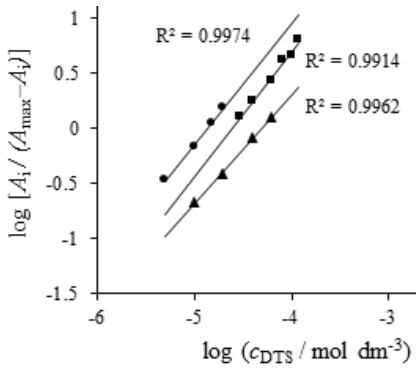

Fig. 3. Straight lines by the mobile equilibrium method during the determination of Co-to-DTC: $c_{Co(II)} = 1.7\times10^{-5}$ mol dm^{-3} = const; $c_{PAR} = 1.4\times10^{-4}$ mol dm^{-3}, ●, BTC, ■, NBTC; $c_{PAR} = 0.8\times10^{-4}$ mol dm^{-3}, ▲, NTC.

applied. The results of the presented studies show that the mole ratio of Co:DTC (BTC, NTC, NBTC) was 1:1. By means of independent method, the method of the continuous variations,[42] it was confirmed that mole ratio Co(II):NTC was 1:1. Based on the performed studies, it could be concluded that Co, PAR and DTC interact in mole ratio 1:2:1.

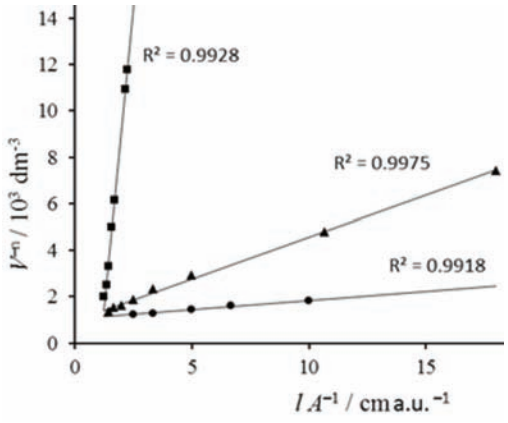

Fig. 4. Determination of the mole ratios of Co-to-DTC by the method of Asmus: $c_{Co(II)}$ = 1.7×10^{-5} mol dm^{-3} = const; c_{PAR} = = 1.4×10^{-4} mol dm^{-3}, ●, BTC, ■, NBTC; c_{PAR} = 0.8×10^{-4} mol dm^{-3}, ▲, NTC.

The performed extraction–spectrophotometric studies of the systems Co(II)–PAR–DTC–H_2O–$CHCl_3$ gave reason to assume that the contact time between the phases was not sufficient for the oxidation of Co(II) to Co(III). In the aqueous phase, the chelate complex [CoH_2R] was formed between PAR (H_2R) and Co(II), which was deprotonated [CoR_2]$^{2-}$ and reacted with a ditetrazolium salts DT^{2+}.

Having in mind the mole ratio, it could be assumed that the complex formation of anionic chelate Co(II)–PAR in the aqueous phase, the formation of ion-associated complex in the aqueous phase, its distribution between the aqueous and the organic phase and its extraction in chloroform are given by the equations:

$$Co^{2+} + 2\ H_2R \rightarrow [CoR_2]^{2-}_{aq} + 4H^+ \quad (1)$$

$$[CoR_2]^{2-}_{aq} + DT^{2+}_{aq} \leftrightarrows (DT)[CoR_2]_{aq} \quad (2)$$

$$(DT)[CoR_2]_{aq} \leftrightarrows (DT)[CoR_2]_{org} \quad (3)$$

$$[CoR_2]^{2-}_{aq} + DT^{2+}_{aq} \leftrightarrows (DT)[CoR_2]_{org} \quad (4)$$

Equilibrium constants, recovery factors and molar absorptivities

The equilibrium constants describing quantitatively the equilibria in the aqueous phase and the extraction of the ion associates into the organic layer are calculated as follows:

The distribution constant, K_D, was calculated by comparing the absorbance for a single extraction (A_1) to that of the triple extraction (A_3) in equal volumes:

$$K_D = \frac{\{(DT)[CoR_2]\}_{org}}{\{(DT)[CoR_2]\}_{aq}} = \frac{A_1}{(A_3 - A_1)} \quad (5)$$

The association constant, β, was obtained by the method of Komar–Tolmachev.[42]

The extraction constant, K_{ex}, was calculated using the equation:

$$K_{ex} = K_D\beta; \log K_{ex} = \log K_D + \log \beta \quad (6)$$

The method of Komar–Tolmachev enables the true molar absorptivities, ε, and K_D to be calculated, which were then used to obtain the recovery factors, R%:

$$R\% = \frac{100K_D}{K_D + 1} \quad (7)$$

The results are presented in Table II. Analysis of the results showed that sufficiently stable ion associates were formed in the aqueous phase that were quantitatively extracted into the organic phase with high sensitivity.

TABLE II. Values of the equilibrium constants, recovery factors and molar absorptivities of the extraction systems Co(II)–PAR–DTC–H_2O–$CHCl_3$

Parameter	Ditetrazolium salt (DTC)		
	NTC	BTC	NBTC
$\log \beta$	4.31±0.25	4.77±0.32	4.79±0.28
$\log K_D$	1.02±0.01	1.41±0.02	0.96±0.01
$\log K_{ex}$	5.33±0.51	6.18±0.55	5.75±0.59
R / %	91.25±0.09	95.64±0.11	89.92±0.08
ε^a / 10^4 dm^3 mol^{-1} cm^{-1}	4.62±0.07	6.43±0.28	5.51±0.21

[a]True molar absorptivity

CONCLUSIONS

Liquid–liquid extractions of Co(II)–PAR–DTC–H_2O–$CHCl_3$ systems were studied. The optimum conditions for the formation of the ion-association complex chelates of Co(II)–PAR with DTC in aqueous medium and their quantitative extraction into chloroform were determined. The equilibrium constants and analytical characteristics needed for the quantitative assessment of the extraction equilibrium were calculated, *i.e.*, the association constant, the distribution constant, the extraction constant, the recovery factor, the apparent molar absorptivity, the true molar absorptivity, the limit of detection (*LOD*), the limit of quantification (*LOQ*) and the Sandell sensitivity (*SS*). The validity of the Beer Law was checked. The mole ratio showed that the ion-association complex chelates of Co(II)–PAR with DTC could be represented by the general formula (DT)[Co(PAR)$_2$]. The presence of hydrophobic substituents, methoxy group in the molecule of the ditetrazolium salt BTC, increased the solubility of the ion-

association complex in the organic solvent, while the hydrophilic nitro groups in the ditetrazolium salt NBTC reduced the solubility of the associate. For this reason, the ion-association complex of Co–PAR–BTC allowed the determination of Co(II) with a higher sensitivity.

ИЗВОД

ТЕЧНО–ТЕЧНА ЕКСТРАКЦИЈА ЈОН-АСОСОВАНИХ КОБАЛТ(II)-4-(2-ПИРИДИЛАЗО)РЕЗОРЦИНОЛ КОМПЛЕКСА СА ДИТЕТРАЗОЛИЈУМ СОЛИМА

VIDKA V. DIVAROVA[1], KIRILA T. STOJNOVA[1], PETYA V. RACHEVA[2], VANYA D. LEKOVA[1] и ATANAS N. DIMITROV[1]

[1]*Department of General and Inorganic Chemistry, Faculty of Chemistry, University of Plovdiv "Paisii Hilendarski", 24 Tsar Assen Street, 4000 Plovdiv, Bulgaria и* [2]*Department of Chemistry and Biochemistry, Faculty of Farmacology, Medical University Plovdiv, 15A Vasil Aprilov Boulevard, 4002 Plovdiv, Bulgaria*

Испитивано је формирање и течно–течна екстракција јон-асосованих комплекса који настају између анјонског Co(II)–4-(2-пиридилазо)резорцинола и три различита катјонска дитетразолијум-хлорида (плави тетразолијум-хлорид, BTC, неотетразолијум-хлорид, NTC и плави нитротетразолијум-хлорид, NBTC). Одређени су оптимални услови за формирање и екстракцију помоћу растварача јон-асосованих комплексних хелата. Нађено је да у Co(II)–PAR–DTC системима долази до реакције реактаната у 1:2:1 молском односу. Претпостављена је општа формула награђених комплексних врста. Екстракционе равнотеже су испитиване и квантитативно окарактерисане помоћу одговарајућих константи. Поред тога, израчунате су аналитичке константе за одговарајуће комплексне врсте.

(Примљено 14. маја, ревидирано 8. октобра, прихваћено 20. октобра 2014)

REFERENCES

1. M. Ince, G. Kaya, M. Yaman, *Environ. Chem. Lett.* **8** (2010) 283
2. V. Divarova, P. Racheva, V. Lekova, K. Gavazov, A. Dimitrov, *J. Chem. Technol. Metall.* **48** (2013) 623
3. A. Afkhami, M. Bahram, *Spectrochim. Acta, A* **61** (2005) 869
4. M. Gharehbaghi, F. Shemirani, F, Baghdadi, *Int. J. Anal. Chem.* **88** (2008) 513
5. L. S. G. Teixeiral, A. C. S. Costa, J. C. R. Assis, S. L. C. Ferreira, M. Korn, *Microchim. Acta* **137** (2001) 29
6. J. Ghasimi, N. Shahababi, H. R. Seraji, *Anal. Chem. Acta* **510** (2004) 121
7. A. Nassir, *National J. Chem.* **26** (2007) 263
8. F. I. El-Dossoki, F. A. El-Seify, *J. Chem. Eng. Data* **55** (2010) 3572
9. A. Tsuyoshi, H. Hoshino, T. Yotsuyanagi, *Chem. Lett.* **30** (2001) 302
10. R. E. Taljaard, J. E. V. Staden, *Anal. Chim. Acta* **366** (1998) 177
11. A. Hol, U. Divrikli, L. Elci, *Environ. Monit. Assess.* **184** (2012) 3469
12. V. M. Ivanov, N. I. Ershova, V. N. Figurovskaya, A. V. Ivanov, *J. Anal. Chem.* **56** (2001) 143
13. G. Ram, R. S. Chauhan, A. K. Goswami, D. N. Purohit, *Rev. Anal. Chem.* **22** (2003) 255
14. H. Ciftci, *Curr. Anal. Chem.* **6** (2010) 154
15. S. Tokalioglu, S. Kartal, *Bull. Korean Chem. Soc.* **27** (2006) 1293
16. V. Cucinotta, R. Caruso, A. Giuffrida, M. Messina, G. Maccarrone, A. Torrisi, *J. Chromatogr., A* **1179** (2008) 17

17. Z. T. Jiang, J. C. Yu, H. Y. Liu, *Anal. Sci.* **21** (2005) 851
18. C. C. Nascentes, M. A. Z Arruda, *Talanta* **61** (2003) 759
19. I. V. Vyshcherevich, I. E. Kalinichenko, *J. Water Chem. Technol.* **32** (2010) 33
20. H. Ciftci, A. Olcucu, A. Ozkaya, T. Ciftci, *Asian J. Chem.* **21** (2009) 2643
21. C. E. Säbel, J. L. Shepherd, S. Siemann, *Anal. Biochem.* **391** (2009) 74
22. B. F. Liu, L. B. Liu, J. K. Cheng, *J. Chromatogr., A* **848** (1999) 473
23. F. Karipcin, B. Dede, S. Ozkorucuklu, E. Kabalcinar, *Dyes Pigm.* **84** (2010) 14
24. H. R. Pouretedal, P. Sononi, M. H. Keshavarz, A. Semani, *Chemistry* **18** (2009) 22
25. S. N. Bhadani, M. Tewari, A. Agraval, C. Sekhar, *J. Indian Chem. Soc.* **75** (1998) 176
26. P. Berton, R. G. Wuilloud, *Anal. Methods* **3** (2011) 664
27. A. G. Gaikwad, H. Noguchi, M. Yoshio, *Anal. Lett.* **24** (1991) 1625
28. P. Racheva, K. Gavazov, V. Lekova, A. Dimitrov, *J. Mater.* **2013** (2013), http://dx.doi.org/10.1155/2013/897343
29. F. Karipcin, E. Kabalcinar, *Acta Chim. Slov.* **54** (2007) 242
30. M. Široki, L. Marić, Z. Štefanac, M. J. Herak, *Anal. Chim. Acta* **75** (1975) 101
31. J. Dolezal, L. Sommer, *Collect. Czech. Chem. Commun.* **59** (1994) 2209
32. T. Okutani, A. Sakuragawa, M. Murakami, *Anal. Sci.* **7** (1991) 109
33. L. Dospatliev, N. V. Georgieva, A. I. Pavlov, Z. Yaneva, *Trakia J. Sci.* **8** (2010) 16
34. K. B. Gavazov, A. N. Dimitrov, V. D. Lekova, *Russ. Chem. Rev.* **2** (2007) 169
35. K. B. Gavazov, K. T. Stojnova, T. S. Stefanova, G. K. Toncheva, V. D. Lekova, A. N. Dimitrov, *Chimija* **23** (2012) 278
36. K. T. Stojnova, K. B. Gavazov, V. D. Lekova, *Acta Chim. Slov.* **60** (2013) 390
37. K. T. Stojnova, K. B. Gavazov, G. K. Toncheva, V. D. Lekova, A. N. Dimitrov, *Cent. Eur. J. Chem.* **10** (2012) 1262
38. G. K. Toncheva, K. B. Gavazov, V. D. Lekova, K. T. Stojnova, A. N. Dimitrov, *Cent. Eur. J. Chem.* **9** (2011) 1143
39. K. Stojnova, K. Gavazov, *J. Mater. Sci. Eng., A* **2** (2012) 423
40. V. V. Divarova, K. B. Gavazov, V. D. Lekova, A. N. Dimitrov, *Chemija* **24** (2013) 81
41. A. I. Busev, V. M. Ivanov, *Zh. Anal. Khim.* **18** (1963) 208
42. M. I. Bulatov, I. P. Kalinkin, *Prakticheskoe rukovodstva po fotometricheskim metodam analiza*, Khimiya, Leningrad, Russia, 1986, p. 239 (in Russian)
43. E. Asmus, *Freseius' J. Anal. Chem.* **178** (1960) 104.

Journal of the Serbian Chemical Society
JSCS-info@shd.org.rs • www.shd.org.rs/JSCS
J. Serb. Chem. Soc. 80 (2) 187–196 (2015)
JSCS–4709
UDC 519.233.5:539.16:66.097.8:547.75
Original scientific paper

Application of genetic algorithm – multiple linear regressions to predict the activity of RSK inhibitors

ZHILA MOHAJERI AVVAL[1], ESLAM POURBASHEER[1]*, MOHAMMAD REZA GANJALI[2] and PARVIZ NOROUZI[2,3]

[1]*Department of Chemistry, Payame Noor University, Tehran, Iran,* [2]*Center of Excellence in Electrochemistry, Faculty of Chemistry, University of Tehran, Tehran, Iran and* [3]*Biosensor Research Center, Endocrinology and Metabolism Molecular-Cellular Sciences Institute, Tehran University of Medical Sciences, Tehran, Iran*

(Received 25 May, accepted 19 June 2014)

Abstract: This paper considers the development of a linear quantitative structure–activity relationship (QSAR) model for predicting the ribosomal S6 kinase (RSK) inhibition activity of some new compounds. A dataset consisting of 59 pyrazino[1,2-α]indole, diazepino[1,2-α]indole, and imidazole derivatives with known inhibitory activities was used. The multiple linear regressions (MLR) technique combined with stepwise (SW) and the genetic algorithm (GA) methods as variable selection tools was employed. For more checking of the stability, robustness and predictability of the proposed models, internal and external validation techniques were used. Comparison of the obtained results, indicate that the GA-MLR model is superior to the SW–MLR model and that it is applicable for designing novel RSK inhibitors.

Keywords: QSAR; genetic algorithms; multiple linear regression; RSK inhibitors.

INTRODUCTION

The RSK (90 kDa ribosomal S6 kinase) family comprises a group of highly related serine/threonine kinases that regulate diverse cellular processes, including cell growth, proliferation, survival and motility. This family consists of four human isoforms (RSK1-4), and single family member orthologues are also present in *Drosophila* and *Caenorhabditis elegans*.[1] RSK1-4 are a family of widely expressed Ser/Thr kinases characterized by two non-identical, functional kinase domains[2] and a carboxy-terminal docking site for extracellular signal-regulated kinases (ERKs).[3] Several sites both within and outside of the RSK kinase domain, including Ser380, Thr359, Ser363, and Thr573, are important for kinase activation.[4] RSK1-3 are activated *via* coordinated phosphorylation by mitogen-

* Corresponding author. E-mail: pourbasheer@ut.ac.ir
doi: 10.2298/JSC140523064A

activated protein kinases (MAPKs), autophosphorylation, and phosphoinositide-3-OH kinase (PI3K) in response to many growth factors, polypeptide hormones, and neurotransmitters.[4] RSK4 appears to demonstrate different pharmacology.

Metastasis, the spreading of cancer cells from a primary tumor to secondary sites throughout the body, is the primary cause of death for patients with cancer. New therapies that prevent invasion and metastasis in combination with current treatments could therefore significantly reduce cancer recurrence and morbidity. Metastasis is driven by altered signaling pathways that induce changes in cell–cell adhesion, the cytoskeleton, integrin function, protease expression, epithelial--to-mesenchymal transition and cell survival. The ribosomal S6 kinase (RSK) family of kinases is a group of extracellular signal-regulated kinase/mitogen-activated protein kinase (ERK/MAPK) effectors that can regulate these steps of metastasis by phosphorylating both nuclear and cytoplasmic targets.

However, the present understanding of the function of RSK in metastasis remains incomplete and is complicated by the fact that the four RSK isoforms perform non-redundant, sometimes opposing functions. Although some isoforms promote cell motility and invasion by altering transcription and integrin activity, others impair cell motility and invasion through effects on the actin cytoskeleton. The mechanism of RSK action depends on both the isoform and the cancer type. However, despite the variance in RSK-mediated outcomes, chemical inhibition of this group of kinases has proven effective in blocking invasion and metastasis of several solid tumors in preclinical models. RSKs are therefore a promising drug target for antimetastatic cancer treatments that could supplement and improve current therapeutic approaches.[5]

The experimental evaluation of the inhibitory activity of chemical structures is difficult, expensive and time-consuming, thus the development of a computational method for its prediction would be useful and of interest.[6–12] Among computational methods, the quantitative structure–activity relationship (QSAR) model has found diverse applications for predicting the properties/activities of a compound, including prediction of biological activity,[13,14] physical properties,[15,16] toxicity[17,18] and antiviral activity.[19,20] This model is a mathematical equation that can express the chemical properties or activities of compounds as a function of their various structural parameters (descriptors). The first step in building a QSAR model is the selection of a set of molecular descriptors that represent variation in the structural property of the molecules by a number. Thus, variable selection methods, as an inseparable part of the model development in QSAR studies, are used to select the best subset of descriptors. There are several variable selection methods, such as genetic algorithm (GA) and stepwise (SW). After selection of the most important descriptors, the model can be generated based on these selected descriptors using multiple linear regressions (MLR). The success of any QSAR model depends on the accuracy of the input data, selection

of appropriate descriptors and most importantly validation of the developed model.[21]The aim of this work was to develop a new QSAR model to predict the (RSK) inhibition activity of pyrazino[1,2-α]indole, diazepino[1,2-α]indole and imidazole derivatives.

MATERIAL AND METHODS

Data set

The data set consisting of 59 molecules of pyrazino[1,2-α]indole, diazepino[1,2-α]indole, and imidazole derivatives along with their experimental inhibitory activities were collected from the literature.[22,23] The chemical structures and their experimental values are presented in Table S-I of the Supplementary material to this paper. The half-maximal inhibitory concentration data (IC_{50} / μM) was converted to the logarithmic scale pIC_{50} (–log (IC_{50} / M)) and then utilized for the subsequent QSAR analyses as the dependent variable. The whole dataset was randomly segregated into a training and a test set consisting of 48 and 11 compounds, respectively. The training set was used to construct a regression model, and the test set was used to evaluate the predictive ability of the obtained model.

Descriptors calculation

The two-dimensional (2D) structures of the molecules were constructed using Hyperchem 7 and pre-optimization was performed using molecular mechanics force field (MM+) and the final optimization of the geometries was realized using a semi-empirical (AM1) procedure with a root mean square gradient of 0.01 kcal mol^{-1}. Dragon 2.1 software was employed to calculate 1497 molecular descriptors for all the studied chemical structures. In order to reduce redundant and non-useful information, constant or near-constant values and descriptors found to be highly correlated pair wise were removed in a pre-reduction step. Thereby, 398 molecular descriptors remained for the variable selection step.

Genetic algorithm (GA)

The main challenges for QSAR practitioners are to find an appropriate set of descriptors and a suitable function that can accurately illustrate the experimental data. Nowadays, the genetic algorithm (GA) method, developed by Holland *et al*.,[24] is considered superior to other variable selection methods. It is a powerful optimization method that was inspired by evolutionary principles, including survival of the fittest, reproduction, crossover, and mutation. In this study, GA-MLR was used to build the QSAR model. The fitness function utilized herein was the leave-one-out (LOO) cross-validated correlation coefficient (Q^2). The GA program was written in Matlab 6.5.[25]

K-*Means cluster analysis*

One of the main non-hierarchical clustering techniques is the *K*-means clustering, which is used in the division of a dataset into the training and test sets.[26] Ideally, this division is performed so as the points representing the training and test set are distributed within the whole descriptor space occupied by the entire data set.[27] In *K*-means cluster analysis (*K*-MCA), the clusters are started randomly and their means are calculated in the descriptor space. Molecules are reassigned to clusters the means of which are closer to the position of the molecules. This is followed by the selection of the test set molecules from each cluster since both test set and training set can represent all clusters and characteristics of the whole data set. In this study, the original data set was partitioned into four clusters based on *K*-means clustering. Then, about 20% of compounds of each cluster were chosen as members of the test set. The *K*-means clustering results are shown in Table S-II of the Supplementary material.

RESULTS AND DISCUSSION

The whole data set was randomly partitioned into the training set of 48 compounds, and the test set of 11 compounds based on rule: the range of the experimental inhibitory activity values of both the training set and test set should be covered from the lowest to the highest. The training and test sets are indicated in Table S-1 of the Supplementary material. After the splitting of the datasets, the stepwise method was performed to select the main descriptors correlated to the activity based on the training set compounds. The six descriptors obtained by the SW–MLR linear model are as follows:

$$\begin{aligned} pIC_{50} = &-6.820(\pm1.315) + 5.757(\pm0.540)BELp5 + 32.252(\pm6.716)HATS6p + \\ &+ 1.362(\pm0.304)GATS8e - 5.443(\pm1.246)E3m + 0.154(\pm0.056)nHDon - \\ &- 0.305\ (\pm0.119)RDF130p \end{aligned} \quad (1)$$

whereby N_{train} = 48, R^2_{train} = 0.824, R^2_{test} = 0.159, R^2_{adj} =0.798, F_{train} = 31.971, F_{test} = 0.369, $RMSE_{train}$ = 0.395, $RMSE_{test}$ = 1.079, Q^2_{LOO} = 0.767, Q^2_{LGO} = = 0.745, Q^2_{BOOT} = 0.751, where N is the number of compounds, R^2 is the squared correlation coefficient, R^2_{adj} is adjusted R^2, *RMSE* is the root mean square error, F is the Fisher F statistic and Q^2_{LOO}, Q^2_{LGO} and Q^2_{BOOT} are the squared cross-validation coefficients for leave one out, leave group out and bootstrapping, respectively.

The obtained statistical parameters indicate that the SW-MLR procedure produced good results for the training set, but it did not produce good results for the test set. Therefore, a genetic algorithm was used to select the best set of descriptors, and various models with various numbers of descriptors were obtained. To select the optimum number of descriptors with GA, the influence of the number of the descriptors was investigated from one to ten descriptors. Finally, a GA–MLR model with six selected descriptors was obtained. This model is described by the following equation:

$$\begin{aligned} pIC_{50} = &+2.713(\pm1.678) + 7.017(\pm1.080)MATS6e - 3.085(\pm0.666)MATS8e + \\ &0.209(\pm0.071)RDF140u - 0.142(\pm0.057)RDF120m - \\ &1.016(\pm0.117)Mor04m + 31.823(\pm10.919)G3e \end{aligned} \quad (2)$$

whereby N_{train} = 48, R^2_{train} = 0.824, R^2_{test} = 0.864, R^2_{adj} = 0.798, F_{train} = 31.90, F_{test} = 3.143, $RMSE_{train}$ = 0.395, $RMSE_{test}$ = 0.483, Q^2_{LOO} = 0.761, Q^2_{LGO} = = 0.749, Q^2_{BOOT} = 0.740.

The GA-MLR model was then used to predict the test set data and the prediction results are given in Table S-I of the Supplementary material. The predicted values of pIC_{50} for the compounds in the training and test sets using the GA-MLR model are plotted against their experimental values in Fig. 1. As can be seen from Table S-I and Fig. 1, the prediction values are in good agreement with the experimental values.

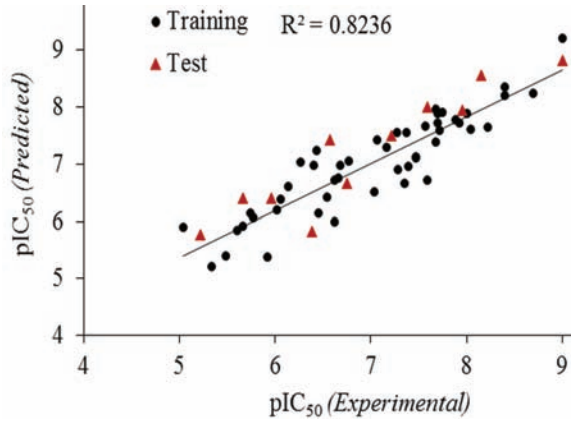

Fig. 1. The pIC_{50} values predicted by GA–MLR modeling *vs*. the experimental pIC_{50} values.

The six selected descriptors using the GA–MLR method were MATS6e, MATS8e, RDF140u, RDF120m, Mor04m and G3e. The multi-colinearity between the selected descriptors was checked by calculating their variation inflation factors (*VIF*), which can be calculated as follows:

$$VIF = \frac{1}{1-r^2} \tag{3}$$

where r^2 is the multiple correlation coefficient of the effect of one descriptor regressed on the remaining molecular descriptors. If *VIF* equals 1, then no inter--correlation exists for each variable; if *VIF* falls into the range of 1–5, the related model is acceptable; and if *VIF* is larger than 10, the related model is unstable and a recheck is necessary.[28] As can be seen from Table I, most variables had *VIF* values of less than 5, indicating that the obtained GA–MLR model has obvious statistical significance.

The correlation matrix for the six selected descriptors is given in Table II, from which, it could be seen that the correlation coefficient value of each of the two descriptors was less than 0.56, which meant that the selected descriptors were independent in the analysis.

In general, the assessment of stability and predictive ability of a model is an important step in the expression of the quality of a model. The ability of the GA--MLR model was verified by the leave-one-out and leave-group-out cross-validated correlation coefficients (Q^2_{LOO} and Q^2_{LGO}). The internal predictive ability of the model was also verified using the bootstrap Q^2_{BOOT} procedure, as is strongly recommended for QSAR modeling. The robustness of the proposed model and its predictive ability was guaranteed by the high value of Q^2_{BOOT} based on the bootstrapping being repeated 5000 times. The cross-validation parameters for the MLR model are given in Eq. (2). The cross-validation results indicate that the obtained regression model has good internal and external predictive power.

TABLE I. Details of the constructed GA-MLR model; *SE* – standard error, *MF* – mean effect, *VIF* – variation inflation factor

Descriptor	Coefficient	*SE*	*MF*[a]	*VIF*[b]	Chemical meaning
Constant	2.713	1.678	0	0	–
MATS6e	7.017	1.080	-0.18954	1.09685	Moran autocorrelation - lag 6 / weighted by atomic Sanderson electronegativities
MATS8e	–3.085	0.666	-0.21865	1.45634	Moran autocorrelation - lag 8 / weighted by atomic Sanderson electronegativities
RDF140u	0.209	0.071	0.02197	1.42781	Radial Distribution Function - 14.0 / unweighted
RDF120m	–0.142	0.057	-0.02503	1.47806	Radial Distribution Function - 12.0 / weighted by atomic masses
Mor04m	–1.016	0.117	0.24938	1.50138	3D-MoRSE - signal 04 / weighted by atomic masses
G3e	31.823	10.919	1.16187	1.65773	3rd component symmetry directional WHIM index / weighted by atomic Sanderson electronegativities

[a]Mean effect; [b]variation inflation factors

TABLE II. Correlation coefficient matrix of the selected descriptors

	MATS6e	MATS8e	RDF140u	RDF120m	Mor04m	G3e
MATS6e	1	0	0	0	0	0
MATS8e	–0.12	1	0	0	0	0
RDF140u	0.05	–0.04	1	0	0	0
RDF120m	0.12	0.01	0.55	1	0	0
Mor04m	0.05	0.45	0.10	–0.12	1	0
G3e	–0.20	0.54	–0.07	–0.15	0.47	1

A Williams plot is used to visualize the applicability domain (AD) of QSAR models. It is a plot of the standardized residuals *vs*. the leverage values (h).[29] From the Williams plot (Fig. 2), it is obvious that there are three compounds (Nos. 38 and 55 in the training set and No. 50 in the test set) that have a leverage value higher than the warning h^* value of 0.44 and thus, they could be considered as structural outliers. Fortunately, in these cases, the data predicted by the model are good for the three compounds and thus, they are "good leverage" chemicals. From Fig. 2, it is obvious that there are no outlier compounds with standard residuals $>3\delta$ for both the training and the test sets.

The *Y*-randomization test is performed to assess the robustness of a QSAR model by building several random models *via* shuffling the dependent variable vector (pIC_{50}), while keeping the independent variables as it is. The resultant random models are expected to have low R^2 and Q^2_{LOO} values.[30] The results of *Y*-randomization tests are shown in Table III.

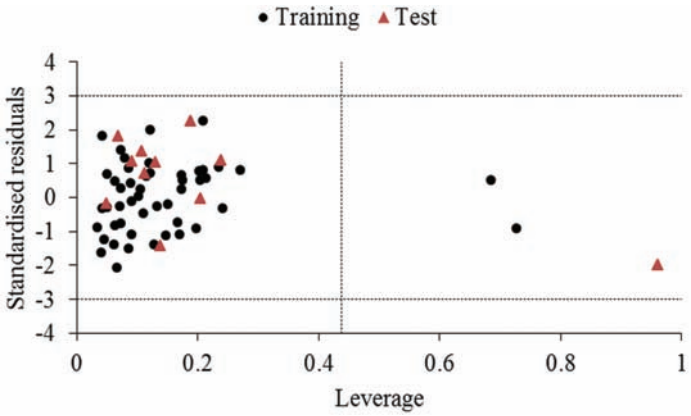

Fig. 2. The William plot of the GA–MLR model.

TABLE III. R^2_{train} and Q^2_{LOO} values after several *Y*-randomization tests

No.	Q^2	R^2
1	0.060	0.082
2	0.214	0.078
3	0.093	0.037
4	0.027	0.109
5	0.007	0.151
6	0.106	0.067
7	0.015	0.085
8	0.102	0.030
9	0.008	0.160
10	0.031	0.090

Interpretation of descriptors

Interpretation of descriptors contained in the best model (GA-MLR) provides useful chemical insights into the mechanism of the inhibitory activity. Thus, an acceptable interpretation of the QSAR results is provided below. The molecular descriptors selected by the genetic algorithm are given in Table I.

The first and second descriptors are MATS6e (Moran autocorrelation - lag 6 / weighted by atomic Sanderson electronegativities) and MATS8e (Moran autocorrelation - lag 8 / weighted by atomic Sanderson electronegativities) that belong to the 2D autocorrelations descriptors. In this descriptor, the Geary coefficient is a distance-type function, this function is any physicochemical property calculated for each atom of the molecule, such as atomic mass, polarizability, *etc*. Thus, the molecule atoms represent a set of discrete points in space and the atomic property is the function evaluated at these points.[31] In these descriptors (MATS6e and MATS8e), the weighting scheme is the atomic Sanderson electronegativities, which show that the electronegativities of the molecule atoms play the main role in these descriptors. MATS6e has a positive sign in equation, which indicates

that the pIC_{50} value is directly related to this descriptor. By increasing the atomic Sanderson electronegativities for each molecule atoms, the value of this descriptor increased, causing an increase in its pIC_{50} value. MATS8e displays a negative sign, which shows that the pIC_{50} value is inversely related to this descriptor. Hence, it was concluded that increasing the value of this descriptor causes a reduction in the pIC_{50} value.

The third and fourth descriptors appearing in the model are RDF140u (Radial Distribution Function - 14.0 / unweighted) and RDF120m (Radial Distribution Function - 12.0 / weighted by atomic masses). These descriptors belong to the radial distribution function (RDF) descriptors. RDF descriptors meet all the requirements for 3D structure descriptors; they are independent of the number of atoms (*i.e.*, the size of a molecule), and are unique regarding the three-dimensional arrangement of the atoms and are invariant against the translation and rotation of the molecules. Additionally, the RDF descriptors can be restricted to specific atom types or distance ranges to represent specific information in a certain three-dimensional structure space (*e.g.*, to describe the steric hindrance or the structure/activity properties of a molecule). Formally, the radial distribution function of an ensemble of *n* atoms can be interpreted as the probability distribution of finding an atom in a spherical volume of radius *R*.[32] RDF140u has a positive sign, and the positive sign indicates that the pIC_{50} value was directly related to this descriptor. The negative sign of RDF120m suggests that the pIC_{50} value was inversely related to this descriptor. Therefore, increasing the atomic masses of molecules leads to decrease in the pIC_{50} value.

The next descriptor is Mor04m (3D-MoRSE - signal 04 / weighted by atomic masses) which is one of the 3D-MoRSE descriptors. 3D-MoRSE descriptors (3D Molecule Representation of Structures based on Electron diffraction) are derived from Infrared spectra simulation using a generalized scattering function.[33] Mor04m had a negative sign in the equation, which indicates that the pIC_{50} value was inversely related to this descriptor.

The last descriptor is G3e (3rd component symmetry directional WHIM index / weighted by atomic Sanderson electronegativities) that belongs to the WHIM descriptors. Weighted holistic invariant molecular (WHIM) descriptors are geometrical descriptors based on the statistical indices calculated on the projections of atoms along the principal axes. The algorithm consists of performing a principal components analysis on the centered Cartesian coordinates of a molecule by using a weighted covariance matrix obtained from different weighting schemes for the atoms. Directional WHIM symmetry descriptors are related to the number of central symmetric atoms (along the m^{th} component), the number of unsymmetrical atoms and the total number of molecule atoms.[34] As it is clear from Table I, G3e has a positive sign, illustrating a greater coefficient

value than that of the other descriptors. This descriptor had a significant effect on the pIC_{50} value of the studied molecules.

From the above discussion, it could be concluded that the atomic Sanderson electronegativities, radial distribution function and atomic masses play an important role in the RSK inhibitory activities of the studied compounds.

CONCLUSIONS

In this work, a linear QSAR model was presented for prediction of RSK inhibitors of pyrazino[1,2-α]indole, diazepino[1,2-α]indole and imidazole derivatives. The best subset of calculated descriptors was selected by use of stepwise and genetic algorithm methods. Validation of the model was performed using separation of the data into two independent sets, *Y*-randomization, cross-validation by LOO, LGO and bootstrap. The results indicated that the constructed GA-MLR model is a valid model with high statistical quality and low prediction errors. The proposed model could identify and provide an insight into some suggestions for the further design of new RSK inhibitors.

SUPPLEMENTARY MATERIAL

Chemical structures, the observed pIC_{50} values and *K*-means clustering of the compounds are available electronically from http://www.shd.org.rs/JSCS/, or from the corresponding author on request.

И З В О Д

ПРИМЕНА ГЕНЕТСКОГ АЛГОРИТМА – ВИШЕСТРУКЕ ЛИНЕАРНЕ РЕГРЕСИЈЕ ЗА ПРЕДВИЂАЊЕ АКТИВНОСТИ ИНХИБИТОРА RSK

ZHILA MOHAJERI AVVAL[1], ESLAM POURBASHIR[1],MOHAMMAD REZA GANJALI[2] и PARVIZ NOROUZI[2,3]

[1]Department of Chemistry, Payame Noor University, Tehran, Iran, [2]Center of Excellence in Electrochemistry, Faculty of Chemistry, University of Tehran, Tehran, Iran and [3]Biosensor Research Center, Endocrinology and Metabolism Molecular-Cellular Sciences Institute, Tehran University of Medical Sciences, Tehran, Iran

Развијен је линеарни QSAR модел за предвиђање RSK инхибиторне активности неких нових једињења. База података се састојала од 59 деривата пиразино[1,2-α]индола, диазепино[1,2-α]индола и имидазола са познатим инхибиторним активностима. Примењена је техника вишеструких линеарних регресија (MLR) комбинована са SW и GA алгоритмима. Оригинални сет података је подељен на тренажни (80 % података) и тест сет (20 % података). Добијени резултати указују на то да је GA-MLR модел бољи од SW-MLR модела, и да је употребљив за дизајнирање нових инхибитора RSK.

(Примљено 25. маја, прихваћено 19. јуна 2014)

REFERENCES

1. R. Yves, Z. Xiaocui, P. R. Philippe, *Biochem. J.* **441** (2012) 553
2. T. L. Fisher, J. Blenis, *Mol. Cell. Biol.* **16** (1996) 1212
3. J. A. Smith, C. E. Poteet-Smith, K. Malarkey, T. W. Sturgill, *J. Biol. Chem.* **274** (1999) 289
4. K. N. Dalby, N. Morrice, F. B. Caudwell, J. Avruch, P. Cohen, *J. Biol. Chem.* **273** (1998) 1496
5. F. J. Sulzmaier, J. W. Ramos, *Cancer. Res.* **73** (2013) 6099

6. S. Vahdani, Z. Bayat, *Der. Chem. Sin.* **2** (2011) 235
7. M. Jalali-Heravi, M. Asadollahi-Baboli, *QSAR Comb. Sci.* **27** (2008) 750
8. A. Habibi-Yangjeh, E. Pourbasheer, M. Danandeh-Jenagharad, *Bull. Korean Chem. Soc.* **29** (2008) 833
9. A. Habibi-Yangjeh, E. Pourbasheer, M. Danandeh-Jenagharad, *Monatsh. Chem.* **140** (2009) 15
10. E. Pourbasheer, R. Aalizadeh, M. R. Ganjali, P. Norouzi, *Struct. Chem.* **25** (2014) 355
11. E. Pourbasheer, S. Riahi, M. R. Ganjali, P. Norouzi, *Mol. Divers.* **15** (2011) 645
12. S. Riahi, E. Pourbasheer, M. R. Ganjali, P. Norouzi, *Chem. Biol. Drug. Des.* **73** (2009) 558
13. O. Deeb, B. Hemmateenejad, *Chem. Biol. Drug. Des.* **70** (2007) 19
14. G. Ramírez-Galicia, R. Garduño-Juárez, B. Hemmateenejad, O. Deeb, M. Deciga-Campos, J. C. Moctezuma-Eugenio, *Chem. Biol. Drug. Des.* **70** (2007) 53
15. R. P. Verma, A. Kurup, C. Hansch, *Bioorg. Med. Chem.* **13** (2005) 237
16. M. H. Knaggs, C. McGuigan, S. A. Harris, P. Heshmati, D. Cahard, I. H. Gilbert, J. Balzarini, *Bioorg. Med. Chem. Lett.* **10** (2000) 2075
17. P. V. Khadikar, A. Phadnis, A. Shrivastava, *Bioorg. Med. Chem.* **10** (2002) 1181
18. V. Agrawal, P. Khadikar, *Bioorg. Med. Chem.* **9** (2001) 3035
19. W. G. Zhao, J. G. Wang, Z. M. Li, Z. Yang, *Bioorg. Med. Chem. Lett.* **16** (2006) 6107
20. V. Pandey, Z. Tusi, M. Tandon, M. Joshi, S. Bajpai, *Indian J. Chem., B* **42** (2003) 2583
21. E. Ibezim, P. Duchowicz, N. Ibezim, L. Mullen, I. Onyishi, S. Brown, E. Castro, *Afr. J. Basic Appl. Sci.* **1** (2009) 76
22. S. J. Boyer, J. Burke, X. Guo, T. M. Kirrane, R. J. Snow, Y. Zhang, C. Sarko, L. Soleymanzadeh, A. Swinamer, J. Westbrook, *Bioorg. Med. Chem.* **22** (2012) 733
23. T. M. Kirrane, S. J. Boyer, J. Burke, X. Guo, R. J. Snow, L. Soleymanzadeh, A. Swinamer, Y. Zhang, J. B. Madwed, M. Kashem, *Bioorg. Med. Chem. Lett.* **22** (2012) 738
24. J. H. Holland, *Adaptation in Natural and Artificial Systems*, University of Michigan Press, Ann Arbor, 1975
25. W. Zhu, G. Chen, L. Hu, X. Luo, C. Gui, C. Luo, C. M. Puah, K. Chen, H. Jiang, *Bioorg. Med. Chem.* **13** (2005) 313
26. E. Pourbasheer, A. Beheshti, H. Khajehsharifi, M. R. Ganjali, P. Norouzi, *Med. Chem. Res.* **22** (2013) 4047
27. Z. Cheng, Y. Zhang, W. Fu, *Med. Chem. Res.* **20** (2011) 1235
28. E. Pourbasheer, R. Aalizadeh, M. R. Ganjali, P. Norouzi, *Med. Chem. Res.* **23** (2014) 57
29. J. E. Riviere, J. D. Brooks, *Toxicol. Sci.* **119** (2011) 224
30. E. Pourbasheer, R. Aalizadeh, M. R. Ganjali, P. Norouzi, J. Shadmanesh, C. Methenitis, *Med. Chem. Res.* **23** (2014) 2264
31. E. Pourbasheer, R. Aalizadeh, M. R. Ganjali, P. Norouzi, A. Banaei, *Med. Chem. Res.* **23** (2014) 3082
32. T. Puzyn, J. Leszczynski, M. T. Cronin, *Recent advances in QSAR studies: methods and applications*, Springer Science & Business Media, Dordrecht, 2010
33. M. Nekoei, M. Mohammadhosseini, A. A. Gharahbagh, *Anal. Bioanal. Electrochem.* **1** (2009) 159
34. E. Pourbasheer, S. Riahi, M. R. Ganjali, P. Norouzi, *J. Enzyme Inhib. Med. Chem.* **25** (2010) 844.

Journal of the Serbian Chemical Society
JSCS@tmf.bg.ac.rs • www.shd.org.rs/JSCS
J. Serb. Chem. Soc. 80 (2) S33–S40 (2015) *Supplementary material*

SUPPLEMENTARY MATERIAL TO

Application of genetic algorithm – multiple linear regressions to predict the activity of RSK inhibitors

ZHILA MOHAJERI AVVAL[1], ESLAM POURBASHEER[1]*, MOHAMMAD REZA GANJALI[2] and PARVIZ NOROUZI[2,3]

[1]Department of Chemistry, Payame Noor University, Tehran, Iran, [2]Center of Excellence in Electrochemistry, Faculty of Chemistry, University of Tehran, Tehran, Iran and [3]Biosensor Research Center, Endocrinology and Metabolism Molecular-Cellular Sciences Institute, Tehran University of Medical Sciences, Tehran, Iran

J. Serb. Chem. Soc. 80 (2) (2015) 187–196

TABLE S-I. Chemical structures and the observed pIC_{50} values and those predicted by the GA–MLR method

No.	General structure	Substituent	Experimental	Predicted
1	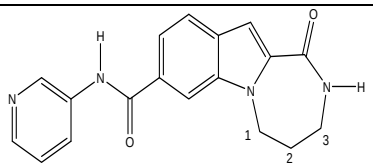	–	6.62	6.00
2		1-Me	7.39	6.96
3		2-Me	5.92	5.37
4		2-CH_2NH_2	5.74	6.15
5		1,2-*cis*-DiMe	6.62	6.72
6[a]		1,2-*trans*-DiMe	5.96	6.39
7		2,2-DiMe	5.34	5.21
8		2,2-DiF	5.77	6.07
9[a]		2-spiro-c-Pr	6.39	5.83
10		2-spiro-c-Bu	5.48	5.40
11		3-Me	5.60	5.85
12	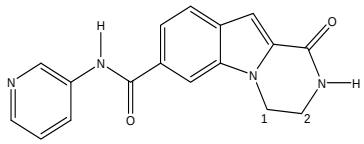	–	6.14	6.61
13		1-Me	6.77	7.06
14		1,1-DiMe	6.68	6.98
15		1,2-*cis*-DiMe	7.35	6.67
16		1,2-*trans*-DiMe	6.06	6.39
17		2-Me	6.46	6.14
18		2-CH_2NH_2	6.01	6.21

* Corresponding author. E-mail: pourbasheer@ut.ac.ir

TABLE S-I. Continued

No.	General structure	Substituent	Experimental	Predicted
19	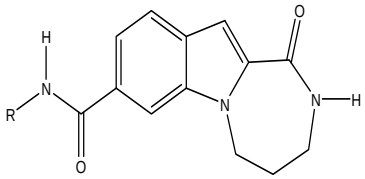	H	5.04	5.90
20		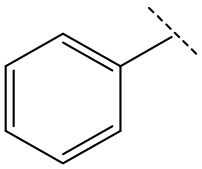	6.54	6.42
21[a]		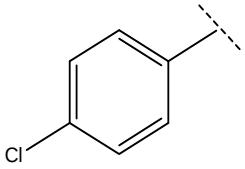	6.74	6.67
22[a]		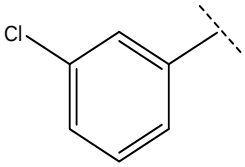	6.57	7.43
23[a]		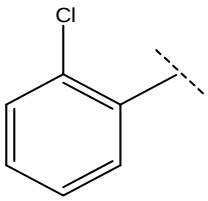	5.22	5.77
24		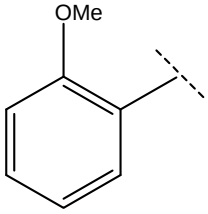	6.40	6.97
25		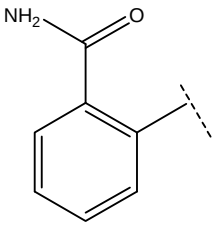	7.68	7.97
26		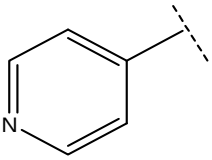	7.47	7.12

TABLE S-I. Continued

No.	General structure	Substituent	Experimental	Predicted
27	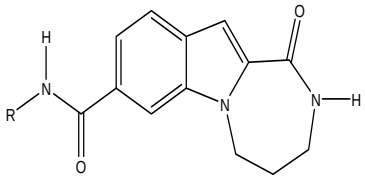	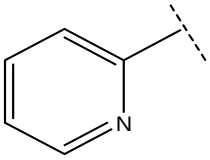	6.66	6.75
28		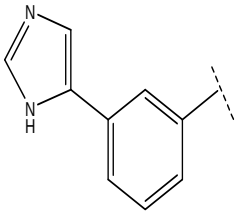	7.28	6.91
29[a]		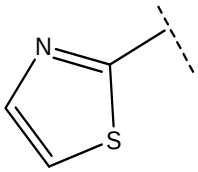	5.66	6.41
30		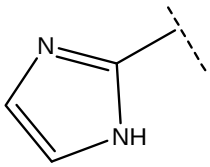	7.59	6.72
31		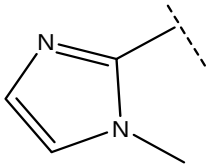	5.66	5.91
32[a]		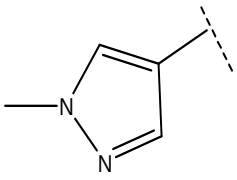	7.96	7.95
33		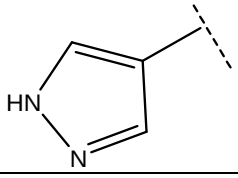	7.37	7.56

TABLE S-I. Continued

No.	General structure	Substituent	Experimental	Predicted
34	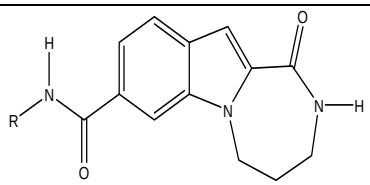	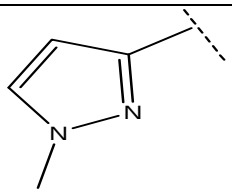	6.27	7.03
35		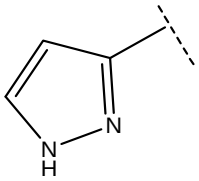	7.03	6.51
36		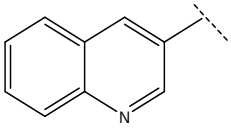	7.47	7.12
37		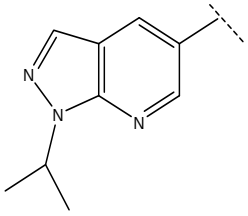	7.28	7.56
38		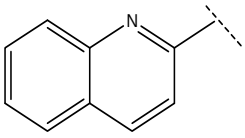	7.17	7.29
39		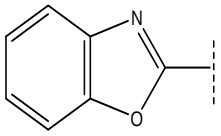	6.44	7.23
40		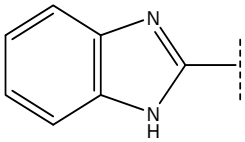	8.40	8.21
41		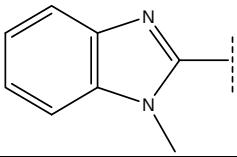	8.05	7.60

TABLE S-I. Continued

No.	General structure	Substituent	Experimental	Predicted
42		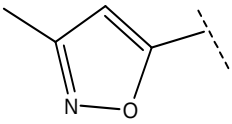	7.72	7.59
43		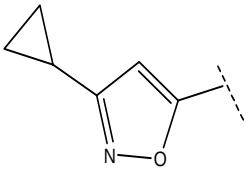	7.74	7.91
44[a]		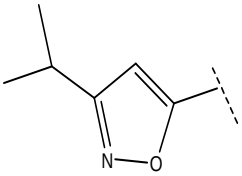	7.59	8.00
45		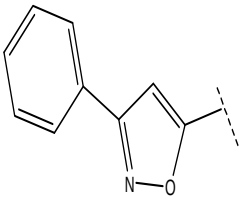	7.07	7.42
46		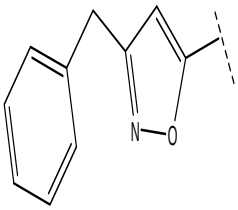	7.89	7.77
47[a]		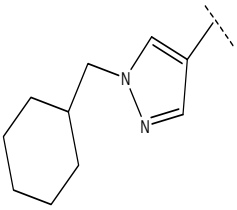	8.15	8.56

TABLE S-I. Continued

No.	General structure	Substituent	Experimental	Predicted
48		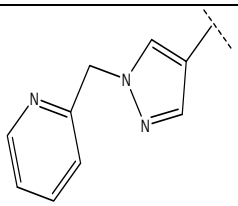	8.00	7.90
49		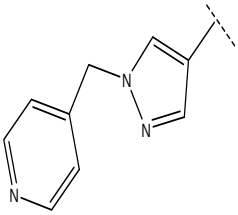	8.70	8.25
50[a]		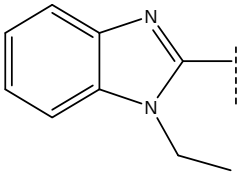	9.00	8.83
51		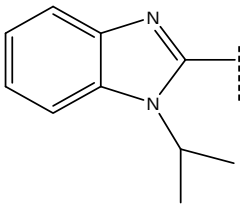	7.70	7.90
52[a]		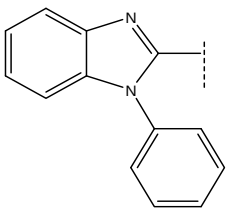	7.21	7.50
53		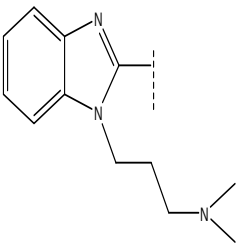	7.68	7.39

TABLE S-I. Continued

No.	General structure	Substituent	Experimental	Predicted
54		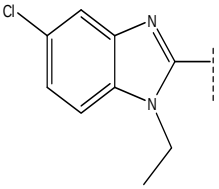	8.22	7.64
55		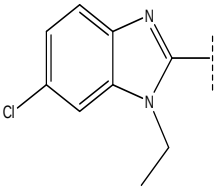	7.92	7.72
56		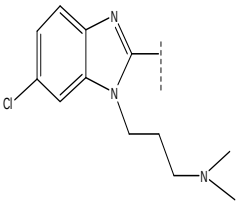	7.70	7.71
57		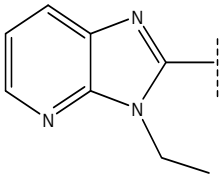	8.40	8.35
58	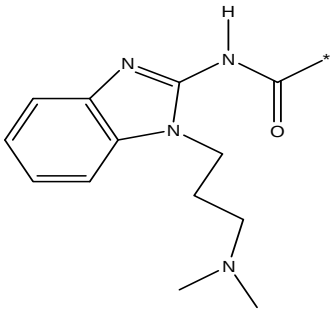	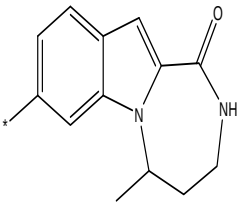	9.00	9.22
59		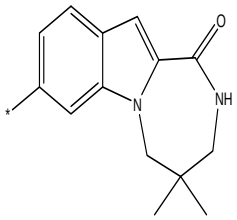	7.57	7.66

[a]Test set

TABLE S-II. *K*-means clustering of the compounds

Cluster	No. of compounds	Serial number of compounds in different clusters									
1	1					58					
2	38	5	8	9[a]	12	13	14	15	17	18	20
		21[a]	24	25	26	27	28	29[a]	30	31	33
		34	35	40	41	42	43	44[a]	45	46	47[a]
		48	49	52[a]	53	56	57	58	59		
						62					
3	18	1	2	3	4	6[a]	7	10	11	16	19
		22[a]	23[a]	32[a]	36	37	39	51	54		
4	2	38	50[a]								

[a]Test set

Journal of the Serbian Chemical Society
JSCS-info@shd.org.rs • www.shd.org.rs/JSCS
J. Serb. Chem. Soc. 80 (2) 197–207 (2015)
JSCS–4710
UDC 546.73–72+544.654.2:621.397.3+621385.833:537.621
Original scientific paper

Correlation between morphology and magnetic properties of electrochemically produced cobalt powder particles

VESNA M. MAKSIMOVIĆ[1]*, NEBOJŠA D. NIKOLIĆ[2#], VLADAN B. KUSIGERSKI[1] and JOVAN L. BLANUŠA[1]

[1]*Institute of Nuclear Sciences, "Vinča", University of Belgrade, P. O. Box 522, 11001 Belgrade, Serbia and* [2]*ICTM – Institute of Electrochemistry, University of Belgrade, Njegoševa 12, P. O. Box 473, 11001 Belgrade, Serbia*

(Received 20 August, revised 8 October 2014, accepted 24 October 2014)

Abstract: Cobalt 3D powder particles were successfully prepared by galvanostatic electrodeposition. The electrodeposited cobalt powders were characterized by X-ray diffraction (XRD) analysis, scanning electron microscopy (SEM), energy dispersive spectroscopy (EDS) and SQUID magnetometry. It was shown that the morphology, structure and magnetic properties of cobalt particles were closely associated and could be easily controlled by adjusting the electrodeposition process parameters. The morphology of cobalt powder particles was strongly affected by the hydrogen evolution reaction as a parallel reaction to cobalt electrodeposition. Depending on the applied current density, two types of powder particles were formed: dendrites at lower and spongy-like particles at higher current densities. Morphologies and structures of powder particles were correlated with their magnetic properties, and compared with those of the bulk cobalt. In comparison with the properties of bulk cobalt, the obtained 3D structures exhibited a decreased saturation magnetization (M_S), but an enhanced coercivity (H_C), which was explained by their peculiar morphology.

Keywords: electrodeposition; cobalt; powder; scanning electron microscope; X-ray diffraction analysis; magnetic properties.

INTRODUCTION

Due to its specific physical properties, ferromagnetic cobalt has received attention in both basic scientific research and technological applications, such as, for example, in high-density information storage, magnetic sensors, *etc*.[1] The fact that the crystal structure and magnetic properties of cobalt are considerably susceptible to particle size and morphology led to development of numerous syn-

* Corresponding author. E-mail: vesnam@vinca.rs
# Serbian Chemical Society member.
doi: 10.2298/JSC200814104M

thetic methods aimed at obtaining specific particle sizes/shapes. These methods included thermal decomposition of cobalt carbonyl and organometallic precursors, template-mediated synthesis, solvothermal and electrodeposition methods. Various morphological forms, such as wires, rods, disk, ring and tree-like cobalt, were successfully synthesized by some of these methods.[2–7]

The crystal structure of cobalt in its bulk form comprises two allotropes, *i.e.*, hexagonal close packed (hcp) and face centred cubic (fcc). The transition from the hcp to the fcc phase can be temperature induced so that the hcp structure is stable at room temperature, while the fcc phase becomes stable at temperatures above approximately 450 °C.[8] It was shown that with reduction in the grain size, the fcc-phase becomes the more stable phase at ambient conditions,[9] although the hcp structure can also be stabilized for nano-sized cobalt under special synthesis conditions.[10,11] In addition, in the nanometre size range, a new metastable phase can also appear, called ε-Co, with properties between the hcp and fcc phases.[12]

From the viewpoint of magnetism, bulk cobalt is a well known ferromagnetic material with the high Curie temperature close to $T_C \approx 1390$ °C.[13] However, hcp-Co is magnetically much harder than fcc-Co, meaning that the coercivity field H_C^{hcp} can be up to an order of magnitude higher than H_C^{fcc}, while the saturation magnetization values M_S of both phases are virtually the same.[13] In practice, the majority of bulk cobalt samples consist of mixed hexagonal and cubic phases[14] so that typical H_C values amount few tens of Oe* while typical M_S values are around 168 emu g^{-1}.

Electrodeposition is very valuable method to obtain a metal in the desired form suitable for applications in the above-mentioned technologies. Morphology, as the most important property of electrodeposited metal, mainly depends on the electrodeposition conditions, such as regime of electrolysis, composition of the solution, type of working electrode and temperature, and the nature of the metal.[15,16] Cobalt belongs to the group of inert metals, together with Fe, Ni, Mn, Cr and Pt.[17] The characteristics of these metals are high melting points, low exchange current densities and low overpotentials for hydrogen discharge. Due to these characteristics, electrodeposition of cobalt occurs together with the hydrogen evolution reaction, enabling the formation of cobalt in powder form over a wide range of potentials and current densities.

For this reason, in the present study, this method was used to produce cobalt 3D powder particles of different surface morphology. The powder particles obtained in the galvanostatic regime of electrolysis were analyzed with respect to their morphology, structure and magnetic properties.

* 1 Oe$\times 10^3/4\pi$ = 1 A/m; 1 emu/g = 1 A m^2/kg

EXPERIMENTAL

Cobalt powders were electrodeposited from the electrolyte containing 0.10 M $CoSO_4$ + + 0.70 M NH_4OH + 1.0 M $(NH_4)_2SO_4$ at a current density of 500 mA cm^{-2} and a current density which corresponded to the limiting diffusion current density of 770 mA cm^{-2}. All chemical reagents in this work were of analytical grade purity. Electrolytes were made from chemicals and pure water (EASY pure UV, 18.3 MΩ, Barnstead). The working electrode was glassy carbon, while the counter electrode was pure platinum.

Cobalt powder samples were electrodeposited at the room temperature in a cylindrical glass cell with a cone-shaped bottom in order to collect the powder particles. The total volume of the cell was 1 dm^3. During the deposition process, the powder was not removed from the electrode surface, but was left to self-detach. After deposition, the powders were washed with EASY pure UV water and ethanol, and left to dry in the air at room temperature.

The morphology of the electrodeposited powders was examined using scanning electron microscopes (SEMs) Philips XL30 and Tescan VEGA TS 5130MM, equipped with an energy-dispersive X-ray spectroscopy (EDS) Oxford Instruments INCA. X-Ray powder diffraction (XRD) analysis of the cobalt powders was realized using a PHILIPS PW 1050 diffractometer. Magnetic measurements were performed using a Quantum Design MPMS SQUID magnetometer at temperatures of 5 K and 300 K.

RESULTS AND DISCUSSION

Morphology and structure analysis

Due to parallelism between reactions of cobalt electrodeposition and hydrogen evolution,[18] the hydrogen generated during the electrodeposition process strongly affected the morphology of the powder particles. The quantity of hydrogen evolved parallel with the process of metal deposition was quantified by the determination of the current efficiency for hydrogen evolution using a well-established experimental procedure.[19] The polarization characteristics of a electrolyte containing 0.1 M $CoSO_4$ +1 M $(NH_4)_2SO_4$ + 0.7 M NH_4OH were previously analyzed, and it was concluded that a current density of 770 mA cm^{-2} corresponded to the limiting diffusion current density for Co electrodeposition ($j_{L(Co)}$ = 770 mA cm^{-2}).[20] The values of the current efficiencies for the Co electrodeposition of 18 and 26 % were extracted from the polarization curve obtained with IR drop correction at 770 and 500 mA cm^{-2}, respectively. Hence, the current efficiencies for hydrogen evolution reaction at these current densities were 82 ($j_{L(Co)}$ = 770 mA cm^{-2}) and 74 % (j = 500 mA cm^{-2}). Typical powder particles of cobalt obtained at a current density of 500 and at a current density corresponding to the limiting diffusion current density for Co electrodeposition of 770 mA cm^{-2} are shown in Figs. 1 and 2, and denoted Co1 and Co2, respectively. The observed powder particles were either dendritic or spongy-like shapes. A mixture of dendritic and spongy-like particles was formed at a current density of 500 mA cm^{-2}, while only the spongy-like particles were formed at the limiting diffusion current density of 770 mA cm^{-2}.

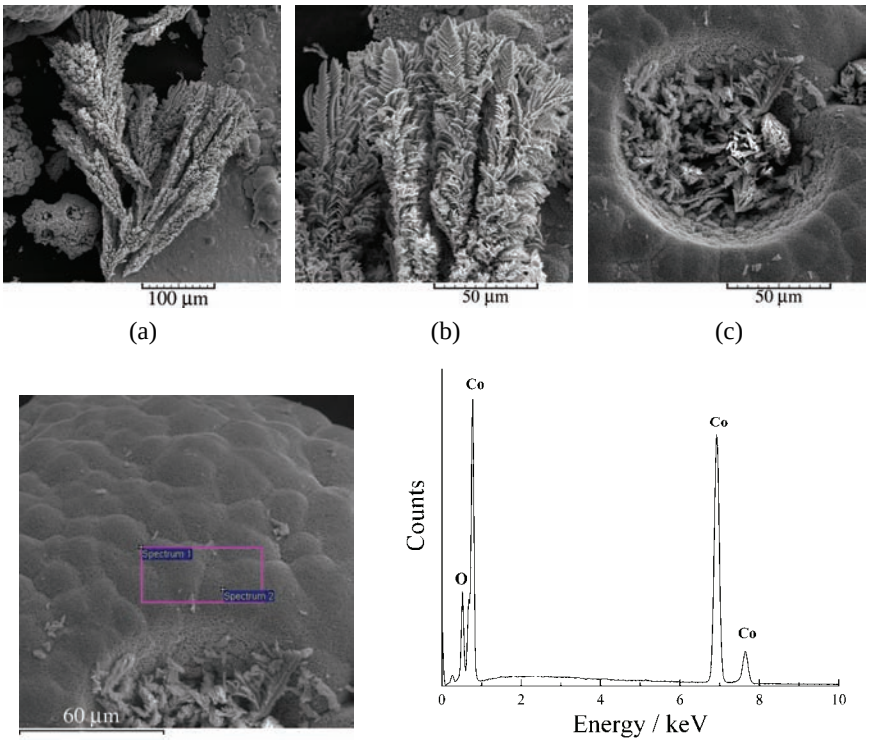

Fig. 1. Morphology of cobalt powder particles obtained by electrodeposition at a current density of 500 mA cm^{-2} (Co1): a) dendrite and spongy-like particles, b) dendrite, c) dendrites formed inside holes, d) structure of grains around hole and e) EDS spectrum of the as-deposited powder.

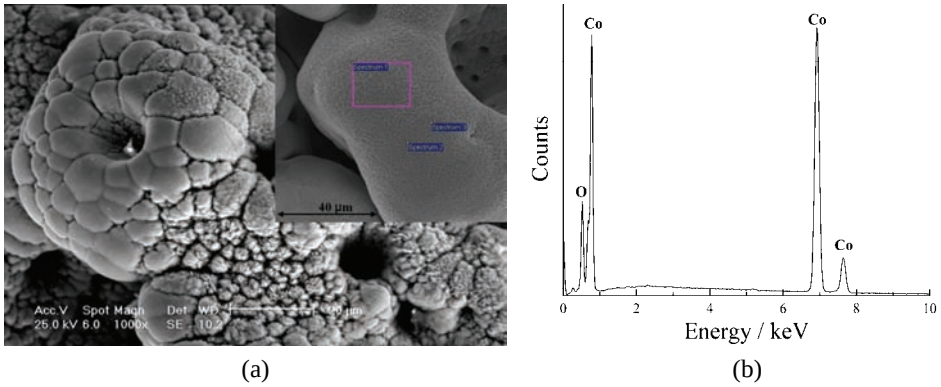

Fig. 2. Morphology of cobalt powder particles obtained by electrodeposition at a current density corresponding to the limiting diffusion current density of 770 mA cm^{-2} (Co2): a) spongy-like particle with magnified details of the surface and b) EDS spectrum of the as-deposited powder.

The cobalt dendrites have the 3D (three-dimensional) fern-like shape (Fig. 1a and b). The cobalt dendrites were also formed in the interior of most holes after the detachment hydrogen bubbles, as shown in Fig. 1c. Regarding the spongy-like particles obtained at 500 mA cm^{-2}, it can be noticed that the spongy character of this particle type is determined by holes formed by detached hydrogen bubbles surrounded by cauliflower-like agglomerates of cobalt grains. The morphology surface of cobalt grains around holes was relatively smooth with numerous nano pores, as shown in Fig. 1d and e shows the energy dispersion spectroscopy (EDS) measurement of the as-deposited powder. A slight peak of oxygen exists, which indicates that the surface of the powder has a quite thin oxide layer due to the passivation of cobalt.

The macrostructure of the spongy-like particles obtained at 770 mA cm^{-2} (Co2) resembled that of those obtained at 500 mA cm^{-2} (Co1, Fig. 2a). Due to vigorous hydrogen evolution during the formation of these particles, small holes inside larger holes were also formed (enlarged part in Fig. 2a). The morphology of the deposits between the holes also (Fig. 2a) consisted of small agglomerates of cobalt grains separated by irregular micro-pores, the origin of which was also due to the hydrogen generated during the electrodeposition process. The morphology of grains around holes was relatively smooth with numerous nano-pores (enlarged parts in Fig. 2a). As in the previous case, there was a quite thin oxide layer on the surface of the powder due to the passivation of cobalt (Fig. 2b).

The effect of hydrogen evolution, as a parallel reaction to cobalt electrodeposition, on the shape of powder particles could be explained as follows: in the case of the formation of dendritic particles, the evolved hydrogen prevented the growth of the dendrites in the lateral directions causing a predominant growth in the vertical direction in the stem-like form, as shown in Fig. 1a and b. The growth of a dendrite commenced from one nucleus (Fig. 1a) and then, the growth of the dendritic particle was determined by the hydrogen evolution reaction. Hydrogen evolution intensified with increasing current density of the electrodeposition leading to inhibition of dendritic growth. Hydrogen evolution became sufficiently vigorous to cause strong stirring of the electrolyte in the near-electrode layer leading to a decrease in the thickness of the diffusion layer, an increase in the limiting diffusion current density and a decrease in the degree of diffusion control of the electrodeposition process.[21] The absence of dendritic-shaped particles in the deposit obtained at 770 mA cm^{-2} actually proved that the degree of diffusion control was lower during electrodeposition at 770 mA cm^{-2} than at 500 mA cm^{-2} due to the intensification of the hydrogen evolution reaction. The quantity of evolved hydrogen during the electrodeposition process can be divided into two parts.[22] One part is spent for the creation of macro-pores or holes and determines the overall specific surface area of the spongy-like particles. This quantity of generated hydrogen does not contribute to the stirring of electrolyte in

the near-electrode layer. The remaining quantity of evolved hydrogen was responsible for the stirring of the electrolyte and, hence, affected the hydrodynamic conditions in the near-electrode layer. The morphology of the spongy-like particles was determined by this remaining quantity of evolved hydrogen, which was also responsible for the formation of the porous structure of this type of particles, *i.e.*, the formation of micro- and nano pores.

The crystal phase composition

The crystallinity and phase composition of the obtained cobalt powders were determined from the XRD patterns depicted in Fig. 3 in the 2θ range of 40–60°. The peak positions of sample Co1 were located at 2θ angles 41.69, 44.60 and 47.52°. The peak positions and intensity ratios matched the corresponding (100), (002) and (101) reflections related to the hexagonal-close packed (hcp) cobalt phase (space group P63/mmc1 (194); JCPDS: 05-0727). No reflections due to cobalt oxides or hydroxides impurities were detected, indicating that the cobalt powder obtained in this way consisted of only the hcp-Co phase. In the case of Co2 sample, notable changes in breadths and relative intensities of the peaks were observed (Fig. 3). Significant broadening of the peaks in this case suggests increased defect concentration (microstrain), as a consequence of the synthesis conditions for this sample. The notable increase in the relative intensity of the (002) peak at 44.60° in Co2 was inconsistent with the XRD pattern of a single hcp phase and pointed to the contribution of the fcc-Co phase through its strongest (111) reflection at the same 2θ angle (space group Fm-3m (225), JCPDS: 15-0806).[23] The detection of both structure phases in the Co2 sample was also in accordance with the higher defect concentration, since it is known that their presence favours the simultaneous existence of hcp and fcc structures in bulk cobalt.[14]

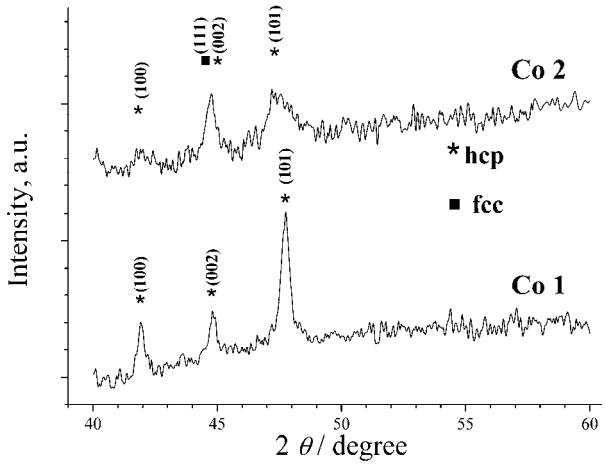

Fig. 3. XRD patterns of cobalt powders deposited at 500 (Co1) and 770 mA cm^{-2} (Co2).

Magnetic properties

Magnetic properties of two cobalt samples were investigated by measurements of field dependence of isothermal magnetization at two temperatures, 5 and 300 K. The recorded magnetization curves in the magnetic field interval of ±50 Oe are depicted in Fig. 4a and b for Co1 and Co2, respectively, while the insets show low-field details of the hysteresis loops. The most important parameters extracted from the obtained M(H) dependencies are listed in Table I. The saturation magnetization M_S values were considered as the measured values in the maximum field of 50 Oe while the coercivity fields H_C were determined as the interpolated field value for zero sample magnetization.

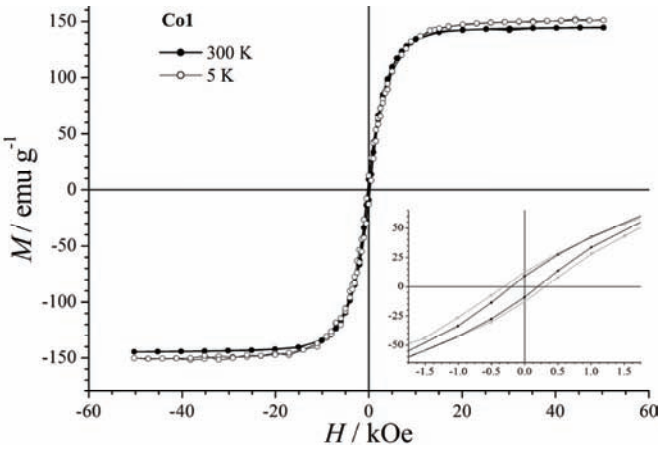

(a)

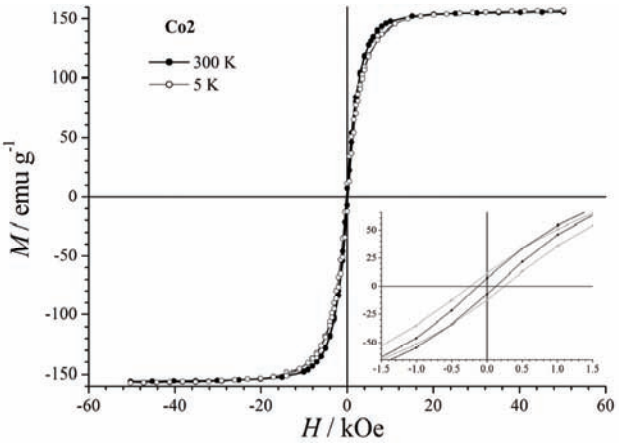

(b)

Fig. 4. Hysteresis loops of cobalt powder electrodeposited at a) 500 (Co1) and b) 770 mA cm^{-2} (Co2) at 5 and 300 K; in insets are the details of the hysteresis loops.

TABLE I. Magnetic parameters for both samples obtained from the *M*(H) curves at two measurement temperatures

Sample	Temperature, K	
	5	300
Co1	M_S = 151 emu g^{-1} H_C = 300 Oe	M_S = 144 emu g^{-1} H_C = 200 Oe
Co2	M_S = 157 emu g^{-1} H_C = 220 Oe	M_S = 156 emu g^{-1} H_C = 160 Oe

The obtained magnetic behaviour of both samples was typical for soft ferromagnetic material that saturates in low to moderate applied fields, and possesses a narrow hysteresis loop. The obtained values of the saturation magnetization M_S were lower than for bulk cobalt (168 emu g^{-1}), which is consistent with the findings of the EDS experiments indicating to the presence of small amount of a cobalt oxide passivation layer at the sample surface. Cobalt oxide possesses antiferromagnetic ordering up to the room temperature,[13] and, consequently, its contribution to the magnetic moment of the material was negligible. Nevertheless, the obtained values of saturation magnetization are among the highest with respect to the values reported in the literature for three-dimensional cobalt structures.[6,24]

Obtained H_C values for both samples were larger than typical literature values for bulk cobalt, while they were similar to these found for other cobalt structures with different morphologies.[1,6,25] It was shown that coercivity predominantly depends on the crystallinity and morphology of materials, so the obtained difference between the Co1 and Co2 samples was understandable. It should be noted that the coercivity of sample Co2 was lower than that of sample Co1, which is in compliance with the findings from both the XRD patterns and the SEM analysis. Namely, from the XRD data, it was concluded that the Co1 sample consisted of pure hcp cobalt phase, while the Co2 sample, besides hcp phase, also contained fcc cobalt phase, which is magnetically softer than hcp phase. In addition, the lower morphological diversity found in Co2 by the SEM analysis could also have caused a decrease of the magnetic anisotropy in the system, which consequently led to a lower H_C value.

An additional interesting point resulting from a comparison of the obtained behaviour of coercivity and saturation magnetization at 5 and 300 K (data in Fig. 4a and b): both H_C and M_S decreased faster with temperature for Co1 than for Co2. In fact, M_S for sample Co2 was virtually the same at 5 and 300 K. A known peculiarity of bulk cobalt magnetism is the increase of its critical ferromagnetic (Curie) temperature T_C with amorphization of the crystal structure, which was demonstrated both experimentally and theoretically.[26,27] It was shown that T_C increased by several hundreds degrees for amorphous cobalt in comparison to well-crystallized bulk cobalt. The present results are in accordance with these

findings since H_C decreased faster with temperature for the well-crystallized sample Co1, while M_S remained almost constant up to 300 K for the poorly crystallized sample Co2.

Correlation between morphology and magnetic properties

Although the values of saturation magnetization M_S for the powder particles obtained at the both current densities were lower than that for the bulk cobalt, it is necessary to note that the value for the particles obtained at 770 mA cm^{-2} was closer to the value for bulk cobalt, which could be explained as follows: the powder particles produced at 770 mA cm^{-2} were obtained under conditions of more vigorous hydrogen evolution than those obtained at 500 mA cm^{-2}. From the viewpoint of the electrodeposition process, this means that potential at which the electrodeposition process really occurred was lower at the current density of 770 mA cm^{-2} than at 500 mA cm^{-2} (the concept of "effective overpotential" or "effective potential").[21] This means a decrease in the degree of diffusion control of electrodeposition process with intensification of hydrogen evolution. As a consequence, the morphologies of deposits became similar to those obtained at lower potentials or current densities, at which hydrogen evolution is less vigorous. This process led to an increase in the compactness of the particles and the structure of these particles approached the structure characteristic for bulk Co.[18]

As already mentioned, the dendritic growth was completely inhibited by the hydrogen evolution reaction during electrodeposition at 770 mA cm^{-2}. The specific surface area of particles obtained in such a manner (cauliflower-like or spongy-like particles) was smaller than that of dendritic particles.[28] Due to smaller specific area of the spongy-like particles, the surface area of these particles was less exposed to air and, hence, to the creation of oxide at their surface than dendritic particles. In this way, the better magnetic characteristics of the particles obtained at 770 mA cm^{-2} than those obtained at 500 mA cm^{-2} may be explained.

CONCLUSIONS

The experimental results demonstrated that it was possible to control the morphology, structure and magnetic properties of cobalt 3D powder particles by adjusting process parameters of electrodeposition such as current density. Dendrites and spongy-like particles were obtained at a current density of 500 mA cm^{-2}, while the only the spongy-like particles were produced by electrodeposition at 770 mA cm^{-2}. XRD analysis indicated that the cobalt powder obtained at 500 mA cm^{-2} consisted of single phase hcp-Co phase but in the cobalt powder sample electrodeposited at 770 mA cm^{-2}, both structure phases of cobalt, hcp and fcc, were detected. The values of obtained saturation magnetization were lower than that for bulk cobalt (168 emu g^{-1}), which is consistent with the findings of the EDS experiments that pointed to the presence of a small amount of a

cobalt oxide passivation layer at the surface of the samples. The enhanced values of coercivity were the result of increased magnetic anisotropy caused by the peculiar morphologies of the powder particles.

Acknowledgment. This work was financially supported by the Ministry of Education, Science and Technological Development of the Republic of Serbia under Grant No. III 45012.

И З В О Д

МЕЂУСОБНА ПОВЕЗАНОСТ МОРФОЛОГИЈЕ И МАГНЕТНИХ СВОЈСТАВА ЧЕСТИЦА ЕЛЕКТРОХЕМИЈСКИ ПРОИЗВЕДЕНОГ ПРАХА КОБАЛТА

ВЕСНА М. МАКСИМОВИЋ[1], НЕБОЈША Д. НИКОЛИЋ[2], ВЛАДАН Б. КУСИГЕРСКИ[1] и ЈОВАН Л. БЛАНУША[1]

[1]Институт за нуклеарне науке „Винча“, Универзитет у Београду, Београд и [2]ИХТМ – Центар за електрохемију, Универзитет у Београду, Његошева 12, Београд

3Д честице праха кобалта су добијене галваностатским таложењем. Електрохемијски исталожен прах кобалта карактерисан је рендгено-дифракционом анализом, техником скенирајуће електронске микроскопије и енергетско-дисперзионом спектроскопијом, као и помоћу SQUID магнетометра. Показано је да су морфологија, структура и магнетна својства честица кобалта тесно повезане и да се могу лако контролисати подешавањем електрохемијских параметара. У зависности од примењене густине струје формирају се две врсте честица праха: дендрити при ниским и сунђерасте честице при вишим вредостима густине струје. Морфологија и структура честица су у међусобној вези са магнетним својствима, а поређене су и са својствима „*bulk*“ кобалта. У поређењу са „*bulk*“ кобалтом, добијене 3Д структуре показују смањену сатурациону магнетизацију (M_S), али побољшану коерцитивност (H_C), што се објашњава њиховом неуобичајеном морфологијом.

(Примљено 20. август, ревидирано 8. октобра, прихваћено 24. октобра 2014)

REFERENCES

1. Z. Lu-Ping, X. Hong-Mei, Z. Wei-Dong, Y. Yang, F. Shao-Yun, *Cryst. Growth Des.* **8** (2008) 1113
2. M. Rivera, C. H. Rios-Reyes, L. H. Medoza-Huizar, *Appl. Surf. Sci.* **255** (2008) 1754
3. A. B. Soto, E. M. Arce, M. Polimar-Pardave, I. Gonzalez, *Electrochim. Acta* **41** (1996) 2647
4. N. Pradhan, P. Singh, B. C. Tripathy, S. C. Das, *Miner. Eng.* **14** (2001) 775
5. H. Cao, L. Wang, Y. Qui, Q. Wu, G. Wang, L. Zhang, X. Liu, *Chemphyschem* **7** (2006) 1500
6. X. Liu, R. Yi, Y. Wang, G. Qui, N. Zhang, X. Li, *J. Phys. Chem. C* **111** (2007) 163
7. V. D. Jović, N. D. Nikolić, U. Č. Lačnjevac, B. M. Jović, K. I. Popov, in *Electrochemical Production of Metal Powders*, Series: *Modern Aspects of Electrochemistry*, S. S. Djokić, Ed., Vol. 54, Springer, Berlin, 2012, p. 63
8. M. Erbudak, E. Wetli, M. Hochstrasser, D. Pescia, D. D. Vvedensky, *Phys. Rev. Lett.* **79** (1997) 1893
9. O. Kitakami, H. Sato, Y. Shimada, F. Sato, M. Tanaka, *Phys. Rev., B* **56** (1997) 13849
10. H. Sato, O. Kitakami, T. Sakurai, Y. Shimada, Y. Otani, K. Fukamichi, *J. Appl. Phys.* **81** (1997) 1858
11. V. V. Matveev, D. A. Baranov, G. Y. Yurkov, N. G. Akatiev, I. P. Dotsenko, S. P. Gubin, *Chem. Phys. Lett.* **422** (2006) 402

12. Y. Song, H. Modrow, L. L. Henry, C. K. Saw, E. Doomes, V. Palshin, J. Hormes, C. S. S. R. Kumar, *Chem. Mater.* **18** (2006) 2817
13. A. Oles, F. Kajzar, M. Kucab, W. Sikora, *Magnetic Structures*, Panstwowe Wydawnictwo Naukowe, Krakow, 1976
14. S. Sun, C. B. Murray, *J. Appl. Phys.* **85** (1999) 4325
15. K. I. Popov, S. S. Djokić, B. N. Grgur, *Fundamental aspects of electrometallurgy*, Kluwer Academic/Plenum Publishers, New York, 2002, p. 1
16. N. D. Nikolić, V. M. Maksimović, G. Branković, P. M. Živković, M. G. Pavlović, *J. Serb. Chem. Soc.* **78** (2013) 1387
17. R. Winand, *Electrochim. Acta* **39** (1994) 1091
18. V. D. Jović, V. M. Maksimović, M. G. Pavlović, K. I. Popov, *J. Solid State Electrochem.* **10** (2006) 373
19. N. D. Nikolić, K. I. Popov, Lj. J. Pavlović, M. G. Pavlović, *J. Electroanal. Chem.* **588** (2006) 88
20. V. D. Jović, B. M. Jović, M. G. Pavlović, *Electrochim. Acta* **51** (2006) 5468
21. N. D. Nikolić, K. I. Popov, in *Electrodeposition: Theory and Practice*, Series: *Modern Aspects of Electrochemistry*, S. S. Djokić, Ed., Vol. 48, Springer, Berlin, 2010, p. 1
22. N. D. Nikolić, G. Branković, M. G. Pavlović, *Powder Technol.* **221** (2012) 271
23. E. A. Owen, D. Madoc Jones, *P. Phys. Soc., B* **67** (1954) 456
24. G. Dumpich, T. P. Krome, B. Hausmanns, *J. Magn. Magn. Mater.* **248** (2002) 241
25. H. L. Niu, Q. W. Chen, H. F. Zhu, Y. S. Lin, X. Zhang, *J. Mater. Chem.* **13** (2003) 1803
26. K. Fukamichi, T. Goto, U. Mizutani, *IEEE Trans. Magn.* **MAG-23** (1987) 3590
27. Y. Kakehashi, *Phys. Rev., B* **43** (1991) 10820
28. N. D. Nikolić, K. I. Popov, in *Electrochemical Production of Metal Powders*, Series: *Modern Aspects of Electrochemistry*, S. S. Djokić, Ed., Vol. 54, Springer, 2012, p. 125.

Journal of the Serbian Chemical Society
JSCS-info@shd.org.rs • www.shd.org.rs/JSCS
J. Serb. Chem. Soc. 80 (2) 209–222 (2015)
JSCS–4711
UDC 547.498.004.12:615.32:543.2
Original scientific paper

Application of experimental design in the examination of the dissolution rate of carbamazepine from formulations. Characterization of the optimal formulation by DSC, TGA, FT-IR and PXRD analysis

MARKO KRSTIĆ[1]*, SLAVICA RAŽIĆ[2#], DRAGANA VASILJEVIĆ[1], ĐURĐIJA SPASOJEVIĆ[1] and SVETLANA IBRIĆ[1]

[1]*Department of Pharmaceutical Technology and Cosmetology, Faculty of Pharmacy, University of Belgrade, Vojvode Stepe 450, P. O. Box 146, 11221 Belgrade, Serbia and* [2]*Department of Analytical Chemistry, Faculty of Pharmacy, University of Belgrade, Vojvode Stepe 450, P. O. Box 146, 11221 Belgrade, Serbia*

(Received 3 August, revised 14 November, accepted 15 November 2014)

Abstract: Poor solubility is one of the key reasons for the poor bioavailability of carbamazepine drugs. This study considers formulation of solid surfactant systems with carbamazepine, in order to increase its dissolution rate. Solid-state surfactant systems were formed by application of fractional experimental design. Poloxamer 237 and Poloxamer 338 were used as the surfactants and Brij® 35 was used as the co-surfactant. The ratios of the excipients and carbamazepine were varied and their effects on the dissolution rate of carbamazepine were examined. Moreover, the effects of the addition of natural (diatomite) and a synthetic adsorbent carrier (Neusilin® UFL2) on the dissolution rate of carbamazepine were also tested. The prepared surfactant systems were characterized and the influences of the excipients on possible changes of the polymorphous form of carbamazepine examined by application of analytical techniques (DSC, TGA, FT-IR and PXRD). It was determined that an appropriate selection of the excipient type and ratio could provide a significant increase in the carbamazepine dissolution rate. By application of analytical techniques, it was found that the employed excipients induce a transition of carbamazepine into the amorphous form and that the selected sample was stable for three months, when kept under ambient conditions.

Keywords: poloxamer; neusilin; diatomite; solid surfactant drug delivery systems; polymorphous transition.

* Corresponding author. E-mail: mkrstic109@gmail.com
# Serbian Chemical Society member.
doi: 10.2298/JSC030814114K

INTRODUCTION

According to Ku and Dulin, the number of new drug candidates that exhibit poor aqueous solubility has increased by up to 70 %.[1] The dissolution of poorly soluble drugs is the rate-limiting step for drug absorption and bioavailability. Therefore, formulation of drug delivery systems that promote drug release could be a useful approach to improve absorption and oral bioavailability.[2] A number of alternative technologies have been developed to overcome the drawbacks associated with poor aqueous solubility, for example, decreases in the particle size, the use of the amorphous form of the active pharmaceutical ingredient, solid dispersions, lipid-based formulations, surfactant application, cyclodextrin complexation, *etc*.[3–8]

In recent years, the application of surfactants has been widely used in the formulation of self-emulsifying drug delivery systems (SEDDS),[9] self-nanoemulsifying drug delivery systems (SNEDDS)[10] and self-microemulsifying drug delivery systems (SMEDDS),[11] as well as in the formulation of surfactant systems.[12] According to the Plouton classification system of lipid formulations, a lipid formulation type IV consists of systems containing only surfactants without the addition of lipid excipients (*e.g.*, surfactant systems).[2] Such surfactant systems (consisting of drug, surfactants and co-surfactants), in contact with gastrointestinal fluids, allow drug solubilization and subsequent absorption.[2]

Poloxamers are non-ionic polyoxyethylene–polyoxypropylene block copolymers widely used in pharmaceutical technologies as gelling, emulsifying or solubilizing agents.[13–15] They are also frequently used in the formulation of solid dispersions.[16] Due to their good solubilization capacities, poloxamers are commonly used in the creation of SEDDS.[17] Brij® 35 is commonly used as a surfactant or co-surfactant in oral drug delivery systems with demonstrated improved drug solubility and bioavailability.[18–20]

Nowadays, porous carriers with a large surface area are used in order to improve dissolution and bioavailability of poorly soluble drugs.[11,21] Most frequently, such carriers are of synthetic origin (for example magnesium aluminometasilicate or porous silica). However, carriers of natural origin, such as diatomite (natural silica) are playing the leading role. Diatomites, as a new potential drug carrier, have several advantages in comparison to synthetic silicas: biocompatibility arising from their natural origin, thermal stability, chemical inertness and low cost. Additionally, the complex 3-dimensional (3-D) architecture of silica walls, called frustules, with highly ordered porous structures and high specific surface areas, provide for potential diffusion and controlled drug release.[22,23] Like many complex silicates, the surface of Neusilin has different types of silanol groups, which make it a potential proton donor as well as an acceptor. The hydrogen bonding potential of silanols in the local environment on silica surfaces is well documented.[24–26]

Carbamazepine (CBZ) is a substance with poor water solubility (0.17 mg mL^{-1} at 24 °C) and high permeability.[27,28] Based on its characteristics, it is classified into class II of the Biopharmaceutics Classification System (BCS).[29] After oral administration, its gastrointestinal absorption is slow and irregular due to poor solubility in water, leading to incomplete bioavailability.[27,28] CBZ is interesting as a model substance not only because of its poor solubility, but also because it exists in multiple polymorphous forms, *i.e.*, 4 crystalline forms, 1 hydrate and an amorphous form. Transition from one to another form during the formulation process in the presence of certain excipients is possible without changes in its stability.[27,30,31]

The objective of this study was the formulation of a solid surfactant system with increased dissolution rate of CBZ. Fractional factorial design was applied in order to evaluate the influence of the following variables on the drug release: a) the type of poloxamer as surfactant (Poloxamer 237 and Poloxamer 338), b) the ratio of Brij® 35 as a co-surfactant, c) the type and ratio of the adsorption carrier (Neusilin UFL2 or Diatomite) and d) the ratio of the drug.

Analysis of potential polymorphous transitions of CBZ was conducted by application of several analytical techniques, *i.e.*, differential scanning calorimetry (DSC), thermal gravimetric analysis (TGA), powder X-ray diffraction analysis (PXRD) and Fourier transform infrared (FT-IR) spectroscopy.

EXPERIMENTAL

Materials

Poloxamer 237 (Kolliphor™ P 237) and poloxamer 338 (Kolliphor™ P 338) were kindly donated by BASF ChemTrade GmbH (Burgbernheim, Germany). Polyoxyethylene(23)lauryl ether (Brij® 35) was obtained from Sigma–Aldrich, Germany. Magnesium aluminometasilicate (Neusilin® UFL2) was gifted by Fuji Chemical Industry (Toyama, Japan). Diatom porous silica particles of different particle size: 1–2 μm (10 %), 10 μm (60 %) and 30–50 μm (30 %) were obtained from Mount Sylvia, Pty. Ltd., Australia. CBZ (Ph. Eur. 8.0) was used as a model of a poorly soluble active ingredient. Double-distilled water was used in all experiments.

Methods

Preparation of solid surfactant systems. All formulations were prepared by melting a mixture of surfactant and co-surfactant at 60 °C. CBZ was then added to the molten mass under vigorous stirring until a homogenous dispersion was obtained. The dispersion was then rapidly cooled on an ice bath to solidify and subsequently pulverized with a pestle and mortar, before being sieved through a 300-μm sieve. The sieved mixtures were mixed with an adsorbent carrier (Neusilin® UFL2 or diatomites) and the final formulations were thus obtained. These formulations were tested with regard to the CBZ dissolution rate, which provided dissolution rate profiles for each formulation.

Two sets of experiments were conducted. In the first set of experiments, the individual effects of the excipients on the CBZ dissolution rate were investigated through a screening study. The following binary and ternary mixtures were prepared: Poloxamer 338/CBZ (80/20); Poloxamer 338/CBZ/Neusilin® UFL2 (40/10/50); Brij® 35/CBZ (80/20); Brij®

35/CBZ/Neusilin® UFL2 (40/10/50), in order to determine the individual effect of the excipients on the CBZ dissolution rate.

In the second set of experiments, fractional factorial experimental design was applied (2^{5-2}) for testing the influence of the formulation factors on the CBZ dissolution rate from the solid surfactant systems. The input parameters and the levels at which they were varied are given in Table I. The experimental plan (according to 2^{5-2} factorial design) is given in Table S-I of the Supplementary material to this paper. According to the experimental plan, a mixture of CBZ, Brij® 35 and poloxamer (comprising the surfactant system) was first created, in the appropriate mass ratio, their individual ratios adding up to 100 %. The adsorbent carrier was added to this mixture at a later stage. The prepared surfactant system/adsorption carrier ratio was varied at two levels: 66.67/33.33 and 33.33/66.67 (Table I). The percentages of released CBZ were followed as output parameters after 10, 20, 30, 45, 60 and 120 min ($Y1$–$Y6$). The influence of the investigated input parameters on the output parameters (*i.e.*, factor effects), according to the 2^{5-2} factorial design, was calculated by fitting the results into the linear model:

$$y = \beta 0 + \beta 1X1 + \beta 2X2 + \beta 3X3 + \beta 4X4 + \beta 5X5 + \varepsilon \quad (1)$$

where y is the output parameter, $X1$–$X5$ are the input parameters, $\beta 1$–$\beta 5$ are the effects of individual input parameters on the output parameter (factor effects) and ε is the experimental error.

TABLE I. Varied input parameters in the second set of experiments

Parameter	Low level (–1)	High level (+1)
Type of Poloxamer ($X1$)	P237	P338
Brij® 35 ratio ($X2$), %	10	20
CBZ ratio ($X3$), %	10	20
Type of adsorption carrier ($X4$)	Neusilin UFL2	Diatomites
Adsorption carrier ratio ($X5$), %	33.33	66.67

Design Expert software (version 7.0.0; Stat-Ease, Inc., Minneapolis, MN, U.S.A.) was applied.

After performing the second set of experiments, the solid surfactant system with the fastest CBZ release was selected. In the selected formulation, the percentage of CBZ was varied at three levels: 10, 15 and 20 %. Dissolution rate profiles of the selected optimal formulation were compared with pure CBZ and commercially available immediate release CBZ tablets (Galepsin®, Galenika a.d, Serbia).

In vitro *drug release studies*

The dissolution profiles of the different solid surfactant systems and pure CBZ were determined using a rotating paddle apparatus (Erweka DT70, Germany). The dissolution conditions were: water as medium; 37±0.5 °C; 900 mL and 50 rpm. Aliquots of 4 mL were withdrawn from the medium at fixed times (10, 20, 30, 45, 60 and 120 min). Sink conditions were maintained at all times. All samples were filtered through a 0.45-μm MF-Millipore® membrane filter (Millipore Corporation, Bedford, NY, USA). The CBZ concentration was determined spectrophotometrically at λ = 287 nm (Evolution 300 spectrophotometer, Thermo Fisher Scientific, UK). The dissolution experiments were performed in triplicate and the data are expressed as the mean value.

The release profiles of CBZ from solid surfactant systems were compared with the dissolution profiles of pure CBZ by calculating the difference ($f1$) and the similarity ($f2$) factors.[32]

Characterization of the solid phase

In order to determine the polymorphous form of CBZ in the final formulation and the influence of individual excipients on the change in the polymorphous form, DSC and TGA analyses were conducted in the first set of experiments. DSC, TGA, X-ray and FT-IR analyses were performed on the optimal formulation and pure CBZ.

The optimal formulation was kept under room conditions (T 25 °C and RH 40 %) for three months in order to assess its stability, after which the DSC, TGA, X-ray and FT-IR analyses were repeated.

Differential scanning calorimetry (DSC) and thermal gravimetric analysis (TGA)

Differential scanning calorimetry (DSC) and thermal gravimetric analysis (TGA) were applied in order to determine thermal properties of the compounds. Thermal properties were examined at temperatures ranging from room temperature up to 250 °C on a SDT Q600 TGA/ /DSC instrument (TA Instruments) under a dynamic dry nitrogen atmosphere (flow rate: 100 $cm^3\ min^{-1}$) at a heating rate of 20 °C min^{-1}. The sample masses were between 7.3 and 11.5 mg.

Fourier transform infrared (FT-IR) studies

FT-IR spectra in the region of 600–4000 cm^{-1} for both starting materials and the solid formulations were obtained using a Shimadzu IR-Prestige-21 FT-IR spectrometer coupled with a horizontal Golden Gate MKII single-reflection ATR system (Specac, Orpington, UK) equipped with a ZnSe lens, after appropriate background subtraction. Sixteen scans over the selected wave number range at a resolution of 4 cm^{-1} were averaged for each sample.

Powder X-ray diffraction analysis (PXRD)

The X-Ray diffraction (PXRD) patterns of the powders were recorded on an Ital Structure APD2000 X-ray diffractometer with Bragg–Brentano geometry using CuK_α radiation (λ =1.5418 Å) in the 2θ range from 4 to 45°.

RESULTS AND DISCUSSION

CBZ release profiles from the binary and ternary mixtures prepared in the first set of experiments, as well as the release profile of the pure drug, are presented in Fig. S-1 of the Supplementary material. The CBZ release was increased in all mixtures compared to that of the pure drug. Similarity and difference factors were calculated for all mixtures (Table II).

TABLE II. The difference ($f1$) and the similarity ($f2$) factors for the mixtures and pure CBZ (from the first set of experiments). The percentage mass loss in the temperature range 100––200 °C for the mixtures prepared in the first set of experiments

Mixtures	$f1$	$f2$	Mass loss, % 100 °C < T < 200 °C
CBZ & CBZ+Brij® 35	8.32	62.15	7.31
CBZ & CBZ+Brij® 35+ Neusilin® UFL2	23.14	36.41	4.34
CBZ & CBZ+P338	51.41	9.15	0.19
CBZ & CBZ+P338+ Neusilin® UFL2	57.98	3.38	4.31

Based on the results presented in Table II, it could be concluded that the CBZ dissolution rate was statistically significantly increased in following mixtures: Brij® 35/CBZ/Neusilin® UFL2 (40/10/50), Poloxamer 338/CBZ (80/20) and Poloxamer 338 /CBZ /Neusilin® UFL2 (40/10/50). The CBZ dissolution rate in the mixture Brij® 35/CBZ (80/20) was similar to that of pure CBZ dissolution.

The increase in the CBZ dissolution rate with the addition of Poloxamer 338 was expected because of its high hydrophilic–lipophilic balance (HLB) value (HLB-27) and solubility characteristics.[33] The adsorbent carrier with its large specific surface leads to better soaking of the substance and more contact with the medium, which also increases the CBZ dissolution rate.[34] The addition of Poloxamer 338 had more effect individually than the addition of Brij® 35, which was expected due to its lower *HLB* value of 16 in comparison to 27 for Poloxamer 338.[33] Therefore, Brij® 35 was used as a co-surfactant in the second set of experiments.

The CBZ dissolution rate profiles obtained from the second set of experiments are given in Fig. 1. Significant increases in the dissolution rate were registered compared to that of pure CBZ.

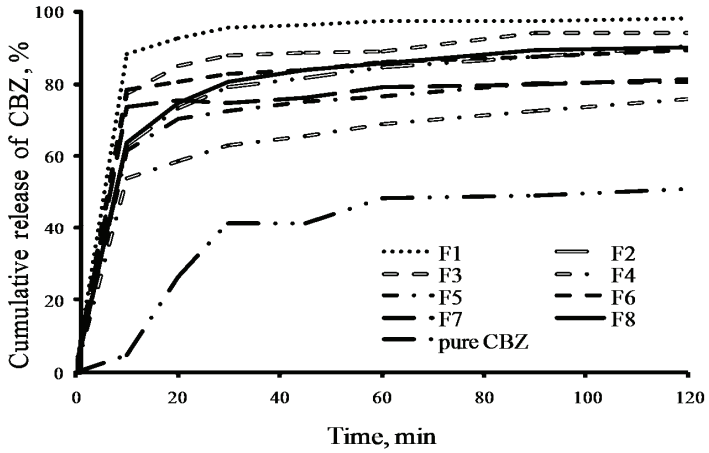

Fig. 1. Dissolution profiles of the CBZ formulation prepared in the second set of experiments and pure CBZ.

The calculated factor effects (Eq. (1)) are given in Table III. The sign of the coefficient shows whether the effect is positive or negative, *i.e.*, whether the CBZ dissolution rate increases (positive effect) or decreases (negative effect) with a change in the parameter value.

The CBZ ratio (*X*3) had the most pronounced influence on the drug release in the first 10 min of the drug release study. This parameter had a negative effect

because of the poor solubility of CBZ. The percentage of released CBZ decreased with increasing of its ratio in the formulation (from 10 to 20 %).

TABLE III. Analysis of the influence of the input parameters on the output parameter, released CBZ, %, in the second set of experiments

Factor effect	τ / min					
	10 (*Y*1)	20 (*Y*2)	30 (*Y*3)	45 (*Y*4)	60 (*Y*5)	120 (*Y*6)
*X*1 (type of Poloxamer)	+1.09	+0.31	+1	+1.01	+1.15	0.9
*X*2 (Brij® 35 ratio)	–1.8	–2.02	–1.31	–1.47	–1.23	0.037
*X*3 (CBZ ratio)	–6.45	–5.8	–5.12	–4.6	–3.86	–3.02
*X*4 (type of adsorption carrier)	–3.17	–5.13	–6.26	–6.15	–5.77	–5.72
*X*5 (adsorption carrier ratio)	–5.87	–4.16	–3.53	–3.15	–3.55	–2.33
*X*2 and *X*3 interaction	–3.23	–2.57	–1.99	–1.81	–1.62	–1.26
*X*2 and *X*5 interaction	+3.31	+1.55	+0.8	+0.24	+0.16	–0.14

After 30 min of the drug release study, the type of carrier had more influence. Initially, CBZ was released from the surfaces of both carriers. Due to the larger specific surface area of Neusilin® UFL2 (300 m^2 g^{-1}) compared to diatomites (211 m^2 g^{-1}), a higher CBZ release rate was achieved [22,35,36] and the significance of this factor increased with time. In solid surfactant systems with diatomites, due to their specific structure, the substance is absorbed into the interior of the diatomite, from where it is gradually released;[37,38] hence, the CBZ release was delayed as the release had to occur from the interior of the system.

It was shown that the higher carrier ratio had a negative impact on drug release. A higher release rate was achieved when the carrier ratio was at its lower level (33.33 %). According to Agarwal *et al.*,[35] the adsorbent magnesium aluminometasilicate, with a large specific active surface (300 m^2 g^{-1}) and small particle size (2−8 μm), has pores in which an adsorbed substance could enter by means of capillary forces. Inside the pores, potential crystallization is disabled. It could be presumed that the decrease in the dissolution rate after adsorption derives from the precipitation of the drug on the surface of the adsorbent and the capturing of the drug inside the carrier. This was particularly evident after 10 and 20 min, when the percentage of the substance to be released was low, due to the poor availability of CBZ to the medium.

The type of employed Poloxamer had the least pronounced influence on the CBZ release rate. The systems created with Poloxamer 338 (HLB 27) showed a slightly higher CBZ release rate compared to those of the Poloxamer 237 systems (HLB 24), which, was expected, due to the higher HLB value of the former.[33] Poloxamer 338 also has a lower value of the critical micellar concentration (*CMC*) compared to Poloxamer 237 and is, therefore, a more efficient solubilizer, which corresponds to the obtained result (the *CMC* of Poloxamer 338 is 2.2×10^{-5} mol L^{-1} while that of Poloxamer 237 is 9.1×10^{-5} mol L^{-1}).[39,40]

Comparing the obtained factor effects from Eq. (1), it is evident that the Brij® 35 ratio had less influence on the CBZ release rate. The formulation with the higher Brij® 35 ratio had a lower Poloxamer ratio. In the first set of experiments, it was shown that the Poloxamer had a greater influence on the increase in the CBZ dissolution rate compared to Brij® 35. However, there was a significant interaction between the CBZ ratio and the ratio of Brij® 35. Formulations with a higher level of the CBZ ratio and a lower level of Brij® 35 showed the highest percentages of released CBZ.

The analysis revealed another significant interaction, *i.e.*, that of the ratios of Brij® 35 and the carrier ratio. When the carrier ratio was at the lowest level, a change of the Brij® 35 ratio from 10 to 20 % decreased the percentage of released substance. From the previous interaction, it could be concluded that higher release rates were achieved with 10 % of Brij® 35 in the formulation. In this case, a higher substance release rate was achieved when the carrier ratio was at the lower level, *i.e.*, 33.33 %.

From second set of experiments, the selected: Poloxamer 338, Brij® 35 10 %, Neusilin UFL2 33.33 % formulation exhibited the highest CBZ release rate. In such a solid surfactant system, the CBZ ratio was set at 10, 15 and 20 %. The results of drug release study from these formulations are shown in Fig. S-2A of the Supplementary material.

The highest percentage of released CBZ was obtained from the formulation with 15 % of CBZ. The CBZ drug release profile from this formulation is compared with the profiles of pure CBZ and commercially available immediate release CBZ tablets in Fig. S-2B of the Supplementary material.

The results of the TGA analysis (Fig. 2A) showed that in the temperature range of 100 to 200 °C, Neusilin® UFL2 exhibited a mass loss of about 8.5 %, whereas the optimal formulation lost 4.31 % of its mass. The mass loss for samples prepared in the first set of experiments in the temperature range of 100 to 200 °C are presented in Table II. CBZ exhibited a small mass loss within the temperature range of 100 to 200 °C, while in the range of 200 to 250 °C, an immediate mass loss of 2.5 % was registered, probably indicating the commencement of its degradation. A somewhat higher loss of mass was registered in the samples in which Brij® 35 was used as the surfactant. Moreover, a significant decrease in mass of all samples was registered in the temperature range of 200 to 250 °C, which correlates with the result obtained for pure CBZ (Fig. 2B).

The DSC curves of the tested samples and pure CBZ showed an endothermic peak at about 60 °C (Fig. 2C). Bearing in mind the very broad range over which the device was calibrated (60–800 °C), this peak could derive from measurement uncertainty, *i.e.*, the imprecision of the instrument. With formulations containing Poloxamer, this peak was somewhat more distinct, because their peak derives from the melting of Poloxamer.[41] This led to an overlapping of the peaks in these

formulations. Based on the two endothermic peaks at 178 and 195.6 °C, it could be concluded that the pure CBZ was in the polymorphous form III.[31,42] The reason for these peaks occurring at higher temperatures than those given in the lite-

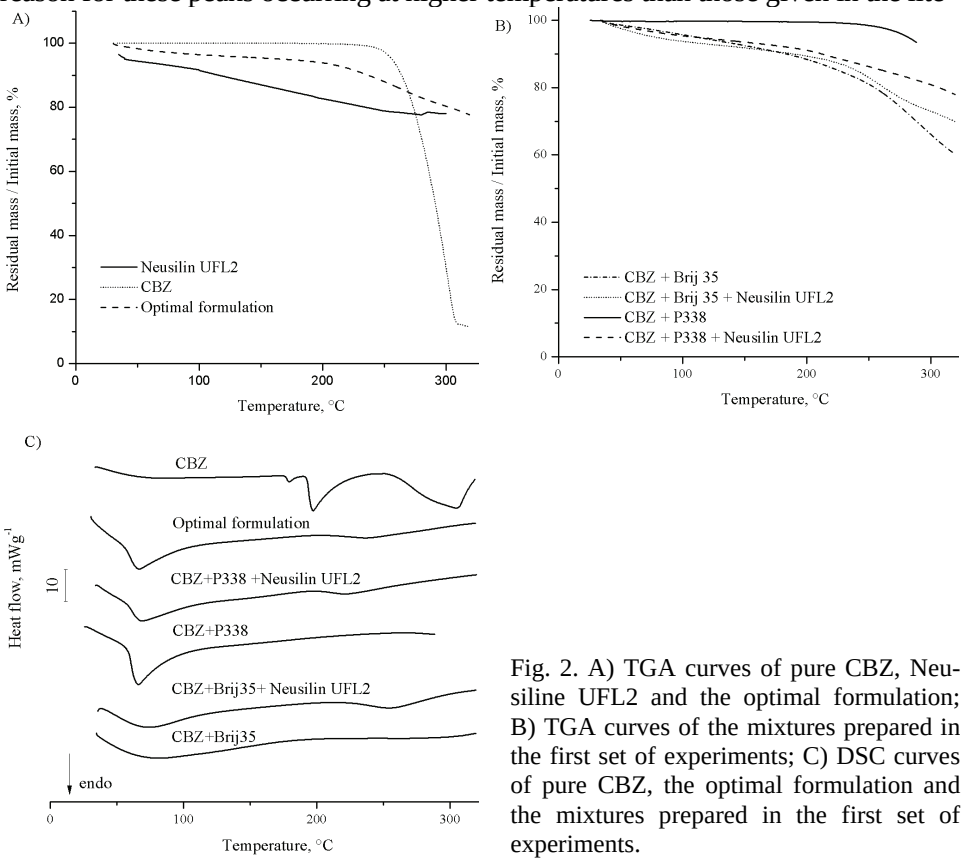

Fig. 2. A) TGA curves of pure CBZ, Neusiline UFL2 and the optimal formulation; B) TGA curves of the mixtures prepared in the first set of experiments; C) DSC curves of pure CBZ, the optimal formulation and the mixtures prepared in the first set of experiments.

rature[31] could be explained by the higher heating rate employed in the present study (20 °C min^{-1}) than the rate used in the literature study (10 °C min^{-1}), *i.e.*, the difference in the temperature lag of the two systems. The balance of the system was achieved slightly later and, therefore, the changes identified by the peaks were delayed by a few °C. In addition, because of the difference in the experimental conditions, no distinct recrystallization peak corresponding to the transition of the sample into the polymorphous form I was visible on the DSC curve of pure CBZ recorded in the present study. Furthermore, on the DSC curves of the samples, a broad endothermic peak was registered in the temperature range 230–240 °C. It is assumed that this peak corresponded to the beginning of CBZ degradation, which is in accordance with the results of the TGA analysis. From this point of view, an analysis of the degradation products and the further clarification of this peak could be a part of further investigations. In all

four tested mixtures, no characteristic melting peaks from polymorphous form III were evidences in the temperature range of 150 to 175.8 °C.[31,42] In addition, no peaks characteristic for other polymorphous forms were registered. Thus, it could be assumed that a transition of CBZ from the crystal polymorphous form III into amorphous form had occurred. It is notable that the application of the individual surfactants (Poloxamer 338 and Brij® 35, with or without the addition of Neusilin® UFL2) led to the transition of CBZ into the amorphous form. Although DSC is a commonly used technique for the determination of crystalline state of drugs and the absence of a melting peak might suggest the formation of an amorphous phase,[43] care should be taken in the interpretation of the results of DSC analysis, particularly when the formulations contain a Poloxamer. Since poloxamers melt at significantly lower temperatures than CBZ, there is a possibility that crystalline CBZ gradually dissolves into a molten polymer during the DSC scan. As the temperature reaches the melting point of CBZ, there may not be sufficient crystalline drug remaining to give a detectable melting endotherm on the DSC curve.[44] Therefore, further characterization of the optimal formulation was performed by application of PXRD and FT-IR analysis in order to confirm the transition of the drug into the amorphous form.

The FT-IR spectra of CBZ and the optimal formulation are given in Fig. 3A and B, respectively. The CBZ spectrum corresponds to those previously reported for the polymorph form III. Characteristic peaks were observed at 3462 (−NH valence vibration), 1674 (−CO−R vibration), 1593 and 1605 cm^{-1} (in the range of −C=C− and −C=O vibration and −NH deformation).[31] Deformation of bands characteristic for the CBZ form III at 1605 and 1593 cm^{-1} (−C=O vibration and −NH deformation) (Fig. 3B.) in FT-IR spectra of the optimal formulation may suggest that a hydrogen bond between the carbonyl group of CBZ and silanol group of adsorbent participate in the formation of the amorphous state of CBZ. There have been reports of drug amorphization by co-grinding with porous silica or magnesium aluminometasilicate.[24–26] Drug amorphization was accompanied by improvement in the drug release rate. CBZ amorphization is a consequence of disruption of the crystalline structure due to hydrogen bonds formation between the drug and adsorbent.

The PXRD patterns of pure CBZ and the optimal formulation are illustrated in Fig. 4. The PXRD pattern of CBZ exhibits characteristic high-intensity diffraction peaks at 2θ 13.02, 15.22, 15.78, 19.40, 24.92, 27.50 and 31.86°, which is in accordance with diffractograms previously reported for the crystal form III.[31,45] These characteristic peaks cannot be seen on the diffractogram of the optimal formulation, which confirms the results obtained by DSC and FT-IR analysis that the carbamazepine had transformed into the amorphous form. The two broad peaks appearing on the diffractogram of the optimal formulation arose from Poloxamer 338.[46]

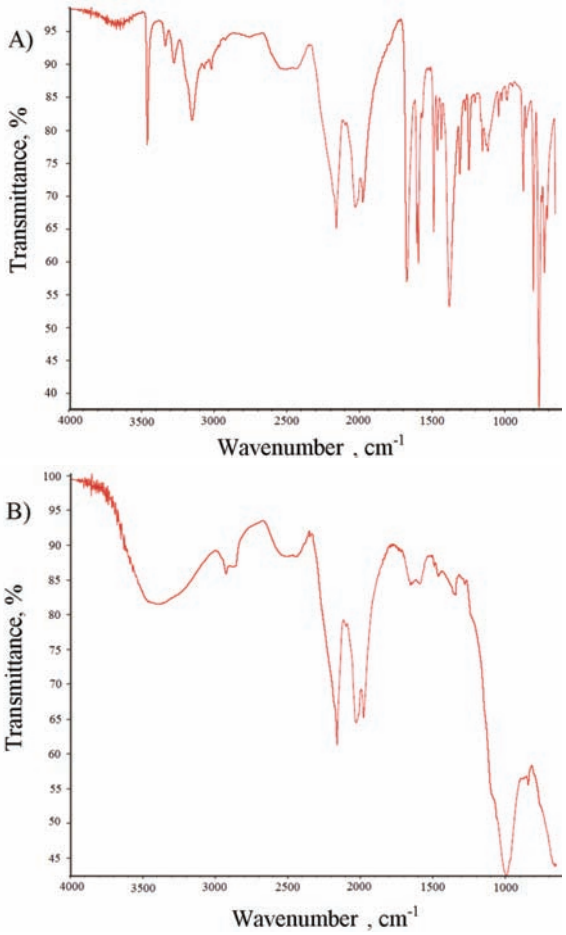

Fig. 3. FT-IR spectra of A) pure CBZ and B) the optimal formulation.

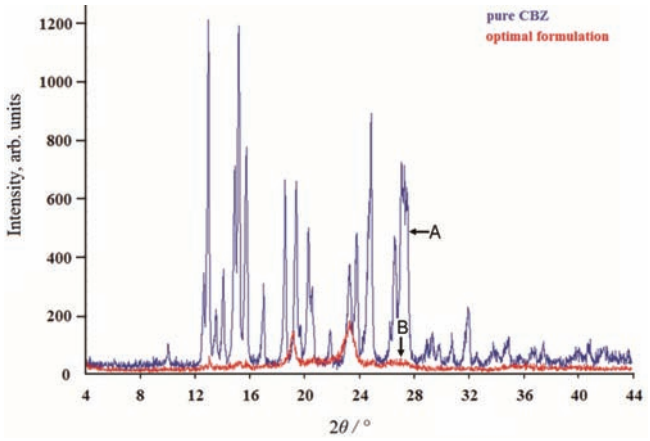

Fig. 4. PXRD patterns of A) pure CBZ and B) the optimal formulation.

DSC, TGA, FT-IR and PXRD analyses of the optimal formulation that had been kept under ambient conditions for three months showed no significant changes in the formulation had occurred. The CBZ remained in the amorphous state and the stability of the formulation was thus confirmed.

CONCLUSIONS

Formulation of solid surfactant drug delivery systems with CBZ as a model drug showed that the addition of Poloxamer (237 or 338), Brij® 35 and an adsorbent (Neusilin UFL2 or diatomite) led to the transition of CBZ into the amorphous state and an increase in its release rate. Poloxamers, as surfactants, had the most significant effect on the increase of the drug release rate. The addition of the adsorbent carrier further increased the CBZ release rate, due to its large specific surface.

The highest carbamazepine release rate was obtained from the optimal formulation in which the surfactant mixture had the following components: 75 % Poloxamer 338; 10 % Brij® 35; 15 % CBZ, while the surfactant mixture and Neusilin® UFL2 as carrier were in 2:1 ratio. This formulation was stable for at least three months.

From all the presented results, it could be concluded that the release rate of poorly soluble CBZ could be increased by solid surfactant systems.

SUPPLEMENTARY MATERIAL

Experimental plan for the second set of experiments, Table S-I, and dissolution profiles of the mixture and CBZ formulation, Figs. S-1 and S-2, are available electronically from http://www.shd.org.rs/JSCS/, or from the corresponding author on request.

Acknowledgement. This work was supported by Project TR34007, funded by Ministry of Education, Science and Technological Development of the Republic of Serbia.

ИЗВОД

ЕКСПЕРИМЕНТАЛНИ ДИЗАЈН ИСПИТИВАЊА БРЗИНЕ РАСТВАРАЊА КАРБАМАЗЕПИНА ИЗ ФОРМУЛАЦИЈА. КАРАКТЕРИЗАЦИЈА ОПТИМАЛНЕ ФОРМУЛАЦИЈЕ ПОМОЋУ DSC, TGA, FT-IR И PXRD МЕТОДА

МАРКО КРСТИЋ[1], СЛАВИЦА РАЖИЋ[2], ДРАГАНА ВАСИЉЕВИЋ[1],ЂУРЂИЈА СПАСОЈЕВИЋ[1] и СВЕТЛАНА ИБРИЋ[1]

[1]*Катедра за фармацеутску технологију и козметологију, Универзитет у Београду, Фармацеутски факултет, Војводе Степе 450, 11221 Београд и* [2]*Катедра за аналитичку хемију, Универзитет у Београду, Фармацеутски факултет, Војводе Степе 450, 11221 Београд*

Слаба растворљивост јесте један од кључних разлога за лошу биолошку расположивост карбамазепина. У овом раду је приказана формулација чврстих површински активних система са карбамазепином, ради повећања његове брзине растварања. Чврсти површински активни системи су формулисани применом фракционог факторског експерименталног дизајна. Као површински активни системи коришћени су Poloxamer 237 и Poloxamer 338, а као ко-површински активни Brij® 35. Варирани су удели ексципијенаса и карбамазепина и испитиван је њихов утицај на брзину растварања карбамазепина. Такође, испитан је и утицај додатка природних (дијатомита) и синтетичких адс-

орпционих носача (Neusilin UFL2) на брзину ослобађања карбамазепина. Извршена је карактеризација израђених површински активних система и испитан је утицај ексципијенаса на могућу промену полиморфног облика карбамазепина применом аналитичких техника (DSC, TGA, FT-IR и PXRD). Утврђено је да се правилним одабиром врсте и удела ексципијенаса може постићи значајно повећање брзине ослобађања карбамазепина. Аналитичким техникама је утврђено да коришћени ексципијенси доводе до преласка карбамазепина у аморфни облик и да је одабрани узорак стабилан 3 месеца, чувањем под собним условима.

(Примљено 3. августа, ревидирано 14 новембра, прихваћено 15. новембра 2014)

REFERENCES

1. M. S. Ku, W. Dulin, *Pharm. Dev. Technol*. **17** (2012) 285
2. C. Pouton, *Eur. J. Pharm. Sci.* **29** (2006) 278
3. J. Y. Kim, Y. S. Ku, *Int. J. Pharm.* **194** (2000) 81
4. A. J. Humberstone, W. N. Charman, *Adv. Drug Deliv. Rev.* **25** (1997) 103
5. C. Leuner, J. Dressman, *Eur. J. Pharm. Biopharm.* **50** (2000) 47
6. G. Serajuddin, A. T. M., *Adv. Drug Deliv. Rev*. **34** (2007) 34
7. J. C. Chaumeil, *Methods Find. Exp. Clin. Pharmacol.* **20** (1998) 211
8. S. M. Ali, S. K. Upadhyay, A. Maheshwari, *J. Incl. Phenomena Macrocycl. Chem.* **59** (2007) 351
9. R. N. Gursoy, S. Benita, *Biomed. Pharmacother*. **58** (2004) 173
10. L. Wang, J. Dong, J. Eastoe, X. Li, *J. Colloid Interf. Sci*. **330** (2009) 443
11. M. Milovic, J. Djuris, Lj. Djekic, D. Vasiljevic, S. Ibric, *Int. J. Pharm.* **436** (2012) 58
12. M. Milovic, J. Djuris, D. Vasiljevic, Z. Djuric. S. Ibric, *Hem. Ind.* **66** (2012) 667
13. D. Vasiljevic, J. Parojcic, M. Primorac, G. Vuleta, *J. Serb. Chem. Soc.* **74** (2009) 801
14. J. H. Collett, In: *Handbook of Pharmaceutical Excipients*, 6th ed., R. C. Rowe, P. J. Sheskey, M. E. Quinn, Eds., Pharmaceutical Press, London, 2009, p. 506
15. G. Dumortier, J. L. Grossiord, F. Agnely, J. C. Chaumeil, *Pharm. Res.* **23** (2006) 2709
16. N. Kolašinac, K. Kacrimanis, I. Homšek, B. Grujić, Z. Đurić, S. Ibrić, *Int. J. Pharm.* **436** (2012) 161
17. A. V. Shah, A. T. Serajuddin, *Pharm. Res.* **29** (2012) 2817
18. M. S. Mesiha, H. E. Bitar, *J. Pharm. Pharmacol*. **33** (1981) 733
19. Y. Hua, H. Y. Qing, C. F. Fanny, Z. Zhong, H. Yi Fan ,Y. Nancy, *Biopharm. Drug Dispos.* **32** (2011) 140
20. A. A. Attama, I. J. Ayogu, F. C. Kenechukwu, J. D. N. Ogbonna, V. C. Okore, *Int. J. Drug Delivery* **3** (2011) 743
21. V. Jannin, J. Musakhanian, D. Marchaud, *Adv. Drug Delivery Rev*. **60** (2008) 734
22. M. Sinn Aw, S. Simovic, Y. Yu, J. Addai-Mensah, D. Losic, *Nanomedicine* **6** (2011) 1159
23. D. Losic, J. G. Mitchell, N. H. Voelcker, *Adv. Mater.* **21** (2009) 2947
24. O. Planinšek, V. Kovačić, F. Vrečer, *Int. J. Pharm.* **406** (2011) 41
25. D. Bahl, R. H. Bogner, *AAPS Pharm. Sci. Tech.* **9** (2008) 146
26. M. Gupta, V. Adam, R. Bogner, *J. Pharm. Sci.* **92** (2003) 536
27. Y. Kobayashi, S. Itai, K. Yamamoto, *Int. J. Pharm.* **193** (2000) 137
28. S. Sethia, E. Squillante, *J. Pharm. Sci.* **91** (2002) 1948
29. G. L. Amidon, R. Löbenberg, *Eur. J. Pharm. Biopharm.* **50** (2000) 3
30. C. Xu, M. Zou, Y. Liu, J. Ren, Y. Tian, J. Yan, Y. Wang, G. Cheng, *Arch. Pharm. Res.* **34** (2011) 1973

31. A. Grzesiak, M. Lang, K. Kim, A. Matzger, *J. Pharm. Sci.* **92** (2003) 2261
32. *Guidance for Industry Dissolution Testing of Immediate Release Solid Oral Dosage Forms*, U.S. Department of Health and Human Services, Food and Drug Administration, Center for Drug Evaluation and Research (CDER), 1997
33. *Solubility Enhancement with BASF Pharma Polymers*, *Solublizer Compendium*, BASF, http://www.pharma-ingredients.basf.com/ (accessed 1.7.2014)
34. Y. Ito, H. Arai, K. Uchino, K. Iwasaki, N. Shibata, K. Takada, *Int. J. Pharm.* **289** (2005) 69
35. V. Agarwal, A. Siddiqui, H. Ali, S. Nazzal, *Int. J. Pharm.* **366** (2009) 44
36. A. Krupa, D. Majda, R. Jachowicz, W. Mozgawa, *Thermochim. Acta* **509** (2010) 12
37. H. Elde, G. Morsy, M. Bakr, *Asian J. Mater. Sci.* **2** (2010) 121
38. M. Bariana, M. S. Aw, M. Kurkuri, D**.** Losic, *Int. J. Pharm.* **443** (2013) 230
39. E. Batrakova, S. Lee, S. Li, A. Venne, V. Alakhov, A. Kabanov, *Pharm. Res.* **16** (1999) 1373
40. A. V. Kabanov, I. R. Nazarova, I. V. Astafieva, E. V. Batrakova, V. Y. Alakhov, A. A. Yaroslavov, V. A. Kabanov, *Macromolecules* **28** (1995) 2303
41. P. J. Marsac, T. Li, L. S. Taylor, *Pharm. Res.* **26** (2009) 139
42. L. Yu, S. M. Reutzel-Edens, C. A. Mitchell, *Org. Process Res. Dev.* **4** (2000) 396
43. C. Leuner, J. Dressman, *Eur. J. Pharm. Biopharm.* **50** (2000) 47
44. M. Yang, P. Wang, C. Y. Huang, M. S. Ku, H. Liu, C. Gogos, *Int. J. Pharm.* **395** (2010) 53
45. C. Rustichelli, G. Gamberini, V. Ferioli, M. C. Gamberini, R. Ficarra, S. Tommasini, *J. Pharm. Biomed. Anal.* **23** (2000) 41
46. W. Ali, A. C. Williams, CF. Rawlinson, *Int. J. Pharm.* **391** (2010) 162.

Journal of the Serbian Chemical Society
JSCS@tmf.bg.ac.rs • www.shd.org.rs/JSCS
J. Serb. Chem. Soc. 80 (2) S41–S43 (2015) *Supplementary material*

SUPPLEMENTARY MATERIAL TO

Application of experimental design in the examination of the dissolution rate of carbamazepine from formulations. Characterization of the optimal formulation by DSC, TGA, FT-IR and PXRD analysis

MARKO KRSTIĆ[1]*, SLAVICA RAŽIĆ[2#], DRAGANA VASILJEVIĆ[1], ĐURĐIJA SPASOJEVIĆ[1] and SVETLANA IBRIĆ[1]

[1]*Department of Pharmaceutical Technology and Cosmetology, Faculty of Pharmacy, University of Belgrade, Vojvode Stepe 450, P. O. Box 146, 11221 Belgrade, Serbia and* [2]*Department of Analytical Chemistry, Faculty of Pharmacy, University of Belgrade, Vojvode Stepe 450, P. O. Box 146, 11221 Belgrade, Serbia*

J. Serb. Chem. Soc. 80 (2) (2015) 209–222

TABLE S-I. Experimental plan for the second set of experiments

Formulation	Input parameters				
	*X*1	*X*2	*X*3	*X*4	*X*5
F1	+1	–1	–1	–1	–1
F2	–1	+1	+1	–1	–1
F3	–1	+1	–1	–1	+1
F4	+1	+1	+1	+1	+1
F5	–1	–1	–1	+1	+1
F6	+1	+1	–1	+1	–1
F7	–1	–1	+1	+1	–1
F8	+1	–1	+1	–1	+1

* Corresponding author. E-mail: mkrstic109@gmail.com

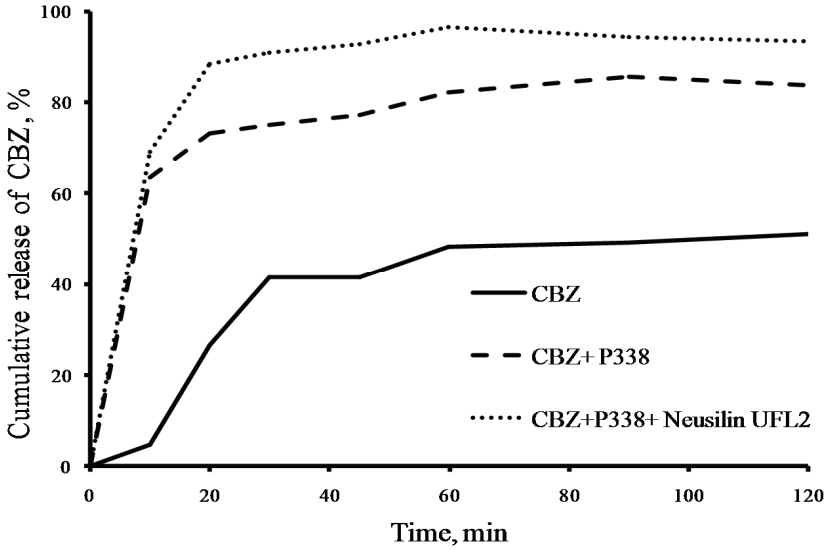

(A)

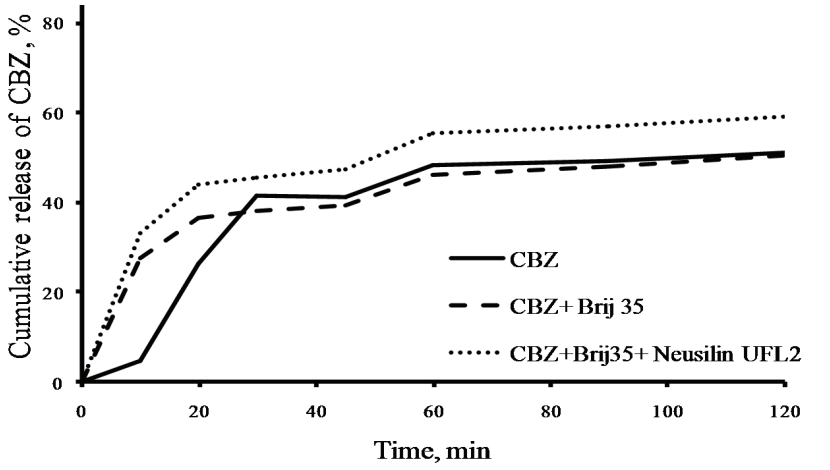

(B)

Fig. S-1. A) Dissolution profile of the mixture prepared with poloxamer 338 (P338) in the first set of experiments and pure CBZ; B) dissolution profile of the mixture prepared with Brij® 35 in the first set of experiments and pure CBZ.

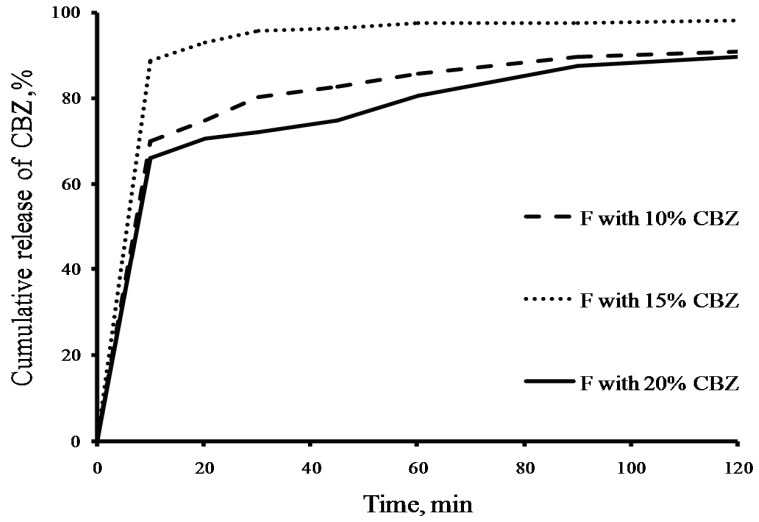

(A)

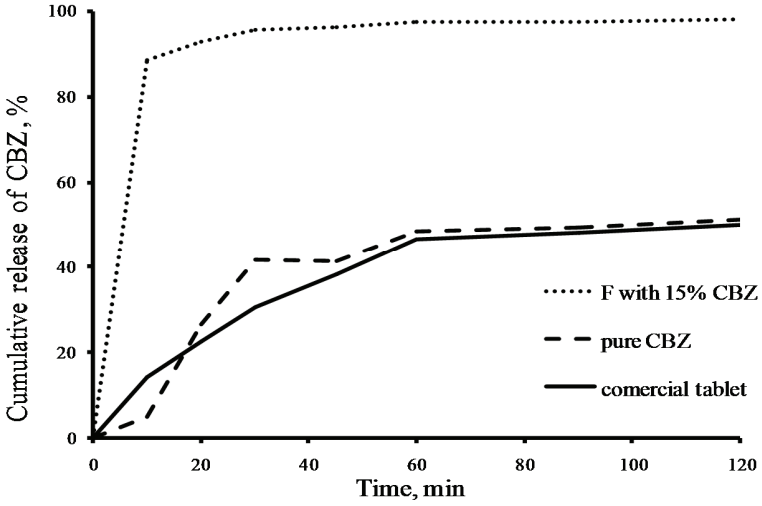

(B)

Fig. S-2. A) Dissolution profile of the CBZ formulation prepared in the second set of experiments with varied CBZ ratios; B) Dissolution profile of CBZ from optimal formulation, pure CBZ and commercial tablets of CBZ with immediate release.

Journal of the Serbian Chemical Society
JSCS-info@shd.org.rs • www.shd.org.rs/JSCS
J. Serb. Chem. Soc. 80 (2) 223–235 (2015)
JSCS–4712
UDC 677.52:678.742:541.124.2:548.3
Original scientific paper

The influence of glass fibers on the morphology of β-nucleated isotactic polypropylene evaluated by differential scanning calorimetry

ACO JANEVSKI[1]* and GORDANA BOGOEVA-GACEVA[2]

[1]*Faculty for Technology, "Goce Delcev" University, 2000 Stip, FYR Macedonia and* [2]*Faculty of Technology and Metallurgy, St. Cyril and Methodius University, 1000 Skopje, FYR Macedonia*

(Received 23 March, revised 26 May 2014, accepted 27 May 2014)

Abstract: The presence of fillers/fibers can significantly affect the polymorphic behavior of semi-crystalline polymers. The influence of glass fibers on morphology of β-nucleated isotactic polypropylene (iPP) during isothermal and nonisothermal crystallization was analyzed in detail by differential scanning calorimetry (DSC), and the kinetics and thermodynamic parameters were determined for the systems containing 10–60 % glass fibers. The presence of glass fibers in the model composites with β-iPP had an insignificant effect on the morphology of the polymer. Thermodynamic and kinetics parameters of crystallization of iPP in model composites were similar to those obtained for the nucleated polymer. The relative content of β-crystalline phase was slightly affected by increasing glass the fiber content from 10 to 60 mas. % due to appearance of α-crystallites. Moreover, the stability of the β-crystalline phase was decreased with increasing glass fiber content and there appeared a certain amount of β_1 and β_2 phases, which are known to be disposed to recrystallization.

Key words: crystallization; composites; DSC; polypropylene; β-nucleated.

INTRODUCTION

Isotactic polypropylene (iPP) is one of the most important commodity semi-crystalline thermoplastic widely used in many areas because of its versatility, good physical and mechanical properties, recyclability and low cost. iPP has been studied extensively for its polymorphic characteristics and crystallization behavior,[1–18] since the formation of specific crystalline forms (α, β and γ, or smectic) can affect the macroscopic behavior quite dramatically.[12–18] Commonly, under usual processing conditions, iPP crystallizes into the thermodynamically most stable monoclinic α-phase, which is responsible for its good

* Corresponding author. E-mail: aco.janevski@ugd.edu.mk
doi: 10.2298/JSC140324055J

strength and modulus. The trigonal β-form is metastable and can be obtained, or can become predominant, under specific crystallization conditions or in the presence of β-nucleating agents. β-Nucleated iPP exhibits large differences in mechanical properties as compared to the usual α-PP, namely higher toughness, ductility and drawability. The orthorhombic γ-form is the least frequently observed, and usually it can be obtained after crystallization at high pressures.[19–21]

The tailoring of polymorphic behavior of iPP, especially in composite materials where additional fiber-nucleating activity is observed,[4,7,22–27] seems to be important for the adjustment of the final properties of a material and the design of materials for certain applications. From a practical point of view, the addition of β-nucleating agents represents the most effective and accessible method to produce different levels of β-form iPP or even pure β-iPP. Among them, quinacridone pigment, pimelic acid/calcium stearate mixture, calcium salts of suberic or pimelic acid, calcium carbonate ($CaCO_3$) modified with dimeric aluminates, *N*,*N*-dicyclohexyl-terephthalamide and *N*,*N*-dicyclohexyl-2,6-naphthalene-dicarboxamide are reported in the literature.[11–14]

The properties of semi-crystalline polymers, used as matrices in composite materials are also related to the conditions during the processing cycle of heating (melting) and cooling (crystallization), since the morphology developed depends mostly on the time–temperature regime. For this reason, the differential canning calorimetry (DSC) method is often used for investigation of the behavior of filler/fiber–polymer composite materials in terms of crystalline structure and influencing parameters during isothermal or nonisothermal regimes.[24–28]

In a previous studies, the crystallization behavior and morphology of modified and unmodified iPP, used as a matrix in composites with differently sized/ /treated glass fibers, were thoroughly studied.[24–28] It was shown that glass fibers with a different surface chemistry exhibited different nucleating effects towards iPP, evaluated by crystallization parameters, but generally, they all acted as weak α-nucleators. In this work, the influence of glass fibers on the crystallization behavior, polymorphic composition and crystalline morphology of β-nucleated iPP was investigated.

EXPERIMENTAL

Commercial grade Shell homo-iPP with a weight-average molecular weight, $\bar{M}_w$, of 158,500 and a polydispersity index, $\bar{M}_w / \bar{M}_n$ of 6.36, as determined by gel permeation chromatography, GPC, was used. The concentrations of meso triads (0.94) and their average lengths (*n*) and probabilities for meso additions (0.96) were determined by ^{13}C-NMR spectroscopy. β-Nucleated iPP (BNP) was obtained by mixing 0.1 mas. % calcium pimelate with iPP in a Brabender mixer PL 2000 at 460 K. To study the influence of glass fibers (GF) on crystallization peculiarities and morphology of the polymer, model composites BNP/glass-fibers were prepared with 10, 20, 30, and 60 mas. % of GF (sized with thermoplastics compatible sizing). The abbreviations of model composites and their compositions are given in Table I.

TABLE I. Designation and content of the samples

Designation	Composition
BNP	iPP + 0.1 mass % Ca pimelate
C1BNPGF	BNP +10 mass % glass fiber
C2BNPGF	BNP + 20 mass % glass fiber
C3BNPGF	BNP + 30 mass % glass fiber
C6BNPGF	BNP + 60 mass % glass fiber
iPP	iPP Shell

Isothermal and nonisothermal crystallization of BNP was analyzed by DSC. In isothermal regime, the sample was rapidly heated to 478 K and held in the molten state for 5 min, to erase the thermal history of the polymer. Then the sample was cooled to a given crystallization temperature, T_c at a cooling rate of 80 K min^{-1}. Isothermal crystallization was realized at T_c until crystallization was completed. The crystallization under nonisothermal conditions was performed by cooling at different cooling rates: 1, 3, 5, 10, 15 and 20 K min^{-1}. The experiments were performed with a Perkin Elmer DSC-7 analyzer under nitrogen and indium and zinc were used for the calibration. The sample weight in all experiments was 7.0 mg. Based on the determined values for the enthalpy of crystallization, the extent of crystallization (crystal conversion), α, was calculated using Eq. (1):

$$\alpha = \frac{\int_0^t \left(\frac{\mathrm{d}H}{\mathrm{d}t}\right)\mathrm{d}t}{\int_0^\infty \left(\frac{\mathrm{d}H}{\mathrm{d}t}\right)\mathrm{d}t} = f(t) \quad (1)$$

From the obtained $\alpha = f(t)$ curves and the induction time (t_i), the half-time of crystallization ($t_{0.5}$) was determined.[28]

The amounts of α- and β-phase iPP in the model composites were calculated based on the corresponding melting enthalpies, $\Delta_{melt}H_\beta^0$ and $\Delta_{melt}H_\alpha^0$, using the following values: 193[29] and 209 J g^{-1},[30-32] respectively. The melting peaks of the both polymorphic phases appeared well resolved on the DSC thermograms, enabling the calculation of the amount of α- and β-phase iPP using Eqs. (2)–(4):[23,33]

$$X_\beta = \frac{\Delta_{melt}H_\beta}{\Delta_{melt}H_\beta^0} \quad (2)$$

$$X_\alpha = \frac{\Delta_{melt}H_\alpha}{\Delta_{melt}H_\alpha^0} \quad (3)$$

$$U_\beta = \frac{X_\beta}{(X_\alpha + X_\beta)} \quad (4)$$

where X_α and X_β are the amount of α- and β-phase, respectively, and U_β is the relative content of the β-phase in the overall crystalline structure of the sample.

Melt nucleation and crystallization of PPs were followed by polarizing light microscope (PLM, Leica, Biomed), equipped with a hot-stage device, temperature controller and photo camera.

The X-ray diffraction patterns were recorded on a Universal X-ray diffractometer with KCu$_\alpha$ radiation at 40 kV and 20 μA.

Theoretical background of the approach applied is given in the Supplementary material to this paper.

RESULTS AND DISCUSSION

Ca-pimelate is known as an efficient β nucleator for iPP.[34] The XRD-patterns of BNP obtained on addition of 0.1 mas. % calcium pimelate are presented in Fig. 1.

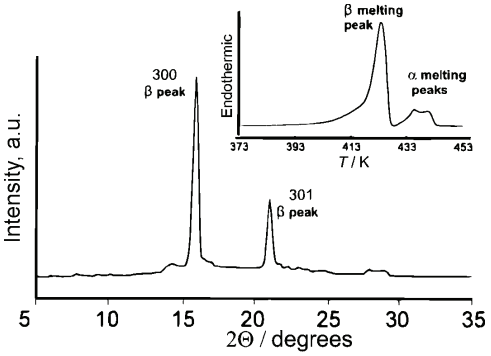

Fig. 1. X-Ray diffraction pattern and DSC melting thermogram (inset) of BNP.

Obviously, the dominant phase in this sample was the β-modification of iPP: the dominant peak at the diffraction angle 16.2° was attributed to the β (300) plane, while those of the α-modification (at 14.2, 17.0 and 18.4°, corresponding to the (110), (040) and (130) planes, respectively) were of weak intensity. Consistent with the results from XRD analysis, the melting DSC peak of the β crystallites (T_m = 424.2 K) was of high intensity, contrary to the one arising from the presence of α crystallites. The characteristic morphology of β-spherulites, originating after mixing iPP with Ca-pimelate, is also clearly illustrated in Fig. 2. The K_β parameter determined from the XRD-patterns by the Turner–Jones method[35] was 0.94, while the U_β-value calculated from the melting endotherm was 0.84 (Fig. 1, inset).

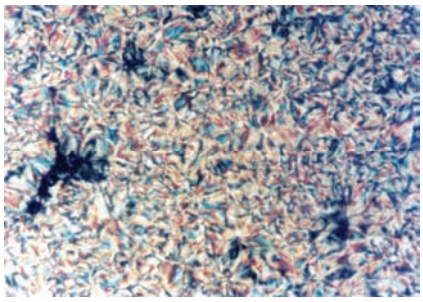

Fig. 2. Polarizing optical micrograph of BNP.

The isothermal crystallization of BNP and the composites were performed at temperatures from 388 to 409 K, the range, according to Hoffman,[36–39] known as

region III. The DSC melting curves of the isothermally crystallized samples at different T_c values are shown in Fig. 3. The melting peak temperature of the samples appeared at 418–428 K.

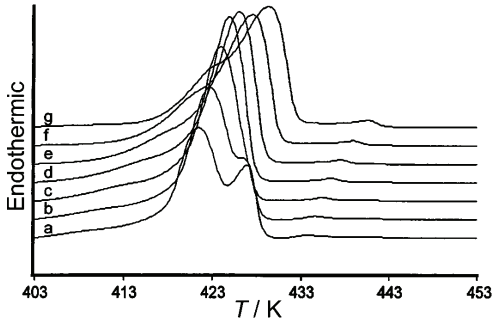

Figure 3. DSC melting thermograms of BNP after isothermal crystallization at different T_c values: a) 391; b) 394; c) 397; d) 400; e) 403; f) 406 K; g) 409 (heating rate 10 K min^{-1}).

Small endotherms, arising from the melting of α-crystallites present in the samples are seen along with the main peak of the β-crystallites (Fig. 3). The crystal structures β_1 and β_2[14] were registered during the melting of the samples crystallized at temperatures lower than 397 K. The DSC melting thermograms obtained after crystallization at T_c values higher than 397 K are used to determine the equilibrium melting temperature, T_m^0, applying the Hoffman–Weeks method,[40] and the results for BNP in comparison to iPP and GF-composites are presented in Table II.

Table II. Surface energies, σ_e, equilibrium melting temperatures, T_m, and the γ constants determined from isothermal DSC data

Parameter	BNP	C1BNPGF	C2BNPGF	C3BNPGF	C6BNPGF	iPP
T_m^0 / K	446.0	451.1	452.0	451.0	451.0	465.7
$\sigma_e \times 10^3$ / J m^{-2}	80.7	93.0	105.0	102.0	101.0	208
γ	2.20	1.84	1.81	1.86	1.87	2.37
θ	0.34	0.44	0.46	0.43	0.43	1.00

The determined value of 446 K for T_m^0 lies in the range of values previously published for β-iPP.[36,38]

The Avrami plots for BNP and the model BNP/glass fiber composites in the investigated region of crystallization temperatures, similarly to other β-nucleated systems,[42–44] were almost linear (Fig. 4), although two crystal phases with different energetic parameters were formed during the crystallization. Linearity of these plots enabled the determination of the overall kinetics parameters, which are not related to the certain crystalline phase but represent overall characteristic of the system as a whole (Table III).

In the Avrami equation, *n* may show values ranging from below 1 to far above 6. Any one value, whole or fractional, however, is not uniquely fixed to

any one set of conditions. Additional information on nucleation, morphology, and possibly even mechanism is necessary to interpret fully the exponent *n*. For many macromolecules, *n* is close to three and a picture of a thermal heterogeneous nucleation followed by spherulitic growth is acceptable; others require = *n* = 4, indicative of thermal nucleation, which is most often thermal heterogeneous nucleation followed by spherulitic growth. The also frequently observed exponent *n* = 2 could well be related to fibrillar or lamellar crystal growth following thermal or athermal nucleation. The Avrami index *n* is composed of both a geometric index *n** and a nucleation index *m*. The latter may have a wide range of values, depending on the nature of the nucleation process. This comprehension provides a basis to understand better the many non-integer values of *n* occurring in the literature, as well as values that are greater than 4.[42]

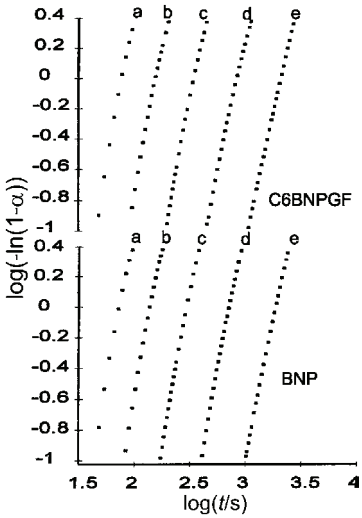

Fig. 4. Avrami plots for BNP and C6BNPGF at different T_c values: a) 397; b) 400; c) 403; d) 406; e) 409 K.

Table III. Avrami index, *n*, and the overall kinetic constant, *k*, at different T_c values

T_c / K	BNP		C1BNPGF		C2BNPGF		C3BNPGF		C6BNPGF	
	n	k / 10^{-10} s^{-n}	*n*	k / 10^{-10} s^{-n}	*n*	k / 10^{-10} s^{-n}	*n*	k / 10^{-10} s^{-n}	*n*	k / 10^{-10} s^{-n}
397	3.9	600	3.8	650	4.1	130	4.3	130	4.0	220
400	3.9	32	3.9	34	3.9	21	3.9	30	3.7	65
403	3.9	1.9	3.8	2.2	3.7	2.8	3.7	4.8	3.7	4.4
406	3.8	0.16	3.8	0.089	3.5	0.67	3.4	1.3	3.4	1.2
409	3.5	0.026	3.8	0.085	3.1	0.74	3.3	0.15	3.3	0.078

The Avrami exponent, *n*, had values between 3.1 and 4.3, indicating that heterogeneous nucleation occurred and a tendency of decreasing *n* with increasing T_c was noticed, and it is more pronounced with increasing glass fiber content.

The exponent n ranging from 3.74 to 4.35 were determined for composite systems with β-nucleated iPP and talc-nucleated iPP.[41]

The results for T_m^0, σ_e, the γ-constant and the parameter θ for the model composites are summarized in Table II. As can be seen, the values of T_m^0 increased with increasing glass fiber content and they had values between those for β-nucleated iPP and iPP.

Generally, a good nucleating agent provides a surface that reduces the free energy barrier for primary nucleation. The low energy required implies a highly effective nucleating agent. The crystal fold surface energy (σ_e) for BNP, determined in this study was 80.7 mJ m^{-2}, which was similar to that found by Varga.[39] Generally, different values for σ_e are reported in the literature, mostly depending on the investigated region of crystallization. The σ_e obtained for region III (that, according to some authors, starts at 410 K[36] and to others at 406 K[37]) ranges from 85.4 to 48–67 mJ m^{-2}.[38,41] The value of 85.5 mJ m^{-2} was determined by Li *et. al* for β-nucleated iPP compared to 107, mJ m^{-2} for the neat polymer.[43] In the present model composite systems, the σ_e values increased with increasing content of glass fibers.

The curves of induction time for crystallization, t_i and the half-time of crystallization, $t_{0.5}$ versus supercooling are shown in Fig. 5. Obviously, the values of both t_i and $t_{0.5}$ determined for the GF-model composites are closer to those determined for BNP. A similar tendency was also found for the values of σ_e.

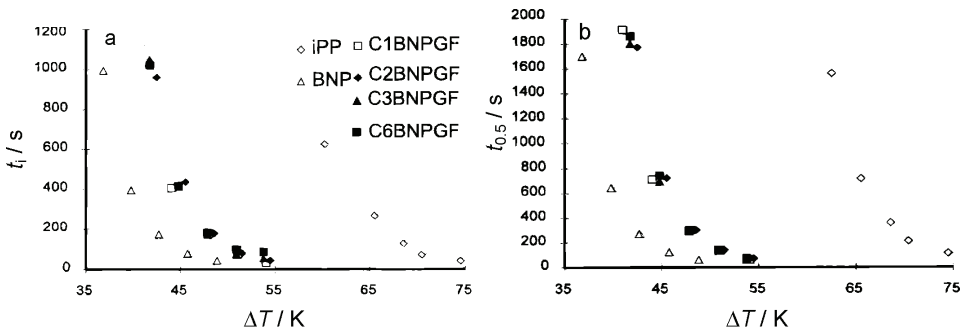

Fig. 5. Dependence of the induction time (a) and the half-time of crystallization (b) for iPP, BNP and the BNP/GF-composites on ΔT_c.

Based on the kinetics parameters and calculated value for T_m^0, the energy of the formation of a nucleus with critical dimensions was determined, and the results are shown in Fig. 6 as the ratio between the energy in a given system (BNP or composite sample) and the energy of a non-nucleated system. It could be concluded that favorable conditions for nucleation were attained in the nucleated polymer, whereas in the model composites with glass fibers, the nucleation

was slightly depressed. This finding was confirmed by the dependence of this factor (obtained for T_c = 409 K) on the content of glass fibers, as shown in Fig. 7.

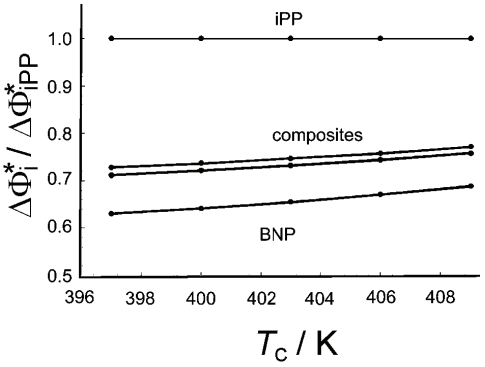

Fig. 6. Ratios of the energy of formation of nuclei of critical dimensions for iPP, BNP and the GF-composites *vs.* T_c.

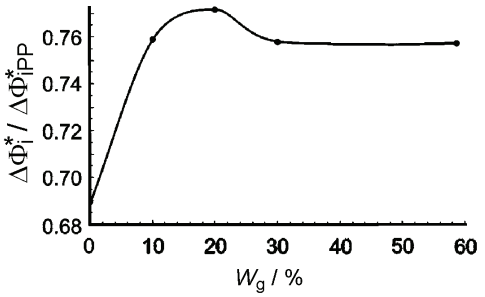

Fig. 7. Ratios of the energy of formation of nuclei of critical dimensions *vs.* the content of glass fibers (W_g / mas. %) at T_c = 409 K.

From the melting thermograms (melting performed after isothermal crystallization), the amounts of the α- and β-phase in the model composites were determined (Fig. 8). The amount of β-phase in iPP and C1BNPGF slightly increased with increasing T_c, while in composites with 20–60 mas. % glass fibers, it decreases at $T_c \geq 403$ K.

The content of α-phase, although low, increased with increasing T_c, while U_β decreased (Fig. 9), and this trend was most pronounced in the composite sample with 60 mas. % glass fibers.

As it is evident from Figs. 8 and 10, despite the high amount of glass fibers in the model composites, the relative content of the β-crystalline phase was over 0.85 for C6BNPGF and even higher for the composites with less than 60 mas. % glass fibers. It should be mentioned that a similar effect was found for PP/multi-walled carbon nanotubes, surface treated with β-nucleators: namely, the amount of β phase decreased by increasing filler content.[7] Investigation of iPP/Kevlar fiber composites revealed the strong α-nucleating ability of these fibers and the presence of a transcrystalline layer on their surface. However, for β-nucleated iPP/Kevlar fiber composites, the dominant modification was the β-form, and their crystallization characteristics were independent of the addition of Kevlar

fibers, indicating that the α-nucleating effect of Kevlar fibers was masked by the β-nucleating effect of the β-nucleator.[46]

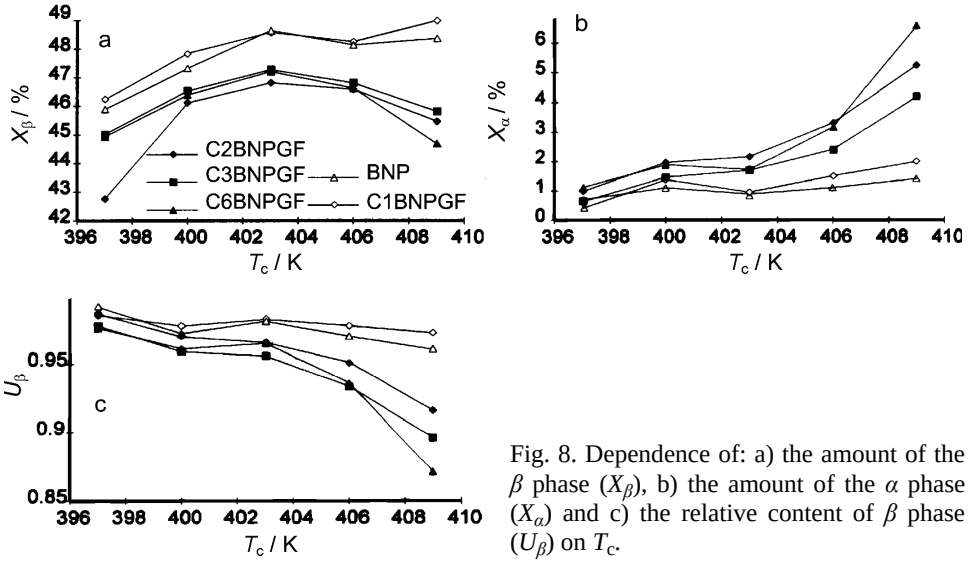

Fig. 8. Dependence of: a) the amount of the β phase (X_β), b) the amount of the α phase (X_α) and c) the relative content of β phase (U_β) on T_c.

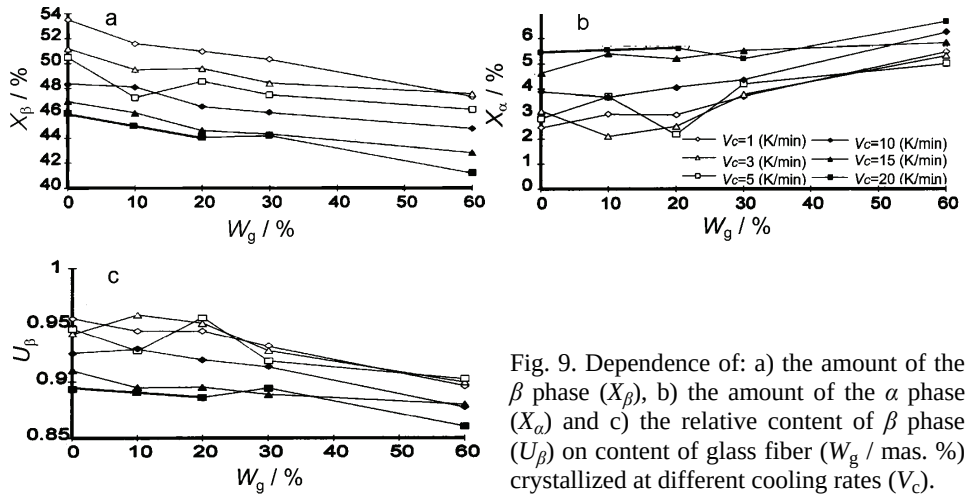

Fig. 9. Dependence of: a) the amount of the β phase (X_β), b) the amount of the α phase (X_α) and c) the relative content of β phase (U_β) on content of glass fiber (W_g / mas. %) crystallized at different cooling rates (V_c).

It could be concluded that the increased T_m^0 and σ_e observed for some model composites resulted from the increased content of α-phase. This is in agreement with the findings of Varga[41] that the variations in the results for the thermodynamic and kinetics parameters for β-iPP are most probably due to the presence of different amounts of α-phase in the examined samples.

The results of nonisothermal crystallization showed that heterogeneous nucleation activity is predominant in the model composites, even at low glass

fiber contents. The nucleation activity during the crystallization of the polymer melt was evaluated by the Dobreva method,[45] which enables the determination of the work of heterogeneous and homogeneous nucleation in polymer systems with different additives/substrates by calculating the θ-parameter. For an extremely active substrate $\theta = 0$ and for an inert substrate $\theta = 1$.

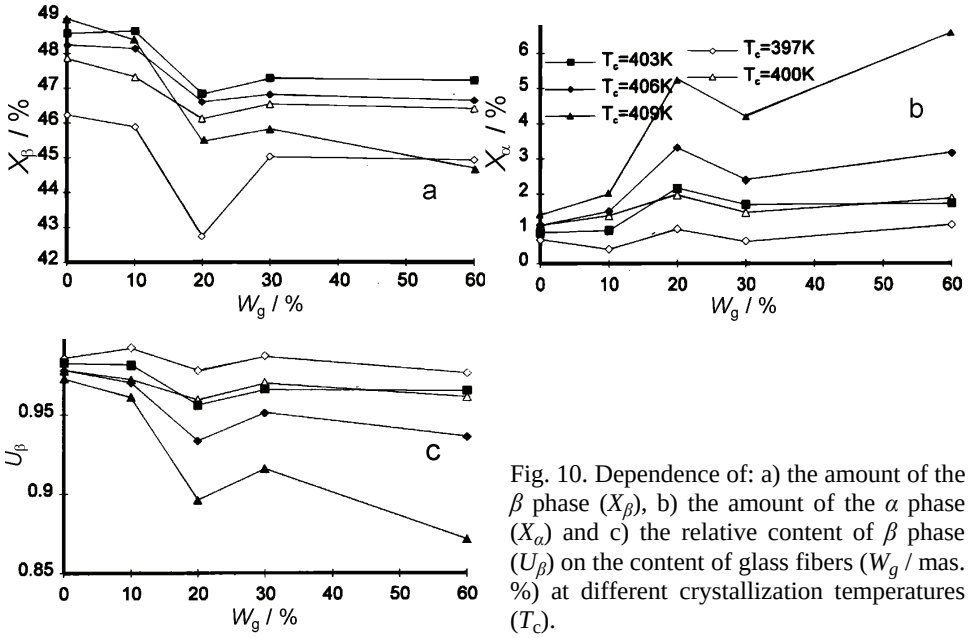

Fig. 10. Dependence of: a) the amount of the β phase (X_β), b) the amount of the α phase (X_α) and c) the relative content of β phase (U_β) on the content of glass fibers (W_g / mas. %) at different crystallization temperatures (T_c).

The results for θ-parameter are collected in Table II. For BNP, $\theta = 0.34$, and this low value was expected, since all the β-phase ($U_\beta = 0.95$ for $V_c = 1$ K min^{-1} and $U_\beta = 0.90$ for $V_c = 20$ K min^{-1}) originated from heterogeneous nucleation. In GF-model composites, the heterogeneous nucleation was obviously depressed to some level by the presence of the fibers and the θ-parameter reached higher values, 0.43–0.46.

The appearance of the α-phase in the model composites was obviously a consequence of the presence of the glass fibers (Fig. 9). In a previous investigation, it was shown that the glass fibers influenced the stability of the α-crystalline phase in glass fiber/iPP composites.[26] Their presence in BNP composites resulted in a similar effect, namely they induced the formation of certain amounts of the α-crystalline phase.

DSC melting traces of the non-isothermally crystallized C6BNPGF sample and BNP are shown in Fig. 11: similarly to the existence of two α phases in iPP (α_1 and α_2 crystalline modifications, susceptible to recrystallization), there appeared two melting peaks characteristic for the corresponding β phases of iPP.[41]

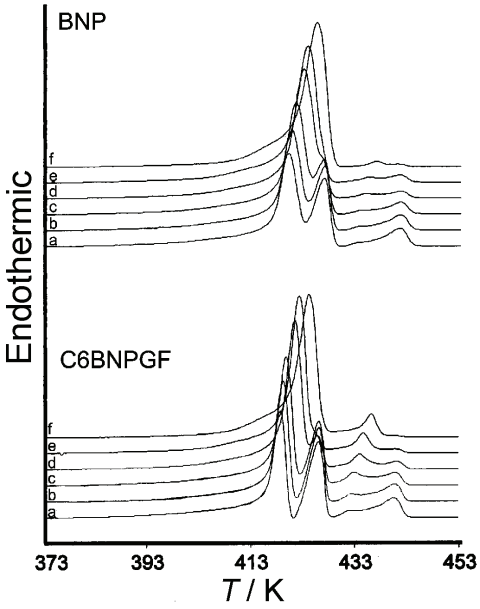

Fig. 11. Heating thermograms of BNP and C6BNPGF crystallized at different cooling rates (V_c): a) 20, b) 15, c) 10, d) 5, e) 3 and f) 1 K min^{-1}.

As a measure of the stability of the β crystal structure, the difference between the maximum of the high and low-melting peaks, ΔT_{mp} were used,[26] which are a consequence of the melting and recrystallization processes of the β_1 and β_2 crystalline modifications.[14] The dependences of ΔT_{mp} on the cooling rate, crystallization peak temperature and glass fiber content are shown in Fig. 12. As could be seen, the presence of glass fibers and their content influences the stability of the β-crystalline phase and this effect becomes more evident at $V_c \geq 3$ K min^{-1}.

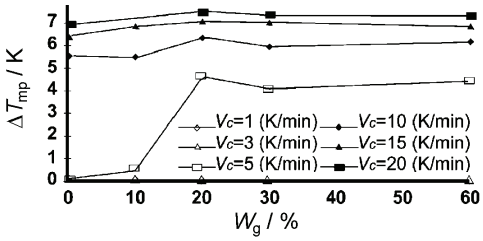

Fig. 12. Dependence of the difference between the maximum of the high and low-melting peaks (ΔT_{mp}) on content of glass fibers crystallized at different cooling rates (V_c).

CONCLUSIONS

Glass fibers, as weak α-nucleators for iPP, had an insignificant effect on the morphology of β-nucleated iPP in glass fiber composites. The thermodynamic and kinetics parameters of crystallization of BNP in the model composites were similar to those obtained for the nucleated polymer. The relative content of β-crystalline phase decreased only by several percents on increasing the content

of glass fibers from 10 to 60 mas. %, due to the appearance of α-crystallites. The relative content of β-phase depended mostly on the crystallization conditions; the lowest value of U_β (for the highest fiber content) was 0.85. The combination of excellent mechanical properties of glass fibers and the high content of the stable β-phase structure of BNP makes this system appropriate for the development of BNP/glass fiber composites with a good balance of strength and toughness.

SUPPLEMENTARY MATERIAL

Theoretical background of the approach applied is available electronically from http://www.shd.org.rs/JSCS/, or from the corresponding author on request.

ИЗВОД

УТИЦАЈ СТАКЛЕНИХ ВЛАКАНА НА МОРФОЛОГИЈУ β-НУКЛЕИСАНОГ iPP АНАЛИЗИРАН ПОМОЋУ DSC

ACO JANEVSKI[1] и GORDANA BOGOEVA-GACEVA[2]

[1]*Faculty for Technology, Goce Delcev University, 2000 Štip, Macedonia и* [2] *Faculty of Technology and Metallurgy, St. Cyril and Methodius University, 1000 Skopje, FYR Macedonia*

Присуство пуниоца и влакана значајно утиче на морфологију семикристалних полимера. Утицај стаклених влакана на морфологију β-нуклеисаног изотактичног поли(припилена) (iPP) формираног током изотермске или неизотермске кристализације, праћен је DSC анализом, а кинетички и термодинамички параметри кристализације су одређени за композите са садржајем стаклених влакана 10–60 mas. %. Присуство стаклених влакана у модел композиту са β-iPP незнатано утиче на морфологију полимерне матрице. Термодинамички и кинетички параметри кристализације i-PP у модел композиту су веома слични добијеним са β-нуклеисаним полимером. Са порастом садржаја стаклених влакана од 10 do 60 mas. % незнатно је промењен и релативни садржај β-кристалне фазе као последица појаве α-кристалита. Међутим, стабилност β-кристалне фазе се смањује са повећањем садржаја стаклених влакана и појаве β_1 и β_2 фаза, које су познате по томе што лако подлежу рекристализацији.

(Примљено 23 марта, ревидирано 26. маја, прихваћено 27. маја 2014)

REFERENCES

1. J. G. Jiang, G. Li, H. Liu, Q. Ding, K. Mai, *Composites, A* **45** (2013) 88
2. T. Bàràny, A. Izer, J. Karger-Kocsis, *Polym. Test.* **28** (2009) 176
3. Q. Ding, Z. Zhanga, C. Wanga, J. Jiang, G. Li, K. Mai, *Thermochim. Acta* **536** (2012) 47
4. J. Jiang, G. Li, N. Tan, Q. Ding, K. Mai, *Thermochim. Acta* **546** (2012) 127
5. Q. Ding, Z. Zhang, C. Wang, J. Jiang, G. Li, K. Mai, *Polym. Bull.* **70** (2013) 919
6. S. Wang, W. Yang, R. Bao, B. Wang, B. Xie, M. Yang, *Colloid Polym. Sci.* **288** (2010) 681
7. N. Zhang, Q. Zhang, K. Wang, H. Deng, Q. Fu, *J. Therm. Anal. Calorim.* **107** (2012) 733
8. A. Menyhàrd, G. Dora, Z. Horvàth, G. Faludi, J. Varga, *J. Therm. Anal. Calorim.* **108** (2012) 613
9. L. Xu, X. Zhang, L. Zhu, X. Lian, K. Xu, M. Chen, *J. Macromol. Sci., B* **50** (2011) 89
10. J. Menczel, J. Varga, *J. Therm. Anal.* **28** (1983) 161
11. C. Grein, *Adv. Polym. Sci.* **188** (2005) 93

12. R. Cermak, M. Obadal, P. Ponizil, M. Polaskova, K. Stoklasa, A. Lengalova, *Eur. Polym. J.* **41** (2006) 1836
13. J. Kotek, M. Raab, J. Baldrian, W. Grellmann, *J. Appl. Polym. Sci*. **85** (2002) 1174–1184.
14. J. Varga, *J. Macromol. Sci. Phys*. **41** (2002) 1121
15. H. B. Chen, J. Karger-Kocsis, J. S. Wu, J. Varga, *Polymer* **43** (2002) 6505
16. R. Cermak, M. Obadal, P. Ponizil, M. Polaskova, K. Stoklasa, A. Lengalova, *Eur. Polym. J.* **42** (2006) 2185
17. C. Grein, G. Plummer, H. Kausch, Y. Germain, P. Beguelin, *Polymer* **43** (2002) 3279
18. M. Fujiyama, *Int. Polym. Proc.* **10** (1995) 172
19. S. Brückner, V. Meille, V. Petraccone, B. Pirozzi, *Prog. Polym. Sci*. **16** (1991), 361
20. B. Lotz, J. C. Wittmann, A. J. Lovinger, *Polymer* **37** (1996) 4979
21. J. Varga, in *Polypropylene: Structure, Blends and Composites*, Vol. 1, *Structure and Morphology*, J. Karger-Kocsis, Ed., Chapman & Hall, London,1995, p. 56
22. A. Zeng, Y. Zheng, Y. Guo, S. Qiu, L. Cheng, *Mater. Design* **34** (2012) 691
23. M. R. Meng, Q. Dou, *J. Macromol. Sci. B* **48** (2009) 213
24. G. Bogoeva-Gaceva, A. Janevski, E. Mader, *Polymer* **42** (2001) 4409
25. G. Bogoeva-Gaceva, A. Janevski, E. Mader, E. *J. Adhes. Sci. Technol.* **14** (2000) 363
26. A. Janevski, G. Bogoeva-Gaceva, E. Mader, *J. Appl. Polym. Sci*. **74** (1999) 239
27. A. Janevski, G. Bogoeva-Gaceva, *J. Appl. Polym. Sci.* **69** (1998) 381
28. G. Bogoeva-Gaceva, A. Janevski, A. Grozdanov, *J. Appl. Polym. Sci*. **67** (1988) 395
29. G. Shi, B. Huang, J. Zhang, *Makromol. Chem.-Rapid Commun.* **5** (1984) 573
30. M. Avella, E. Martuscelli, C. Sellit, E. Garagnani, *J. Mater. Sci.* **22** (1987) 3185
31. B. Monasse, J. M. Haudin, *Colloid Polym. Sci*. **264 (**1986) 117
32. S. Brandup, and E. H. Imergut, , *Polymer Handbook*, Interscience, New York, 1975, p. 24
33. M. Liu, B. Guo, M. Du, F. Chen, D. Jia, *Polymer* **50** (2009) 3022
34. J. Varga, F. Schulec-Toth, M. Pati, (J. Varga), Hungarian Patent Application, P92 01422, 1992
35. A. Turner-Jones, J. M. Aizlewod, D. R. Beckett, *Makromolekul. Chem.* **75** (1964) 134
36. G. Shi, X. Zhang, Z. Qui, *Makromolekul. Chem.* **193** (1992) 583
37. J. Garbarczuk, *Makromolekul. Chem.* **186** (1985) 2145
38. J. Varga, Y. Fujiwara, A. Ille, *Periodica Polytech. Chem. Eng.* **34** (1990) 255
39. J. Varga, in *Polypropylene: Structure, Blends and Composites*, Vol. 1, *Structure and Morphology*, J. Karger-Kocsis, Ed., Chapman & Hall, London, 1995, p. 80
40. J. D. Hoffman, *Soc. Plast. Eng. Trans.* **4** (1964) 315
41. J. Varga, I. Mudra, G. Ehrenstein, *J. Appl. Polym. Sci*. **74** (1990) 2357
42. J. Duan, Q. Dou, *J. Appl. Polym. Sci*. **130** (2013) , 206
43. R. Zhang, R. K. Y. Li, *Polym. Int*. **62** (2013) 919
44. Z. Zhao, Z. Cai, Z. Xin, *Polymer* **49** (2008) 2745
45. V. Dobreva, I. Gutzov, *Cryst. Res. Technol.* **25** (1990) 927
46. Y. Cao, J. Feng, P. Wu, *J. Therm. Anal. Calorim.* **103** (2011) 339.

Journal of the Serbian Chemical Society
JSCS@tmf.bg.ac.rs • www.shd.org.rs/JSCS
J. Serb. Chem. Soc. 80 (2) S44–S46 (2015) *Supplementary material*

SUPPLEMENTARY MATERIAL TO

The influence of glass fibers on the morphology of β-nucleated isotactic polypropylene evaluated by differential scanning calorimetry

ACO JANEVSKI[1]* and GORDANA BOGOEVA-GACEVA[2]

[1]*Faculty for Technology, "Goce Delcev" University, 2000 Stip, FYR Macedonia and* [2]*Faculty of Technology and Metallurgy, St. Cyril and Methodius University, 1000 Skopje, FYR Macedonia*

J. Serb. Chem. Soc. 80 (2) (2015) 223–235

THEORETICAL BACKGROUND

From the DSC scans (isothermal crystallization at given T_c and then melting of the crystallized sample), the equilibrium melting temperature (T_m^0) was determined by the Hoffman–Weeks method:[1]

$$T_m' = \frac{T_m^0(\gamma-1)}{\gamma} + \frac{T_c}{\gamma} \quad (1)$$

where γ is a constant that represents the ratio between the final thickness of the crystalline lamellae and the initial critical thickness, and T_m' is the observed melting temperature of the sample isothermally crystallized at T_c. According to the kinetic theory of polymer crystallization,[2] assuming that the growth of lamellae is controlled by a process of secondary nucleation, the temperature dependence of the overall kinetic constant, k, is given by the Eq. (2):

$$\frac{\log(k)}{n} = A_0 - \frac{\Delta F^*}{2.3RT_c} - \frac{\Delta \Phi^*}{2.3KT_c} \quad (2)$$

where A_0 is a constant (assuming that the primary nucleation density at each T_c examined does not vary with time), ΔF^* is the activation energy for the transport of crystallizing units across the liquid–solid interface, K is the Boltzmann constant, n is the Avrami exponent, and $\Delta\Phi^*$ is the energy of formation of a nucleus with critical dimensions, expressed by Eq. (3):[2]

$$\Delta \Phi^* = \frac{4b_0\sigma\sigma_e T_m}{\Delta_{melt}H\Delta T} \quad (3)$$

where b_0 is the molecular thickness, and σ and σ_e are the crystal growth lateral surface energy and the crystal fold surface energy, respectively. $\Delta_{fus}H$ is the enthalpy of fusion and

* Corresponding author. E-mail: aco.janevski@ugd.edu.mk

$\Delta T = T_m^0 - T_c$ is the supercooling. ΔF^* is usually expressed as the activation energy of viscous flow given by the Williams–Landel–Ferry relation, Eq. (4):[3]

$$\Delta F^* = \frac{C_1 T_c}{(C_2 + T_c - T_g)} \tag{4}$$

where C_1 and C_2 are constants (C_1 = 17.2 kJ mol^{-1}; C_2 = 51.5 K) and T_g is the glass transition temperature. In further calculations, the literature value of T_g = 260 K was used for iPP.[4] The plot of: [log k/n + $\Delta F^*/2.3RT_c$] *vs.* $T_m^{'}/T_c\Delta T$ yields a straight line with a negative slope equal to:

$$\frac{4b_0\sigma\sigma_e}{2.3K\Delta_{fus}H} \tag{5}$$

from which ΔF^* and σ_e are obtained assuming that b_0 = 0.525 nm[5] and $\Delta_{fus}H$ of 193 and 209 J g^{-1}, and $\sigma = 0.1b_0\Delta_{fus}H$.

To calculate the nucleation activity (θ) of foreign additives and substrates during the crystallization of a polymer melt, a method was proposed by Dobreva *et al.*[6] for analyzing DSC data. θ is defined as:

$$\theta = \frac{A_{k3}^*}{A_{k3}^0} \tag{6}$$

where

$$A_{k3}^0 = \frac{16\pi\sigma V_m^2}{3\Delta_{melt}S^2\Delta T_p^2} \tag{7}$$

is the work of homogeneous nucleation, in which V_m is molar volume of the crystallizing substance, $\Delta_{melt}S$ is entropy of melting and $\Delta T_p = T_m^0 - T_{cmax}$ (where T_{cmax} corresponds to the crystallization peak temperature in the nonisothermal regime), and A_{k3}^* is the work of heterogeneous nucleation, Clearly, θ is unity for absolutely inert substrates and is practically zero for very active substrates. Following the formalism presented by Dobreva *et al.*,[6] the Avrami equation[7] (8):

$$\alpha = 1 - \exp(-kt^n) \tag{8}$$

for nonisothermal conditions can be transformed into:

$$\log(V_c) = \text{const} - \frac{B^0}{2.3\Delta T_p^2} \tag{9}$$

where

$$B^0 = \frac{16\pi\sigma V_m^2}{3T_m^0\Delta_{melt}S^2} \tag{10}$$

and where V_c is the cooling rate. The activity of a substrate, θ, is then given by the ratio of the two slopes B^* and B_0.

REFERENCES

1. J. D. Hoffman, *Soc. Plast. Eng. Trans.* **4** (1964) 315

2. J. D. Hoffman, G. T. Davis, S. I. Lauritzen Jr., in *Treatise on Solid State Chemistry*, N. B. Hannay, Ed., Plenum, New York, 1976, p. 407
3. H. L. Williams, R. F. Landel, J. D. S. Ferry, *J. Am. Chem. Soc.* **77** (1995) 3701
4. L. Grispino, E. Martusceli, M. Pracella, *Makromolekul. Chem.* **181** (1980) 1747
5. J. Garbarczuk, *Makromolekul. Chem.* **186** (1985) 2145.
6. V. Dobreva, I. Gutzov, *Cryst. Res. Technol.* **25** (1990) 927
7. M. Avrami, *J Chem. Phys* **7** (1939) 1103.

Journal of the Serbian Chemical Society
JSCS-info@shd.org.rs • www.shd.org.rs/JSCS
J. Serb. Chem. Soc. 80 (2) 237–251 (2015)
JSCS–4713
UDC 546.41'185+544.27+544.654.2:
621.793:539.217
Original scientific paper

The porosity and roughness of electrodeposited calcium phosphate coatings in simulated body fluid

MARIJA S. DJOŠIĆ[1], MIODRAG MITRIĆ[2] and VESNA B. MIŠKOVIĆ-STANKOVIĆ[3*#]

[1]Institute for Technology of Nuclear and Other Mineral Raw Materials, Franše d'Epere 86, 11000 Belgrade, Serbia, [2]Institute of Nuclear Sciences "Vinča", University of Belgrade, P. O. Box 522, 11001 Belgrade, Serbia and [3]Faculty of Technology and Metallurgy, University of Belgrade, Karnegijeva 4, P. O. Box 3503, 11120 Belgrade, Serbia

(Received 26 June, revised 1 October, accepted 2 October 2014)

Abstract: Calcium phosphate coatings were electrochemically deposited on titanium from an aqueous solution of $Ca(NO_3)_2$ and $NH_4H_2PO_4$ at a current density of 10 mA cm^{-2} for a deposition time of 15 min. The obtained brushite coatings ($CaHPO_4 \cdot 2H_2O$), were converted to hydroxyapatite (HA) by soaking in simulated body fluid (SBF) for 2, 7 and 14 days. The brushite and hydroxyapatite coatings were characterized by X-ray diffraction (XRD), scanning electron microscopy (SEM) and atomic force microscopy (AFM). It was shown that increasing the soaking time increased the porosity, roughness and crystallite domain size of the HA coatings and decreased the unit cell parameters and unit cell volume, while the mean pore area of HA was unaffected. The calcium and phosphorus ions concentrations in SBF were determined by atomic absorption spectroscopy (AAS) and UV–Vis spectroscopy, respectively, and a mechanism of HA growth based on dissolution–precipitation was proposed.

Keywords: hydroxyapatite; brushite; coatings; nanostructures; titanium.

INTRODUCTION

Metals have been used in various forms as implants due to their excellent mechanical properties, but lack of biocompatibility and corrosion resistance make metals inadequate for implantation in the body. The main reasons for applying ceramic coating on metal substrates are to protect the substrate against corrosion, to make the implant biocompatible and to turn the non-bioactive metal surface into a bioactive one.[1,2]

* Corresponding author. E-mail: vesna@tmf.bg.ac.rs
# Serbian Chemical Society member.
doi: 10.2298/JSC140626098D

The main constituents of human bone are calcium orthophosphates, collagen and water. Hydroxyapatite (HA, $Ca_{10}(PO_4)_6(OH)_2$), constitutes the majority of the inorganic component. HA is the only compound among calcium phosphate-based ceramics that is stable in a physiological environment and is biologically active. Applications of HA bioceramics are based on its excellent bioactivity, biocompatibility and porous structure. Both the micro- and macro-porosity of HA coatings are important. The macroporosity controls access of tissue and biological fluids to HA coatings. The microporosity controls protein adsorption, body fluid circulation and the resorption rate of calcium phosphate. The porous structure of HA improves the mechanical interlock between the cells and the surface of an implant, promotes osteoconductivity and enhances the adhesion between natural bone and an implant by the formation of an apatite layer.[3–5] Besides the coating porosity, a very important characteristic is the roughness of a coating, because the biocompatibility and corrosion resistance of implants are, also, determined by surface microstructural properties, such as surface roughness and grain size, which influence cell attachment, proliferation and differentiation.[6,7] There are a great number of methods for HA preparation,[8–12] including transformation of more soluble metastable phosphates, as precursors, *e.g.*, brushite, monetite and octacalcium phosphate, in an aqueous environment.[13–20]

The application of HA coatings depends on its crystallite size. It is possible to improve the characteristics of HA by controlling the particle size, particle distribution and agglomeration of precursors. Nanocrystalline HA exhibits a greater surface area and has better bioactivity than coarser crystals.[21–24]

Brushite, $CaHPO_4{\cdot}2H_2O$, is a metastable compound, known as mineral brushite. It can be observed when calcium phosphate is precipitated at low pH values and low temperatures.[20,25,26] As a precursor, brushite transforms into thermodynamically more stable calcium phosphates. Brushite can be converted to HA by alkaline treatment or by soaking in simulated body fluid (SBF).[20,27–31] The kinetics of brushite transformation to HA is of great importance because the success of osseointegration is defined by tissue–material integration during the early period of implantation.[32]

The aim of this work was to evaluate the ability of electrochemically deposited calcium phosphate coatings on titanium for conversion to HA in SBF solution. Additionally, the purpose was to investigate the influence of the soaking time in SBF on the composition and morphology (crystallite domain size, pore number, porosity, mean pore area and roughness) of the converted HA coatings. An attempt was made to propose a mechanism of HA growth on the electrodeposited calcium phosphate coatings on titanium.

EXPERIMENTAL

Electrochemical deposition of calcium phosphate coatings

Calcium phosphate coatings were electrochemically deposited on titanium plates (15 mm×10 mm×0.127 mm, Alfa Aesar, Johnson Matthew Co., purity: 99.7 %) from a stirred aqueous solution of 0.042 M $Ca(NO_3)_2$ and 0.025 M $NH_4H_2PO_4$. The initial pH value of the solution was 4.0. All chemicals were of reagent grade (Sigma–Aldrich) and used without further purification. The electrodeposition was performed at current density of 10 mA cm^{-2} for deposition time of 15 min.

Chronopotentiometric curve was recorded during the calcium phosphate deposition in a three-electrode cell arrangement using Gamry Reference 600 potentiostat–galvanostat/ZRA. The working electrode was titanium plate. The counter electrode was platinum plate, placed parallel to the working electrode. The saturated calomel electrode (SCE) was used as reference electrode. Prior to the deposition, titanium plates were degreased in acetone and then in ethanol for 15 min in an ultrasonic bath.

Conversion of the calcium phosphate coatings to hydroxyapatite upon soaking in SBF

The calcium phosphate coatings were soaked in SBF solution for 2, 7 and 14 days. SBF solution was prepared by dissolving the reagent-grade chemicals of NaCl, $NaHCO_3$, KCl, $K_2HPO_4 \cdot 3H_2O$, $MgCl_2 \cdot 6H_2O$, $CaCl_2$ and Na_2SO_4 in deionized water.[33] The prepared SBF solution was buffered with tris(hydroxymethyl)aminomethane, $(CH_2OH)_3CNH_2$, and the pH was fixed to 7.4 by the addition of 1.0 mol dm^{-3} HCl. For the experiments, the calcium phosphate coatings were placed in plastic containers and SBF was added. The containers were kept at a constant temperature of 37 °C. All the SBF solution was replaced by a fresh charge every 48 h.

X-Ray diffraction

The phase composition and structure of calcium phosphate coatings and HA coatings were determined by XRD, using a Philips PW 1050 diffractometer with CuK_α radiation (λ = 1.5418 Å) and Bragg–Brentano focusing geometry. Measurements were realized in the 2θ range of 8–70° with scanning step width of 0.05° and time of 6 s per point-step. The lattice parameters and crystallite domain size were obtained using the X-ray line profile-fitting program XFIT with a fundamental parameters convolution approach to generate line profiles.[34]

Atomic absorption spectroscopy

During soaking period of calcium phosphate coatings in SBF solution, the concentration of calcium ions was determined by atomic absorption spectroscopy, using a Perkin Elmer 703 atomic absorption spectrometer.

UV–Vis spectroscopy

During the soaking period, the concentration of phosphorus ions of the calcium phosphate coatings in the SBF solution was determined by UV–Vis spectroscopy, using a Philips UV–Vis 8610 spectrophotometer.

Scanning electron microscopy

The microstructure of calcium phosphate coatings and HA coatings was examined by SEM using a JSM-20 (JEOL) instrument. The micrographs were subjected to image analysis processing using Image-J software.[35] The images were converted to grayscale, thresholded to binary images and the pore area and porosity were estimated using Image-J software.

Atomic force microscopy

In order to characterize the surface topography of the calcium phosphate coatings and HA coatings, atomic force microscopy (AFM) was used. The measurements were performed using a Quesant Universal SPM instrument operating in the non-contact mode.

RESULTS AND DISCUSSION

Electrochemical deposition and characterization of calcium phosphate coatings on titanium

The chronopotentiometric curve for calcium phosphate electrodeposition in a solution containing 0.042 M $Ca(NO_3)_2$ and 0.025 M $NH_4H_2PO_4$, at a constant current density of 10 mA cm^{-2} for a deposition time of 15 min, is shown in Fig. 1.

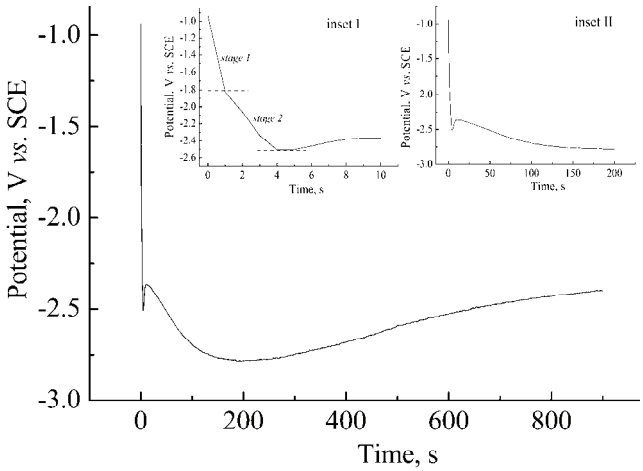

Fig. 1. Chronopotentiometric curve at a current density of 10 mA cm^{-2}.

For the initial very short time of deposition, up to 4 s, two stages could be distinguished (Fig. 1, inset I): stage 1, during the first second of deposition, with a corresponding potential of –1.8 V and stage 2, during the following 3 s of deposition, with a corresponding potential of about –2.5 V. The slopes of these two stages are different and suggest that stage 1 is a faster electrochemical reaction, and stage 2 is a slower reaction. This is in good agreement with proposed mechanism for electrochemical deposition of calcium phosphate coatings on titanium.[20,36,37] Briefly, at a potential up to –1.9 V, two processes occur: hydrogen reduction from NH_4^+ (originating from the starting $NH_4H_2PO_4$), which causes a local increase in pH (around 9) in the vicinity of the cathode and conversion of $H_2PO_4^-$, (originating from the starting $NH_4H_2PO_4$), into HPO_4^{2-}. In the presence of Ca^{2+} (originating from the starting $Ca(NO_3)_2$) and HPO_4^{2-}, brushite is deposited onto the cathode, which was confirmed by XRD analysis (Fig. 2):

$$Ca^{2+} + HPO_4^{2-} + 2H_2O \rightarrow CaHPO_4 \cdot 2H_2O \quad (1)$$

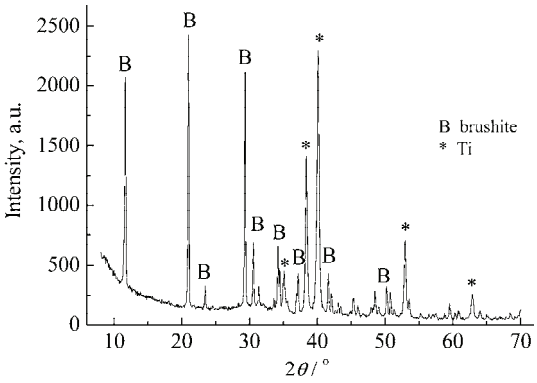

Fig. 2. XRD pattern of a brushite coating deposited on titanium.

Simultaneously, the brushite coating deposited at the cathode and hydrogen bubbles evolved on the cathode, causes a decrease in slope of chronopotentiometric curve (Fig. 1, inset I, stage 2). Namely, at potentials below –1.9 V, hydrogen evolution from water occurs, leading to the formation of a great number of H_2 molecules.[20] Hence, at the potentials up to –2.5 V, two parallel reactions occur: brushite deposition and growth and, on the other hand, the electrochemical reaction of hydrogen evolution. After the initial interval of 4 s, the electrochemical deposition of brushite occurs mainly through the porous film and this step is represented with maximum of the potential–time curve followed by decrease in the potential during further 200 s (Fig. 1, inset II). For deposition time longer than 200 s, the potential increases, suggesting that the H_2 bubbles are leaving the electrode surface.

The XRD pattern for the calcium phosphate coating electrochemically deposited on titanium is shown in Fig. 2. The identified diffraction maxima correspond to brushite, $CaHPO_4 \cdot 2H_2O$ (JCPDS No. 72-0713) and α-Ti as the substrate (JCPDS No. 89-3073).

SEM micrograph of the brushite coating is represented in Fig. 3, where the plate-like structure of the coating could be observed.

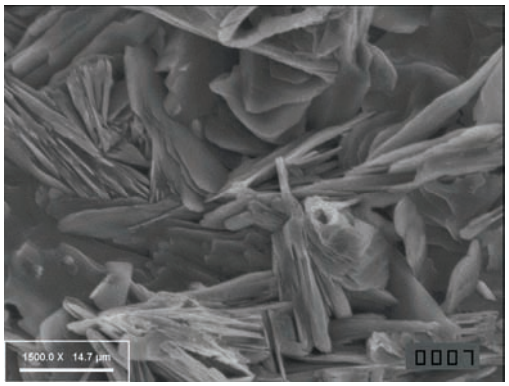

Fig. 3. SEM micrograph of a brushite coating.

The histogram of pore area distribution for a brushite coating, represented in Fig. 4, was determined using Image-J software. From Fig. 4, it could be seen that the majority of the pores had a pore area under 3 μm^2. The values of the mean pore area and percentage of surface covered by pores (porosity) were calculated to be 1.204 μm^2 and 4.88 %, respectively (Table I).

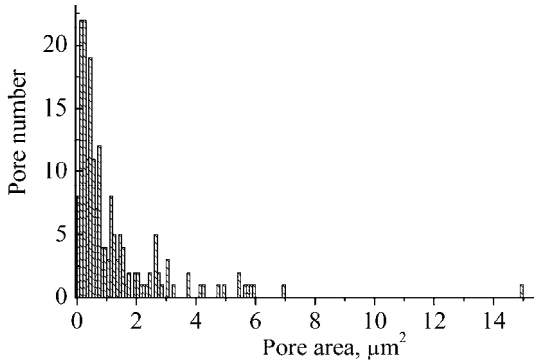

Fig. 4. Pore area distribution for a brushite coating.

TABLE I. Pore number, mean pore area, porosity and surface roughness of brushite and HA coatings after 7 and 14 days in SBF

Sample	Pore number	Mean pore area μm^2	Porosity %	Roughness	
				RMS / nm	R_a / nm
Brushite coating	186	1.204	4.88	148.4	125.7
HA coating (7 days in SBF)	329	0.492	6.30	294.8	231.1
HA coating (14 days in SBF)	510	0.475	9.41	726.4	567.0

The AFM surface topography of brushite coating is represented in Fig. 5 (10 × 10 μm area). The plate-like structure of the brushite coating could be observed, while the roughness parameters, RMS and R_a, amount to 148.4 and 125.7 nm, respectively (Table I).

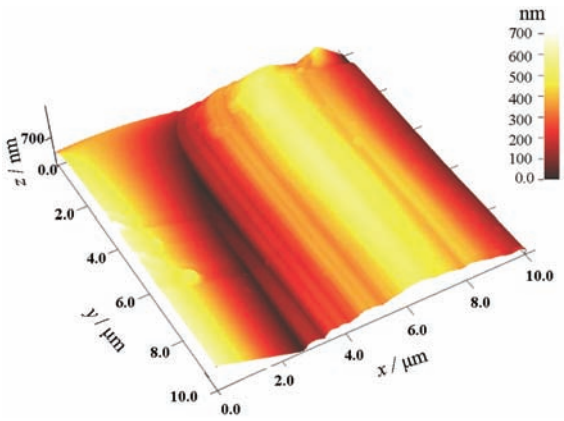

Fig. 5. AFM micrograph of a brushite coating.

Hydroxyapatite coatings on titanium

XRD analysis. The XRD patterns of the converted coatings, obtained after soaking the brushite coating in SBF for 2, 7 and 14 days, are represented in Fig. 6. The phase composition of converted coatings corresponded to hydroxyapatite, $Ca_{10}(PO_4)_6(OH)_2$ (JCPDS No. 86-1199) and α-Ti (originating from the substrate). The absence of diffraction maximums for brushite confirmed that the complete surface, primarily coated with brushite, was fully converted to HA.

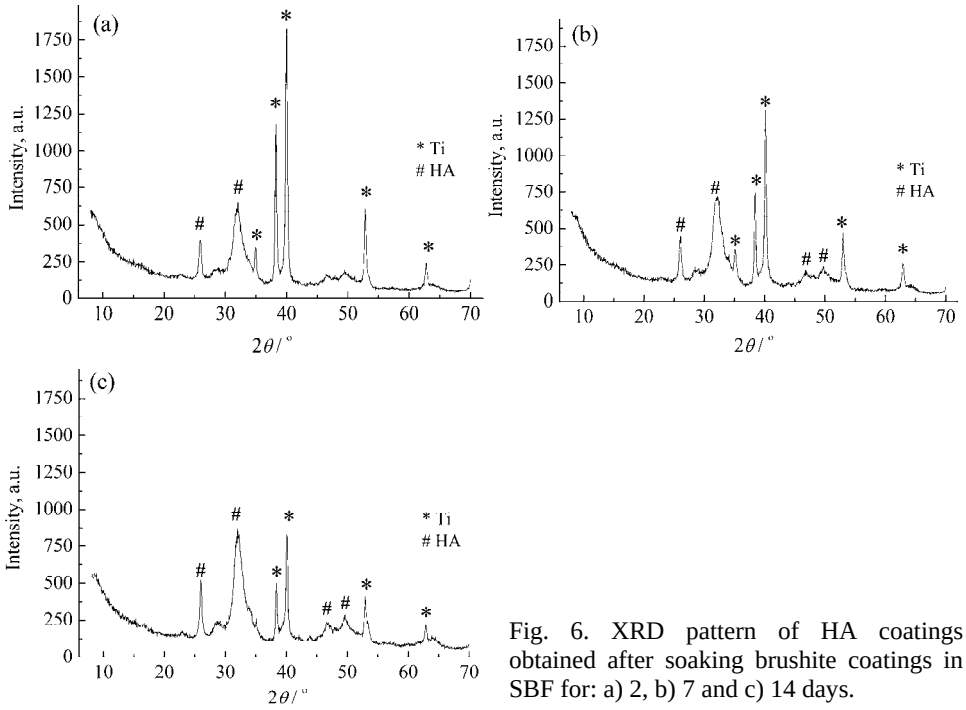

Fig. 6. XRD pattern of HA coatings obtained after soaking brushite coatings in SBF for: a) 2, b) 7 and c) 14 days.

The crystallite domain size, calculated for the (002) plane, as well as the unit cell parameters and unit cell volume for the HA coatings obtained after soaking the brushite coatings in SBF for 2, 7 and 14 days, are presented in Table II.

TABLE II. The crystallite domain size, unit cell parameters, *a* and *c*, and unit cell volume, *V*, for HA coatings obtained after soaking of brushite coatings for 2, 7 and 14 days in SBF

Days in SBF	Crystallite domain size, nm	Unit cell parameters, Å		Unit cell volume, Å^3
		a	*c*	
2	14.4	9.5111	6.9585	545.14
7	15.0	9.5105	6.9487	544.30
14	16.2	9.4843	6.9265	539.58

The results suggest that increasing the soaking time slightly increased the crystallite domain size of the converted HA coatings and decreased the unit cell parameters and unit cell volume, because of the increased crystal density.

In vitro *tests of HA coating in SBF*

In order to investigate the mechanism of brushite conversion to HA, the concentrations of Ca and P ions during 14 days of immersion of the brushite coating in SBF solution were determined by AAS and UV–Vis spectroscopy, respectively. The dependences of the concentrations of Ca and P ions in SBF on the soaking time are presented in Fig. 7a and b, respectively. For shorter immersion times, during the first two days, rapid decreases in both the concentrations of Ca and P ions were observed. Namely, the high rate of consumption of Ca and P ions indicates the high reactivity of brushite with SBF that induces the transformation of brushite and the nucleation of HA. XRD results for the HA coating observed after two days of immersion (Fig. 6a), confirmed that the brushite had completely transformed to HA, indicating the ability of brushite to generate HA by intake of Ca and P ions from the surrounding solution. This is in good agreement with the literature.[33,38] Namely, once immersed in SBF (pH 7.4), brushite dissolves rapidly because brushite is stable under acidic aqueous conditions at pH < 4.2. The increase in the local concentration of Ca and P ions resulted in the precipitation of calcium phosphates. Bearing in mind that the pH of the SBF was 7.4 and that SBF is supersaturated with respect to apatite (the Ca/P mole ratio was 2.50), the only stable phase that could be precipitated is HA. The rapid formation of a Ca and P rich layer in a relatively short time of immersion is of special interest because the success of osseointegration is defined by tissue–material interaction during the early days of implantation.[32,39,40]

In general, both dissolution and precipitation of calcium phosphates occur simultaneously, but the kinetics of these two processes are different. The dissol-

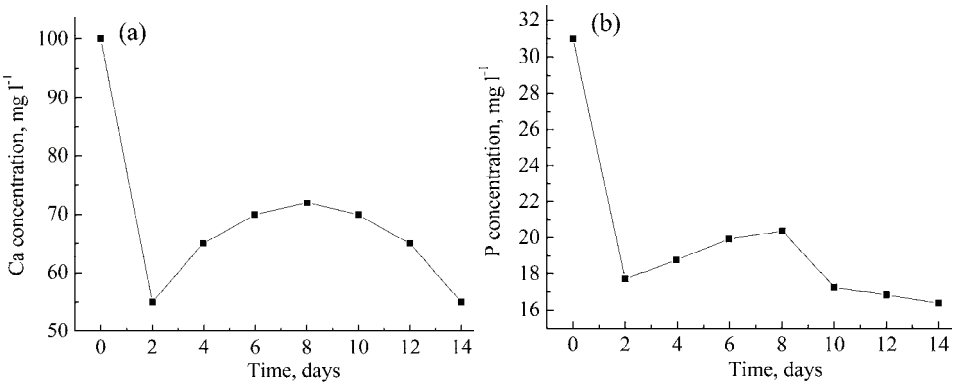

Fig. 7. The dependences of (a) the Ca concentration and (b) the P concentration in SBF on the soaking time of brushite coating.

ution process is governed by ion exchange, while the precipitation process is controlled by the product of the ion concentrations and the solubility of the particles. The dissolution and precipitation of calcium phosphates in SBF is a reversible reaction.[41–43]

The increase in the Ca concentration between days 2 and 8 of immersion is shown in Fig. 7a, meaning that the precipitation rate decreased, while the dissolution rate increased. After 8 days of immersion, the concentration of Ca ions decreased, indicating that further precipitation of HA coating dominated over dissolution. Indeed, the increase in the mass of the HA coating during exposure to SBF solution (6.6, 13.8 and 19.0 mg after 2, 7 and 14 days, respectively) confirmed that precipitation of HA coating prevailed.

The increase in the P ions concentration between day 2 and 8 of immersion is shown in Fig. 7b, suggesting that the precipitation rate slowed down, while the dissolution rate increased. The HA coating dissolution created a great number of the nucleation sites on the coating surface. During longer immersion time (between 8 to 14 days), a decrease in P ions concentration could be observed, indicating the consumption of P ions during soaking.

SEM analysis of HA coatings

The SEM micrographs of the HA coatings after soaking in SBF for 7 and 14 days are presented in Figs. 8a and 9a, respectively. Figure 8a shows the agglomerated sphere-like crystallites of different size after 7 days of immersion, while after 14 days (Fig. 9a), the morphology of the coating had changed and less agglomerates could be observed. The SEM micrographs of HA coatings were analyzed by "Image-J" software.[35] After 7 days of soaking, the surface of the HA coating was fully covered by a HA layer, which was confirmed by XRD (Fig. 6b). A 3D plot of a sphere-like agglomerate, with a size of approximately 4.0 μm in diameter is presented in Fig. 8b (detail from Fig. 8a, marked with an arrow). The sphere-like agglomerate consisted of very fine crystallites, suggesting a high

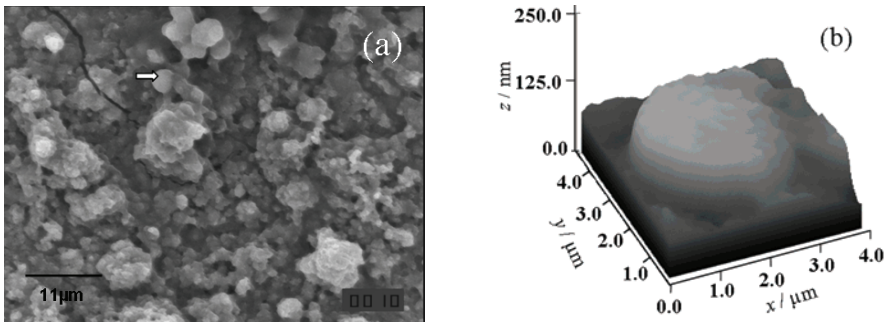

Fig. 8. SEM micrograph of: a) an HA coating obtained by soaking a brushite coating in SBF for 7 days and b) a 3D plot of the sphere-like agglomerate marked with an arrow in (a).

nucleation rate of HA. After a soaking period of 14 days, the HA coating surface had fewer agglomerates. A new spherical particle, with a size of approximately 1.0 μm in diameter, presented in Fig. 9b (the detail from Fig. 9a, marked with arrow), appeared on the surface of the previously precipitated HA as a consequence of further deposition of HA with soaking time.[44] Namely, when calcium phosphates were incubated in SBF solution, the formation of HA layer on the surface of the coating occurs, including dissolution, precipitation and growth of HA.[4,45,46] The formation of new agglomerates of HA on the surface of the previously precipitated hydroxyapatite, observed on the SEM micrographs (Fig. 9b), is in good agreement with results presented in Fig. 7, where the decrease in the concentration of Ca and P ions, after 8 days of soaking can be attributed to further HA precipitation. The formation of HA is very important in the formation of chemical bonds between tissue and bioactive material.

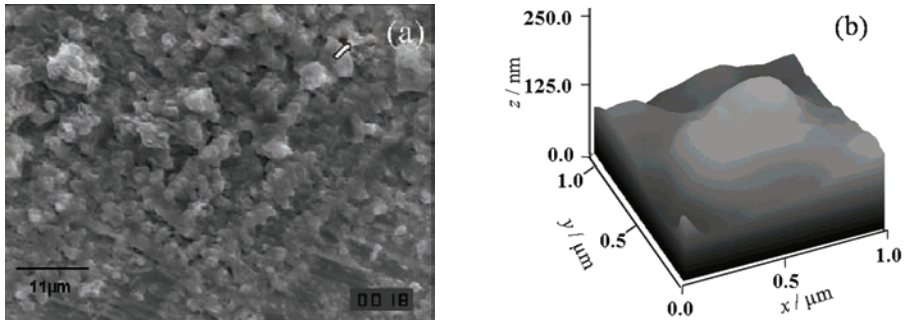

Fig. 9. SEM micrograph of: a) an HA coating obtained by soaking a brushite coating in SBF for 14 days and b) a 3D plot of the sphere-like agglomerate marked with an arrow in (a).

The pore area distribution for HA coatings, obtained after soaking in SBF for 7 and 14 days, using Image-J software, are represented in Fig. 10a and b, respectively.

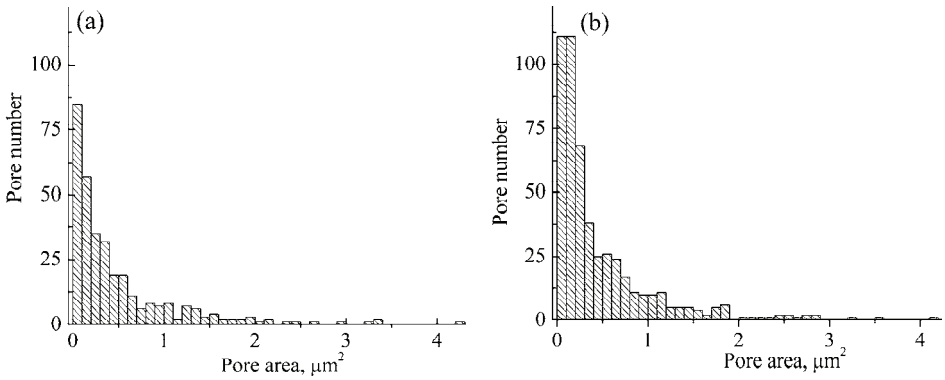

Fig. 10. Pore area distribution for HA coatings obtained by soaking brushite coatings in SBF for: a) 7 and b) 14 days.

The values of the number of pores, mean pore area and porosity, and the roughness parameters of the brushite and HA coatings obtained after soaking in SBF for 7 and 14 days are presented in Table I.

The brushite coating exhibited a relatively small number of pores (Table I) with a larger pore area. Upon soaking the brushite coating in SBF, since the conversion process occurred, the pore number increased significantly, while the mean pore area decreased during soaking for 14 days. Comparison of the histograms of the pore area distribution for HA coatings upon soaking for 7 and 14 days (Fig. 10a and b, respectively), indicates that the majority of the pores had a small pore area, up to 1 μm^2, and that there were only a small number of pores having a larger area. In addition, increasing the soaking time from 7 to 14 days increased the number of pores with areas up to 1 μm^2. Consequentially, the porosity of the HA coating increased with increasing soaking time, while the mean pore area did not change significantly. The increase in porosity of the HA coating for longer soaking times could be attributed to the simultaneous dissolution and precipitation of HA under physiological conditions, whereby precipitation dominates, which was confirmed by the increase in the mass of the HA coating, as was discussed earlier. Microporosity is very important parameter because it influences the adsorption of proteins by providing a greater surface area, as well as bone-like apatite formation by dissolution and precipitation.[47] Thus, it could be proposed that the HA coatings obtained after 14 days of soaking might have better protein adsorption ability due to their greater porosity with respect to HA coatings obtained after 7 days of soaking in SBF.

AFM analysis of HA coatings

AFM analysis of HA coatings obtained after soaking of brushite coatings in SBF for 7 and 14 days are represented in Fig. 11.

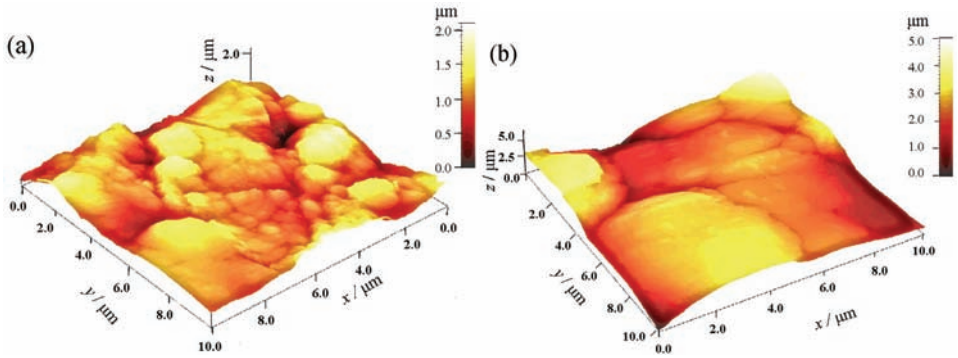

Fig. 11. AFM micrographs of HA coatings obtained by soaking brushite coatings in SBF for: a) 7 and b) 14 days.

Roughness is represented by the arithmetical mean deviation, R_a, and root mean square deviation, RMS. The results of the statistical analysis of the AFM micrographs for both the brushite and HA coatings are listed in Table I. The RMS and R_a values of the brushite coating were smaller than the corresponding values for the HA coating. Moreover, the RMS and R_a values of HA coatings increase with increasing soaking time from 294.8 nm to 726.4 nm and from 231.1 to 567.0 nm, respectively. According to the literature, an increase in the surface roughness of HA surfaces increases osteoblastic cell adhesion, proliferation and detachment strength.[6,48,49] On the other hand, a problem with highly rough surfaces is connected with cellular mobility. It was reported[7] that osteoclastogenesis could be induced if surface roughness, R_a, achieves values between 0.04 and 0.58 μm. This means that the present results are comparable with the results from the literature. The HA coatings obtained in SBF from brushite coating electrochemically deposited on titanium at constant current density could stimulate a cellular response.

CONCLUSIONS

In order to investigate the ability of HA formation on titanium substrate from brushite precursor under *in vitro* conditions, electrochemical deposition of a brushite coatings on titanium was performed galvanostatically at a current density of 10 mA cm^{-2} for a deposition time of 15 min.

The brushite coatings were soaked in an SBF solution and conversion to HA coatings was monitored by XRD, SEM, AFM, AAS and UV–Vis spectroscopy during *in vitro* tests. Increase in soaking time slightly increases the crystallite domain size of the HA coatings and decreases the unit cell parameters and unit cell volume, because of increased crystal density. Moreover, an increase in soaking time increased the mass, roughness, pore number and porosity of the HA coating, whereas the mean pore area was not significantly affected.

An *in vitro* study was used to investigate the biological response of HA coatings under physiological conditions and Ca and P ions concentration in SBF were determined, confirming the dissolution–precipitation mechanism. Since the crystallite domain size slightly increased, it could be proposed that nucleation of HA dominates over crystal growth and, consequently, an increase in coating roughness was observed, suggesting that precipitation of HA occurred through heterogeneous nucleation. Bearing in mind that increasing the soaking time increased the mass of the HA coating, it could be proposed that precipitation dominate over dissolution.

Based on all experimental results, it could be concluded that the increase in the HA coating porosity and coating roughness, resulting in a larger surface area, make this coating suitable for biomedical applications, because it is believed that the porosity contributes to better protein adsorption as well as bone-like apatite formation by the dissolution and precipitation mechanism. Additionally, the inc-

rease in HA coatings roughness indicates that the HA coatings could stimulate cellular response.

Acknowledgements. This research was financed by the Ministry of Education, Science and Technological Development, Republic of Serbia, contracts Nos. III 45019, III 45015 and OI 172004. The authors would like to thank Dr. Zoran Stojanović, Vinča Institute of Nuclear Sciences, University of Belgrade, for his help in the AFM measurements.

И З В О Д

ПОРОЗНОСТ И ХРАПАВОСТ ЕЛЕКТРОХЕМИЈСКИ ТАЛОЖЕНИХ ПРЕВЛАКА КАЛЦИЈУМ-ФОСФАТА У СИМУЛИРАНОЈ ТЕЛЕСНОЈ ТЕЧНОСТИ

МАРИЈА С. ЂОШИЋ[1], МИОДРАГ МИТРИЋ[2] и ВЕСНА Б. МИШКОВИЋ-СТАНКОВИЋ[3]

[1]Институт за технологију нуклеарних и других минералних сировина, Франше д'Епереа 86, 11000 Београд [2]Институт за нуклеарне науке "Винча", Универзитет у Београду, 11001 Београд и [3]Технолошко–металуршки факултет, Универзитет у Београду, Карнегијева 4, 11120 Београд

Превлаке калцијум-фосфата су електрохемијски таложене на титану из воденог раствора $Ca(NO_3)_2$ и $NH_4H_2PO_4$ при густини струје од 10 mA cm^{-2} за време од 15 мин. Добијене превлаке брушита ($CaHPO_4{\cdot}2H_2O$) су конвертоване у хидроксиапатит у симулираној телесној течности током 2, 7 и 14 дана. Превлаке брушита и хидроксиапатита су карактерисане дифракцијом X-зрака, скенирајућом електронском микроскопијом и микроскопијом атомских сила. Показано је да са продужавањем времена конверзије у симулираној телесној течности долази до повећања порозности, храпавости и величине кристалита превлаке хидроксиапатита, али и смањења параметара јединичне ћелије и запремине јединичне ћелије хидроксиапатита. Са друге стране, време конверзије не утиче на средњу површину пора превлака хидроксиапатита. Концентрације јона калцијума и фосфора у симулираној телесној течности одређиване су атомском апсорпционом спектроскопијом и UV–Vis спектроскопијом, редом. Предложен је механизам раста хидроксиапатита у симулираној телесној течности, базиран на теорији растварање–таложење.

(Примљено 26. јуна, ревидирано 1. октобра, прихваћено 2. октобра 2014)

REFERENCES

1. C. B. Carter, M. G. Norton, *Ceramic Materials Science and Engineering*, Springer, New York, 2007, p. 645
2. A. Janković, S. Eraković, A. Dindune, Dj. Veljović, T. Stevanović, Dj. Janaćković, V. Mišković-Stanković, *J. Serb. Chem. Soc.* **77** (2012) 1
3. F. Zeng, J. Wang, Y. Wu, Y. Yu, W. Tang, M. Yin, C. Liu, *Colloids Surfaces, A* **441** (2014) 737
4. P. N. Chavan, M. M. Bahir, R. U. Mene, M. P. Mahabole, R. S. Khairnar, *Mater. Sci. Eng., B* **168** (2010) 224
5. Dj. Veljović, R. Jančić-Hajneman, I. Balać, B. Jokić, S. Putić, R. Petrović, Dj. Janaćković, *Ceram. Int.* **37** (2011) 471
6. B. D. Hahn, D. S. Park, J. J. Choi, J. Ryu, W. H. Yoon, J. H. Choi, J. W. Kim, Y. L. Cho, C. Park, H. E. Kim, S. G. Kim, *Appl. Surf. Sci.* **257** (2011) 7792
7. J. Costa-Rodrigues, A. Fernandes, M. A. Lopes, M. H. Fernandes, *Acta Biomater*. **8** (2012) 1137
8. M. P. Ferraz, F. J. Monteiro, C. M. Manuel, *J. Appl. Biomater. Biom.* **2** (2004) 74

9. M. S. Djošić, V. B. Mišković-Stanković, S. Milonjić, Z. M. Kačarević-Popović, N. Bibić, J. Stojanović, *Mater. Chem. Phys.* **111 (**2008) 137
10. B. Bracci, S. Panzavolta, A. Bigi, *Surf. Coat. Technol.* **232** (2013) 13
11. S. Eraković, Dj. Veljović, P. N. Diouf, T. Stevanović, M. Mitrić, Dj. Janaćković, I. Z. Matić, Z. D. Juranić, V. Mišković-Stanković, *Prog. Org. Coat.* **75** (2012) 275
12. S. Eraković, Dj. Veljović, P. N. Diouf, T. Stevanović, M. Mitrić, S. Milonjić, V. B. Mišković-Stanković, *Int. J. Chem. React. Eng.* **7** (2009) A62
13. R. Štulajterová, L'. Medvecký, *Colloids Surfaces, A* **316** (2008) 104
14. W. Jiang, X. Chu, B. Wang, H. Pan, X. Xu, R. Tang, *J. Phys. Chem., B* **113** (2009) 10838
15. J. A. Juhasz, S. M. Best, A. D. Auffret, W. Bonfield, *J. Mater. Sci: Mater. Med.* **19** (2008) 1823
16. R. Horváthová, L. Müller, A. Helebrant, P. Greil, F. A. Müller, *Mater. Sci. Eng., C* **28** (2008) 1414
17. J. Hu, C. Wang, W. C. Ren, S. Zhang, F. Liu, *Mater. Chem. Phys.* **119** (2010) 294
18. A. V. Zavgorodniy, O. Borrero-López, M. Hoffman, R. Z. LeGeros, R. Rohanizadeh, *J. Mater. Sci: Mater. Med.* **22** (2011) 1
19. M. S. Djosic, V. B. Miskovic-Stankovic, Z. M. Kacarevic-Popovic, B. M. Jokic, N. M. Bibic, M. N. Mitric, S. K. Milonjic, R. M. Jancic-Heinemann, J. N. Stojanovic, *Colloids Surfaces, A* **341** (2009) 110
20. M. S. Djošić, V. Panić, J. Stojanović, M. Mitrić, V. B. Mišković-Stanković, *Colloids Surfaces, A* **400** (2012) 36
21. L. M. Rodríguez-Lorenzo, M. Vallet-Regí, *Chem. Mater.* **12** (2000) 2460
22. M. H. Fathi, V. Mortazavi, S. I. R. Esfahani, *Dent. Res. J.* **5** (2008) 81
23. R. Murugan, S. Ramakrishna, *J. Cryst. Growth* **274** (2005) 209
24. A. Hanifi, M. H. Fathi, *Iranian J. Pharm Sci.* **4** (2008) 141
25. H. E. L. Madsen, G. Thorvardarson, *J. Cryst. Growth* **66** (1984) 369
26. A. C. Tas, S. B. Bhaduri, *Ceram. Trans.* **164** (2005) 119
27. W. J. Shih, Y. H. Chen, S. H. Wang, W. L. Li, M. H. Hon, M. C. Wang, *J. Cryst. Growth* **285** (2005) 633
28. A. C. Tas, S. B. Bhaduri, *J. Am. Ceram. Soc.* **87** (2004) 2195
29. J. Peña, I. Izquierdo-Barba, A. Martínez, M. Vallet-Regí, *Solid State Sci.* **8** (2006) 513
30. J. H. Park, D. Y. Lee, K. T. Oh, Y. K. Lee, K. N. Kim, *J. Am. Ceram. Soc.* **87** (2004) 1792
31. A. Rakngarm, Y. Mutoh, *Mater. Sci. Eng., C* **29** (2009) 275
32. M. L. R. Schwarz, M. Kowarsch, S. Rose, K. Becker, T. Lenz, L. Jani, *J. Biomed. Mater. Res., A* **89** (2009) 667
33. T. Kokubo, H. Takadama, *Biomaterials* **27** (2006) 2907
34. R. W. Cheary, A. A. Coelho, *J Appl. Cryst.* **25** (1992) 109
35. ImageJ-Image processing and analysis in Java. Available on Web site: http:// //rsb.info.nih.gov/ij on 21.2.2015
36. N. Dumelié, H. Benhayoune, C. Rousse-Bertrand, S. Bouthors, A. Perchet, L. Wortham, J. Douglade, D. Laurent-Maquin, G. Balossier, *Thin Solid Films* **492** (2005) 131
37. E. A. Abdel-Aal, D. Dietrich, S. Steinhaeuser, B. Wielage, *Surf. Coat. Technol.* **202** (2008) 5895
38. M. C. Kuo, S. K. Yen, *J. Mater. Sci.* **39** (2004) 2357
39. M. Bohner, J. Lemaitre, *Biomaterials* **30** (2009) 2175
40. X. Lu, Y. Leng, *Biomaterials* **26** (2005) 1097
41. Q. Zhang, J. Chen, J. Feng, Y. Cao, C. Deng, X. Zhang, *Biomaterials* **24** (2003) 4741

42. M. Kumar, H. Dasarathy, C. Riley, *J. Biomed. Mater. Res.* **45** (1999) 302
43. R. Sun, K. Chen, Y. Lu, *Mater. Res. Bull.* **44** (2009) 1939
44. J. X. Zhang, R. F. Guan, X. P. Zhang, *J. Alloys Compd.* **509** (2011) 4643
45. H. Kim, R. P. Camata, S. Chowdhury, Y. K. Vohra, *Acta Biomater.* **6** (2010) 3234
46. S. Eraković, A. Janković, Dj. Veljović, E. Palcevskis, M. Mitrić, T. Stevanović, Dj. Janaćković, V. Mišković-Stanković, *J. Phys. Chem., B* **117** (2013) 1633
47. K. A. Hing, *Int. J. Appl. Ceram. Technol.* **2** (2005) 184
48. D. D. Deligianni, N. D. Katsala, P. G. Koutsoukos, Y. F. Missirlis, *Biomaterials* **22** (2001) 87
49. S. Sandukas, A. Yamamoto, A. Rabiei, *J. Biomed. Mater. Res., A* **97** (2011) 490.

Journal of the Serbian Chemical Society
JSCS-info@shd.org.rs • www.shd.org.rs/JSCS
J. Serb. Chem. Soc. 80 (2) 253–264 (2015)
JSCS–4714
UDC 66.011+577.354:541.121
Original scientific paper

Evaluation of optimization methods for solving the receptor model for chemical mass balance

N. ANU, S. RANGABHASHIYAM, ANTONY RAHUL and N. SELVARAJU*

Department of Chemical Engineering, National Institute of Technology Calicut Kozhikode-673601, Kerala, India

(Received 14 November 2013, revised 31 March, accepted 18 May 2014)

Abstract: The chemical mass balance (CMB 8.2) model has been extensively used in order to determine source contribution for particulate matters (size diameters less than 10 and 2.5 μm) in air quality analysis. A comparison of the source contribution estimated from three CMB models was realized through optimization techniques, such as 'fmincon' (CMB–fmincon) and genetic algorithm (CMB–GA) using MATLAB. The proposed approach was validated using a San Joaquin Valley Air Quality Study (SJVAQS) California Fresno and Bakersfield PM_{10} and $PM_{2.5}$ followed with Oregon PM_{10} data. The source contribution estimated from CMB–GA was better in source interpretation in comparison with CMB 8.2 and CMB–fmincon. The performance accuracies of three CMB approaches were validated using R^2, reduced χ^2 and percentage mass tests. The R^2 (0.90, 0.67 and 0.81, 0.83), χ^2 (0.36, 0.66 and 0.65, 0.43) and percentage mass (67.36, 55.03 and 94.24 %, 74.85 %) of CMB–GA showed high correlation for PM_{10}, $PM_{2.5}$, Fresno and Bakersfield data, respectively. To make a complete decision, the proposed methodology was bench marked with Portland, Oregon PM_{10} data with the best fit with R^2 (0.99), χ^2 (1.6) and percentage mass (94.4 %) from CMB–GA. Therefore, the study revealed that CMB with genetic algorithm optimization method exhibiting better stability in determining the source contributions.

Keywords: receptor model; chemical mass balance; source contribution; source profiles; genetic algorithm.

INTRODUCTION

Air pollution is a major concern in the current century due to population exposure, urbanization and industrialization. The concentration level of particulate matter (particles with aerodynamic diameters less than 10 and 2.5 μm) in the urban environment remains a serious problem.[1–3] The term particulate matter (PM_{10} and $PM_{2.5}$) is used to describe solid or liquid particles that are airborne

* Corresponding author. E-mail: selvaraju@nitc.ac.in
doi: 10.2298/JSC131124052A

and dispersed. Particles vary in number, size, shape, surface area, chemical composition, solubility and origin across both space and time. Particulate matter originates from a variety of natural and anthropogenic sources[4] and possesses a range of morphological, physical, chemical and thermodynamic properties.[5] Emissions of mineral particulate matter adversely impact on environmental quality in mining regions,[6] transport regions,[7] and even on a global scale.[2] Various anthropogenic (traffic, power plants, biomass burning, etc.) and natural sources (forest fires, soil re-suspension, *etc*.) emit primary particulate matters (PM_{10} and $PM_{2.5}$) and gaseous pollutants such as SO_2, NO_x, NH_3 and VOC directly into the atmosphere.[8] Secondary particles, formed by transformation of these primary emissions, contribute to the concentrations of ambient particulate matter, which cause adverse effects on human health.[9] Industrialization patterns changed due to stringent air quality standards with many heavily polluting industries moving from developed countries.[10]

Source identification of particulate matter is one of the key components in air quality management planning. Apportionment studies were attempted to develop and implement air pollution control strategies in many urban areas across the world.[4,11–16] Receptor models are widely used to estimate the source contribution of construction activities, fossil fuel combustion, traffic re-suspension, geologic, motor vehicle exhaust, vegetative burning to ambient air pollution. The CMB model combines the chemical and physical characteristics of particles or gases measured at the sources and the receptors to quantify the source contribution to the receptor.[17] The CMB enables the source contributions of ambient PM_{10} and $PM_{2.5}$ to be determined through effective-variance least squares regression,[18] weighted least square regression and the method of moments.[19,20,5] Source apportionment (SA) of PM using robotic chemical mass balance (RCMB) reduces the uncertainty due to the human judgment through the best-fit combination of source profiles used as input data.[21,22] Quantification of uncertainty in RCMB using the traditional Monte Carlo approach[23] and polynomial chaos method[24] were also proposed. Uncertainties in the input variable used to solve the chemical mass balance are the receptor concentration uncertainty and source profile uncertainty. The United States Environmental Protection Agency (USEPA) developed the tool CMB8.2 that resolves using both the uncertainties to obtain the source contribution at the receptor locations[25]. The combined CMB and multivariate source apportionment methods, such as positive matrix factorization (PMF) and the Unmix model, has been widely used for the refined source contribution and source profile estimation in air quality research.[26,27]

The current research article compares the source contribution results of CMB8.2, CMB–fmincon and CMB–GA. The difference in the estimation of the source contributions by the three approaches were illustrated using San Joaquin Valley Air Quality Study (SJVAQS) of Fresno and Bakersfield, the PM_{10} and

$PM_{2.5}$ data were taken from Chow *et al*. (1992 and 1993).[28,29] These data were collected every six days between June 1988 and 1989. A total of 35 and 49 observations of $PM_{2.5}$ and PM_{10}, respectively, from the Fresno site and 48 and 33 observations of $PM_{2.5}$ and PM_{10} from Bakersfield sites were respectively obtained. The profile data of ten different sources, such as paved road dust, vegetative burning, crude oil combustion, motor vehicles, lime stone (construction), marine, ammonium sulfate, ammonium nitrate, secondary organic carbon (SOC) and sodium nitrate are available in the literature.[28,29] The proposed methodology were validated through Portland, Oregon PM_{10} data with marine, urban dust, auto exhaust and residual oil combustion as possible sources of emission.[30] Source contribution estimates from CMB8.2, CMB–fmincon and CMB–GA models were used to predict the receptor concentration (C_{pre}) data. The percentage error between the experimental (c_{exp}) and predicted concentrations (c_{pre}) were compared using the statistical approach of R^2, χ^2 and percentage mass to validate the effect of uncertainty and optimization solvers in the three CMB models.

EXPERIMENTAL

CMB receptor model

The CMB receptor model expresses the concentrations of different chemical species ($c_{i\times1}$ / μg m^{-3}) measured at a monitoring site (or receptor) as a linear sum of products of the source profile ($F_{i\times j}$ / μg μg^{-1}) and source contribution ($S_{j\times1}$ / μg m^{-3}):

$$c_{(i\times1)} = \sum F_{(i\times j)} S_{(j\times1)} \quad (1)$$

where i is the number of species measured; j is the number of source categories for one receptor sample. The mass fraction of the emissions from each source type is known as the source profile, μg μg^{-1}. Profiles are measured on samples from these sources at times and locations to represent emission compositions, μg m^{-3} while receptor measurements are made. The basic assumptions of CMB model are: 1) compositions of source emissions are constant over the period of ambient and source sampling; 2) no reaction between the chemical species (*i.e*., they add linearly); 3) all sources with a potential for contributing to the receptor have are identified and have had their emissions characterized; 4) the number of sources or source categories is less than or equal to the number of species; 5) the source profiles are linearly independent of each other; 6) measurement uncertainties are random, uncorrelated, and normally distributed. CMB quantifies contributions from chemically distinct source-types rather than contributions from individual emitters. Sources with similar chemical and physical properties cannot be distinguished from each other by CMB. The CMB model calculates source contribution estimates for each individual ambient sample. The combination of source profiles that best explains the ambient measurements may differ from one sample to the next owing to differences in emission rates.[12,25]

CMB 8.2

CMB software version 8.2 was developed by the United States Environmental Protection Agency (USEPA). The input to the software contains one day or average receptor concentration, μg m^{-3}, data and measured source profile of the possible sources of air pollution at the locality and their corresponding uncertainties. The output of the model is source contribution

to air pollution, μg m^{-3}. Performance measures for the least squares calculation in CMB 8.2 are R^2, reduced χ^2 and percent mass. The χ^2 is the weighted sum of the squares of the differences between the measured (c_{exp}) and calculated (c_{pre}) fitting species concentrations:

$$\chi^2 = \frac{1}{I-J}\sum_{i=1}^{I}\left[\frac{\left(c_i - \sum_{j=1}^{J} F_{ij}S_j\right)^2}{V_{e_{ii}}}\right] \quad (2)$$

The weighting, $V_{e_{ii}}$, is inversely proportional to the squares of the uncertainty in the source profiles and ambient data for each species.

Ideally, there should be no difference between the calculated and measured concentrations of the species and χ^2 would equal zero. A value less than 1 indicates a very good fit to the data, while values between 1 and 2 are acceptable. χ^2 values greater than 4 indicate that concentrations of one or more species are not well explained by the source contribution estimates.

The percent mass can be expressed by Eq. (3), the percent ratio of the sum of the source contribution estimated by the model to the measured mass concentration:

$$\text{Percent mass} = \frac{100\left(\sum_{j=1}^{J} S_j\right)}{C_t} \quad (3)$$

where C_t is the total measured mass.

Percentage mass should equal 100 %, although values ranging from 80 to 120 % are acceptable. If the measured mass is very low (<5 to 10 μg m^{-3}), the percent mass may be outside this range because the uncertainty in the mass measurement is of the order of 1 to 2 μg m^{-3}.

R^2 is the fraction of the variance in the measured concentrations that is explained by the variance in the calculated concentrations of the species:

$$R^2 = 1 - \frac{\left[(I-J)\chi^2\right]}{\left[\sum_{i=1}^{I} c_i^2 \Big/ V_{e_{ii}}\right]} \quad (4)$$

R^2 is determined by linear regression of the measured *vs*. model-calculated values for the fitted species. The value of R^2 ranges from 0 to 1.0. The closer the value is to 1.0, the better is the source contribution estimates explaining the measured concentrations. When R^2 is less than 0.8, the source contribution estimates do not explain the observations with the fitting source profiles and/or species very well.[25] The effective variance solution is derived by minimizing the weighted sums of the squares of the differences between the measured and calculated values of c_i and the measured values of F_{ij}.[30]

CMB–fmincon

The ambient data for 26 species from PM_{10} and $PM_{2.5}$ as well as the profiles and uncertainties for ten sources are available.[17] The constrained optimization routine in MATLAB R2008a 'fmincon' were used to optimize the source contributions and thus the difference between c_{pre} and c_{exp} of the species involved in this problem. The objective was to minimize the sum of the squares of differences between the experimental (c_{exp}) and model

predictions (c_{pre}) of the receptor concentrations. Both the uncertainties in the receptor concentrations and in the source profiles were taken into consideration in the model to calculate the optimized source contribution from CMB–fmincon. The source profile (10×26), receptor concentration (26×1) and receptor concentration uncertainty (26×1) were arranged in a Microsoft Excel sheet and used while executing the program in MATLAB R2008a. The calculated source contribution from the model was used to predict the concentration (c_{pre}) of the species in PM_{10} and $PM_{2.5}$ of the SJVAQS Fresno and Bakersfield data. The execution of CMB by 'fmincon' solver in MATLAB R2008a is shown in Fig. S-1 of the Supplementary material to this paper. In comparison with CMB8.2, CMB–fmincon makes use of an objective function, which significantly reduces the run time between c_{exp} and c_{pre} species concentrations. CMB–fmincon accounts both the uncertainties and hence reduces the error in the source contribution estimation with constrained optimization of chemical mass balance function.

CMB with genetic algorithms (CMB–GA)

A genetic algorithm (GA) is a stochastic global search method that works in the same manner as natural biological evolution. GA operates on a population of potential solutions applying the principle of survival of the fittest to produce better approximations to the solution. At each generation, a new set of approximations is created by the process of selecting individuals according to their level of fitness in the problem domain and breeding them together using operators borrowed from natural genetics. This process leads to the evolution of populations of individuals that are better suited to their environment than the individuals from which they were created, just as in natural adaptation.[31] The algorithm consists of a main routine containing the optimization code and a subroutine containing the objective function of the code. In MATLAB R2008a, this is represented as shown in Fig. S-2 of the Supplementary material. Some details of the method are also given in the Supple–mentary material.

Analysis of Fresno and Bakersfield PM_{10} and $PM_{2.5}$ data[28,29]

California San Joaquin Valley (SJV) encompasses nearly 64,000 km^2 and a population in excess of three million people. The majority of this population is centered in the large urban areas of Bakersfield and Fresno, although nearly 100 smaller communities are situated in the region. This population base, combined with oil and gas production and refining, waste incineration, electrical cogeneration, agriculture, transportation, commerce, and light manufacturing activities, leads to air pollution emissions and concentrations that approach those of the metropolitan area of Los Angeles (South Coast Air Basin-SOCAB) in southern California.[28]

The average concentrations of PM_{10} and $PM_{2.5}$ containing 26 species observed at Fresno and Bakersfield, California, in 1988–1989 were used to model in the CMB from Chow *et al.*, (1992 and 1993).[28,29] Hence, the receptor concentration matrix had a size of 26×1. The contents of NO_3^-, SO_4^{2-}, NH_4^+, elemental carbon (EC), organic carbon (OC), Al, Si, P, S, Cl, K, Ca, Ti, V, Cr, Mn, Fe, Ni, Cu, Zn, Se, Br, Sr, Zr, Ba and Pb in PM_{10} and $PM_{2.5}$ were analyzed to estimate the source contributions. The 26 species present in PM_{10} and $PM_{2.5}$ were identified as originating from ten sources according to the emission inventory, which is known as the source profile (percentage of mass emitted) for central California.[29] Hence, the source profile matrix had the size of 26×10. Since the elemental compositions of several sources were identified in the data base of USEPA (SPECIATE) and various studies,[5,30,32] it was recommended that the particulate matter ($PM_{2.5}$ & PM_{10}) sources be characterized locally for source apportionment studies.[33]

Analysis of Portland, OR, PM_{10} data[30]

The average concentrations of 23 species in PM_{10} analyzed at Portland, OR, were used to model the proposed CMB from Watson *et al.* (1984).[30] The source composition data and 24 h average concentration of OC, EC, NO_3^-, SO_4^{2-}, F^-, Na, Mg, Al, Si, S, Cl, K, Ca, Ti, V, Cr, Mn, Fe, Ni, Cu, Zn, Br and Pb were used as the input species in the three CMB models. The sources compositions of marine, urban dust, auto exhaust and residual oil combustion were used as source profile data in the CMB. The corresponding uncertainty values were also determined as per the literature followed.[30]

Source contribution and predicted concentration

Source contribution values of each source were obtained from CMB8.2, CMB–fmincon and CMB–GA for the Fresno, Bakersfield and Oregon data. The measured source profile and obtained source contribution were used to calculate c_{pre} of the species measured through backward trajectory. The errors between the experimental and predicted concentrations for the three approaches were also estimated.

RESULTS AND DISCUSSIONS

The source contributions for the analyzed species in PM10 and PM2.5 obtained using CMB8.2, CMB–fmincon and CMB–GA for the Fresno, Bakersfield and Oregon stations are presented, respectively, in Figs. S-3–S-5 of the Supplementary material. It was observed that the source contributions obtained using CMB–fmincon and CMB–GA fitted better than those obtained using CMB8.2. The statistical parameters obtained for the PM_{10} and $PM_{2.5}$ samples from the Fresno, Bakersfield and Oregon sites using CMB8.2, CMB–fmincon and CMB–GA software are presented in Tables I–III.

TABLE I. Statistical validation of the results obtained for the analysis of the SJVAQ, California, Fresno data using the three chemical mass balance models

Statistical parameter	CMB8.2		CMB–fmincon		CMB–GA	
	PM_{10}	$PM_{2.5}$	PM_{10}	$PM_{2.5}$	PM_{10}	$PM_{2.5}$
R^2	0.80	0.56	0.87	0.59	0.90	0.67
χ^2	0.57	1.03	0.60	0.89	0.36	0.66
Mass, %	63.23	53.81	65	54.1	67.36	55.03

TABLE II. Statistical validation of the results obtained for the analysis of the SJVAQ, California, Bakersfield data using the three chemical mass balance models

Statistical parameter	CMB8.2		CMB–fmincon		CMB–GA	
	PM_{10}	$PM_{2.5}$	PM_{10}	$PM_{2.5}$	PM_{10}	$PM_{2.5}$
R^2	0.71	0.62	0.78	0.75	0.81	0.83
χ^2	1.13	0.85	0.80	0.83	0.65	0.43
Mass, %	88.4	65.64	91.37	71.23	94.24	74.85

The two stations Fresno and Bakersfield were significant receiving various types of atmospheric pollution from large urban locations in California. The significant quantities of sulfate and nitrate in the ambient aerosol may be of second-

ary origin. Hence ammonium sulfate, ammonium nitrate, sodium nitrate and organic carbon (OC) were considered as a "pure" secondary source profile.[28] Ammonium nitrate, paved road dust, secondary organic carbon, motor vehicle, ammonium sulfate, limestone were observed as the major contributors to PM_{10} at the Fresno station. Primary crude oil, marine and vegetation burning were the successive emission sources of PM_{10} to the ambient air (Fig. S-3a–c). Secondary aerosols (NH_4NO_3, secondary OC and $(NH_4)_2SO_4$) were observed as the major sources of $PM_{2.5}$ with contributions from paved road dust, primary crude oil and marine sources as not neglectable sources of $PM_{2.5}$ at the Fresno station (Fig. S--3d–f). Moreover, vegetative burning, limestone (construction activities) and motor vehicle emissions were other possible sources of $PM_{2.5}$ at the Fresno station.

TABLE III. Statistical validation of the results obtained for the analysis of the Portland, Oregon data using the three chemical mass balance models

Statistical parameter	CMB8.2	CMB–fmincon	CMB–GA
R^2	0.97	0.98	0.99
χ^2	1.89	1.63	1.6
Mass, %	93.1	93.5	94.4

Paved road dust, motor vehicle emission, secondary nitrate, secondary sulfate, limestone (construction activities), primary crude oil and marine sources were observed as the major PM_{10} emissions at Bakersfield (Fig. S-4a–c). Secondary aerosols, paved road dust, primary crude oil, marine, limestone were observed as the major $PM_{2.5}$ emission sources (Fig. S-4d–f). Vegetative burning seems to have contributed less to both PM_{10} and $PM_{2.5}$ emissions at the Bakersfield station.

The source contribution optimized using the genetic algorithm (CMB–GA) showed the least percentage error between c_{exp} and c_{pre} concentrations of the species at Fresno and Bakersfield based on statistical parameters, as can be seen in Tables I and II. The Percentage mass value obtained from CMB–GA for PM_{10} and $PM_{2.5}$ were acceptable for both Fresno (67.36 and 55.03 %) and Bakersfield (94.24 and 74.85 %) sites than CMB8.2 and CMB–fmincon optimization. The percentage mass values obtained for PM_{10} *via* all three approaches were acceptable (63.23, 65 and 63.58 % for Fresno and 88.4, 91.37 and 94.24 % for Bakersfield), which indicates the estimates of the source contribution were well fitted in all three models. Hence, it could be predicted that optimization with the genetic algorithm yields better source contribution compared to CMB8.2 and CMB––fmincon optimizations. The performance measure by the χ^2 values from the respective three approaches were acceptable and the values obtained from CMB––GA for PM_{10} and $PM_{2.5}$ were 0.36 and 0.66 for the Fresno site and 0.65 and 0.43 for the Bakersfield site, the data of which proved the good results. Hence, all the concentrations of the species were best explained by the source contribution

estimate from the genetic algorithm optimization, then from the fmincon and then from the CMB8.2 models. It was found that the error percentages between the experimental and predicted receptor concentrations were the lowest from the genetic algorithm approach as compared to the CMB8.2 and CMB–fmincon approaches. The successive R^2 values for the PM_{10} data were best fit in the order of CMB–GA (0.81), then CMB–fmincon (0.78) and then CMB8.2 (0.71) and for $PM_{2.5}$ CMB–GA (0.83), then CMB–fmincon (0.75) and then CMB8.2 (0.62).

The source contributions obtained from the three respective CMB models for Portland, Oregon PM_{10} data are shown in Fig. S-5a–c. The best source estimation was observed form CMB–GA with the best R^2 (0.99), χ^2 (1.6) and percentage mass (94.4 %) then CMB–fmincon and then CMB8.2, as can be seen in Table III. The χ^2 value between 1 and 2 is acceptable and the large percentage mass indicates the better estimation of the source contribution through CMB–GA.

Comparison between the experimental and calculated concentrations of 26 species in PM_{10} and $PM_{2.5}$ analyzed through estimates of the source contribution from the three respective CMB approaches in the Fresno (Fig. 3) and Bakersfield

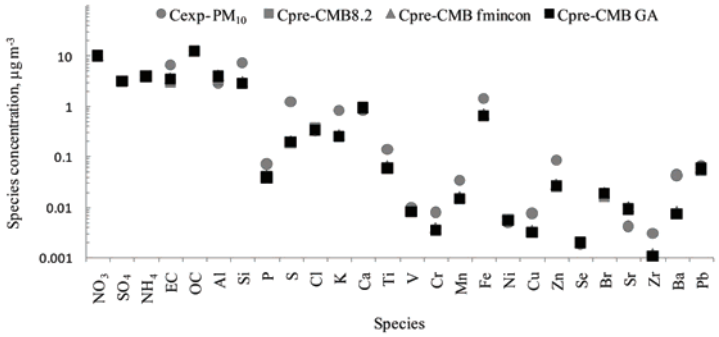

(a)

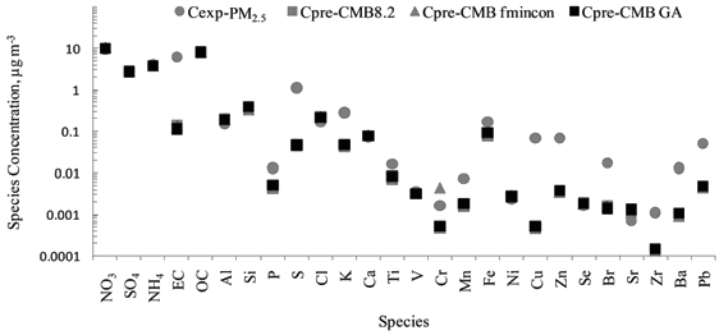

(b)

Fig. 3. Experimental concentrations (c_{exp}) and the concentrations of species predicted by CMB8.2, CMB–fmincon and CMB–GA ($c_{pre\text{-}CMB8.2}$, $c_{pre\text{-}CMB\text{-}fmincon}$ and $c_{pre\text{-}CMB\text{-}GA}$, respectively) in: a) PM_{10} and b) $PM_{2.5}$ from Fresno data.

(Fig. 4) data revealed possible deviations of the concentrations species from the real data. Since the genetic algorithm approach revealed large percentage mass (both Fresno and Bakersfield) with low χ^2 and a better R^2 value, accurate concentrations of the species are predicted than the respective values obtained from CMB–fmincon and CMB8.2. The experimental and predicted species concentration data obtained for Portland, Oregon PM_{10} is shown in Fig. 5. The least errors between C_{exp} and C_{pre} were observed for the data analyzed by CMB––GA than the data analyzed by CMB–fmincon or CMB8.2.

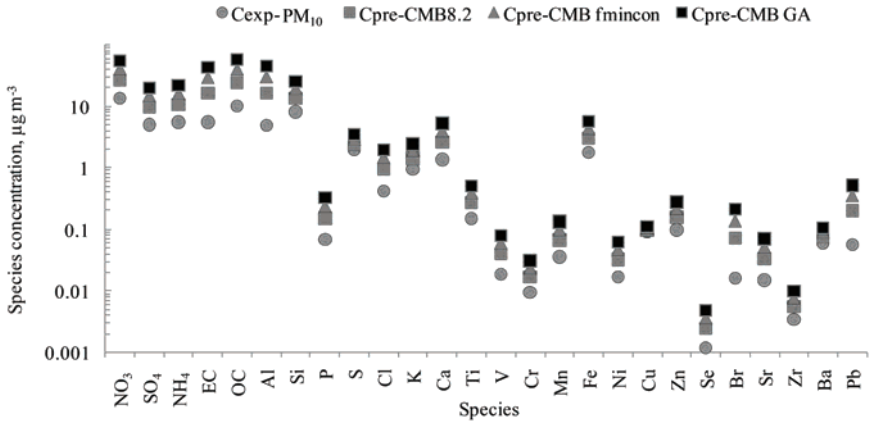

(a)

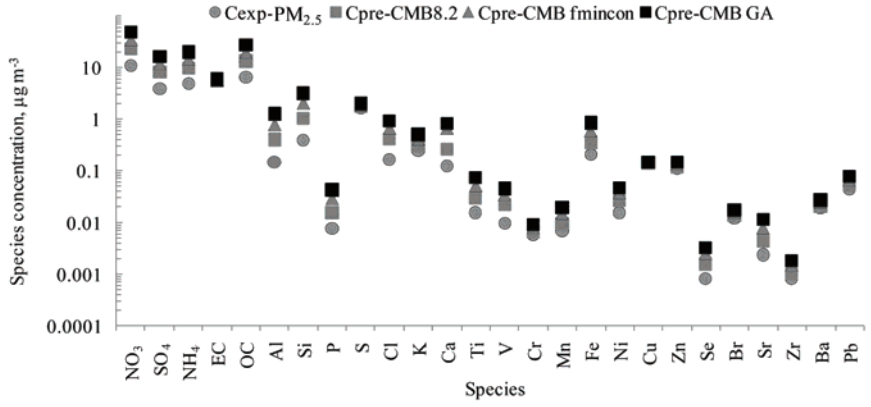

(b)

Fig. 4. Experimental concentrations (c_{exp}) and concentrations of species predicted by CMB8.2, CMB–fmincon and CMB–GA ($c_{pre\text{-}CMB8.2}$, $c_{pre\text{-}CMB\text{-}fmincon}$ and $c_{pre\text{-}CMB\text{-}GA}$, respectively) in: a) PM_{10} and b) $PM_{2.5}$ from Bakersfield data.

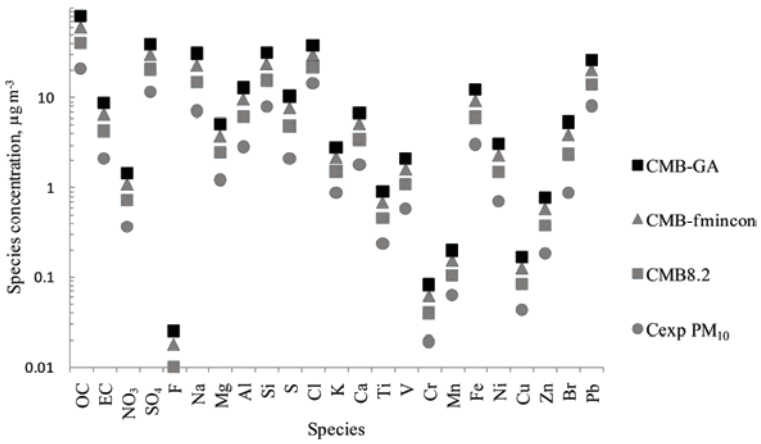

Fig. 5. Experimental concentrations (c_{exp}) and concentrations of species predicted by CMB8.2, CMB–fmincon and CMB–GA ($c_{pre\text{-}CMB8.2}$, $c_{pre\text{-}CMB\text{-}fmincon}$ and $c_{pre\text{-}CMB\text{-}GA}$, respectively) in PM_{10} from Portland, OR, data.

CONCLUSIONS

The output of chemical mass balance model gives the contribution of each source type represented by a composition to the total mass, as well as to each chemical species in the receptor concentration. A comparison of CMB receptor models was performed to understand the efficiency in source contribution through various optimization techniques. The source profile uncertainty and receptor concentration uncertainties were used in the CMB8.2 software tool developed by USEPA. Optimized source contributions were obtained by CMB–GA and CMB–fmincon. The best estimate of the source contributions from the converged solution through CMB–GA was possible by a large number of generations. The source contributions obtained from the CMB8.2 deviated more in comparison with those obtained from the CMB–fmincon and CMB–GA because of the constrained optimization by 'fmincon' and GA solvers. The model accuracy was validated by various performance measures such as R^2, χ^2 and percentage mass for the three respective CMB approaches. Very high correlations between c_{pre} and c_{exp} were obtained from CMB–GA for the Bakersfield data (0.81 and 0.83) than from CMB–fmincon and CMB8.2. χ^2 (0.36, 0.66 and 0.65, 0.43) and percentage mass (67.36 , 55.03 and 94.24 %, 74.85 %) from the CMB–GA model illustrated more accurate data for PM_{10} and $PM_{2.5}$ from Fresno and Bakersfield. The methodology was followed with Portland, OR, PM_{10} data that also resulted in the best fit from CMB–GA with R^2, χ^2 and percentage mass values of 0.99, 1.6 and 94.4 %, respectively. The study revealed that CMB method with genetic algorithm optimization has better stability and more accuracy in determining the contributions of sources than CMB–fmincon and CMB8.2.

SUPPLEMENTARY MATERIAL

The execution of CMB by 'fmincon' solver in MATLAB R2008a, Fig. S-1, execution of the genetic algorithm code, Fig. S-2, details of the CMB–GA method and source contributions for the analyzed species in PM10 and PM2.5 obtained using CMB8.2, CMB–fmincon and CMB–GA for the Fresno, Bakersfield and Oregon stations, Figs. S-3–S-5, are available electronically from http://www.shd.org.rs/JSCS/, or from the corresponding author on request.

Acknowledgement. The authors are very grateful to the editors and reviewers for their valuable comments and suggestions, which helped to improve the quality of the manuscript.

И З В О Д

ЕВАЛУАЦИЈА ОПТИМИЗАЦИЈЕ МЕТОДЕ ЗА РЕШАВАЊЕ МОДЕЛА ХЕМИЈСКОГ БИЛАНСА МАСЕ

N. ANU, S. RANGABHASHIYAM, RAHUL ANTONY и N. SELVARAJU

Department of Chemical Engineering, National Institute of Technology Calicut Kozhikode-673601, Kerala, India

Модел хемијског биланса масе (CMB) се користи да би се одредили доприноси извора честица (пречника мањих од 10 и 2,5 μm) у анализи квалитета ваздуха. Поређење доприноса извора одређених на основу три CMB модела (CMB 8.2, CMB fmincon и CMB–GA) је вршено коришћењем оптимизационих техника, као што су 'fmincon' (CMB–fmincon) и генерички алгоритам (CMB–GA), у програмском пакету MATLAB. Предложени приступ је потврђен коришћењем података *San Joaquin Valley Air Quality Study* (SJVAQS) *California Fresno* и *Bakersfield* PM_{10} и $PM_{2,5}$, као и *Oregon* PM_{10}. Допринос извора одређен из CMB–GA је био бољи по питању интерпретације извора, у поређењу са CMB 8.2 i CMB–fmincon. Валидација поузданости три CMB приступа је вршена коришћењем следећих параметара: R^2, редуковани χ^2 и проценат масе. R^2 (0,90, 0,67 и 0,81, 0,83), χ^2 (0,36, 0,66 и 0,65, 0,43) и проценат масе (67,36, 55,03 и 94,24 %, 74,85 %) тестови за CMB–GA су показали добру корелацију за PM_{10} и $PM_{2,5}$ Fresno и Bakersfield податке. Да би се дошло до коначне одлуке, предложена методологија је била примењена на Portland, OR, PM_{10} податке са најбољим слагањем са R^2 (0,99), χ^2 (1,6) и проценат масе (94,4 %) из CMB–GA. Због тога је ово испитивање показало да CMB са генеричким алгоритмом оптимизације има бољу стабилност у одређивању доприноса извора.

(Примљено 14. новембра 2013, ревидирано 31. марта, прихваћено 18. маја 2014)

REFERENCES

1. A. O. M. Carvalho, M. C. Freitas, *Procedia Environ. Sci*. **4** (2011) 184
2. X. Zhang, W. Chen, C. Ma, S. Zhan, *Sci. Total Environ*. **449** (2013) 168
3. A. Kristin, W. Shuxiao, *Sci. Total Environ*. **481** (2014) 186
4. S. Yatkin1, A. Bayram, *Chemosphere* **71** (2008) 685
5. B. Srimuruganandam1, S. M. Shiva Nagendra, *Sci. Total Environ*. **433** (2012) 8
6. Z. Huarong, X. Beicheng, F. Chen, Z. Peng, S. Shili, *Sci. Total Environ*. **417**–**418** (2012) 45
7. M. Viana1, M. Pandolfi, M. C. Minguillon, X. Querol, A. Alastuey, E. Monfort, I. Celades, *Atmos. Environ*. **42** (2008) 3820
8. C. A. Belis, F. Karagulian, B. R. Larsen, P. K. Hopke, *Atmos. Environ*. **69** (2013) 94
9. A. Lukewille, I. Bertok, M. Amann, J. Cofala, F. Gyarfas, M. Johansson, Z. Klimont, E. Pacyna, J. Pacyna, *Water Air Soil Pollut*. **130** (2001) 229
10. P. K. Hopke, *Atmos. Environ*. **43** (2009) 87

11. R. C. Henry, C. W. Lewis, P. K. Hopke, H. J. Williamson, *Atmos. Environ.* **18** (1984) 1507
12. J. C. Chow, J. G. Watson, *Energy Fuels* **16** (2002) 222
13. B. R. Larsen, H. Junninen, J. Monste, M. Viana, P. Tsakovski, R. M. Duvall, G. A. Norris, X. Querol, *The Krakow Receptor Modelling Intercomparison Exercise Rep.* JRC Scientific and Technical Reports, EUR 23621 EN 2008, Ispra, 2008
14. M. Pandolfi, M. Viana, M. C. Minguillon, X. Querol, A. Alastuey, F. Amato, I. Celades, A. Escrig, E. Monfort, *Atmos. Environ*. **42** (2008) 9007
15. S. Kong, B. Han, Z. Bai, L. Chen, J. Shi, Z. Xu, *Sci. Total Environ*. **408** (2010) 4681
16. S. Yatkin, A. Bayram, *Environ. Monit. Assess*. **167** (2010) 125
17. J. H. Seinfeld, S. N. Pandis, *Atmospheric chemistry and physics from air pollution to climate change*, 2nd ed., Wiley, Hoboken, NJ, 2006, p. 1136
18. L. W. A. Chen, J. G. Watson, J. C Chow, D. W. DuBois, L. Herschberger, *Atmos. Environ*. **44** (2010) 4908
19. W. F. Christensen, *Atmos. Environ*. **38** (2004) 4305
20. W. F. Christensen, R. F. Gunst, *Atmos. Environ*. **38** (2004) 733
21. G. Argyropoulos, C. Samara, *Environ. Modell. Softw*. **26** (2011) 469
22. G. Argyropoulos, Th. Grigoratos, M. Voutsinas, C. Samara, *Environ. Sci. Pollut. Res. Int*. **20** (2013) 7214
23. H. S. Javitz, J. G. Watson, N. Robinson, *Atmos. Environ*. **22** (1988) 2309
24. H. Cheng, A. Sandu, *Environ. Modell. Software* **24** (2009) 917
25. T. C. Coulter, *EPA-CMB8. User's Manual*, EPA-452/R-04-011 United States Environmental Protection Agency, Research Triangle Park, NC, 2004
26. N. Selvaraju, S. Pushpavanam, N. Anu, *Environ. Monit. Assess*. **185** (2013) 10115
27. N. Anu, S. Rangabhashiyam, N. Selvaraju, S. Pushpavanam, *J. Sci. Ind. Res.* **72** (2013) 754
28. J. C. Chow, J. G. Watson, D. H. Lowenthal, P. A. Solomon, K. L. Magliano, S. D. Ziman, L. W. Richard, *Atmos. Environ*., *A* **26** (1992) 3335
29. J. C. Chow, J. G. Watson, D. H. Lowenthal, P. A. Solomon, K. L. Magliano, S. D. Ziman, L. W. Richard, *Aerosol Sci. Technol*. **18** (1993) 105
30. J. G. Watson, J. A. Cooper, J. J. Huntzicker, *Atmos. Environ*. **18** (1984) 1347
31. A. Chipperfield, P. Fleming, H. Pohlheim, C. Fonseca, *Genetic Algorithm TOOLBOX User's Manual*, version 1.2, University of Sheffield, Sheffield, https://www.sheffield.ac.uk/polopoly_fs/1.60188!/file/manual.pdf (accessed in Feb, 2015)
32. K. F. Ho, S. C. Lee, J. C. Chow, J. G. Watson, *Atmos. Environ*. **37** (2003) 1023
33. R. D. Paode, U. M. Shahin, J. Sivadechathep, T. M. Holsen, W. J. Franek, *Aerosol. Sci. Technol*. **31** (1999) 473.

Journal of the Serbian Chemical Society
JSCS@tmf.bg.ac.rs • www.shd.org.rs/JSCS
J. Serb. Chem. Soc. 80 (2) S47–S54 (2015) *Supplementary material*

SUPPLEMENTARY MATERIAL TO

Evaluation of optimization methods for solving the receptor model for chemical mass balance

N. ANU, S. RANGABHASHIYAM, ANTONY RAHUL and N. SELVARAJU*

Department of Chemical Engineering, National Institute of Technology Calicut Kozhikode-673601, Kerala, India

J. Serb. Chem. Soc. 80 (2) (2015) 253–264

SOME DETAILS OF THE CMB WITH A GENETIC ALGORITHM (CMB–GA)[1]

The main routine has a program for the genetic algorithm and the other sub-routine is for the calculation of the objective function based on simulation in MATLAB. This starts execution by assigning the maximum number of generations. To commence with, the first initial population is created in the zeroth generation from two different sets of chromosomes having *p* individuals. For each set of chromosomes, objective functions are calculated from the subroutine. The function calls once for each set. In each call, it creates a binary population based on the bounds provided in the FieldD. FieldD is a field descriptor that is constructed using the matrix replication function, *rep*, to build the matrix 'FieldD', describing the representation and interpretation of the chromosomes. It describes number of variable (*Nvar*), each Gray coded using 20 (*Preci*) bits over the interval [lb, ub]. An initial population is then created with the function *crtbp* thus, producing a matrix, Chrom′, of Nind′ uniformly distributed random binary strings of length *Nvar*×*Preci*. This is decoded to phenotypic values then it is passed to the subroutine for objective function calculation. The subroutine returns the objective function values of an array of size *p*. These returned values are arranged in ascending order. This is repeated for next set of chrome, the return values from the subroutine are again sorted then stored in an array. The first half of the first set and second half of the second set will be the initial population for the first generation.

The selected individuals recombine to generate the offspring by crossover and mutation. Mutation is randomly applied with a low probability, typically in the range of 0.001 and 0.05. The parent chromes will be replaced with the child, once the offspring are created. Then the objective function calculation performed

* Corresponding author. E-mail: selvaraju@nitc.ac.in

again and fitness values are assigned to them. This process continues until all the parameter values converge. If the parameter values and the objective function value became the same over 1000 generations, the program is terminated. The objective function can be expressed as:

$$\text{Objective function} = \left\| (c_{\text{pre}} - c_{\text{exp}})^2 \right\| \quad (5)$$

where c_{exp} and c_{pre} are the concentrations of the species determined experimentally by Chow *et al.*[2] and those predicted by the model, respectively. The above results multiplied with the source profile can enable the source contributions to be obtained directly. The subroutine calculates the objective functions for 'P' individuals. Each individual contains *Nvar*, no tuning parameters. For an individual run, the respective parameters are positioned in their respective index of the tuned parameter.[3] The converged solution for a 1000 generations, a stall limit of infinity, a population matrix size of 50×300 and the basic mass equation were used as the selection functions and a tolerance limit of 0.00001 that gave an estimation of a source contribution and the calculated species concentration (c_{pre}).

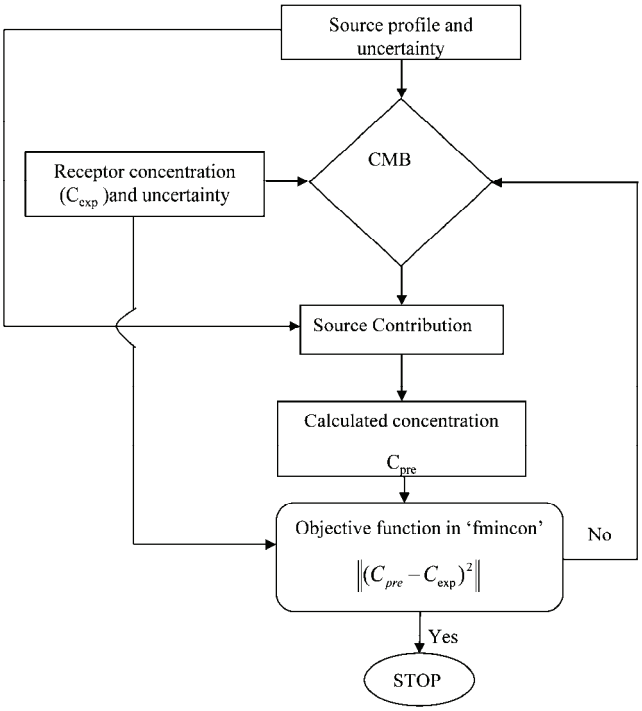

Fig. S-1. Execution of the CMB source contribution by the *fmincon* solver in MATLAB.

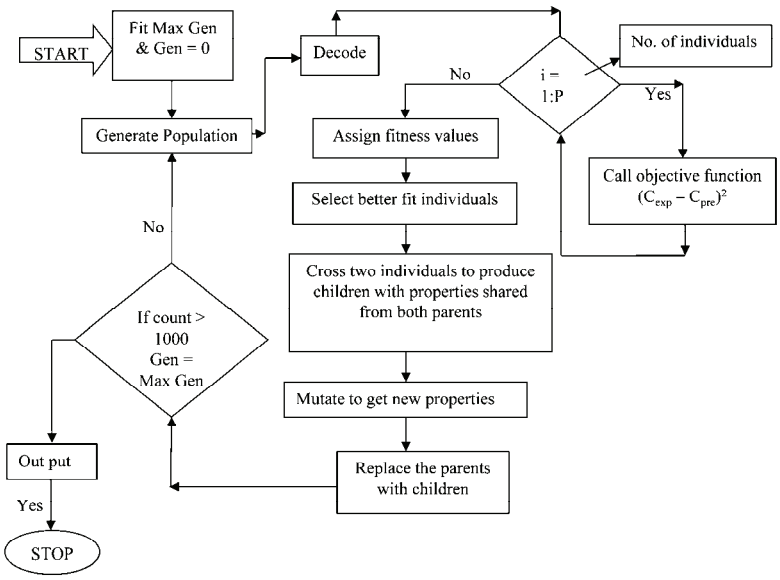

Fig. S-2. Execution of the genetic algorithm code.

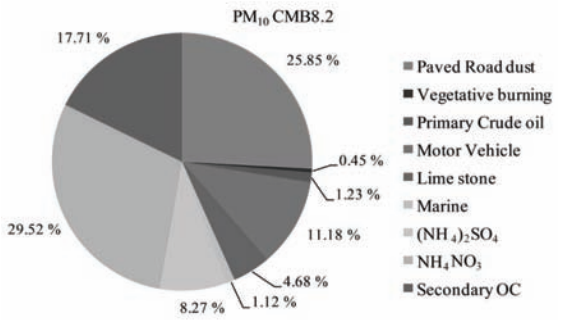

Fig. S-3a. Source contributions obtained for the PM_{10} Fresno data using CMB8.2.

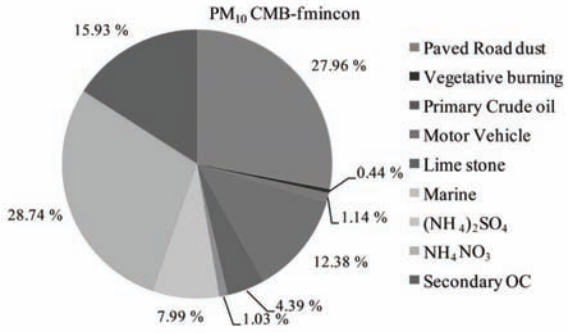

Fig. S-3b. Source contributions obtained for the PM_{10} Fresno data using CMB–fmincon.

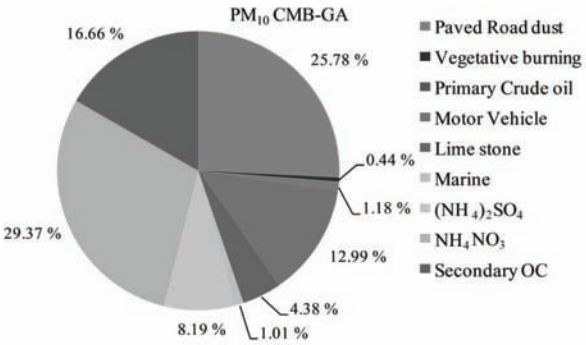

Fig. S-3c. Source contributions obtained for the PM_{10} Fresno data using CMB–GA.

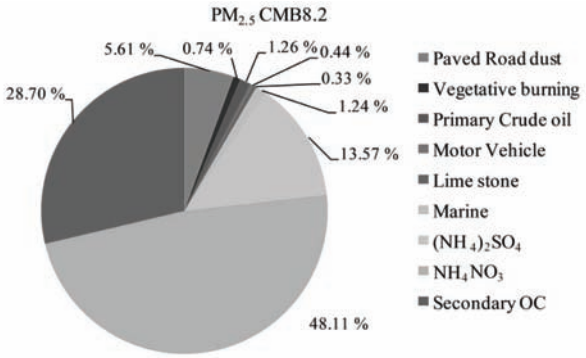

Fig. S-3d. Source contributions obtained for the $PM_{2.5}$ Fresno data using CMB8.2.

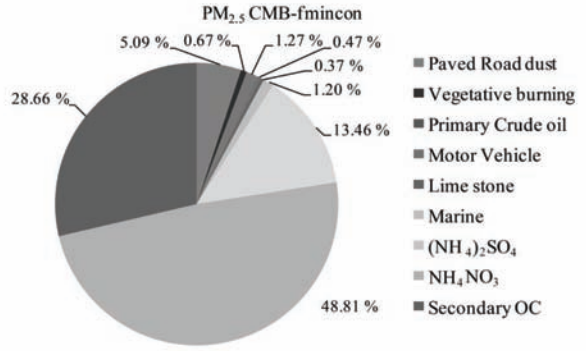

Fig. S-3e. Source contributions obtained for the $PM_{2.5}$ Fresno data using CMB–fmincon.

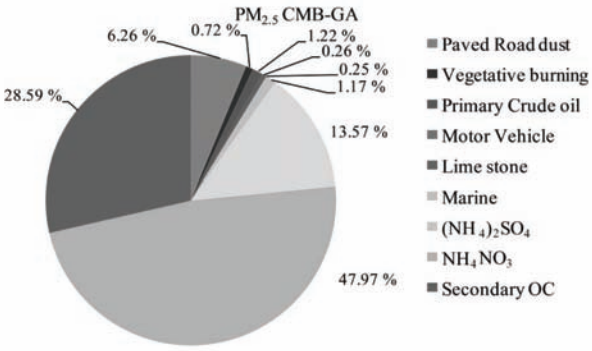

Fig. S-3f. Source contributions obtained for the $PM_{2.5}$ Fresno data using CMB–GA.

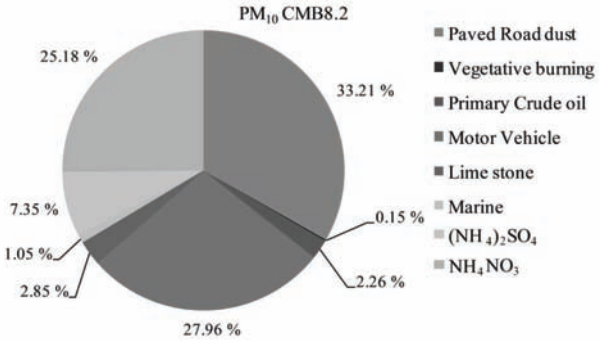

Fig. S-4a. Source contributions obtained for the PM_{10} Bakersfield data using CMB8.2.

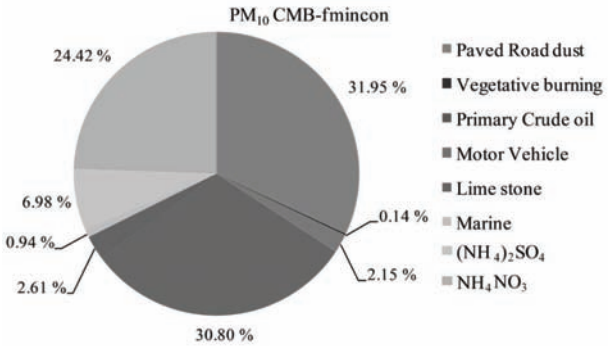

Fig. S-4b. Source contributions obtained for the PM_{10} Bakersfield data using CMB–fmincon.

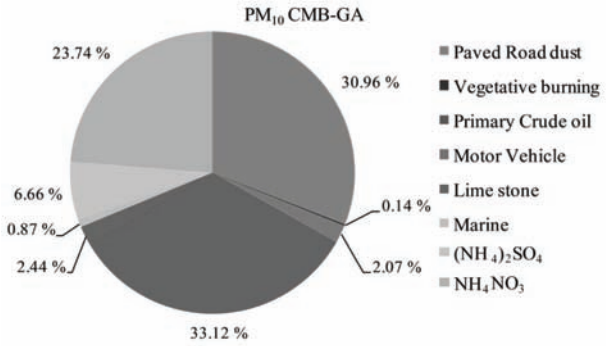

Fig. S-4c. Source contributions obtained for the PM_{10} Bakersfield data using CMB–GA.

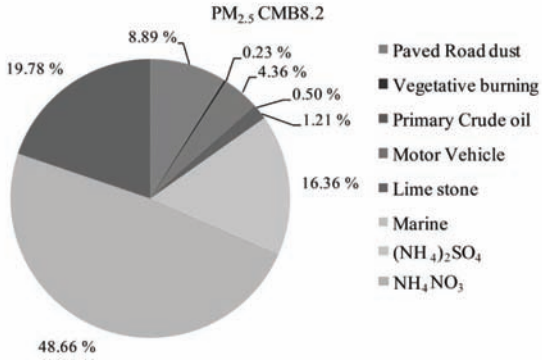

Fig. S-4d. Source contributions obtained for the $PM_{2.5}$ Bakersfield data using CMB8.2.

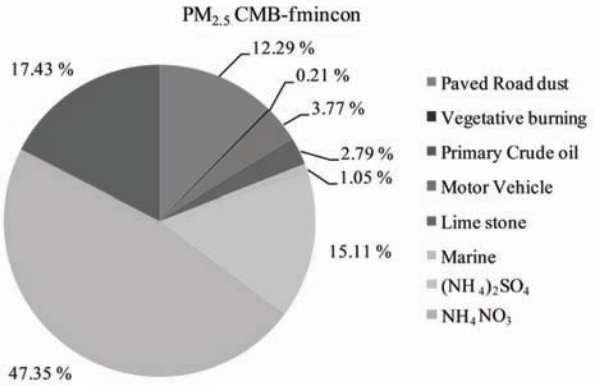

Fig.S-4e. Source contributions obtained for the $PM_{2.5}$ Bakersfield data using CMB–fmincon.

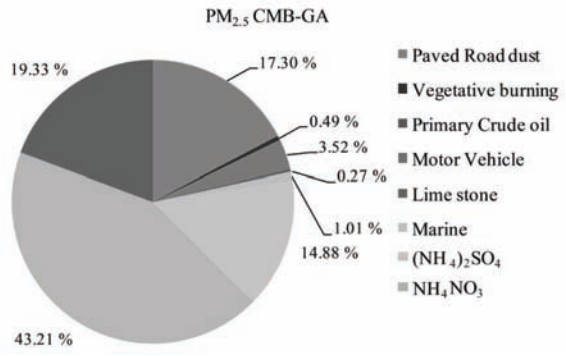

Fig. S-4f. Source contributions obtained for the $PM_{2.5}$ Bakersfield data using CMB–GA.

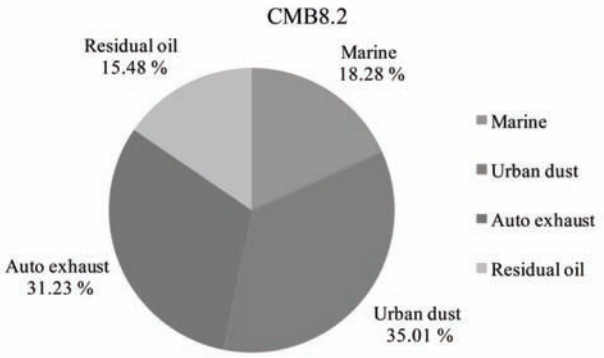

Fig. S-5a. Source contributions obtained for the PM_{10} Portland, Oregon data using CMB8.2.

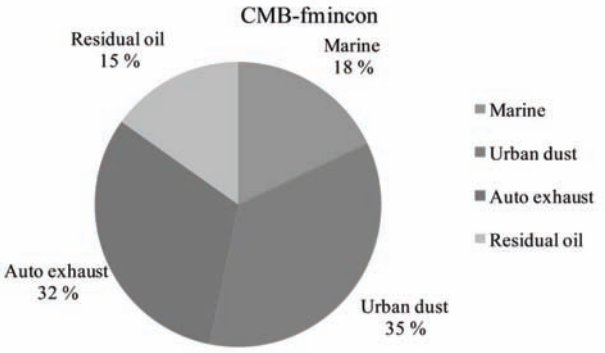

Fig. S-5b. Source contributions obtained for the PM_{10} Portland, Oregon data using CMB–fmincon.

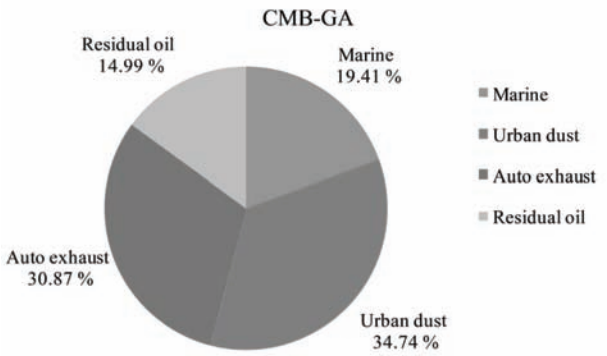

Fig. S-5c. Source contributions obtained for the PM_{10} Portland, Oregon data using CMB–GA.

REFERENCES

1. A. Chipperfield, P. Fleming, H. Pohlheim, C. Fonseca, *Genetic Algorithm TOOLBOX User's Manual*, Version 1.2, University of Sheffield, Sheffield, UK
2. J. C. Chow, J. G. Watson, D. H. Lowenthal, P. A. Solomon, K. L. Magliano, S. D. Ziman, L. W. Richard, *Aerosol Sci. Technol*. **18** (1993) 105
3. S. E. Haupt, G. S. Young, C. T. Allen, *J. Appl. Meteorol*. **45** (2006) 476.

Journal of the Serbian Chemical Society
JSCS-info@shd.org.rs • www.shd.org.rs/JSCS
J. Serb. Chem. Soc. 80 (2) 265–275 (2015) UDC 54–44+544.275–128+541.183:546.264–31
JSCS–4715 *Original scientific paper*

Molecular sieve-supported ionic liquids as efficient adsorbents for CO_2 capture

NA YANG[1] and RUI WANG[2]*

[1]*School of Environmental Science and Engineering, Shandong University, Jinan 250100, Shandong, China, E-mail: yangna13579@tom.com and* [2]*School of Environmental Science and Engineering, Shandong University, Jinan 250100, Shandong, China*

(Received 22 February, revised 29 September 2014, accepted 23 October 2014)

Abstract: Amino ethyl-3-methylimidazolium tetrafluoroborate, [NH_3e-mim][BF_4], amino ethyl-3-methylimidazolium tetrafluoroborate, [OHe-mim][BF_4], and 2-hydroxyethylammonium lactate, [HOEAm], were selected and supported onto a variety of molecular sieves, NaY, USY, SAPO-34 and MCM-41, to prepare supported ionic liquids. It was found that [NH_3e-mim][BF_4]/NaY showed an excellent CO_2 adsorption performance, with an adsorption capacity of 0.11 mmol CO_2 g^{-1}. In this study, the optimal adsorption conditions and recyclability of [NH_3e-mim][BF_4]/NaY were investigated. The results showed that [NH_3e-mim][BF_4]/NaY showed good CO_2 adsorption under the conditions of 20 °C and 20 % loading of the IL. By vacuum heating, the CO_2 adsorption capacity reached 0.45 mmol CO_2 g^{-1} in the fifth adsorption run but was reduced to 0.29 mmol CO_2 g in the tenth run. The structure and characterization of [NH_3e-mim][BF_4]/NaY were examined by FT-IR, XRD, SEM and TG–DSC. The TG–DSC results showed that the thermostability of NH_3e-mim][BF_4]/NaY was good below 50 °C.

Keywords: ionic liquid; molecular sieve; CO_2; adsorption capacity.

INTRODUCTION

It is well recognized that CO_2 is one of the most important greenhouse gases in the global warming phenomenon.[1–3] Many technologies on CO_2 capture and storage (CCS) are being investigated to control CO_2 emissions.[4–6] The employment of ionic liquids (ILs) for CO_2 capture was discussed in many reports and review articles.[7] As a new type of green solvent,[8] ILs have unique characteristics, such as wide liquid range, thermal stability, negligible vapor pressure and tunable physicochemical characteristics.[9–11] However, the much discussed important drawbacks of ionic liquids are their high viscosity, slow adsorption rate and high costs, which has constrained the industrial application of ILs.[12] Scovazzo[13] and

* Corresponding author. E-mail: ree_wong@hotmail.com
doi: 10.2298/JSC220214103Y

Hconich[14] attempted to prepare ionic liquids supported on porous materials (SIL), and found that the porous material could well disperse ILs, improving the gas adsorption rate and reducing the amount of ILs used. Zhang *et al.*[15] successfully prepared ionic liquids supported on SiO_2, with a CO_2 adsorption efficiency of 1.92 %. Fu *et al.*[12] investigated amino functionalized ionic liquids supported by Al_2O_3, SiO_2 and activated carbon, and found that the Al_2O_3-supported ionic liquids exhibited higher adsorption capacities for CO_2, with values of 0.359, 0.286 and 0.228 mmol g^{-1} for $[NH_3p\text{-}mim][Br]/Al_2O_3$, $[NH_3p\text{-}mim][PF_4]/Al_2O_3$ and $[NH_3p\text{-}mim][BF_4]/Al_2O_3$, respectively. A molecular sieve was also investigated for CO_2 adsorption because of its large specific surface area and pore volume.[16] Carbon dioxide capture by molecular sieve-supported ionic liquids is one of the promising methods. In this paper, ionic liquids supported on several molecular sieves were prepared. The optimal one was selected to optimize the adsorption conditions and investigate adsorbent reuse. Fourier transform infrared (FT-IR), powder X-ray diffraction (XRD), scanning electron microscopy (SEM), thermogravimetric analysis (TG) and differential scanning calorimetry (DSC) were used to characterize the obtained ionic liquids containing adsorbents.

EXPERIMENTAL

Chemical reagents and test equipment

Aminoethyl-3-methylimidazolium tetrafluoroborate ($[NH_3e\text{-}mim][BF_4]$), 1-hydroxy ethyl-3-methylimidazolium tetrafluoroborate ($[OHe\text{-}mim][BF_4]$) and 2-hydroxyethylammonium lactate ([HOEAm]), all A.R. grade, were supplied by Shanghai Chengjie Chemical Plant. The molecular sieves NaY, USY, SAPO-34, MCM-41, all A.R. grade, were received from the NanKai University Catalyst Institute. Ethanol, A.R. grade, was obtained from the Tianjin Fuyu Fine Chemical Co. Ltd. N_2 with a purity of 99.999 % and CO_2 with 10 % volume fraction, were supplied by Jinan Deyang Gas Co. Ltd.

Gas mass flow controllers, D08-1D/ZM for N_2 and D08-1F for CO_2, were supplied by Beijing Sevenstar Electronics Co. Ltd. Electric heating (DF-101S) and a rotary evaporator (Fre-52C) were produced by Henan Yuhua Instrument Co. Ltd. A portable IR CO_2 analyzer (GXH-3010E) was purchased from Beijing HuaYun Instrument Co. Ltd. A powder compressing machine (769YP-15A) was supplied by Tianjin Keqi Instrument Co. Ltd. A mortar, sieve and absorber were supplied by Jinan Bangen Instrument Co. Ltd.

Preparation of molecular sieve-supported ionic liquids

An IL (2 g) was dissolved in 75 mL of ethanol under vigorous stirring for 5 min, and the required quantity of molecular sieve was added to give the stipulated IL loading. The resulting mixture was stirred for 3 h at 20 °C, and then the ethanol was removed under vacuum in a rotary evaporator. The resulting solid was pressed into the form of a pellet using a powder compressing machine and then crushed into particles using a mortar. After screening of the 0.2–0.4 mm diameter particle using sieves, the molecular sieve-supported ionic liquid was obtained.

CO_2 adsorption and desorption test

The gas flow containing 10 % volume fraction of CO_2 was generated by mixing CO_2 at 8 mL min^{-1} and N_2 at 192 mL min^{-1}. The system employed for the CO_2 adsorption experiments,

which included gas cylinders (CO_2, N_2), pressure regulators, gas mass flow controllers, absorber and CO_2 analyzer, is shown in Fig. 1. The absorber was a glass tube of inner diameter 1.0 cm with a gas dispersion orifice to support the fixed absorbent bed. The temperature of the absorber was controlled by a thermostated water bath. CO_2 desorption was performed in a vacuum rotary evaporator operated at 100 °C for 3 h.

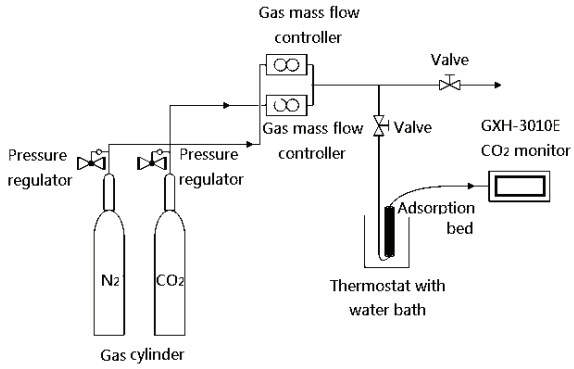

Fig. 1. Schematic presentation of the apparatus employed for the CO_2 adsorption experiments. (IL loading on molecular sieve: 20 %, mass of SIL: 4g; concentration of CO_2: 3928 mg N m^{-3}; *T*: 20 °C).

Characterization

The FT-IR spectra were recorded on a 5DXC IR spectrometer in the wavenumber range 4000 to 400 cm^{-1} with a 2 cm^{-1} resolution using 10 mg samples diluted with 150 mg KBr and pressed into a 13 mm pellet.

XRD measurements were performed on a Bruker D8 Advanced diffractometer with a Cu target, K_α-rays and a nickel filter. A scanning rate of 28 per minute in the 2θ scanning angle range of 3° and 70° was used.

The SEM pictures were acquired on a JEOL JSM-6700F microscope. Samples were coated with osmium. Particle size and size distribution analyses were performed on a dynamic light scattering (DLS) instrument.

TG and DSC analyses were realized on a SDT Q600 Universal V4.1D instrument (TA Instruments) under a dynamic N_2 atmosphere from room temperature to 700 °C at a heating rate of 10 °C min^{-1}.

RESULTS AND DISCUSSION

Adsorption performance of different supported ionic liquids

The three studied ILs, [NH_3e-mim][BF_4], [OHe-mim][BF_4] and [HOEAm], were supported on NaY, USY, SAPO-34 and MCM-41 at a loading of 20 % (*w*/*w*). The adsorption capacities of the prepared adsorbents (4 g) for CO_2 were determined at 20 °C. The performances of [NH_3e-mim][BF_4] supported on the different types of molecular sieves are shown in Fig. 2, from which it could be seen that [NH_3e-mim][BF_4]/NaY exhibited an excellent performance with a 24-min adsorption time, while the others had no obvious adsorption effect. The results

for [OHe-mim][BF_4] supported on the studied molecular sieves are shown in Fig. S-1 of the Supplementary material to this paper, showing that [OHe-mim][BF_4]/ /USY and [OHe-mim][BF_4]/MCM-41 had weak adsorption capacities with a 4-min effective adsorption time. The results for supported [HOEAm] are shown in Fig. S-1c, from which it could be observed that IL/NaY adsorbed CO_2 for only 5 min. The CO_2 adsorption by pure NaY was also tested and the result is presented in Fig. S-2 of the Supplementary material. Thus, NaY showed no obvious adsorption capacity. The corresponding adsorption capacities of the SIL samples and pure NaY were calculated and the results are presented in Table I. Thus that CO_2 adsorption capacity of [NH_3e-mim][BF_4]/NaY was the highest with a value of 0.11 mmol CO_2 g^{-1} SIL, which is nearly three times higher than the corresponding value for [HOEAm]/NaY and five times than for [OHe-mim][BF_4]/USY.

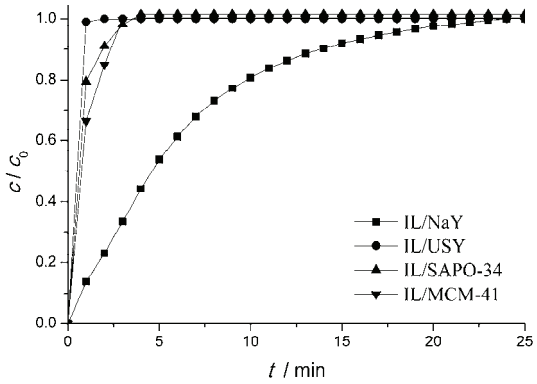

Fig. 2. Comparison of the CO_2 adsorption behavior of [NH_3e-mim][BF_4] supported on the different molecular sieves. Ionic liquid loading: 20 %, *T*: 20 °C; c_0: initial concentration of CO_2 before the adsorbent (mol/mol); *c*: concentration of CO_2 after the adsorbent (mol/mol).

TABLE I. CO_2 adsorption capacities (mmol CO_2 g^{-1}) of the molecular sieves and supported ionic liquids

Support	IL			
	NaY	USY	SPAO-34	MCM-41
[NH_3e-mim][BF_4]	0.108	0.009	0.009	0.017
[OHe-mim][BF_4]	0.009	0.022	0.012	0.017
[HOEAm]	0.030	0.013	0.009	0.006
	0.010	–	–	–

The support and the ionic liquid jointly affect the CO_2 adsorption performance of SILs, with the effect of the later being predominant. Amino functional ionic liquids adsorb CO_2 by chemical action, which to better CO_2 adsorption performances than other ionic liquids adsorb by the formation of hydrogen bonds between networks and Lewis acid–base actions between CO_2 and the anion. The different adsorption mechanisms led to the different behavior of the three studied SILs. The specific surface area and pore structure of different supports also greatly influenced the CO_2 adsorption performance of the studied SILs. Thus, [NH_3e-mim][BF_4]/NaY adsorbed CO_2 by chemical action between –NH_2 and

CO_2, which was determined by the density of the electron cloud on the nitrogen atom of the $–NH_2$ group. Hence, it could be seen that CO_2 reacts with $–NH_2$ in NaY-supported ionic liquids easier and [NH_3e-mim][BF_4]/NaY was the best adsorbent of all the studied SILs.

Effect of temperature on the CO_2 adsorption capacity

[NH_3e-mim][BF_4]/NaY with a 20 % loading was chosen to investigate the CO_2 adsorption at 20, 30, 40 and 50 °C. The obtained results are shown in Fig. S-3 of the Supplementary material. From Fig. S-3, it could be seen that [NH_3e-mim][BF_4]/NaY exhibited the best adsorption at 20 °C and based on the presented results, the absorption capacities at the different temperatures were calculated. As can be seen in Table II, the value of the adsorption capacity at 20 °C was about two-times higher than those at the other temperatures. In addition, the CO_2 adsorption capacities at 30, 40 and 50 °C showed a slight decreasing tendency with increasing temperature. As a whole, considering also energy consumption, 20 °C could be recommended as the best adsorption temperature.

TABLE II. Relationships between CO_2 adsorption capacities (mmol CO_2/g) and temperature and IL loading amount for [NH_3e-mim][BF_4]/NaY

ILs loading, %	Temperature, °C			
	20	30	40	50
10	0.071	–	–	–
20	0.108	0.057	0.055	0.054
30	0.039	–	–	–

The temperature is one of the influential factors on adsorption capacity and penetration time. When the temperature increases, the adsorption capacity for CO_2 and adsorption time were significantly decreased. The reason may be that increasing temperature limited the adsorption capacity for CO_2 because the interaction between CO_2 and $–NH_2$ is weak and reversible and thus, higher temperatures lead to desorption of CO_2. Thus, the lowest temperature was adventageous to the adsorption of CO_2 on the surface of [NH_3e-mim][BF_4]/NaY.

Effect of the ILs loading amount on CO_2 adsorption capacity

[NH_3e-mim][BF_4]/NaY was selected to investigate the effect of IL loading on the adsorption of CO_2. Hence, [NH_3e-mim][BF_4]/NaY sorbents with IL loadings of 10, 20 and 30 % were prepared. The capacities of these SILs for CO_2 adsorption at 20 °C are presented in Fig. S-4 of the Supplementary material, from which it could be seen that the SILs with 10 and 30 % loadings reached saturation after 10 min, while the SIL with a 20 % loading attained saturation after 25 min. The CO_2 adsorption capacities calculated from the data presented in Fig. S-4 for the differently loaded ILs are listed in Table II. The SIL with a 30 % loading

had the lowest CO_2 capacity, less than half of that of the SIL with a 20 % loading. The reason lies in two aspects. On the one hand, increasing the loading with IL can enhance the adsorption; on the other hand, when reaching a certain degree of loading, the micropores of the support would be blocked, and hence the process of mass transfer during CO_2 adsorption would be markedly retarded. As a result, there should be a maximum loading corresponding to a higher CO_2 adsorption capacity. From this study, the favored loading was at around 20 %.

Recyclability of the adsorbent

To examine the recyclability of [NH_3e-mim][BF_4]/NaY, the CO_2 desorption test was performed in a rotary evaporator operated under vacuum at 100 °C for 3 h. As shown in Fig. 3, the CO_2 adsorption capacity increased during the first five repetitive runs and thereafter, gradually decreased during the following cycles. The adsorption capacity reached 0.45 mmol CO_2 g^{-1} at the fifth run and decreased to 0.29 mmol CO_2 g^{-1} at the tenth run. This may be the result of loss of crystal water during vacuum heating, which would change the morphology of the IL and increase the specific surface area of the adsorbent. With less retained water, the silica–alumina ratio would become higher, the SIL more alkaline and, consequentially, the CO_2 adsorption stronger. In addition, vacuum heating may increase the viscosity of the ILs supported on NaY. Fu[12] reported that the adsorption capacity for CO_2 could be improved by increasing the viscosity of supported ILs. The decline observed in the adsorption capacity is due to the leaking of IL during transport from the reactor to the regeneration container.

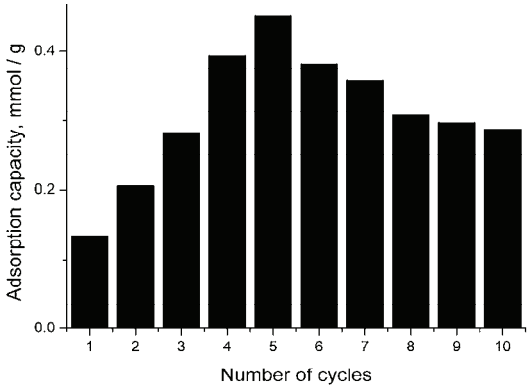

Fig. 3. Results of the recycling experiment for the adsorption of CO_2 by [NH_3e-mim][BF_4]/NaY.

Characterization of the adsorbent

A comparison of the FT-IR spectra of [NH_3e-mim][BF_4]/NaY, [NH_3e-mim][BF_4] and [NH_3e-mim][BF_4]/NaY after 10 cycles presented in Fig. 4. The comparison of FT-IR curves indicates that [NH_3e-mim][BF_4] was successfully supports on NaY. The imidazole ring skeleton stretching vibration band of [NH_3e-

-mim][BF_4] at 1571 cm^{-1} was shifted to 1573 cm^{-1} under the influence of NaY, and moved to 1575 cm^{-1} after 10 cycles. This means that the level of conjugation changed. Combined with the way of the vibration spectra changed, it could be seen that the weak interaction between [NH_3e-mim][BF_4] and NaY led to a decrease in the level of conjugation, which could increase the functional site for CO_2 capture on [NH_3e-mim][BF_4]/NaY. Vacuum heating had the same effect of increasing the functional site for CO_2 capture by decreasing the conjugation, which is consistent with the experimental results of recycling the adsorbent.

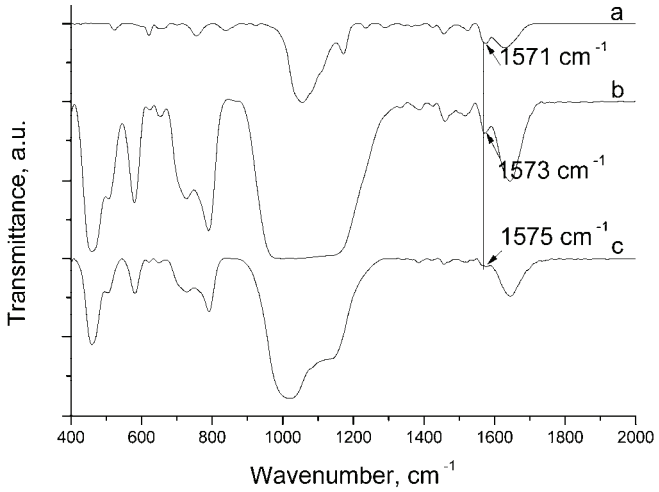

Fig. 4. FT-IR spectra of: a) [NH_3e-mim][BF_4]; b) [NH_3e-mim][BF_4]/NaY; c) [NH_3e-mim][BF_4]/NaY after 10 cycles.

The XRD patterns for NaY, [NH_3e-mim][BF_4]/NaY, [NH_3e-mim][BF_4]/ /NaY with adsorbed CO_2, [NH_3e-mim][BF_4]/NaY after 4 and adsorption cycles are shown in Fig. 5. The XRD curves indicate that the diffraction peaks of NaY supported IL were much weak at 2θ values 6.1, 9.9, 11.8, 15.6, 18.6, 20.2, 24.8 and 26.9° but they reappeared after CO_2 adsorption. By comparing the XRD patterns (c), (d) and (e) in Fig. 5, it could be seen that the characteristic peaks of NaY gradually reappear on recycling [NH_3e-mim][BF_4]/NaY. The results may probably result from changes in the intensity of light reaching NaY, due to the presence of ILs. Actually, the structure of NaY remained intact. This demonstrates that [NH_3e-mim][BF_4] had been successfully supported on NaY, which was gradually reduced on recycling. In addition, the chemical properties of NaY were stable.

The morphologies of NaY and [NH_3e-mim][BF_4]/NaY were observed using scanning electron microscopy, and the images are shown in Fig. 6. NaY had a plain surface Fig. 6a, while [NH_3e-mim][BF_4]/NaY had a rough surface, with

tiny particles evenly distributed, Fig. 6b. This confirms the FT-IR and XRD results that [NH_3e-mim][BF_4] had been successfully supported on NaY.

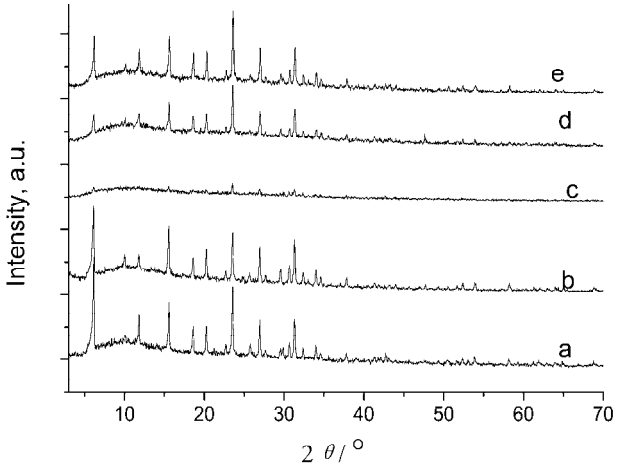

Fig. 5. The XRD patterns of: a) [NH_3e-mim][BF_4]/NaY containing adsorbed CO_2; b) NaY; c) [NH_3e-mim][BF_4]/NaY; d) [NH_3e-mim][BF_4]/NaY after 4 cycles; e) [NH_3e-mim][BF_4]/NaY after 10 cycles).

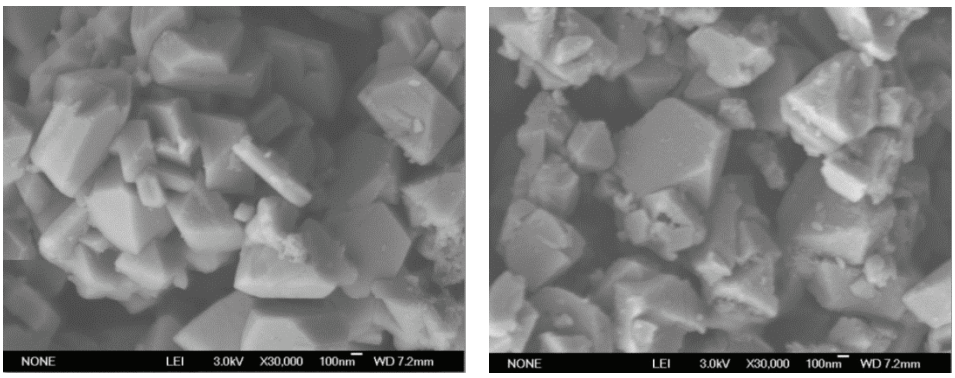

(a) (b)

Fig. 6. Scanning electron microscopy (SEM) images of (a) NaY; (b) [NH_3e-mim][BF_4]/NaY).

TG–DSC curves of [NH_3e-mim][BF_4] and [NH_3e-mim][BF_4]/NaY, both containing adsorbed CO_2 are shown in Fig. 7. As shown in Fig. 7b, the gradual weight loss of [NH_3e-mim][BF_4]/NaY had three weight loss steps. The first step from 31 to 212 °C with a weight loss 7.18 % may result from the loss of small molecules and CO_2 desorption. The second one, assigned to the decomposition of SIL, appeared from 250 to 500 °C, with weight loss 14.42 %. Compared to the decomposition temperature from 300 to 400 °C of [NH_3e-mim][BF_4] in Fig. 7a, the nature of the IL had changed. This proved that [NH_3e-mim][BF_4]/NaY ads-

orbed CO_2 by chemical action. The observed decreased stability of SIL may be due to the alkaline characteristics of NaY promoting the decomposition of IL. At 50 °C, weight loss was about 5 %. This demonstrated that [NH_3e-mim][BF_4]/ /NaY was thermally stable during the adsorption experiments. The third decomposition step from 610 to 790 °C was due to further decomposition of the SIL.

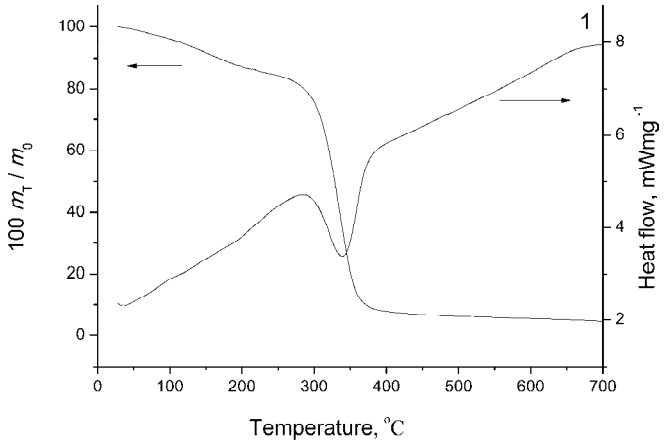

(a)

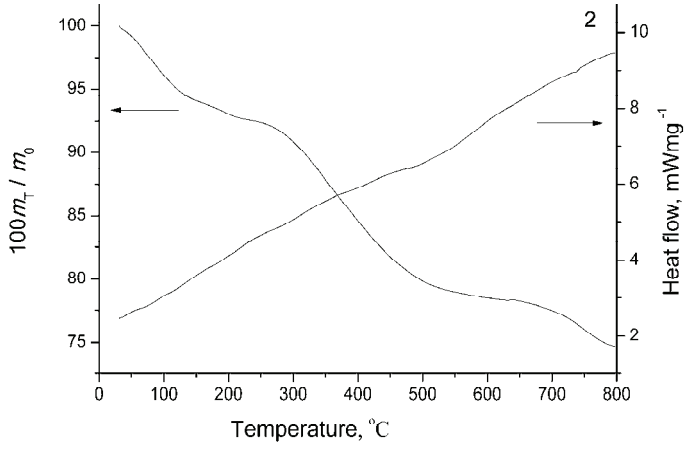

(b)

Fig. 7. TG–DSC curve of: a) [NH_3e-mim][BF_4] and b) [NH_3e-mim][BF_4]/NaY with adsorbed CO_2; m_T: mass at temperature T and m_0: initial mass.

CONCLUSIONS

FT-IR, XRD, SEM and TG–DSC results demonstrated that molecular sieve--supported ionic liquids had been successfully prepared. [NH_3e-mim][BF_4]/NaY had an excellent CO_2 adsorption performance with adsorption capacity of 0.108

mmol CO_2 g^{-1} SIL. Under the experimental temperatures, the adsorbent has good thermal stability. By optimizing the adsorption conditions, the optimal temperature was found to be 20 °C, and the optimal IL loading was 20 %. In the investigation of the recyclability of the adsorbent, the CO_2 adsorption capacity was found to increase in the first five repeated runs and gradually decrease with subsequent recycling. Vacuum heating could improve the CO_2 adsorption capacity of [NH_3e-mim][BF_4]/NaY.

SUPPLEMENTARY MATERIAL

CO_2 adsorption behaviors of supported ionic liquids and NaY, Figs. S-1 and S-2, as well as the effects of temperature and ILs loading on CO_2 adsorption by [NH_3e-mim][BF_4]/NaY, Figs. S-3 and S-4, are available electronically from http://www.shd.org.rs/JSCS/, or from the corresponding author on request.

Acknowledgments. We wish to thank the PetroChina Innovation Foundation (2013D-5006-0507) and Jinan R&D Innovation Project (201102041) for financial support.

ИЗВОД

ЈОНСКЕ ТЕЧНОСТИ НА НОСАЧУ ОД МОЛЕКУЛСКИХ СИТА КАО ЕФИКАСНИ АДСОРБЕНСИ ЗА CO_2

NA YANG[1] и RUI WANG[2]

[1]*School of Environmental Science and Engineering, Shandong University, Jinan 250100, Shandong, China и* [2]*School of Environmental Science and Engineering, Shandong University, Jinan 250100, Shandong, China*

Одабране су јонске течности [NH_3e-mim][BF4], [OHe-mim][BF_4] и [HOEAm] и нанесене на молекулска сита NaY, USY, SAPO-34 и MCM-41 као носаче. Нађено је да [NH_3e--mim][BF_4]/NaY има одличне перформансе у адсорпцији CO_2, са адсорпционим капацитетом од 0,108 mmol CO_2 g^{-1}. Испитани су оптимални адсорпциони услови и рециклибилност [NH_3e-mim][BF_4]/NaY. Резултати показују да [NH_3e-mim][BF_4]/NaY добро адсорбује CO_2 при 20 °C и 20 % садржаја јонске течности. Загревањем у вакууму адсорпциони капацитет CO_2 достиже 0,451 mmol CO_2 g^{-1} у петом пролазу, а смањује се на 0,29 mmol CO_2 g^{-1} на десетом пролазу. Одређивање структуре и карактеризација [NH_3e-mim][BF_4]/NaY је урађена FT-IR, XRD, SEM и TG–DSC методама. TG–DSC анализа је показала добру термичку стабилност [NH_3e-mim][BF_4]/NaY на температурама испод 50 °C.

(Примљено 22. фебруара, ревидирано 29. септембра, прихваћено 23. октобра 2014)

REFERENCES

1. D. L. Cui, L. Ma, *Huaxue-gongye-yu-gongcheng* **43** (2012) 12 (in Chinese)
2. F. Yang, R. Wang, *Meitan Xuebao* **38** (2012) 1060 (in Chinese)
3. K. L. In, Y. H. Ju, G. C. Chen, *Catal. Today* **148** (2009) 389
4. Z. H. Sun, Q. Wang, M. X. Song, *Chemical Industry and Engineering Progress* **32** (2013) 1666
5. X. K. Jian, S. C. Liu, Y. Bian, *Biomass Chem. Eng.* **46** (2012) 20
6. T. Yang, J. Bi, K. H. Guo, *CIESC J.* **63** (2012) 3150
7. M. Hasib-ur-Rahman, M. Siaj, F. Larachi, *Chem. Eng. Process.* **49** (2010) 313
8. S. Subbiah, S. Venkatesan, T. Ming-Chung, *Molecules* **14** (2009) 3780
9. J. Sun, W. G. Cheng, W. Fan, *Catal. Today* **148** (2009) 361

10. R. LPN, L. JNC, E. JMSS, *J. Phys. Chem., B* **109** (2005) 040
11. J. L. Anderson, D. M. Armstrong, *Anal. Chem.* **75** (2003) 4851
12. G. H. Fu, G. X. Lv, J. T. Ma, *Fenxi Ceshi Jishu yu Yiqi* **19** (2013) 41 (in Chinese)
13. P. Scovazzo, J. Kieft, D. A. Finan, *J. Membr. Sci.* **238** (2004) 57
14. H. Jeffery, M. Christina, P. Hennry, *J. Membr. Sci.* **298** (2007) 41
15. H. Zhang, J. M. Zhu, K. G. He, *Modern Chem. Ind.* **31** (2011) 45
16. L. Zhou, J. Fan, G. Cui, *Green Chem.* **16** (2014) 4009.

Journal of the Serbian Chemical Society
JSCS@tmf.bg.ac.rs • www.shd.org.rs/JSCS
J. Serb. Chem. Soc. 80 (2) S55–S57 (2015)
Supplementary material

SUPPLEMENTARY MATERIAL TO

Molecular sieve-supported ionic liquids as efficient adsorbents for CO_2 capture

NA YANG[1] and RUI WANG[2]*

[1]School of Environmental Science and Engineering, Shandong University, Jinan 250100, Shandong, China, E-mail: yangna13579@tom.com and [2]School of Environmental Science and Engineering, Shandong University, Jinan 250100, Shandong, China

J. Serb. Chem. Soc. 80 (2) (2015) 265–275

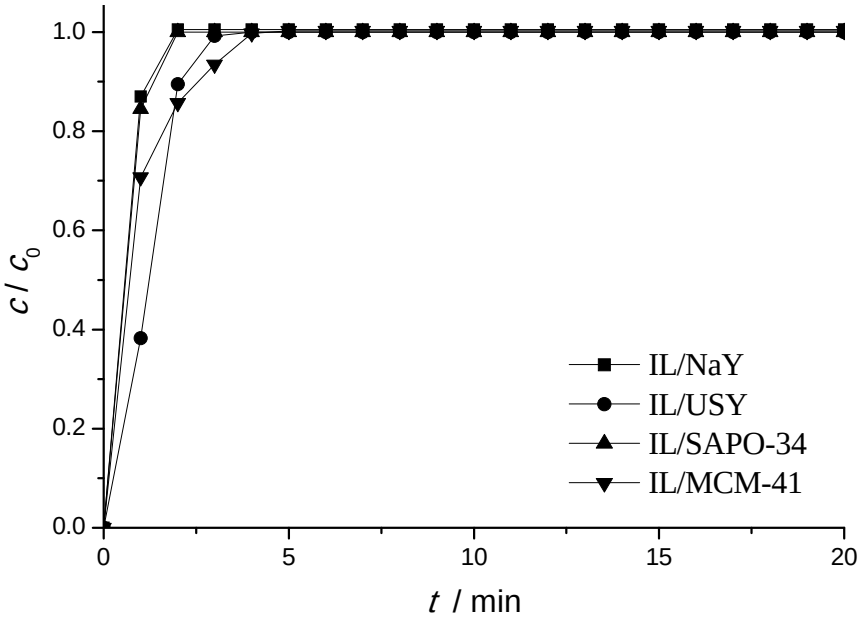

(a)

* Corresponding author. E-mail: ree_wong@hotmail.com
doi: 10.2298/JSC220214103Y

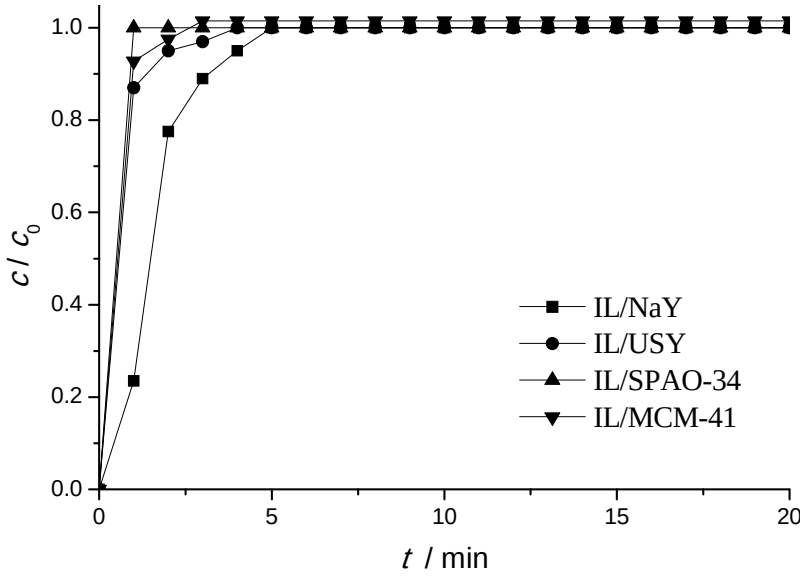

(b)

Fig. S-1. CO_2 absorption behaviors of supported ionic liquids: a) [OHe-mim][BF_4] and b) [HOEAm], ionic liquid loading: 20 %, T: 20 °C; c_0: initial concentration of CO_2 before the adsorbent (mol/mol) and c: the concentration of CO_2 after the adsorbent (mol/mol).)

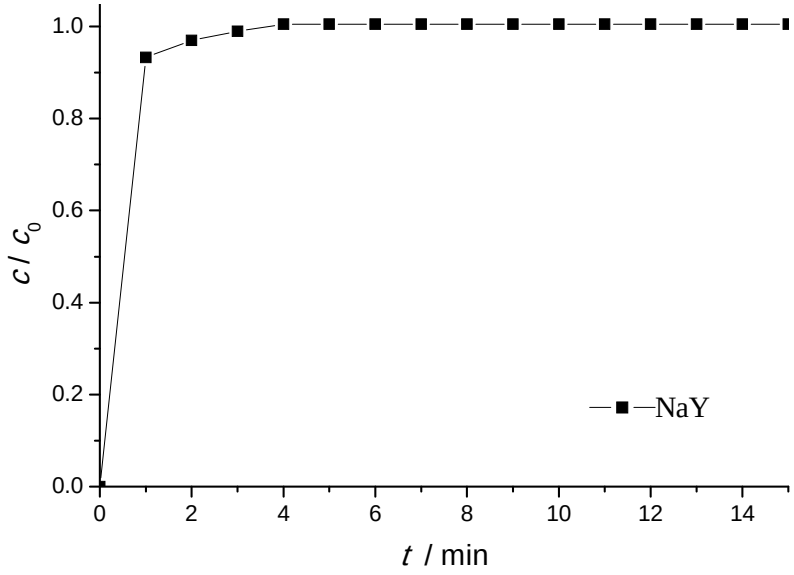

Fig. S-2. CO_2 absorption behavior of NaY.

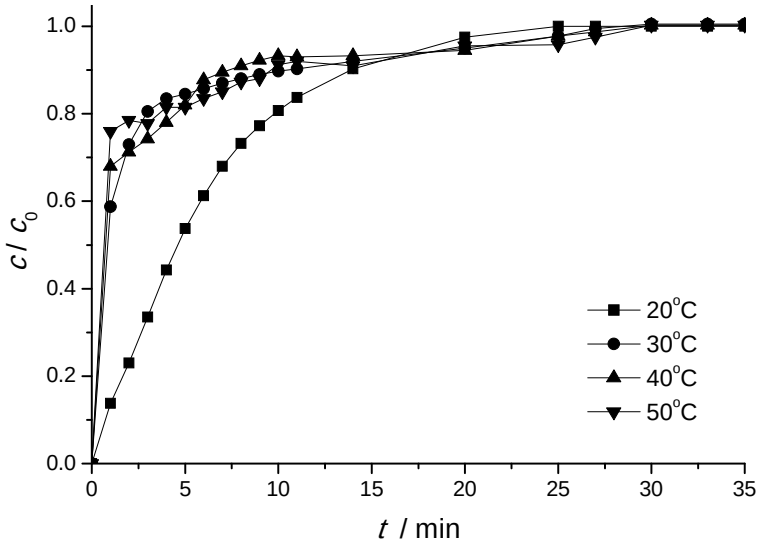

Fig. S-3. Effect of temperature on CO_2 adsorption by [NH_3e-mim][BF_4]/NaY.

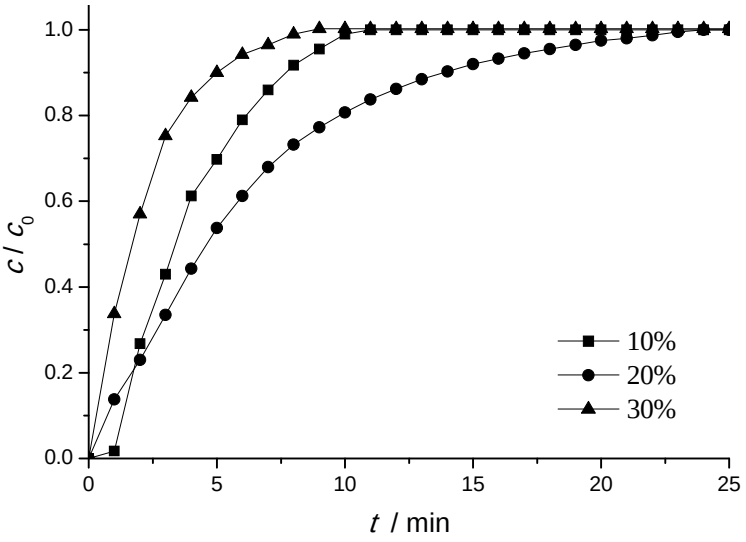

Fig. S-4. Effect of the ILs loading on CO_2 adsorption by [NH_3e-mim][BF_4]/NaY.

Journal of the Serbian Chemical Society
JSCS-info@shd.org.rs • www.shd.org.rs/JSCS

J. Serb. Chem. Soc. 80 (2) 277 (2015)

Erratum

Issue No. 9 (2014), Vol. 79, paper No. *JSCS-4656*, pp. 1185–1198:

– Supplementary material Section should read:

SUPPLEMENTARY MATERIAL

Experimental details, total concentrations of the elements in soil and the sum of the available fractions are available electronically from http://www.shd.org.rs/JSCS/, or from the corresponding author on request.